Importance of CSF circulation following ischaemic stroke: A novel MRI investigation of CSF parenchymal flow

Mohammed Shenan Alshuhri
B.A. Medical Imaging, MSc. MRI technology

Submitted in fulfilment of the requirements for the degree of
Doctor of Philosophy

Institute of Neuroscience and Psychology
College of Medical, Veterinary, and Life Science
University of Glasgow

Abstract

It has been proposed that intracranial pressure (ICP) elevation and collateral failure are responsible for unexplained early neurological deterioration (END) in stroke. Our aim was to investigate whether cerebrospinal fluid (CSF) dynamics, rather than oedema, are responsible for elevation of ICP after ischaemic stroke. Permanent middle cerebral artery occlusion (pMCAO) was induced with an intraluminal filament. At 24 hours after stroke, baseline ICP was measured, and CSF dynamics were probed via a steady-state infusion method. For the first time, we found a significant correlation between the baseline ICP at 24 hours post-stroke and the value of CSF outflow resistance. Results show that CSF outflow resistance, rather than oedema, was the mechanism responsible for ICP elevation following ischaemic stroke. This challenges current concepts and suggests the possibility that intracranial hypertension may be occurring undetected in a much wider range of stroke patients than is currently considered to be the case.

Over the last decade, there has been significant renewed interest in the anatomical pathways and physiological mechanisms for the circulation of CSF. The glymphatic system is one such pathway that has been recently characterised. This network drives CSF into the brain along periarterial spaces and interstitial fluid (ISF) out along perivenous spaces. Aquaporin-4 (AQP4) water channels, densely expressed at the vascular endfeet of astrocytes, facilitate glymphatic transport. Glymphatic failure has been linked to a broad range of neurodegenerative diseases including ischaemic stroke. Accordingly, if the glymphatic circulation is a major outflow route for CSF, glymphatic dysfunction following ischaemic stroke could alter CSF dynamics and, therefore, ICP.

Nevertheless, the glymphatic hypothesis is still controversial. All *in vivo* and biomechanical modelling studies that have investigated the glymphatic system have been based on utilizing a solute tracer to track the movement of CSF within the intracranial space. Since 99% of CSF is water, it is questionable whether non-water tracer molecules can ever show the real dynamic flow of CSF. Hence, we sought the develop of a new MRI method to directly image CSF dynamics in-vivo, by exploiting an isotopically enriched MRI tracer, namely, $H_2^{17}O$. Our results reveal glymphatic flow that is dramatically faster and more

extensive than previously thought. Moreover, we confirm the critical role of aquaporin-4 (AQP4) channels in glymphatic flow by imaging CSF water dynamics in the brain using $H_2^{17}O$ alongside a potent blocker of AQP4. We hope in future that this new method can be used to investigate the responsible mechanism for the increased CSF resistance and ICP elevation following ischaemic stroke.

Table of Contents

List of Tables

List of Figures

List of Publications

Alshuhri MS, Gallagher L, McCabe C, Holmes WM. Change in CSF Dynamics Responsible for ICP Elevation After Ischemic Stroke in Rats: a New Mechanism for Unexplained END? Transl Stroke Res. 2020 Apr;11(2):310-318. doi: 10.1007/s12975-019-00719-6. Epub 2019 Aug 15. PMID: 31418164.

Alshuhri MS, Gallagher L, Work LM, Holmes WM. Direct imaging of glymphatic transport using H217O MRI. JCI Insight. 2021 May;6(10). DOI: 10.1172/jci.insight.141159.

List of Conference Presentations

Alshuhri MS, Gallagher L, McCabe C, Holmes WM. Change in CSF Dynamics after Ischemic Stroke in Rats. 3rd UK Stroke Conference 2019. Chancellor's Hotel & Conference Centre, Manchester.

Alshuhri MS, Gallagher L, McCabe C, Holmes WM. Change in CSF Dynamics after Ischemic Stroke in Rats. UK Preclinical Stroke Symposium 2019

Acknowledgement

Throughout the writing of this dissertation, I have received a great deal of support and assistance.

I would like to thank the Minister of Education in Saudi Arabia who provided me with an opportunity to study in the UK, without the financial support, it would not have been possible to achieve all of this.

I would like to express my sincere gratitude to my supervisor Dr William Holmes for his invaluable supervision, support, and tutelage during the course of my PhD degree.

Also, I would like to offer my appreciation of my other supervisors, Dr Christopher McCabe, and Dr Lorraine Work.

Further, I wish to acknowledge the help provided by Lindsay Gallagher, Jim Mullins, Linda Carberry, and Conor Martin of GEMRIC. To Lindsay, I cannot put into words how much I appreciate your help with the animal surgery, none of my experiments would have been possible without your help.

I would like to acknowledge my colleagues for their wonderful collaboration. You supported me greatly and were always willing to help me.

Finally, I would like to express my gratitude to my parents, my wife, and my children. Without their tremendous understanding and encouragement in the past few years, it would be impossible for me to complete my study.

Definitions/Abbreviations

aCSF	Artificial cerebrospinal fluid
ADC	Apparent diffusion coefficient
AQP4	Aquaporin-4
AQP1	Aquaporin-1
AUC	Area under curve
BBB	Blood brain barrier
CBV	Cerebral blood volume
CNS	Central nervous system
CSF	Cerebrospinal fluid
DCE-MRI	Dynamic enhanced magnetic resonance imaging
DTPA	Diethylenetriamine pentaacetic acid
DWI	Diffusion weighted imaging
ECS	Extracellular space
END	Early neurological deterioration
EPI	Echo planar imaging
FLASH	Fast low angle shot
FOV	Field-of-view
FT	Fourier transform
FID	Free induction decay
Gd	Gadolinium
GE	Gradient echo
ICP	Intracranial pressure
ISF	Interstitial fluid
IP	Intraperitoneal
IR	Inversion recovery
IV	Intravenous
LSCI	Laser speckle contrast imaging

MAP	Mean arterial pressure
MCA	Middle cerebral artery
MCAO	Middle cerebral artery occlusion
MRI	Magnetic resonance imaging
NA	Number of averages
$PaCO_2$	Arterial carbon dioxide tension
PaO_2	Arterial oxygen tension
pMCAO	Permanent middle cerebral artery occlusion
PET	Positron emission tomography
RARE	Rapid acquisition with refocused echoes
RF	Radio frequency
ROI	Region of interest
SAS	Subarachnoid space
SE	Spin echo
SNR	Signal-to-noise ratio
TE	Echo time
TI	Inversion time
TR	Repetition time
WKY	Wistar Kyoto rat

1 Chapter 1: Literature review

This Chapter discusses the current understanding of cerebrospinal fluid (CSF) physiology and controversies in the field, while exploring how altered secretion and drainage may link to ICP in Ischaemic stroke. The Chapter closes by investigating the current and potential magnetic resonance imaging (MRI) techniques, along with non-MRI methods, for a better understanding of the CSF system.

1.1 Cerebrospinal fluid dynamics

1.1.1 CSF function

Within the central nervous system (CNS), 60–68% of the total water content is found within the intracellular space and the remaining 32–40% occupies the extracellular compartment. CSF comprises approximately 10% of extracellular fluid (Oliver, 2004). In humans, the secretion rate is 0.3–0.4 ml min^{-1} and the total CSF volume is 90–150 ml (Ekstedt, 1978). CSF serves as a fluid envelope that protects the brain and spinal cord, cushioning them from mechanical injury. Further, CSF plays an essential role in maintaining homeostasis in the extracellular environment of neurons and glia. CSF is in free communication with the extracellular fluid, thus indirectly regulating its composition. CSF has also been suggested as playing a role in the clearance of potentially harmful metabolites within the CNS, particularly high-molecular weight substances such as proteins (Oliver, 2004; Hladky and Barrand, 2014). Further, reduced CSF secretion as a function of aging (Sakka, Coll and Chazal, 2011) leads to increased protein aggregation and is associated with increased beta-amyloid deposition in Alzheimer's disease (May *et al.*, 1990; Ueno *et al.*, 2014).

1.1.2 CSF secretion

According to the traditional hypothesis, CSF is formed in brain ventricles, mostly by secretion from the choroid plexus. Because of its glandular appearance and ventricular location, the choroid plexus has been suggested as the major site of CSF secretion. Some of the first supporting evidence for the role of the choroid plexus in CSF secretion came from the historical canine experiment of Dandy (Dandy and Blackfan, 1914). In his famous experiment using a dog, he

1 demonstrated that ventricular dilation does not occur when foramen of Monro is

2 occluded and the choroid plexus excised from the lateral ventricle. The

3 dilatation is observed on the side in which choroid plexuses are preserved,

4 suggesting that choroid plexuses are the site of CSF production. Further

5 evidence includes experiments by Welch et al. (1972) in which the authors

6 measured the haematocrit in the main choroidal artery and choroidal vein in an

7 animal study which demonstrated a higher haematocrit in the main choroidal

8 vein when compared to the main choroidal artery. In addition, based on

9 histological observation, Davson suggested that the choroid plexus structure is

10 ideal for CSF production (Davson, Domer and Hollingsworth, 1973). The choroid

11 plexus is highly organized and lines all the ventricles of the brain except the

12 frontal/occipital horn of the lateral ventricles and the cerebral aqueduct. The

13 choroid plexus is well perfused by numerous villi, each having a central capillary

14 with fenestrated endothelium and surrounded by a single layer of secretory

15 epithelial cells. This permits the movement of crystalloids, colloids, and fluid

16 from the blood into the ventricles by a combined process of passive filtration of

17 fluid across the highly permeable capillary endothelium and a regulated

18 secretion across the single-layered choroidal epithelium (Brinker *et al.*, 2014).

19 The capillaries of the choroid are freely permeable to solutes. However, the

20 tight junctions between epithelial cells of the choroid plexuses form the blood–

21 CSF barrier, which control the passage of molecules and water into the CSF

22 (Price, 2008; Jorge, 2010). Aquaporin-1 (AQP1) water channels are highly

23 expressed on the ventricular-facing cell plasma membrane of choroid plexus

24 epithelial cells, suggesting a role for these water channels in CSF secretion

25 (Mobasheri and Marples, 2004). Consistent with the classic CSF secretion theory,

26 AQP1-null mice showed a reduction of 20% in CSF production compared with

27 wild-type mice (0.38 ± 0.02 vs. 0.30 ± 0.01 $\mu l\ min^{-1}$), suggesting a prominent role

28 of the AQP1 on CSF formation (Oshio, 2004).

29 Several studies have suggested structures, other than the choroid plexus, as sites

30 of CSF production. It was shown that removal of the choroid plexuses within the

31 bilateral ventricles had no significant effect on the amount and composition of

32 CSF produced (Hammock and Milhorat, 1973). Other studies with radioactive

33 water provided evidence that the brain itself is another source of CSF (Cohen

34 and Davies, 1937; Bering, 1959; Bering and Sato, 2009). Furthermore, by

1   examining the ependymal surface, it was calculated that nearly 30% of the total

2   CSF production may come from the ependyma of the spinal cord's central canal

3   (Pollay and Curl, 1967). Filtration or secretion of fluid across capillary walls may

4   also contribute to total CSF production (Klarica, Radoš and Orešković, 2019).

5   Other extrachoroidal sources of CSF proposed in the literature include the

6   subarachnoid space, the perivascular system or the pial artery (Weed, 1914;

7   Hassin, 1948; Sato *et al.*, 1971), although their relative contributions have not

8   yet been established.

9   ### 1.1.3 CSF absorption

10   In 1875, Key and Peele performed crucial experiments that showed that the

11   arachnoid villi were the drainage points connecting the CSF and blood from the

12   venous sinuses (Key and Peele, 1875). For a long time thereafter, there was a

13   broad consensus about arachnoid granulation (villi) being the main absorption

14   pathway for CSF.

15   Arachnoid granulations project from the subarachnoid space and protrude the

16   overlying dura and invaginate through the walls of the superior sagittal sinus.

17   Arachnoid villi act as one-way valves allowing the transcellular bulk transport of

18   fluid with hydrostatic pressure being the main stimulus that causes these valves

19   to open (Levine, Povlishock and Becker, 1982). Extracorporeal perfusion of

20   excised dura has demonstrated the passage of particles up to the size of

21   erythrocytes (~6–8 μm) at the same flow rate, suggesting that CSF compositions

22   did not measurably affect the absorption rate (Pollay and Welch, 1962).

23   While the arachnoid granulations (villi) provide a simple mechanism for resorbing

24   CSF, several studies suggest that alternative mechanisms may operate as well.

25   An interesting observation from human studies indicated that arachnoid villi do

26   not exist during prenatal and neonatal stages (Gomez *et al.*, 1983). Similarly,

27   the pressure gradient necessary for CSF absorption across the arachnoid villi is

28   not reached until several weeks after birth. Together, these data suggest the

29   existence of alternate CSF absorption routes, at least during the foetal and

30   neonatal stages in humans (Bueno and Garcia-Fernàndez, 2016).

1 Considerable volume of CSF may be absorbed into the cervical lymphatics. It has
2 long been known that contrast material injected into the subarachnoid space
3 can later be found in cervical and spinal lymphatics across several species (Kida,
4 Pantazis and Weller, 1993). Other studies showed that injection of albumin dye
5 into the lateral ventricle of rabbits travelled into the cervical lymph nodes in a
6 few hours (Kida, Pantazis and Weller, 1993). The use of specific tracers has
7 demonstrated an extension of the subarachnoid space that follows the olfactory
8 tracts, crosses the cribriform plate, and projects into the nasal submucosa
9 alongside olfactory nerves responsible for removal of some of the CSF solute.
10 This fraction appears to be closer to 50% in rats and rabbits, but its magnitude in
11 humans is not known (Arnold, Ritter and Wagner, 1973; Jackson, Tigges and
12 Arnold, 1979; Szentistvanyi *et al.*, 1984). More recent published paper
13 convincingly provided, for the first time, evidence of the presence of lymphatic
14 vessels immediately adjacent to the Dural sinuses of the meninges, including the
15 superior sagittal sinus and the transverse sinuses, as well as aligning the
16 meningeal vascular supply (Louveau *et al.*, 2015). These lymphatic vessels were
17 connected to deep cervical lymph nodes, expressed all the markers for
18 endothelial cells, and carried fluid containing monocytes, macrophages (the
19 primary immune cells within the brain) and T cells.

20 ### 1.1.4 CSF circulation

21 According to the classical textbook model of CSF circulation in the brain, CSF in
22 CNS compartment consists mainly of two kinds of motion: a net flow and a
23 pulsatile flow. The net flow is based on a hydrostatic pressure gradient primarily
24 between the choroidal plexus and arachnoid granulations (Pollay and Curl, 1967;
25 Davson, 1969; Levine, Povlishock and Becker, 1982; Walter, 2015) (Figure 1-1).
26 Pulsatile flow is based on the Monro (1783) and Kellie (1824) doctrine which
27 states that the sum of blood, CSF, and brain parenchyma volumes is constant,
28 limited by the volume of the skull; therefore, an increase in one compartment
29 leads to a decrease in another one (Mokri, 2001). It results in cranio-caudal
30 movement during the systolic phase and caudo-cranial movement during the
31 diastolic phase (Ohara *et al.*, 1988; Greitz, Franck and Nordell, 1993; Jeong *et*
32 *al.*, 2004). Recent research has further correlated CSF flow through the system
33 with respiration rate (Yamada *et al.*, 2013). Over the last decade, there has
34 been several views imply that the whole process of CSF circulation seems to be

1   more complicated and reveal the need for further exploration (Iliff *et al.*, 2012;

2   Bakker *et al.*, 2016; Klarica, Radoš and Orešković, 2019). A continuous pathway

3   along the capillaries to the perivenous space has been proposed (Iliff *et al.*,

4   2012), and capillaries continuously filter and absorb water within the cerebral

5   parenchyma, but not usually with a net flow of water (Klarica, Radoš and

6   Orešković, 2019).

7
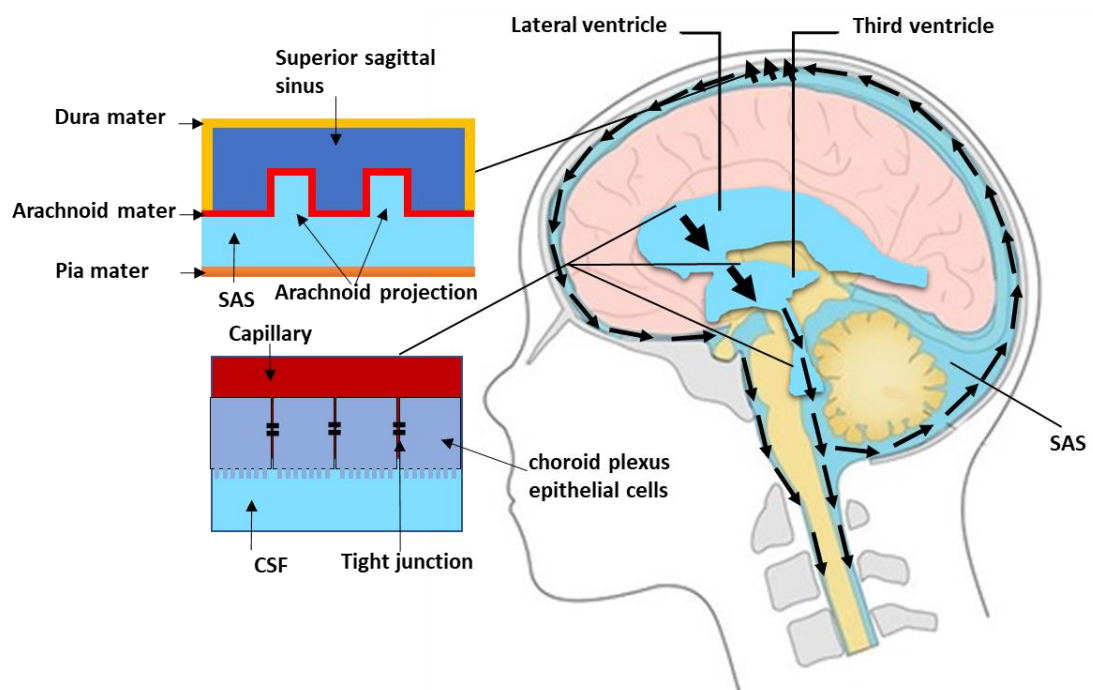
8

9   **Figure 1-1. Conventional view of CSF flow. CSF is produced mainly by the choroid plexus**

10   **that surrounds the ventricles, beginning in the lateral ventricles, and flows through the**

11   **ventricular spaces, the cisterns, the subarachnoid space and the spinal cord, finally to be**

12   **retained in the blood at the level of the arachnoid granulation (villi). Arrows depict the flow**

13   **of CSF from the lateral ventricle origin.**

14

15

16

17

1.1.5 The exchange between CSF and ISF

To fulfil its suggested lymphatic function, CSF in the subarachnoid space must then be able to enter the brain to renew ISF, and solute must be able to drain back to CSF to achieve waste removal and volume homeostasis (Hassin, 1924; Bradbury and Kleeman, 1967). However, controversies exist regarding the nature of the exchange between ISF and CSF (Szentistvanyi *et al.*, 1984; Abbott, 2004; Liao and Padera, 2013; Brinker *et al.*, 2014). The movement of fluids through the brain interstitial space has been traditionally attributed to diffusion processes. Early observations by Fenstermacher and Patlak (1975) characterized the material exchange between the CSF and extracellular fluid in the brain parenchyma as a diffusion process. Nevertheless, from time to time, this hypothesis has been challenged on the basis of experimental data. When tracers of different molecular weight, including albumin (69 kDa) and polyethylene glycols (4 kDa), were injected into the caudate nucleus of rats, despite there being an approximately five-fold difference in diffusion coefficients between these molecules all were cleared with a nearly equivalent half-life (Cserr, Cooper and Milhorat, 1977). From this it was concluded that bulk flow mechanisms contributed to the clearance of tracers. Further, following the injection of horseradish peroxidase (HRP) into the lateral ventricles or subarachnoid space of anesthetized cats and dogs, Rennels et al. (1985). showed a rapid movement of the tracer into the brain along para-arterial pathways. Interestingly, a recent 3D electron microscopy (EM) reconstruction revealed that cerebral blood vessels are completely sheathed by astrocyte endfeet, ensuring the patency of this perivascular compartment (Mathiisen *et al.*, 2010). More recently, the glymphatic system was proposed as macroscopic waste clearance system that utilizes a unique system of perivascular channels (Iliff *et al.*, 2012).

1.1.6 Glymphatic system

The proposed glymphatic system operates as a clearance mechanism that relies on AQP4 water channels, expressed in the end feet of astrocytes, to facilitate CSF bulk flow through brain tissue, washing away toxic proteins and other waste as it proceeds (Figure 1-2) (Iliff *et al.*, 2012). The dynamics of the glymphatic system were characterized by labelling CSF with fluorescent tracers injected into the cisterna magna of mice. The tracer movement was monitored in real-

1 time using *in vivo* two-photon microscopy via a closed cranial window

2 preparation, and *ex vivo* confocal microscopy (Iliff *et al.*, 2012). From the

3 subarachnoid space, CSF follows arteries at the pial surface, running across the

4 cortical surface and descending along penetrating arteries through Virchow-

5 Robins spaces/perivascular spaces. The perivascular spaces are filled with CSF

6 and are bordered by a leptomeningeal cell layer on both the inner wall facing

7 the vessel and on the outer wall facing the perivascular astrocytic end feet.

8 From the perivascular spaces, CSF then flows across the glial basement

9 membrane and astroglial end feet bordering the brain parenchyma. AQP4 water

10 channels are expressed in a highly polarized manner in astrocytic end feet. They

11 operate as a highway for CSF water influx into the brain parenchyma, where it

12 exchanges with ISF before flushing out of the brain along the perineural sheaths

13 of cranial nerves, meningeal lymphatic vessels and arachnoid granulations

14 (Jessen *et al.*, 2015).

15 Following these initial findings, further studies have found a wide variety of

16 physical factors that affect glymphatic transport. It has been demonstrated that

17 levels of arousal help govern glymphatic CSF and ISF dynamics. Nedergaard and

18 colleagues revealed that the CSF influx increases naturally during sleep or

19 ketamine/xylazine anaesthesia, which they linked with the increased

20 extracellular space (ECS) associated with the sleep state (Xie *et al.*, 2013). In a

21 subsequent experiment, the crucial role of arterial pulsation was identified, by

22 showing that glymphatic flux was diminished when the carotid artery was ligated

23 to reduce arterial pulsatility in the brain by 50% (Iliff *et al.*, 2013). Conversely,

24 increasing pulsatility by 60% using an adrenergic agonist enhanced the flux (Iliff

25 *et al.*, 2013). These findings suggested that glymphatic flow, at least in part, is

26 driven by arterial pulsatility and this could explain why perivascular influx occurs

27 preferentially around pulsating arteries and not cerebral veins.

28 Body posture also regulates clearance, with glymphatic transport being shown to

29 be more efficient in the lateral position compared with other positions (Lee *et*

30 *al.*, 2015). Other mechanisms also have been proposed as the driving force for

31 this flow: an overall pressure gradient created by the production of CSF in the

32 choroid plexuses; or a pressure gradient driven by respiration (Yamada *et al.*,

33 2013).

The dysfunction of the glymphatic system has been implicated in a variety of neurologic diseases. Reduced glymphatic flow has been detected in animal models of Alzheimer's disease (Iliff *et al.*, 2013; Xu *et al.*, 2015), vascular dementia (Venkat *et al.*, 2018), traumatic brain injury (Ren *et al.*, 2013), subarachnoid haemorrhage and acute ischaemia (Gaberel *et al.*, 2014).

1.1.7 Controversies related to Glymphatic system

In contrary to initial glymphatic experiments, other researchers have found, that tracers injected directly into the parenchyma were washed out along basement membranes of capillaries and arteries, going in the opposite direction of blood flow. It was suggested that this flow is driven by the movement of smooth muscle cells (Carare *et al.*, 2008; Bakker *et al.*, 2016).

With regard to AQP4 channels, the proposed glymphatic system emphasizes a significant role for these channels in facilitating the CSF-ISF exchange of water molecules. Monitoring CSF radiolabelled tracer movement in AQP4 knockout mice revealed a reduction of ~65% in CSF flux through the parenchyma compared with wildtype control mice. Clearance of radiolabelled tracer substances from the brain also reduced by 55% (Iliff *et al.*, 2012). Conversely, the contribution of AQP4 in this system has been questioned by Verkman and Smith as, in their own mouse model, AQP4 was not needed for solute removal in the brain (Smith and Verkman, 2018). With the aim of resolving this discrepant finding, a study representing the work of five research groups using five different mouse strains supported the key role of AQP4 in facilitating brain waste clearance (Mestre *et al.*, 2018).

The initial description of the glymphatic system suggested the presence of a bulk water flow directed from arterial to venous PVS through the interstitium. However, this hypothesis is controversial. Currently, one of the leading theories opposed to the glymphatic hypothesis suggests that convective flow of CSF influx takes place along the perivascular spaces of larger vessels, but that diffusion dominates in the tortuous interstitium (Brinker *et al.*, 2014; Jin, Smith and Verkman, 2016). Further, several mathematical models proposed that high hydraulic resistance from tight extracellular spaces cannot permit bulk flow (Asgari, de Zélicourt and Kurtcuoglu, 2016; Abbott *et al.*, 2018; Smith and

1   Verkman, 2018). Recently, Ray et al. simulated both interstitial diffusion and

2   bulk flow, comparing the results with a variety of experimental data. They

3   concluded that, for the large molecules, bulk flow may be an important

4   mechanism of transport (Ray, Iliff and Heys, 2019).

5
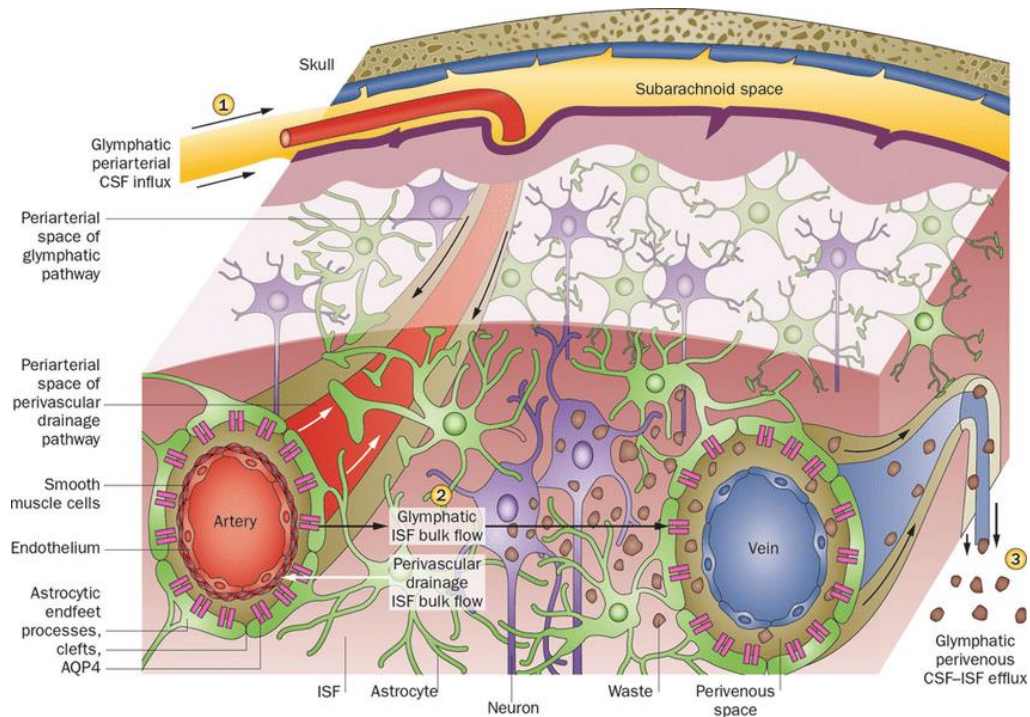
6

7   **Figure 1-2. Schematic of glymphatic and perivascular waste clearance routes. According to**
8   **the glymphatic model, CSF flows along para-arterial spaces, mixes with ISF, and is cleared**
9   **from the brain along para-venous spaces. Efficient glymphatic clearance of waste and**
10   **solutes is dependent on fluid movement across AQP4 channels located on astrocytic end**
11   **feet surrounding the parenchymal vasculature. Reproduced with permission from Conway**
12   **et al. (2015)**

13

14

15

16

17

18

1.2 CSF and intracranial pressure elevation in ischaemic stroke

The relationship between CSF and intracranial pressure (ICP) originated in the Monro-Kellie doctrine, which proposed that, because the skull cannot expand, the sum of the volumes of the brain, cerebrospinal fluid and intracranial blood is constant (Mokri, 2001). An increase in one should be compensated by a decrease in one or both of the remaining two compartments. Once these compensatory mechanisms are exhausted, ICP will rise dramatically (Figure 1-4). Hence, CSF is an important component in maintaining a stable ICP. Most mathematical models that have been developed focus on CSF formation and resistance as key factors involved in the regulation of steady state ICP (Davson, Domer and Holungsworth, 1973; Ekstedt, 1977; Marmarou, Shulman and Rosende, 1978). Davson's mathematical model provided an improved understanding of secretion and absorption mechanisms of CSF (Davson, Domer and Hollingsworth, 1973). Davson suggested that, under normal conditions, mean ICP is balanced by CSF formation rate and absorption resistance if venous pressure remained constant (Davson, Domer and Hollingsworth, 1973):

$$\text{ICP} = \text{CSF formation rate} \times \text{CSF outflow resistance} + \text{venous pressure} \tag{2.1}$$

We can conclude that within the rigid, non-expandable system, mean ICP remains constant under normal balance between formation and absorption. However, when the balance is disrupted, this will result in raised ICP. Accordingly, altering CSF dynamics in terms of rates of production and outflow resistance has been considered with elevated ICP in neuropathologies including hydrocephalus (Jergović *et al.*, 2016), idiopathic intracranial hypertension (Segal and Pollay, 1977; Fraser and Plant, 2011; Goudie, Burr and Blaikie, 2018), intracerebral haemorrhage (Williamson *et al.*, 2019), and subarachnoid haemorrhage (Fujii *et al.*, 2013).

1.2.1 Ischaemic stroke

Stroke is a catastrophic disease with high rates of morbidity and the fourth most frequent cause of death in the UK. Every year in the UK over 100,000 individuals suffer a stroke, which equates to a stroke occurring in the population every 5 minutes (Stroke.org.uk, 2018). Between 1990 and 2010, the incidence of stroke fell by almost 25% across the UK due to improvements in stroke prevention and increasing awareness of healthy living. However, it is estimated that the incidence of stroke will increase in the coming decades in developed countries due to the ageing population and an expected increase in population size (Stevens and Emmett, 2017). The economic burden of stroke is huge. From the most recent academic and National Audit office analyses, the estimated health and societal costs of stroke are £25.6 billion annually in the UK (Stroke.org.uk, 2018).

The World Health Organization defined stroke as "rapidly developing clinical signs of focal (or global) disturbance of cerebral function, lasting more than 24 hours or leading to death, with no apparent cause other than that of vascular origin" (Aho *et al.*, 1980). Transient ischaemic attacks (TIAs) have the same clinical characteristics as stroke, but symptoms can be resolved within 24 hours. As 15 to 30 percent of cerebral infarctions are accompanied by a TIA, a TIA should be considered a warning sign of stroke or other cardiovascular complications (Stroke.org.uk, 2018).

The vascular mechanisms leading to stroke can be classified as haemorrhagic and ischaemic. Haemorrhagic strokes account for a small proportion of cases (~15%) and commonly occur due to the rupturing of a vessel within the brain (intracerebral haemorrhage) or on the surface of the brain (subarachnoid haemorrhage) (Warlow *et al.*, 2003). The majority of strokes are ischaemic, accounting for approximately 85% of all stroke cases (Figure 1-3). This type of stroke results from blood flow disruption caused by blood vessel occlusion. The reduction in blood flow can be transient or permanent and the territory of the occluded cerebral artery determines the brain area affected by the stroke and the symptoms exhibited by the patient.

1 Ischaemic stroke often arises either from atherosclerotic plaques, or from a

2 displaced embolus. Fifty percent of ischaemic strokes are a direct result of

3 vascular blockage or stenosis often associated with an atherosclerotic plaque in

4 a damaged artery within or leading to the brain (thrombotic stroke) (Warlow *et*

5 *al.*, 2003). The site of the occlusion is often at bifurcation points of the arterial

6 system due to a combination of turbulent flow and weakened vessel walls at

7 these regions. Emboli which arise during atrial fibrillation account for 20% of

8 occlusive strokes. A clot that forms elsewhere in the body then travels to the

9 brain where it blocks a cerebral artery (embolic stroke). The remainder are the

10 result of occlusions in small intracranial vessels and lacunar strokes, which

11 affect small arterioles, often caused by hypertension leading to morphological

12 changes (Arboix, 2014).

13 **1.2.1.1 Animal models of ischemic stroke**

14 Ischaemic stroke has been modelled in a variety of animal species, enabling an

15 extensive understanding of the mechanisms and pathways associated with

16 cerebrovascular occlusion (Mhairi, 1992; Hunter, Green and Cross, 1995; Cenci,

17 Whishaw and Schallert, 2002). Rats and mice have very similar cerebral blood

18 vessel anatomy to humans and, as such, are the most widely used animals in

19 stroke models. Studies in rodents are also economically viable due to low

20 maintenance costs and the availability of inbred strains bred for genetic

21 homology means that infarction size and distribution is relatively reproducible

22 (Casellas, 2011). The middle cerebral artery (MCA) is the most commonly

23 affected artery of acute ischaemic stroke (Ng *et al.*, 2007). It is therefore the

24 most commonly occluded artery in experimental ischaemic stroke models (Cenci,

25 Whishaw and Schallert, 2002). The most widespread method of MCA occlusion in

26 rats and mice is the intraluminal filament technique (E Z Longa *et al.*, 1989;

27 Yoshimoto *et al.*, 1990; Mhairi, 1992).

28 Modelling MCAO has several advantages. MCAO models in rat mimics human

29 ischaemic stroke, which often originates from MCAO, and exhibits a penumbra

30 that is similar to that of human stroke (Derugin *et al.*, 2000). Also, the model is

31 suitable for permanent or transient ischaemia. The procedure is relatively easy

32 to perform and not time-consuming. Additionally, the brain injury produced by

33 MCAO in rodents varies considerably in its size and distribution (Longa *et al.*,

1989). Even though, the latter is considered one of the main disadvantages of this type of model, but it was an advantage within the current work, as this will allow us to compare ICP values with a variety of oedema and infarct volumes. On the other hand, this model presents some limitations. Successful MCAO cannot be confirmed visually. Also, MCAO models can result in high mortality rate (Wiendl *et al.*, 2015). Other limitations include the error of inducing subarachnoid haemorrhage due to advancing the filament well beyond the origin of the MCA (Longa *et al.*, 1989).

1
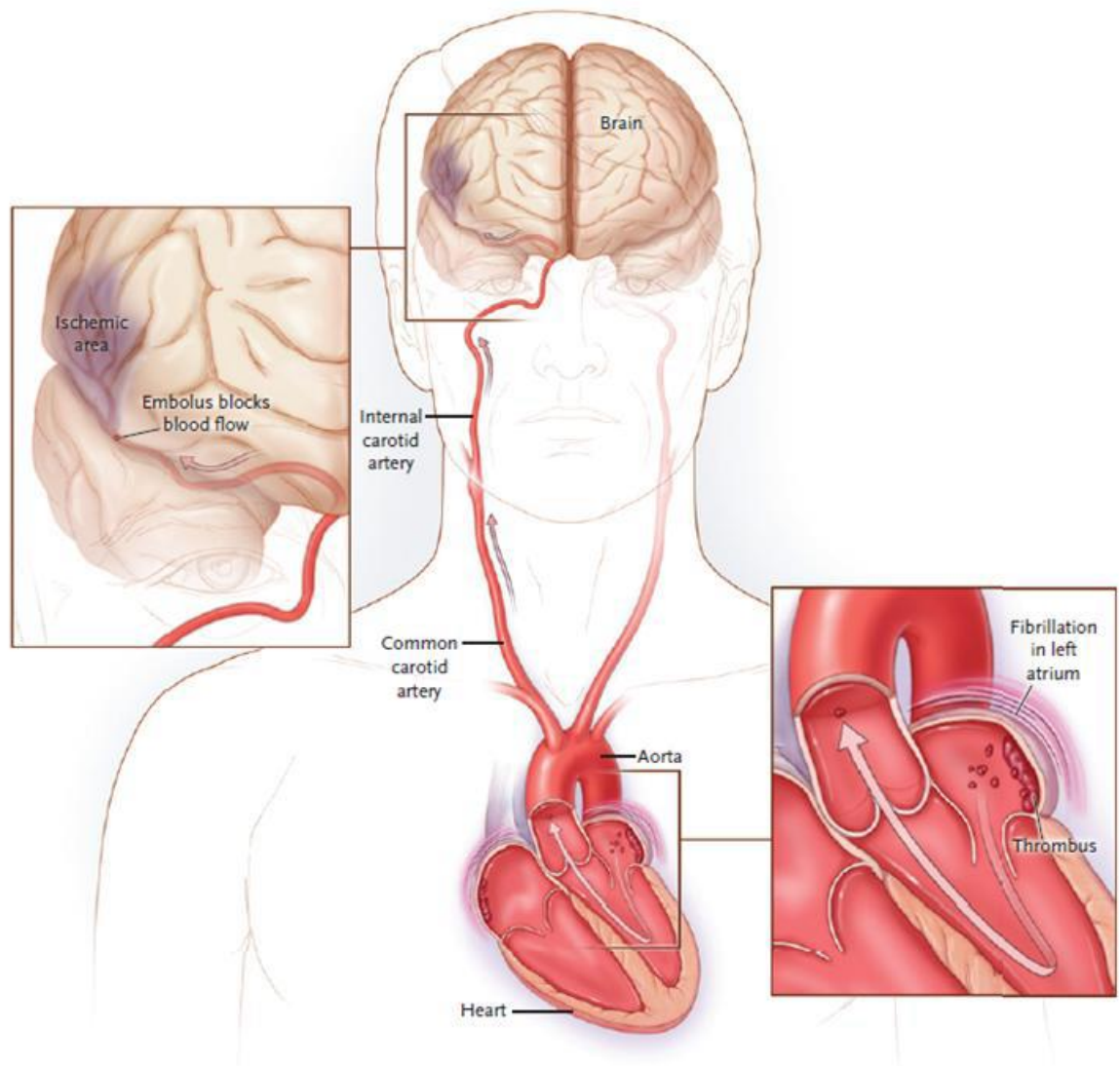
Figure 1-3. Ischaemic stroke arising from a cardiac embolus.Stroke arising from a cardiac embolus accounts for around a quarter of all cases of ischaemic stroke. Reproduced with permission from (Go, 2009). Copyright Massachusetts Medical Society.

2
3
4
5

6

7

8

9

10

11

12

13

14

15

16

1.2.2 Impact of ICP on Ischaemic stroke

There are two significant regions of tissue injury as a result of an ischaemic insult: ischaemic core and penumbra. The ischaemic core is an area of severe ischaemia (blood flow below 10-25% of normal). Cells in this region will die within minutes due to a severe deficiency in energy stores and subsequent ionic disruption and metabolic failure. The ischaemic core is therefore non-salvageable. Reduction of blood flow within the penumbra is less severe than that of the core, often due to residual blood flow from leptomeningeal collateral vessels. Therefore, one of the most critical issues in stroke is the need to increase perfusion to the ischaemic penumbra. Cerebral perfusion pressure (CPP) is governed by a relationship between mean arterial pressure (MAP) and ICP: CPP = MAP – ICP. Under normal circumstances cerebral blood flow is maintained by the process of local cerebral autoregulation, which involves local changes in the resistance of blood vessels in response to changes in pressure and is not CPP-dependent except at the two extremes of CPP (Jordan and Powers, 2012). Cerebral autoregulation can maintain relatively constant cerebral blood. However, these autoregulatory mechanisms are exhausted within the ischaemic penumbra, and cerebral perfusion becomes CPP-dependent (Strandgaard, 2004). Consequently, in the absence of compensatory blood pressure (BP) elevation, ICP elevation will reduce CPP and cerebral perfusion (Figure 1-4). Subsequently, this reduction in CPP may have potentially devastating effects on the CPP dependent leptomeningeal collateral vessels, which supply blood to the penumbral tissue (Beard *et al.*, 2016). Recently, a series of preclinical studies have further linked the early increased ICP in the first 24 hours post-ischaemic stroke with collateral failure seen in a subset of ischaemic stroke patients presenting with progressive stroke (Murtha *et al.*, 2014; Beard, Mcleod, *et al.*, 2015; Beard *et al.*, 2016; Lalou *et al.*, 2018).

1.2.2.1 Stroke in progression

Stroke-in progression is a term used to describe a subset of stroke patients (10-40%) who initially present with mild symptoms but suffer an early neurological deterioration (END), typically over the first 24 hours in hospital. It was assumed that patients suffering from stroke-in-progression showed initial clinical improvement due to spontaneous reperfusion and that the subsequent

1   deterioration was the result of a reformation of the clot (Caplan, 1991).

2   However, recent imaging data strongly suggest that the vessel does not

3   recanalize and that the neurological deterioration may be the result of

4   leptomeningeal collateral blood vessel failure (Campbell *et al.*, 2013). More

5   recently, in a series of *in vivo* studies, Professor Spratt and colleagues suggested

6   that, following ischaemic stroke, ICP elevation is a likely explanation for

7   collateral failure and may be the mechanism responsible for late infarct

8   expansion in ischaemic stroke patients (Murtha *et al.*, 2014; Beard, Mcleod, *et*

9   *al.*, 2015; Beard *et al.*, 2016; Lalou *et al.*, 2018) (Figure 1-5).

10

11

12

13

14

15

16

17

18

19

20

21

22

23
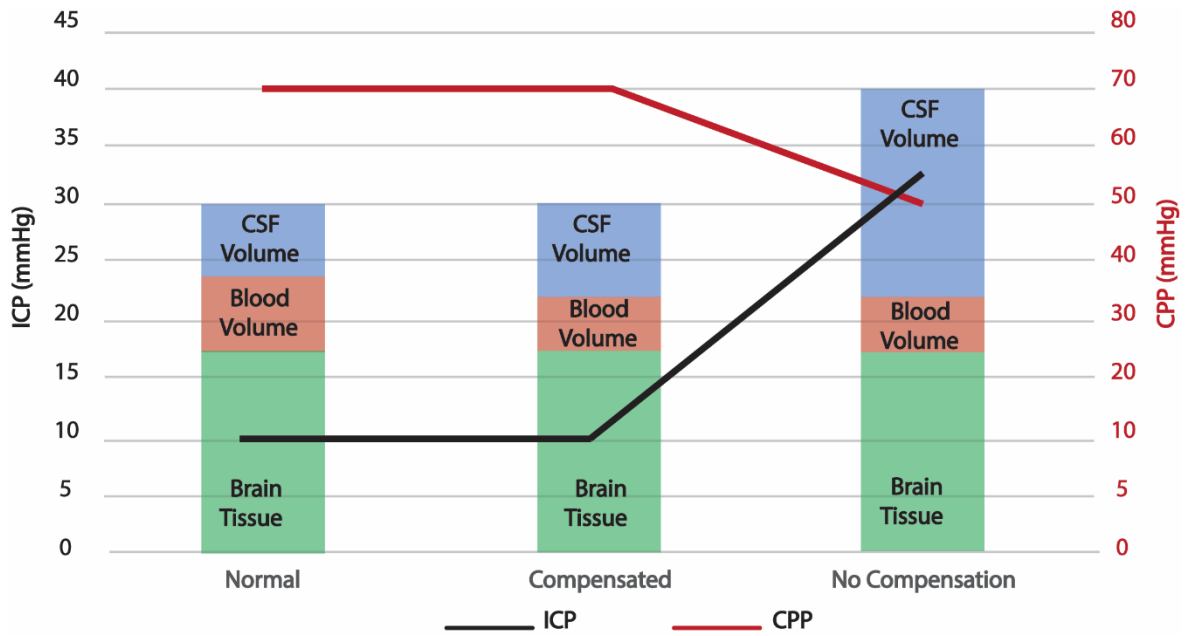
1

2 **Figure 1-4. Schematic drawing of relationship between ICP and CPP. According to Monro-**
3 **Kellie hypothesis increase in volume of cranial constituents (blood, CSF, and brain tissue)**
4 **must be compensated by a decrease in the volume of other constituents. In the model of**
5 **compensation, an increase in cerebral blood volume produces a decrease in cerebrospinal**
6 **fluid (CSF) volume; this allows ICP and CPP to remain at a baseline level. However, in the**
7 **absence of compensatory mechanisms, ICP elevation will reduce CPP. Adapted from**
8 **(Bothwell, Janigro and Patabendige, 2019).**

9

10

11

12

13

14

15

16

17
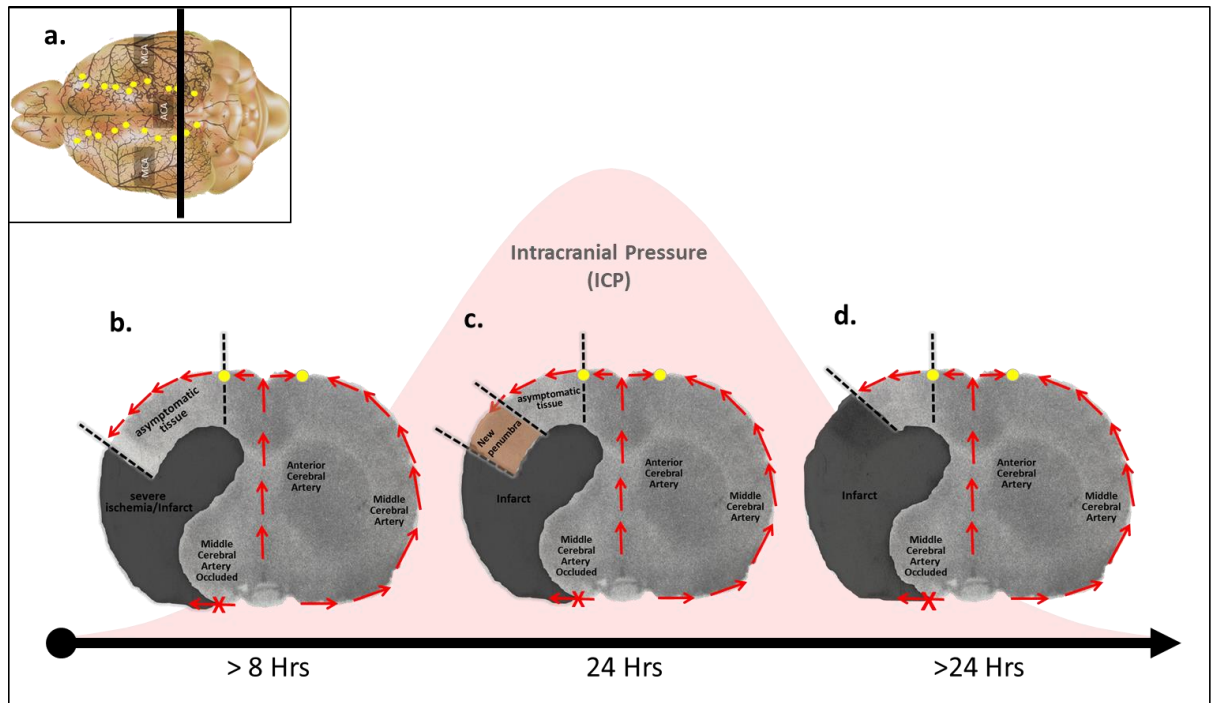
Figure 1-5. Representation of the relationship between elevated ICP and infarct expansion in acute stroke. a) Schematic drawing of pial collateral vessels in Rat brain. Collateral vessels between the anterior cerebral artery (ACA) and the middle cerebral artery (MCA) are marked with yellow circles. b) Following the hyperacute phase after permanent MCAO, >8 hours, the irreversibly damaged ischaemic core (grey zone) is surrounded by asymptomatic tissue (oligemia or non-hypoperfused tissue). If ICP remains low, the collateral perfusion will help limit the extent of the ischaemic core after stroke. Red arrows indicate direction of blood flow during permanent MCAo. c) Dramatic elevation of ICP at around 24hrs, will lead to reduction of collateral blood flow putting previously asymptomatic tissue at risk, (i.e. new penumbral tissue). d) This tissue will go on to infarct, resulting in delayed infarct expansion.

1   **1.2.3 Mechanism responsible for ICP elevation post-stroke**

2   It is widely accepted that cerebral oedema is the sole determinant of increased

3   ICP in stroke as stated in the Monro-Kellie Doctrine. Following the occurrence of

4   stroke, cerebral oedema of the brain begins to develop during the first 24-48

5   hours and reaches its maximum extent at 3-5 days (Ropper, 1984; Schwab *et al.*,

6   1996). Therefore, ICP has been assumed not to be a significant problem during

7   the first 24 hours.

8   Cerebral oedema is an excess accumulation of fluid in brain tissue, causing

9   detrimental swelling. Cytotoxic and vasogenic oedema are the two most

10   important clinical types of cerebral oedema. Cytotoxic oedema is localized and

11   will occur within minutes to hours. In this type of oedema, the brain blood

12   barrier (BBB) remains intact. It involves extracellular water passing into cells

13   due to the failure of cellular ion pumps. Thus, there is cellular retention of

14   sodium and water leading to cellular swelling (Katzman *et al.*, 1977). Vasogenic

15   oedema occurs more slowly, over hours to days. This phenomenon is due to the

16   endothelial tight junctions disruption which leads to a breakdown of the BBB,

17   resulting in intravascular water penetrating extravascular compartments

18   (Katzman *et al.*, 1977).

19   By contrast to the traditional interpretation, the relationship between oedema

20   and ICP is more complicated than it appears. Recent animal studies have

21   revealed that, even in small strokes, animals with little oedema had a significant

22   increase in ICP, reaching its peak 24 hours post-stroke onset (Silasi, MacLellan

23   and Colbourne, 2009; Bragin, Bush and Nemoto, 2013). Interestingly, a recent

24   study using a preclinical rodent model of ischaemic stroke reported that ICP

25   elevation within the first 24 hours post-stroke was independent of oedema size.

26   This finding casts doubt on the causative relationship of oedema and ICP that

27   was previously accepted (Murtha *et al.*, 2015).

28

29

1.2.4 Stroke induced disturbances in CSF circulation

Ischaemic stroke can be a major stressor in the physiology of brain cells, tissue, and fluid transport. This could lead to altered CSF secretion or drainage as an outcome of ischaemic stroke and, consequently, altered ICP (Davson, Domer and Holungsworth, 1973). As discussed earlier in this Chapter, the choroid plexus is known to be a major site of CSF secretion; thus, alterations to its function as a result of an ischaemic stroke can have an effect on the CSF secretion. The influence of cerebral ischaemia on blood-CSF barrier (BSCFB) integrity have been examined in the MCAO rodent model. Ennis and Keep (2006) observed a reduction on blood flow that supply the choroid plexus within lateral ventricle (Ennis and Keep, 2006). Additional morphological experiments have identified swelling of the choroid plexus epithelium and markers of proliferation through bromodeoxyuridine staining post-stroke (Ennis and Keep, 2006).

In terms of CSF microcirculation, multiple preclinical stroke models were employed to measure the influence of stroke on glymphatic transport using dynamic contrast-enhanced MRI (DCE-MRI) (Gaberel *et al.*, 2014). This study found that the glymphatic system was severely impaired after subarachnoid haemorrhage (SAH) and in the acute phase of ischaemic stroke but was not altered after carotid ligation or intracerebral haemorrhage. In addition, glymphatic perfusion after SAH was found to be improved by intracerebroventricular injection of a tissue-type plasminogen activator. It should be mentioned that the very recent paper by Nedergaard and her group reported that the glymphatic system is the major contributor to the acute tissue swelling in the brain in the early stage after ischaemic stroke (Mestre *et al.*, 2020). Their findings demonstrated that within 30 minutes after MCAO, a spreading depolarization was initiated along with subsequent contraction of vessels which, in turn, enlarged the perivascular spaces resulting in enhanced CSF influx into the brain and driving tissue swelling.

1.3 CSF circulation and glymphatic flow using Magnetic Resonance Image

1.3.1 Non-MRI tracer methods

Glymphatic transport have been studied using two-photon laser scanning microscopy through a closed cranial window (Iliff *et al.*, 2012; Mestre *et al.*, 2018). This method enables real-time *in vivo* observations and can examine differences in behaviour based on molecular size. However, one criticism is that two-photon laser-scanning microscopy is an invasive method that requires the removal of a portion of the animal's cranial bone, and visualization is limited to the subcortical regions (at a depth of 100 μm). Further, observations of a fluorescent tracer by laser-scanning microscopy, can only visualize the surface of the brain and only provide a snapshot view of isolated components of the glymphatic system.

Alternative imaging methods such as MRI can provide a tomographic image and evaluation of CSF flow pathways, perivascular influx, parenchymal uptake, and clearance rates. In addition, its non-invasiveness, tunability (i.e. diffusion weighted, T_1 and T_2 weighted, Phase contrast), and lack of ionising radiation makes it favoured for brain imaging. MRI probes hydrogen protons in water molecules, making it ideal to measure compartments with high water content, such as the CSF and interstitial fluids.

1.3.2 MR imaging methods

Several published reports have attempted to visualize the CSF dynamic within the CNS, including the glymphatic system, using MRI exogenous or endogenous tracer studies.

1.3.2.1 MRI exogenous tracer methods

Paramagnetic contrast agents, such as gadolinium (Gd) chelates, are often used to highlight areas of interest or view more defined structures. Iliff et al. (2013) first employed MRI using intrathecal administration of Gd chelates as a tracer to monitor glymphatic function. In that study, dynamic contrast-enhanced MRI (DCE-MRI) was applied to capture temporal and spatial characteristics of Gd

1   chelates tracer transport via the glymphatic system. Briefly, by using DCE-MRI,

2   the transport of the Gd chelates tracer was tracked in the CSF and brain

3   parenchyma over time through a time series of post-contrast–enhanced images.

4   They also compared the influx of small molecular weight Gd-Diethylene Triamine

5   Penta acetic Acid (Gd-DTPA, MW 938 Da) with a larger molecular weight

6   polymeric Gd-chelate (GadoSpin, MW 200 kDa) over the early infusion period.

7   This demonstrated clear differences in whole-brain distributions between the

8   small and large Gd chelates tracers.

9   There were certain assumptions made in this system when employing DCE-MRI

10   and gadolinium tracers. First, the Gd chelates tracer is treated by the brain as a

11   metabolic waste product within the CSF and intersitial space. Second, brain

12   physiology is not altered after injecting the Gd chelates tracer.

13   DCE-MRI methods have also been employed to study the glymphatic system after

14   a number of neurological injuries and diseases. The impairment of glymphatic

15   system in diabetes animals were examined by monitoring the clearance profile

16   of the injected GD-DTPA tracer (Jiang *et al.*, 2017). It has been demonstrated

17   that the glymphatic system was severely impaired in diabetes, leading to an

18   accumulation of tracers in multiple brain regions which correlated with the

19   degree of cognitive decline. Interestingly, when compared with functional

20   behavioural tests and vascular dysfunction, MRI measures have been shown to be

21   highly sensitive indices of pathological changes occurring early during the

22   development of diabetes mellitus (DM) (Jiang *et al.*, 2017).

23   In humans, following intrathecal gadobutrol (Gadovist/MW 550 Da)

24   administration, the tracer distributed widely throughout the entire brain and

25   spinal cord, thereby indicating the presence of a glymphatic system in the

26   human brain (Eide *et al.*, 2018). Further, the intrathecal MRI method was

27   applied in a prospective study of idiopathic normal pressure patients (iNPH)

28   (Ringstad, Vatnehol and Eide, 2017). MRI images findings indicated delayed

29   enhancement and decreased clearance of Gadovist at the Sylvian fissure. This

30   study also found that parenchymal enhancement peaked overnight in both iNPH

31   patients and control groups, suggesting a crucial role of sleep (Ringstad,

32   Vatnehol and Eide, 2017). There have been a number of published MRI studies

33   which map and model CSF flow through the glymphatic system based on DCE-MRI

data. Lee et al. (2015) first used two compartment kinetic modelling to quantify CSF-ISF exchange rates in different postures. Based on their proposed analytical model, glymphatic transport was shown to be more efficient in the lateral position compared with other positions. Further, an optimal mass transport (OMT) method was proposed for studying the glymphatic system based on DCE-MRI images (Ratner *et al.*, 2015). This method provided evidence of both diffusion and advective solute transport modes in the brain parenchyma. More recently, a quantitative DCE-MRI approach (T_1 mapping) was applied to quantify longitudinal relaxation time measurements both before and after contrast enhancement (Lee *et al.*, 2018). In their study, they demonstrated that from the total amount of MRI contrast agent injected into the cisterna magna of rat, merely 19% enriched the brain parenchyma and the remainder escaped via other routes.

1.3.2.2 MRI endogenous tracer

Endogenous tracer methods utilize the water signal of CSF as an internal tracer for CSF flow information. This approach is completely non-invasive and suitable for human applications but is less sensitive when it comes to determining CSF flow compared to the exogenous tracer method.

Phase-contrast (PC) MRI is a technique that provides qualitative and quantitative assessment of the movement of CSF (Battal *et al.*, 2011). The sequence is based on the use of bipolar gradients that create a phase shift of moving spins proportional to their velocities in the gradient direction (Bryant *et al.*, 1984). A number of MRI studies have employed the PC technique to quantify CSF flow velocity in different anatomical locations (sylvian aqueduct, foramen magnum) for the diagnosis of several CNS pathologies such as NPH (Bradley, 2015),Chiari type I (Meadows *et al.*, 2000) and syringomyelia (Brugieres *et al.*, 2000). While phase contrast methods have been shown to be powerful tools for evaluating CSF pulsatile flow (Mean velocity of CSF ~5-8 cm/s) (Sakka, Coll and Chazal, 2011), it has generally been difficult to measure the slow CSF net flow (~1 µm/s) (Sakka, Coll and Chazal, 2011).

Diffusion weighted imaging (DWI) is another approach that uses water molecules in the system as an endogenous freely diffusible tracer. Evaluation of diffusion

1 using MR techniques was first presented by Stejskal and Tanner in their seminal

2 paper (Stejskal and Tanner, 1965). In brief, they modified a standard T_2-

3 weighted spin-echo sequence by applying a symmetric pair of strong diffusion-

4 sensitizing gradients (DG's) on either side of the 180^0radiofrequency refocusing

5 pulse. This approach was later combined into an imaging sequence, which

6 enables diffusion coefficients to be spatially mapped (Basser, Mattiello and

7 LeBihan, 1994). There have been several attempts to analyse ISF dynamics in the

8 brain using diffusion-based techniques. A study in rodents to evaluate

9 glymphatic function used an ultralong echo time, low b-value, multi-direction

10 diffusion-weighted MRI sequence (Harrison *et al.*, 2018). That study indicated a

11 significant increase in fluid movement with vascular pulsation compared with

12 diastole. A recent study conducted in healthy human subjects aimed to evaluate

13 sleep by measuring the slow and fast components of the apparent diffusion

14 coefficient (ADC) of water in the brain (Demiral *et al.*, 2019). This study

15 provided evidence of increased CSF volume during sleep in humans. The

16 diffusion of water can be impeded by tissue microstructures such as in white

17 matter, resulting in a state called anisotropic diffusion. Glymphatic system

18 function was also investigated using "diffusion tensor image analysis along the

19 perivascular space" (DTI-ALPS) in Alzheimer patients (Taoka *et al.*, 2018). The

20 results of that study demonstrated a reduction in water diffusivity along

21 perivascular space in those patients, which may reflect impairment of the

22 glymphatic system.

23

24

25

26

27

28

29

30

31

32

33

34

1.3.3 ^{17}O-labelled water as MRI contrast agent

The tremendous biological relevance of ^{17}O water (H$_2$^{17}O) comes from its use as an MR tracer with particular application to the measurement of flow and metabolism.

1.3.4 ^{17}O properties

Oxygen 17 (^{17}O), one of the most abundant elements, has been the subject of study for centuries. Given its abundant and reactive nature, oxygen is of central importance to biological, chemical, and physical processes. Three naturally occurring isotopes of oxygen exist, of masses 16. 17. and 18. ^{16}O is by far the most abundant of these isotopes. Giauque and Johnston discovered the oxygen isotopes ^{17}O and ^{18}O (Giauque and Johnston, 1929). The first observation of the ^{17}O nuclear magnetic resonance signal was reported by Alder and Yu in 1951 (Alder and Yu, 1951). ^{17}O is a stable, non-toxic isotope of oxygen with a natural abundance of 0.037%. a nuclear spin of 5/2 and a gyromagnetic ratio (γ) of -36.281 rad s^{-1} T^{-1}. As the spin of ^{17}O nucleus (I=5/2) is exhibit a quadrupole moment, Q, where the charge distribution surrounding the nucleus is asymmetric and therefore and the electric field gradient can interact with the nucleus and exhibit a torque on the nucleus. For ^{17}O, the nuclear ground state splits into six sublevels in the applied magnetic field (since $2 \times (5/2) + 1 = 6$) and therefore multiple transitions are expected. In analytical chemistry, the dramatic chemical shifts and sensitivity to electric field gradients have made ^{17}O useful to investigate the structure, bonding, and dynamics of oxygen-containing compounds.

1.3.4.1 Metabolized H$_2$^{17}O as endogenous contrast agent

In comparison to another isotope of oxygen, oxygen-15, which is used as a positron emission tomography tracer (^{15}O-PET), ^{17}O-MRI can be used as a non-invasive method without any radioactive exposure to directly measure cerebral oxygen metabolism (Arai *et al.*, 1998; Zhu *et al.*, 2005; Graaf *et al.*, 2008). ^{17}O molecules can be delivered either in the form of free gas or dissolved in water. Following inhalation of ^{17}O$_2$ gas, it binds to the haemoglobin (Hb) in the blood and then enters the brain via the arteries and blood circulation. The ^{17}O-labeled

1 oxygen gas will be metabolized in the brain mitochondrion to produce $H_2^{17}O$ as

2 shown in the following equation:

$$4H^+ + 4e^- + {}^{17}O_2 \rightarrow 2H_2{}^{17}O \qquad (2.2)$$
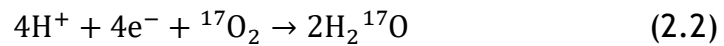
3 The production rate of the metabolized $H_2^{17}O$ water reflects the rate of oxygen

4 metabolism in the brain tissue (Rolfe and Brown, 1997). Thus, using the ^{17}O in

5 the brain will provide important information regarding the oxygen metabolism of

6 the brain tissue. Another advantage of ^{17}O over ^{15}O is that no on-site production

7 is needed (Zhu and Chen, 2011). In case of ^{15}O experiments, the tracer must be

8 produced on-site due to its very short half-life of approximately 2 mins. Further,

9 since ^{15}O and $H_2^{15}O$ are both positron emitters, it is difficult to differentiate

10 these two compounds with PET potentially complicating the measurement of

11 $H_2^{15}O$ accumulation (Herscovitch, Mintun and Raichle, 1985). On the other hand,

12 ^{17}O is only detectable by means of MR if it is bound to protons as water

13 molecules ($H_2^{17}O$), which is a unique feature of ^{17}O-NMR techniques (Zhu *et al.*,

14 2005). This phenomenon allows the selective detection of metabolically

15 generated $H_2^{17}O$ without confounding signals from the ^{17}O molecules bound to

16 haemoglobin.

17 **1.3.4.2 ^{17}O-labelled water as an exogenous contrast agent**

18 Detection of externally administered ^{17}O-labelled exogenous tracers (e.g., $H_2^{17}O$)

19 *in vivo* has been used by several investigators for cerebral blood flow (CBF)

20 measurement (Arai *et al.*, 1998). After administrating a bolus injection of $H_2^{17}O$,

21 an initial rapid increase in $H_2^{17}O$ concentration in brain tissues can be observed.

22 Then the concentration of $H_2^{17}O$ in the brain starts to decrease; meanwhile some

23 $H_2^{17}O$ molecules are brought back to the brain from the body by blood

24 recirculation. These two processes give rise to a net effect of $H_2^{17}O$ washout and

25 finally achieve a new steady state of $H_2^{17}O$ concentration in the brain. Hence,

26 assessment of CBF and water movement across blood brain barrier (BBB) can be

27 assessed by monitoring the behaviour of $H_2^{17}O$ signal (Arai *et al.*, 1998).

28 Glucose homeostasis plays a key role in numerous fundamental aspects of life,

29 and its dysregulation is associated with many important human diseases such as

30 cancer. During cancer progression, tumour cells gain energy by anaerobic

1 glycolysis (Warburg effect) and therefore have an elevated glucose turnover

2 compared with normal tissue (Vander Heiden, Cantley and Thompson, 2009). At

3 present, 2-deoxy-2-[^{18}F] fluoro-glucose (^{18}F-FDG) is the gold standard to monitor

4 the metabolic rates of glucose (Kao *et al.*, 1998). As an alternative to PET,

5 administration of highly labelled ^{17}O-glucose, together with dynamic^{17}O-MRS

6 have provided a non-radioactive alternative to FDG-PET to follow up glucose

7 consumption during glycolysis (Borowiak *et al.*, 2017).

8 **1.3.4.3 ^{17}O-labelled water contrast agent for studying CSF**

9 In recent years, similar $H_2^{17}O$ MR imaging approaches have been applied to

10 evaluate CSF status in animals (Igarashi *et al.*, 2014) and humans (Kudo *et al.*,

11 2018). Igarashi et al. (2014) conducted MRI experiments utilizing $H_2^{17}O$ JJVCPE

12 imaging to investigate water flux into CSF in AQP1 and AQP4 knockout mice.

13 These observations seem to indicate that water influx into the CSF is regulated

14 by AQP4 (not by AQP1). Further, water movement within the perivascular space,

15 rather than in choroid plexus and arachnoid villi, was found to be essential for

16 CSF volume homeostasis. In human studies, following intravenous administration

17 of $H_2^{17}O$, transition into the brain parenchyma and CSF regions has been

18 reported (Kudo *et al.*, 2018). In this study, dynamic steady-state sequences were

19 acquired to detect the T_2-shortening effect of $H_2^{17}O$. Different kinetic

20 parameters between the brain parenchyma and CSF spaces were found. The

21 cerebral cortex and subarachnoid spaces on the brain surface showed a prompt

22 signal drop, indicating quick transmission of $H_2^{17}O$ from arteries to these regions.

23 By contrast, the signal drop in the ventricle containing the choroid plexus was

24 significantly delayed, indicating that fluid exchange is less active in the ventricle

25 (Kudo *et al.*, 2018).

26

27

28

29

1.4 Thesis aims

1. To investigate the relationship between CSF dynamics, vasogenic oedema, and ICP following experimental stroke.

2. To demonstrate the true magnitude of the CSF water flow through the glymphatic system by using a novel MRI tracer, namely, $H_2^{17}O$ as opposed to the conventional gadolinium-based tracers (Gd-DTPA).

3. To build on the understanding of the function of AQP4, by modulating it pharmacologically and using MRI $H_2^{17}O$ as a direct imaging method.

2 Chapter 2: Magnetic Resonance Imaging

This Chapter describes the theory of magnetic resonance imaging (MRI) and how to form an MR image from a sequence of radiofrequency and magnetic field gradient pulses. The imaging techniques relevant to this thesis are introduced, followed by a detailed description of the hardware requirements of an MR system. Information has come from multiple sources; (Callaghan, 1993), (Levitt, 2013), (Cercignani, Dowell and Tofts, 2018), (Elster, 1994), unless specifically stated.

2.1 Dipole to Image

2.1.1 Nuclear spin angular momentum

An elementary particle possesses a variety of properties such as mass or charge, another being its intrinsic angular momentum, also known as spin. Electrons, protons, and neutrons all possess spin angular momentum, which is quantised and is related to the spin quantum number, I. The magnitude of the spin angular momentum is given by the formula:

$$|L| = \hbar \sqrt{I(I+1)} \qquad (2\text{-}1)$$

Where $\hbar$ is Planck's constant (h= 6.63×10^{-34} m^2 kg s^{-1}) divided by 2π. Also, the direction of the spin angular momentum is quantized and hence the possible z components are given by:

$$L_z = m_I \hbar \qquad (2\text{-}2)$$

Where, $m_I = -I, -I+1, \dots I$.

I may take zero, integer, or half integer values. The number of orientations of a possible spin angular momentum with spin I, is 2I +1. For hydrogen nuclei (^{1}H), the spin quantum number is $I = \frac{1}{2}$ giving two spin states, thus:

$$m_I = -\frac{1}{2}, \frac{1}{2} \qquad (2\text{-}3)$$

2.1.2 Magnetic moment

Nuclei and particles with a spin quantum number larger than zero have an observable associated magnetic moment. This magnetic moment, μ, describes the tendency of an object to interact with an external magnetic field. μ is related to the nuclear spin through a nuclei-specific constant called the gyromagnetic ratio, γ (for hydrogen, $\gamma = 2.675 \times 10^8$ rad $s^{-1}T^{-1}$). Where μ is given by:

$$\mu = \gamma\hbar I \qquad (2\text{-}4)$$

When a static magnetic field, B_0, is applied to the spin system along the z axis, magnetic moments are aligned in the field with certain allowed orientations, (m_I), giving 2I+1 energy levels (see Figure 2-1), While in the absence of a magnetic field, these energy levels are degenerate.
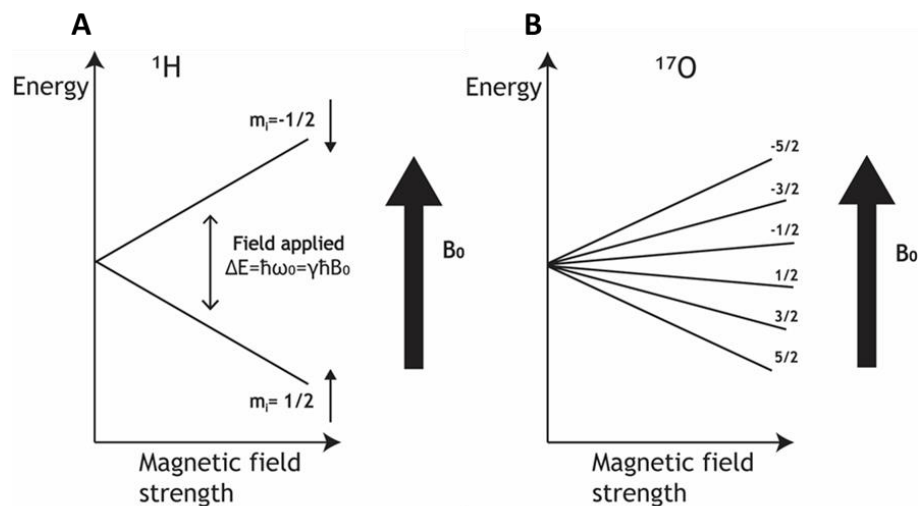
Figure 2-1. Zeeman energy levels. Splitting of the energy levels of ¹H (*I*=1/2) and ¹⁷O nucleus (*I*=5/2). The diagram progresses from the no magnetic field to the Zeeman splitting.

This behaviour is the so-called Zeeman effect, where the energy of interaction for each orientation is given by:

$$E = -\gamma\hbar\, m_I B_0 \qquad (2\text{-}5)$$

Therefore, for hydrogen nuclei (^{1}H), the energy difference between the two spin states ($-\frac{1}{2}, \frac{1}{2}$) is given by:

$$\Delta E = E_{m_I = -\frac{1}{2}} - E_{m_I = \frac{1}{2}} = \left[-\left(-\frac{1}{2} \right) \gamma . \hbar . B_0 \right] - \left[\left(-\frac{1}{2} \right) \gamma . \hbar . B_0 \right]$$
$$= \gamma \hbar B_0$$

(2-6)

At thermal equilibrium, the populations of two energy states is given by Boltzmann distribution:

$$\frac{N_\uparrow}{N_\downarrow} = e^{(-\Delta E / K_B T)}$$

(2-7)

Where $N_\uparrow$ is the population of the spin up state ($m_{I=1/2}$) and $N_\downarrow$ is the population of the spin down state ($m_{I=-1/2}$), K_B is the Boltzmann constant ($1.3805 \times 10^{-23} JK^{-1}$) and T is the temperature in degrees Kelvin. This difference in population of the two states induces a net magnetisation, which represents the vector summation of all the magnetic moments of the individual nuclei.

$$M_x = \sum_i \mu_x^i$$

(2-8)

$$M_y = \sum_i \mu_y^i$$

(2-9)

$$M_z = \sum_i \mu_z^i$$

(2-10)

Where μ_x, μ_y, μ_z are the components of magnetic moments for the specific nucleus, i, in the x, y and z directions. At equilibrium, the net magnetisation is aligned along the direction of the main magnetic field (B_0), this equilibrium net magnetisation, M_0, is given by:

$$M_0 = \frac{\gamma^2 \hbar^2 B_0 N_s}{4 K_B T} \tag{2-11}$$

Where N_s, is the number of spins. It is worth noting at this time that factors which influence the MRI signal; field strength of the scanner B_0, the natural abundance and gyromagnetic ratio, γ, of the particular nuclei.

2.1.3 Larmor Precession

When looking at individual nuclear magnetic moments, μ, placed in a magnetic field, they do not align exactly with B_0, and rather process about B_0 (see Figure 2-2).
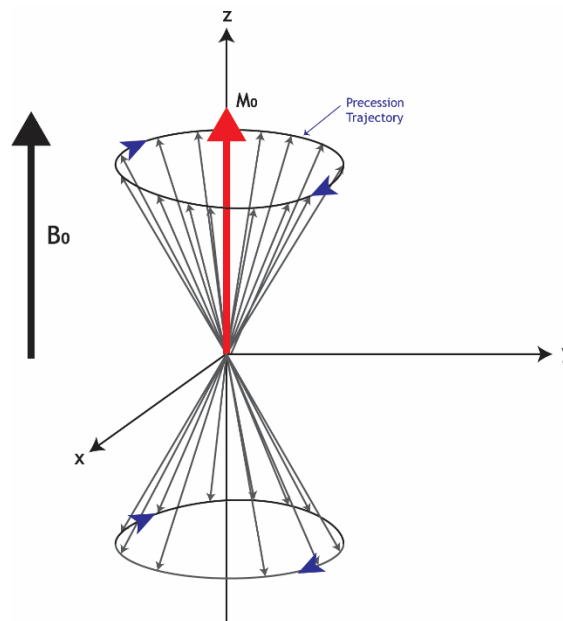
Figure 2-2. Schematic representation of the magnetic moment of a nucleus and its precession about a magnetic field, B$_o$.

The frequency of precession is called the Larmor frequency (ω_0) which is an angular frequency, giving by:

$$\omega_0 = -\gamma B_0 \tag{2-12}$$

According to quantum theory of radiation, ω_0 is frequency at which the nuclei absorb energy and is related to the energy difference between levels (ΔE). We can now rewrite equation (2-6):

$$\Delta E = \hbar\omega_o \qquad (2\text{-}13)$$

The higher the magnetic field strength, the greater ω_0 and ΔE (Figure 2-1). Different nuclei have a different ω_0 because of their different gyromagnetic ratios, γ. For the hydrogen nucleus, ^1H, at 7 Tesla, the value of γ is 42.58 MHz/Tesla, which gives a precession frequency of ~ 300 MHz.

2.1.4 Radiofrequency pulse

RF radiation is electromagnetic radiation and is a combination of an oscillating electric field (which does not interact with M_0) and an oscillating magnetic field perpendicular to each other. If the oscillating magnetic field, B_1, of the RF pulse is applied perpendicular to the external magnetic field, B_0, the net magnetisation will precess about the B_1 field with a frequency:

$$\omega_1 = -\gamma B_1 \qquad (2\text{-}14)$$

The B_1 field is only able to exert a constant direction torque if its frequency (ω_1) is close to the precession frequency, ω_0. To visualize the effect of an RF pulse on M_0, it is common to consider a reference frame rotating at the RF frequency, ω_1, about the z-axis. The new frame of reference is denoted (x', y', z) and is called the rotating frame (see Figure 2-3). In this rotating reference frame, the B_1 field appears stationary. Additionally, if $\omega_1 = \omega_0$ (On-resonance) the contribution of the B_0 field is removed.
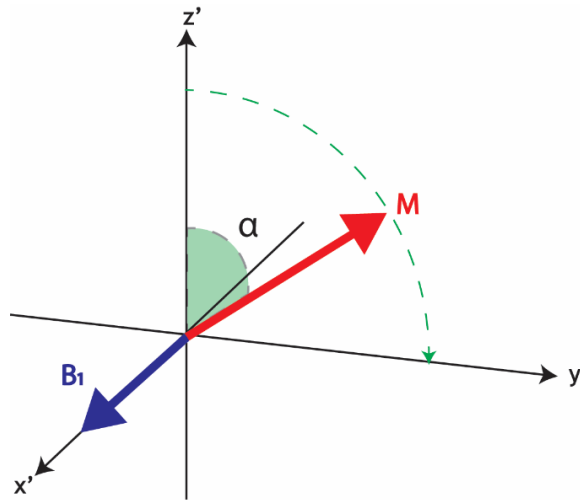
Figure 2-3. The evolution of the bulk magnetisation vector, M, under the application of an RF pulse B_1 in rotating frame.

During an RF pulse the net magnetisation precesses about the B_1 field. The flip angle, α, by which the magnetisation is tipped away from the z-axis, is dependent on the power of the RF pulse and the length of time that it is applied:

$$\alpha = \omega_1 t_p = \gamma B_1 t_p \qquad (2\text{-}15)$$

where t_p, is the duration of the RF pulse. Arbitrary α can be achieved but commonly pulses have either $\alpha = 90^0$ or 180^0.

2.1.5 Spin echo

The most basic method for recovering phase coherence is the Spin Echo (SE) which was first introduced by Hahn in 1950 (Hahn, 1950). The simplest experiment is the application of 180^0 pulse after the initial 90^0 pulse. Following a period, τ, of dephasing, the 180^0 pulse flips the orientations of the dephasing (see Figure 2-4).
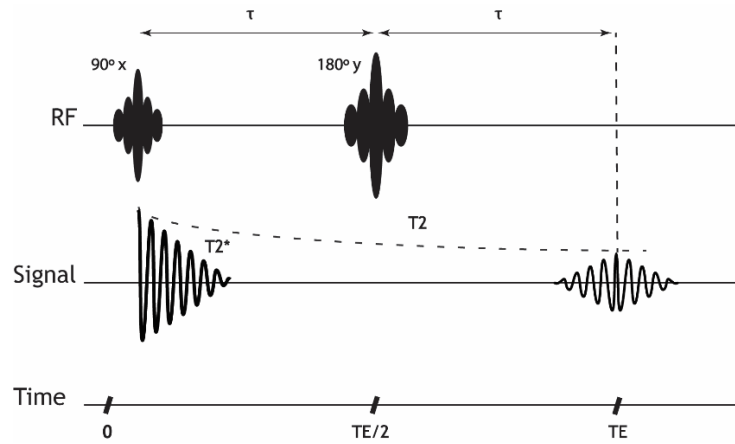
Figure 2-4. Simplified pulse diagram of the spin echo imaging sequence.

2.1.6 Generating MR Image

Once the magnetisation has a transverse component, the detection of its precession about B_0 can be examined. To detect the signal, the same RF coil (or a separate RF coil) as that for transmission of the B_1 field can be used. A change of the magnetic flux, Φ, which is caused by the precessing net magnetisation, induces an electromotive force (emf). The emf induced in a coil by a change in its magnetic flux can be calculated by Faraday's law of induction:

$$\text{emf} = \frac{-d\Phi}{dt} \qquad\qquad (2\text{-}16)$$

The MRI signal produced by the precessing net transverse magnetisation can be expressed mathematically as follows:

$$s \propto e^{(i\varphi)} \qquad\qquad (2\text{-}17)$$

Where φ is the phase of the transverse magnetisation, as a function of time and can be expressed as:

$$\varphi = \omega t \qquad\qquad (2\text{-}18)$$

And therefore:

$$s \propto e^{(i\gamma B_0 t)} \qquad\qquad\qquad (2\text{-}19)$$

MR imaging seeks to acquire spatial information about the sample. Therefore, the resonance frequency of nuclei must be encoded as a function of their spatial position. This can be achieved using pulses of magnetic field gradients, which forms the basis of MRI (see section 2.5.3). To spatially encode nuclear spins, a magnetic field gradient is applied in the direction that the spatial encoding is required, these gradients are defined as follows:

$$G_x = \frac{\partial B_z}{\partial x} \, , \qquad G_y = \frac{\partial B_z}{\partial y} \, , \qquad G_z = \frac{\partial B_z}{\partial z} \qquad\qquad (2\text{-}20)$$

The Larmor frequency of the spins at position (x_1) is then a function of the applied gradient:

$$\omega_{(x_1)} = \gamma(B_0 + G_x . x_1) \qquad\qquad (2\text{-}21)$$

It is often convenient to use the concept of a rotating frame of reference, where the new reference frame rotates about the z-axis at ω_1, the same frequency as the B_1 field of the RF radiation. At resonance ($\omega_1 = \omega_0$), the net magnetisation will appear stationary due to the effects of the B_0 field disappearing. The signal intensity is now acquired as a function of time and the applied gradient:

$$s \propto e^{(i\gamma G_x . x_1 t)} \qquad\qquad (2\text{-}22)$$

MRI Data acquired with respect to time and to gradient strength and duration is referred to as k-space (Figure 2-5).
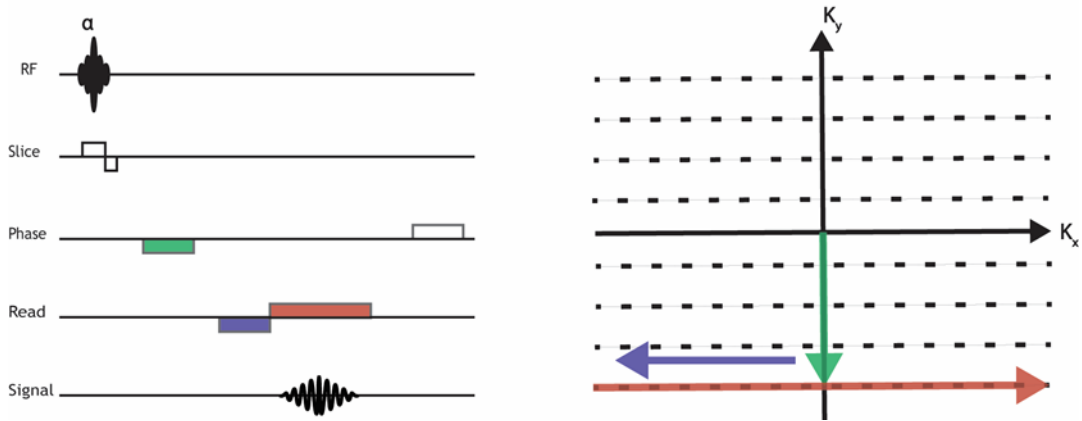
Figure 2-5. Acquiring data in k-space for MR imaging.Acquisition of an echo in the presence of a read gradient fills one horizontal line of k-space. The vertical position of each line of k-space is determined by the strength of the phase encoding gradient applied during the pulse sequence. An image is reconstructed by applying two Fourier transforms, first in read direction and second in the phase direction, of the k-space data.

Thus, the position and separation of points along each axis of k-space are defined by the gradient duration (t) multiplied by the gradient strength:

$$k_x = \frac{1}{2\pi}\, \gamma G_x.\, t_x \; , \qquad k_y = \frac{1}{2\pi}\, \gamma G_y.\, t_y \tag{2-23}$$

By using the substitution, $k_x = \frac{1}{2\pi}\, \gamma G_x.\, t_x$, and integrating the signal for over the whole sample, now the total signal can be expressed as the following:

$$S_{(k)} = \int_{-\infty}^{+\infty} \rho(x)\, e^{i2\pi(k_x.x)} dx \tag{2-24}$$

Where $\rho(x)$ is the spin density of a sample at position x. It is easy to see in equation that the signal $S_{(k)}$ is the Fourier transform of the spin density ($\rho(x)$). To generate a 2D MR image from the data in k-space data, the data must be Fourier transformed twice, first in the read direction (k_x) and then in the phase direction (k_y):

$$S_{(k)} = \int_{-\infty}^{+\infty}\int_{-\infty}^{+\infty} \rho(x,y)\, e^{i2\pi(k_x.x+k_y.y)} dx\, dy \tag{2-25}$$

For MR imaging, we generate transverse magnetisation, M_{xy}, only from spins contained in a small and well-defined slice of the whole volume (see Figure 2-6). This is achieved by applying the RF pulse, with a defined frequency bandwidth $\Delta\omega$, during the application of a magnetic field gradient.
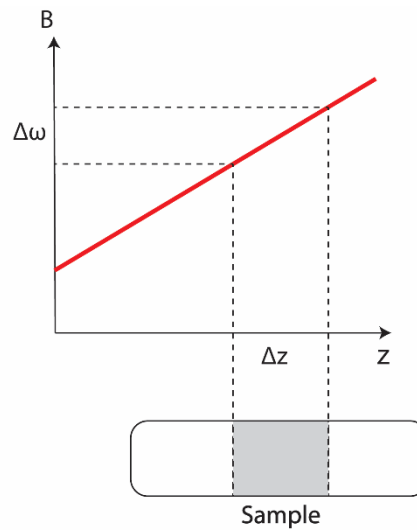
Figure 2-6. Slice selection. The resonance frequency is varied by the use of a magnetic field gradient in the z-direction. Applying a RF-pulse with the right frequency bandwidth, Δω, only spins in a slice with a thickness Δz are excited.

2.2 MRI Relaxation

2.2.1 Transverse relaxation

Transverse relaxation (spin-spin relaxation), T_2, is a measure of the rate at which phase coherence is lost (see Figure 2-7). This is can be described mathematically by the Bloch Equation for transverse magnetisation:

$$\frac{dM_{xy}}{dt} = -\frac{M_{xy}}{T_2} \qquad (2\text{-}26)$$

Following a 90^0 excitation the solution of equation (2-26) is simply:

$$M_{xy} = M_o \, e^{\frac{-t}{T_2}} \qquad (2\text{-}27)$$

The rapid tumbling motion of molecules, which contain nuclear magnetic moments, results in a rapidly fluctuating local magnetic field, B_{local}. This tiny fluctuating local field is superimposed on the larger static B_0 field, causing random fluctuations in the Larmor frequency. This results in stochastic dephasing of the spins, leading to irreversible decay of the transverse magnetization. In addition, there is the dephasing due to inhomogeneities in the B_0 magnetic field and local differences in magnetic susceptibilities. These types of effects are constant in time, and they act on a spatially macroscopic scale. The combined transverse relaxation is often called the T_2^* where:

$$M_{xy} = M_o \, e^{\frac{-t}{T_2^*}} \qquad (2\text{-}28)$$

Incoherent dephasing due to T_2^* effects are reversible. This can be achieved by applying a refocusing RF pulse of typically 180^0.
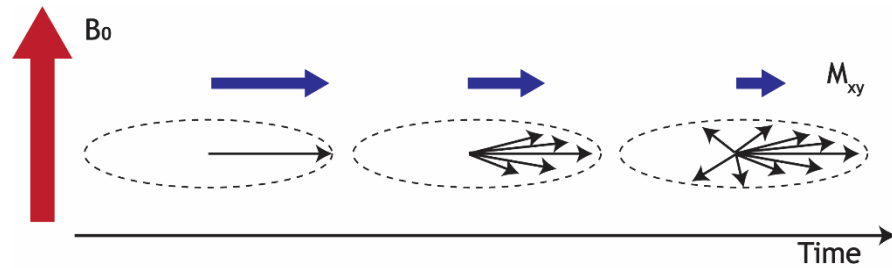
Figure 2-7. T_1 relaxation process. Diagram showing the process of transverse relaxation after a 90^0 RF pulse is applied. Initially, the transverse magnetization (black arrow) has a maximum amplitude as the spins rotate in phase. The amplitude of the net transverse magnetization decays as the spins move out of phase with one another (shown by the small black arrows).

2.2.2 Longitudinal relaxation

Longitudinal relaxation, T_1, is the process by which the net longitudinal magnetization (M_z) returns to its equilibrium state (M_0) (see Figure 2-8). Mathematically, this process is described by the following term in the Bloch equations, assuming that the static magnetic field is applied along the z-axis:

$$\frac{dM_Z}{dt} = -\frac{M_Z - M_o}{T_1} \qquad (2\text{-}29)$$

Following a 90^0 pulse, the solution of Equation (2-29) describes an exponential growth of M_z towards its equilibrium value M_0:

$$M_z = M_o(1 - e^{\frac{-t}{T_1}}) \qquad (2\text{-}30)$$

The process by which the excited spins lose their energy to the surrounding system is called spin-lattice relaxation. It is, in fact, the mechanism by which the population difference between the two spin energy levels returns to equilibrium.
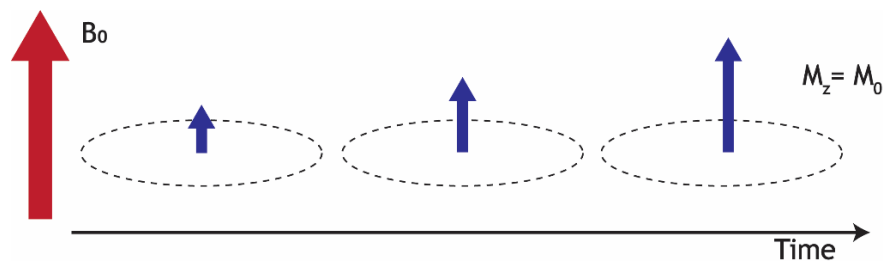
Figure 2-8. T$_1$ relaxation process. Diagram showing the process of T$_1$ relaxation after a 90^0 RF pulse is applied. The z component of the net magnetization, M$_z$ is reduced to zero, but then recovers gradually back to its equilibrium value (M$_0$).

2.2.3 Other Relaxation mechanisms

2.2.3.1 Spin coupling

The magnetic moment of each spin generates a small local magnetic field with a direction dependent upon the alignment of the spin either parallel or anti-parallel with B$_0$. These local fields alter the B$_0$ field experienced by another spin in close proximity. These interactions of magnetic moments can be transmitted either through space (dipolar coupling) or via the bonding electrons (scalar or indirect coupling). For molecules in solution undergoing tumbling and rotating, the dipolar coupling is averaged to zero since it is dependent upon the distance between, and the orientation of, the nuclei. Scalar coupling, however, is not affected by B$_0$ field strength or molecular tumbling.

2.2.3.2 Relaxation mechanism of ^{17}O

In the case of dipolar nuclei (I = 1/2), the main interaction is generally the magnetic dipole-dipole interaction between the nuclei. Nuclei with I = 1/2 possess a spherical distribution of the nuclear charge and are, therefore, not affected by the electric environment within the molecule. The so-called quadrupolar nuclei (i.e., those with I > 1/2), such as ^{17}O, possess an electric quadrupole moment in addition to the magnetic dipole moment. The electric quadrupole moment produces a non-symmetric nuclear charge distribution (non-spherical charge) that interacts with the electric field gradient in the surrounding electron clouds.
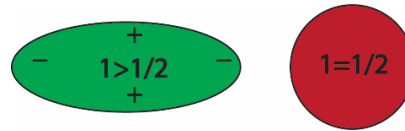
Figure 2-9. Charge distribution. Spherical (red) and non-spherical nuclei (green).

The temporal fluctuation in this interaction induced by molecular motion can dominate ^{17}O relaxation processes and determines both T_1 and T_2 relaxation times. In the case of the water molecule, the values of ^{17}O T_1 and T_2 can be approximated by:

$$\frac{1}{T_2} \cong \frac{1}{T_1} = 0.948 \left(1 + \frac{\eta^2}{3}\right)\left(\frac{e^2 Qq}{h}\right)^2 \tau_c \qquad (2\text{-}31)$$

The term $(e^2 Qq)$ is the ^{17}O quadrupolar coupling constant for bulk water, and η is an asymmetry parameter ($0 \leq$ η ≤ 1). τ_c is the rotational correlation time and ω is the ^{17}O Larmor frequency.

The T_2/T_2^* relaxation of ^{17}O water in a biological sample or water is smaller than the T_1 relaxation time of ^{17}O because of the combined effects of the $^{17}O\text{-}^1H$ scalar coupling and the nucleus exchange on the ^{17}O transverse relaxation process. *In vivo* rat brain studies show that the longitudinal and transverse relaxation times of the ^{17}O signal in natural abundance $H_2^{17}O$, are on the order of a few milliseconds and are field independent (T_2 = 3 ms, T_2^* = 1.8 ms at both 4.7T and 9.4T; T_1 = 4.5 ms at 4.7T versus 4.8 ms at 9.4T).

In NMR spectroscopy, the ^{17}O nucleus in water can interact with the two ^1H nuclei, resulting in the ^{17}O signal being a 1:2:1 triplet at extremely low water concentration. However, the ^{17}O triplets collapse to one single and well-defined $H_2^{17}O$ resonance peak in a biological samples, due to rapid ^1H nucleus exchange and quadrupolar relaxation leading to a large line broadening effect.

2.2.3.3 The detection of ^{17}O "indirectly", via effect on ^1H relaxation.

The MR sensitivity of ^{17}O is about five orders of magnitude lower than that of ^1H due to the low natural abundance of ^{17}O (0.037%) the approximately seven-fold lower gyromagnetic ratio. Hence, direct detection of ^{17}O has inherently very low

SNR and therefore has posed a fundamental challenge to the development of these techniques. An alternative to direct detection of ^{17}O, is to detect the effect of the quadrupolar ^{17}O nucleus on the much larger ^{1}H MRI signal from $H_2^{17}O$ molecules. This phenomenon was first investigated by Meiboom (1961) and occurs via scalar coupling between the quadrupolar ^{17}O nucleus and bonded ^{1}H nuclei. This effect is further magnified by the rapid exchange of H^+ ions with the $H_2^{17}O$ molecule:

$$H^+ + {}^{17}_{1}OH^- = H_2{}^{17}O \tag{2-32}$$

According to Meiboom, for low concentrations of $H_2^{17}O$ in $H_2^{16}O$, the resulting ^{1}H transverse relaxation time of water is given by:

$$\frac{1}{T_2} = \frac{1}{T_2^{16}} + PA \tag{2-33}$$

Where

$$A = \frac{35}{12}\tau \left(\frac{JT_1}{T_1 + \tau}\right)^2 \tag{2-34}$$

Where P is the fraction of water molecules containing ^{17}O, J is the scalar coupling constant for ^{1}H-^{17}O bond, T_1 is the ^{1}H longitudinal relaxation time and τ is the ^{1}H exchange lifetime. Hence, the presence of $H_2^{17}O$ water can be detected by a reduction in the ^{1}H signal on T_2-weighted MRI.

Both ^{17}O-^{1}H scalar coupling and the chemical exchange between $H_2^{17}O$ and $H_2^{16}O$ are all sensitive to some physiological parameters such as pH (Meiboom, 1961). At near-neutral pH, the scalar coupling has a maximal effect for enhancing the apparent transverse relaxation rate, while this effect can completely disappear when pH is shifted away from neutral.

2.2.3.4 Paramagnetic Relaxation

Gadolinium (Gd) chelates are the most widely used of all MR paramagnetic contrast agents. The gadolinium ion is strongly paramagnetic and contain seven unpaired electrons, giving rise to very large magnetic moment, since the

magnetic moment of the electron is about 700 times larger than that of the nucleus. Gadolinium contrast agents induce significant enhancement of both transverse and longitudinal relaxation times through dipole interaction between free water nuclei and electron spins. The relationship between the change in relaxation rate (i.e. $R_1 = (1/T_1)$ and $R_2 = (1/T_2)$) and the contrast agent concentration, C, is linear assuming fast water exchange between tissue compartments:

$$R_1 = R_1^0 + r_1 C \qquad\qquad\qquad (2\text{-}35)$$

$$R_1 = R_1^0 + r_1 C \qquad\qquad\qquad (2\text{-}36)$$

Where R_1^0 and R_2^0 are the native tissue longitudinal and transverse relaxation rates, and r_1 and r_2 are relaxivity constants (units of mM^{-1} s^{-1}) reflecting the ability of the contrast agent to increase the relaxation rates .

2.3 Pulse sequences

2.3.1 TR and TE

The application of various RF pulses and the alteration of receiving times have a major impact on the contrast of the resultant image (Figure 2-10). TR is the repetition time and is the time between the beginning of a pulse sequence, and the beginning of the next identical pulse sequence for the same slice of spins. TE is the echo time and is the time between the RF pulse which initially generates transverse magnetisation, and the peak signal received by the coil.

Img. technique	TR	TE
T1 weighted	Short	Short
T2 weighted	Long	Long
PD weighted	Long	Short
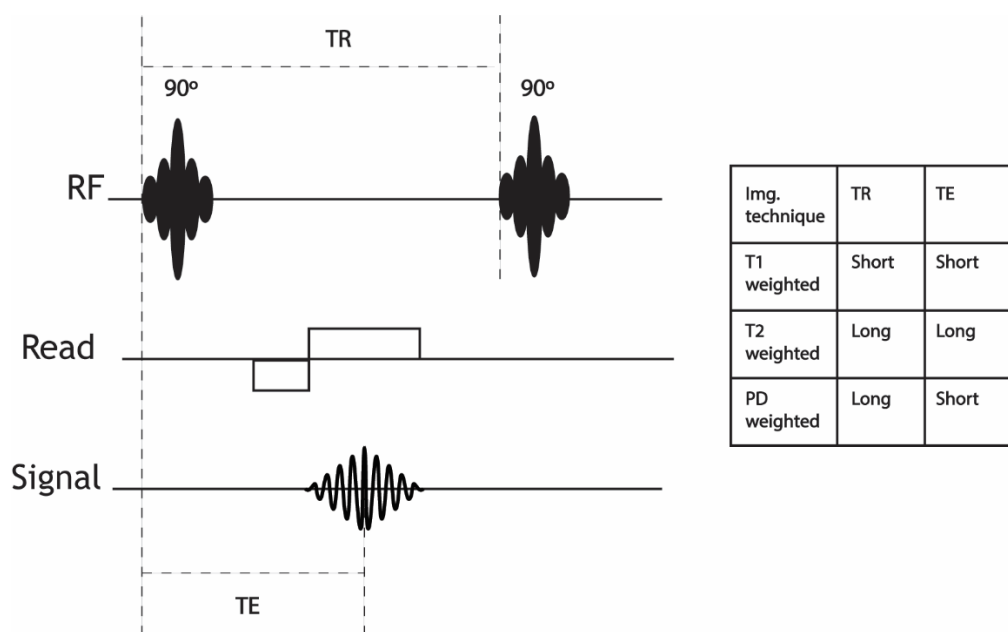
Figure 2-10. Effect of TR and TE on MR image contrast.

2.3.2 Multi spin echo sequence (RARE & MSME)

The RARE (rapid acquired relaxation enhanced) technique is based on the CPMG (Carr-Purcell-Meiboom-Gill) sequence, where transverse magnetization following a slice selective 90° pulse is refocused by a train of slice selective 180^0 pulses generating a series of echoes (Meiboom and Gill, 1958). Each echo is separately phase-encoded, and the phase encoding is incremented within one echo train to accelerate the acquisition (see Figure 2-11). The contribution to image contrast will be greatest for echoes acquired at the centre of k-space. Hence, the contrast of the image will be weighted by the central TE value (effective TE).
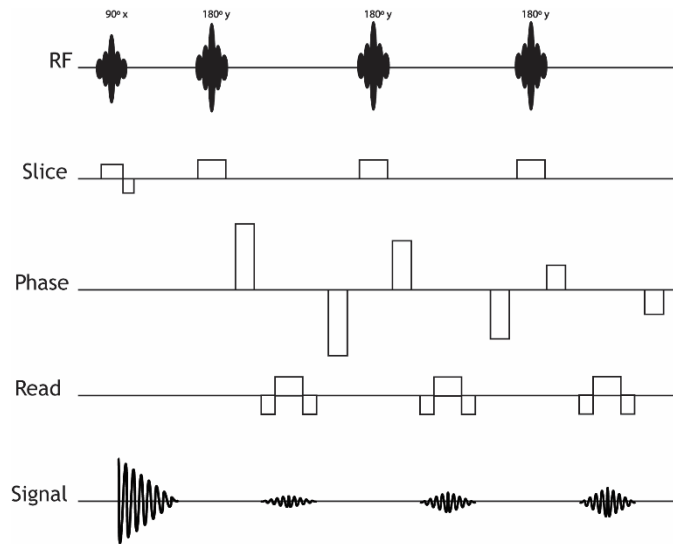
Figure 2-11. Simplified pulse diagram of the RARE imaging sequence.

Quantitative T_2 mapping can be achieved using the multi-slice-multi-echo (MSME) method. As with the RARE technique, multiple spin echoes are generated using the CPMG sequence with slice selective RF pulses. However, with MSME technique the same phase gradient is applied to each echo, whereby each echo is used to obtain an image with a different TE. Each voxel in an image is fitted to a single exponential decay using equation (2-28) to provide a map of transverse relaxation time throughout the imaged sample.
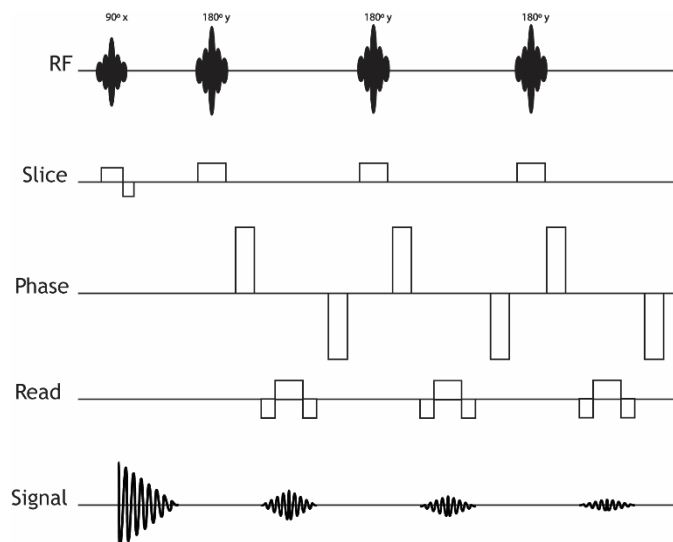
Figure 2-12. Simplified pulse diagram of the MSME sequence.

2.3.3 Gradient echo

The gradient echo pulse sequence allows the formation of a gradient echo, where the signal intensity is dependent on the T_2^* signal decay of the sample. With TR less than $5 \times T_1$ and pulse angles less than 90^0, the maximum steady state signal is obtained using The Ernst angle (α_E) is calculated using:

$$Cos\ \alpha_E = \exp\left(-\frac{TR}{T_1}\right) \qquad\qquad (2\text{-}37)$$

This demonstrates that the maximum steady state signal intensity occurs with a smaller pulse angle as the repetition time of the pulse sequence is decreased.

2.3.3.1 FLASH sequence

This sequence was first described by Haase et al. (1986) and is termed as FLASH (fast low angle shot) image. Repetition times for FLASH are typically tens of milliseconds, with echo times of a few milliseconds. In a FLASH sequence, it is important to note that when the TR is less than or equivalent to T_2^*, the gradients from next repetitions of the sequence may refocus spin coherence from previous read gradients. This would add signal to the acquisition of the next echo, causing artefacts and changing the expected contrast of the image. To eliminate this effect, all phase coherence should be destroyed or spoiled by application of a crusher gradient (see Figure 2-13).
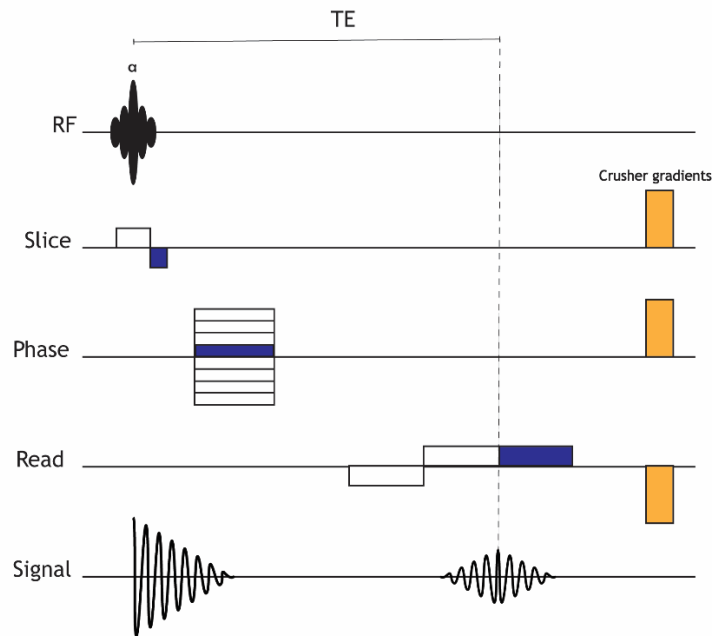
Figure 2-13. Simplified pulse diagram of the FLASH sequence.

2.3.4 Inversion pulse

The Inversion Recovery (IR) technique is the gold-standard method for T_1 mapping. It consists of inverting the longitudinal magnetization and sampling the MR signal at several later inversion times (TI_n) along its exponential recovery (see Figure 2-14). The IR pulse sequence is repeated N times, each time applying the same (typically adiabatic) inversion pulse, followed by a different inversion time (TI), and an imaging module (e.g. spin echo (SE), and echo planar imaging (EPI)). TR must be on the order of the longest measured T_1 to achieve sufficient magnetization recovery. The general equation used for the fitting procedure is given by:

$$M_z = M_0(1 - 2e^{\frac{-TI_n}{T_1}})\qquad(2\text{-}38)$$

Where TI_n is the inversion recovery time of the nth IR scan. By varying TI, T_1 can be obtained via exponential data fitting.
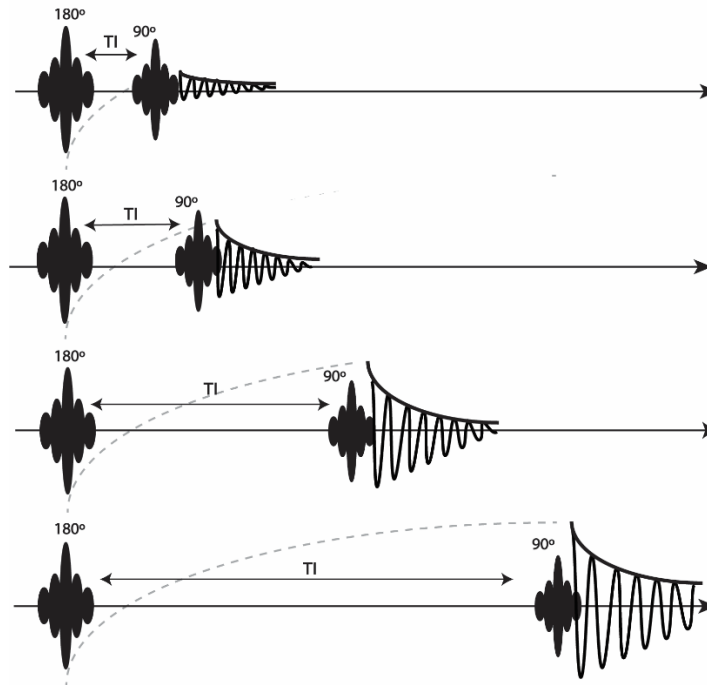
Figure 2-14. Simplified pulse diagram of Inversion Recovery (IR) sequence. This method is based on several IR measurements with different inversion times (TI).

2.4 Diffusion Weighted Imaging

Stejskal and Tanner (1965) showed that the echo magnitude can be sensitised to the random motion of the molecules caused by diffusion. In their experiment, a pair of diffusion gradients were applied on each side of the refocusing 180^0 RF pulse (see Figure 2-15).
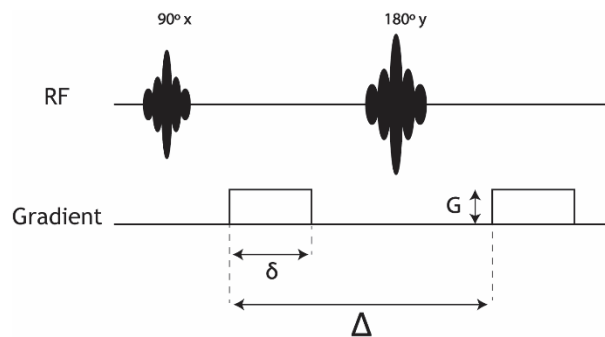
Figure 2-15. Simplified pulse diagram of the Stejskal-Tanner diffusion weighted pulse sequence

The relation between MR signal and the bipolar gradient parameter scan be written as:

$$S_{DWI} = S_0 \exp^{(-bD)} \qquad (2\text{-}39)$$

where (S_0 is the signal at the absent of diffusion gradients (b = 0)). D is diffusion coefficient (mm^2/sec). b value is the diffusion weighting factor, For the spin echo diffusion weighted sequence seen in <u>Figure 2-15</u>, the calculation for b is:

$$b = \gamma^2 G^2 \delta^2 \left(\Delta - \frac{\delta}{3} \right) \qquad (2\text{-}40)$$

The diffusion coefficient can then be calculated as:

$$D = \frac{-1}{b} \ln \left(\frac{S_1}{S_0} \right) \qquad (2\text{-}41)$$

Calculating the diffusion coefficient of each voxel allows a diffusion map to be generated. Using the average value of diffusion coefficient in three orthogonal directions ((D_{xx} + D_{yy} + D_{zz})/3), reduces the multi-directional diffusivity at each point into a single number that can be considered a consolidated apparent diffusion coefficient (ADC).

2.5 Magnetic Resonance Instrumentation

2.5.1 Main Magnet

Superconducting systems are used almost exclusively and form the basis of the vast majority of clinical MRI systems. A typical superconductor used for MR is a Niobium-Titanium (NbTi) alloy in a copper matrix and anywhere from 50 to 400 km of the wire is required for a modern MR magnet. NbTi coils are often kept at approximately 4.2K, which is the boiling point of liquid helium. In the current thesis, all MRI data were acquired using a Bruker PharmaScan 7T system. It has a 16 cm clear bore size with 72 mm free access for the animal.

2.5.2 Shimming

From the bore of the magnet inwards, the first unit is normally the shims coils. The magnet usually requires shimming to correct field distortions, and so reach an acceptable level of homogeneity. In general, there may be a combination of passive and active shims. Passive shims are an array of thin metal plates placed in trays along the bore and their purpose is to remove B_z inhomogeneities. Active shims are a matrix of electromagnets (coils) inside the cryostat, in which each coil carries a different current. The shim coils produce small magnetic field, that vary as functions of position (e.g. dB_z/dx, d^2B_z/dx^2). These small fields superimpose on the B_0 field and are used to improve the B_0 homogeneity.

2.5.3 Gradients

The next unit is the gradient coil set. Normally containing 3 actively shielded gradients, x, y and z. The gradients make the magnetic field vary with position, providing spatial encoding of the Larmor precessional frequency and therefore allowing a determination of where the MR signal is coming from in 3D space (see equation (2-20)). The quality of the gradient system is characterized by the maximum gradient strength (G_{max}) and the ratio of G_{max} over the shortest time required to switch on the gradient (slew rate). For the Bruker PharmaScan 7T system used in this research, the gradient strength is 300 mT/m and slew rates of 6840 T/m/s.

2.5.4 RF coils

The closest piece of equipment to the patient is RF coil. A transmitter RF coil provides pulsed, radiofrequency radiation at the Larmor precessional frequency and generates a magnetic field, B_1 that is orthogonal to the B_0 field (i.e. in the x-y plane) (see section 2.1.4). Transmitter coils may also be used for receiving the MR signal. Further improvements in signal-to-noise ratio (SNR) may be obtained by using a separate local receiver coil. For this experiment described in this thesis the B_1 transmit field was generate using a volume birdcage coil and the MRI signal was detected using a 4-channel phased array rat head receiver coil.
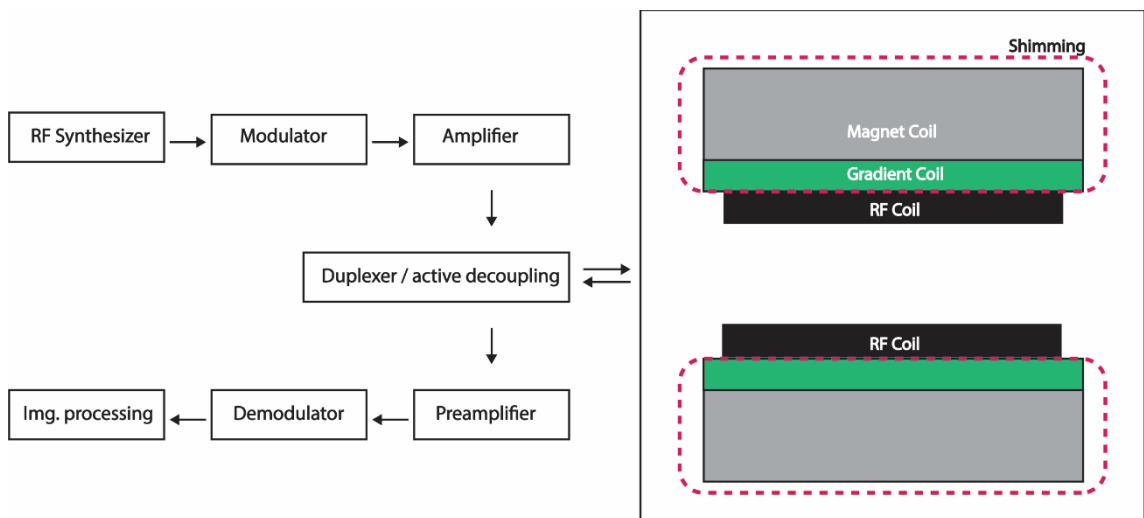
Figure 2-16. Representative of basic component of MRI Scanner.

2.5.5 RF transmission / MR signal reception and digitization

2.5.5.1 RF synthesizer

The central computer controls the RF frequency ω_1, the RF synthesiser generates a low power electrical signal with this frequency. Note that the frequency synthesiser is also linked to the receiver unit to provide a reference frequency.

2.5.5.2 RF modulator

Through the RF modulator, the RF reference wave is modulated into RF pulses with modified amplitude and time according to the sequence design.

2.5.5.3 RF amplifier

The RF transmission pulses are then scale up to high power by changing the gain of the amplifier using a transmit attenuator (300-1000 kW) to produce a large-amplitude RF pulses for transmission to RF transmitter coil.

2.5.5.4 Decoupling box

During transmit pulse, the decoupling boxes move the receiver coil OFF resonance. Then during acquisition, it moves the transmit coil off resonance

2.5.5.5 RF preamplifier

The MR signal is detected by the RF receiver coil and is extremely weak (on the order of millivolts). To prevent contamination by environmental noise, the signal is immediately amplified to a higher power signal (on the order of volts) through a pre-amplifier.

2.5.5.6 RF demodulator

The MR signal then passes into the receiver unit where the signal transformed to the audio frequency range. This is achieved by mixing the signal with a reference frequency, a process called demodulation. This simplifies the analysis of the data. To be able to discriminate between frequencies either side of the carrier or central frequency, quadrature demodulation is used.

2.5.5.7 Image digitization

An Analog-to-Digital converter (ADC) is used to change the analog signal into digital representation for input to a computer system. The number of bits in the ADC determines the dynamic range of the receiver and the sampling rate determines the bandwidth of the acquisition. The ADC on the pharmascan scanner is a 16-bit ADC meaning it has the ability to detect 65,536 (2^{16}) discrete analog levels.

3 Chapter 3: Methods

3.1 Animal preparation and Surgical Procedures

In this thesis, all surgical procedures and cannula implantation for infusion studies were carried out by Mrs Lindsay Gallagher (Personal license number 60/713). Study design, surgical assistance, MRI imaging, MATLAB coding for image analysis, physiological data analysis, and infusion experiments were carried out by myself.

3.1.1 Preparation of animal for surgery and imaging

All experiments and procedures in this thesis were carried out under license from the UK Home Office (Personal Licence number 60/11925, working under Project Licence numbers 60/3759 and 60/3618) and in accordance with the Animals (Scientific Procedures) Act, 1986, incorporating European Directive 2010/63/EU and approved by the University of Glasgow Ethical Review Panel. Also, the Animal Research: Reporting *in vivo* Experiments (ARRIVE) guidelines (http://www.nc3rs.org.uk/arrive-guidelines) was observed during planning, experimentation, analysis, and documentation of all procedures.

3.1.2 Animal Housing

Adult male Wistar Kyoto (WKY) or Wistar rats were obtained from Charles River Laboratories and housed in an animal care facility at the University of Glasgow. After their arrival, all rats were acclimatised for one week before any experimentation. Rats were housed in groups with water and food freely available and were maintained on a 12-hour light/dark cycle.

3.1.3 Anaesthesia

Anaesthesia was induced in an anaesthetic gas chamber, with 5% isoflurane (Baxter Healthcare Ltd, UK) administered in a 30:70% O_2:NO_2 mixture. The depth of anaesthesia was assessed by means of the withdrawal reflex, where the footpad of the hindlimb is tightly squeezed to evoke a reflex withdrawal of the foot. Once deeply anaesthetised, the rat was immediately transferred to a designated area within the laboratory and the fur overlying any planned incision

sites was removed using electric clippers (Wella, Germany) and cleared using a handheld vacuum (Black & Decker, USA). Then, the rat was transferred to operating table within the laboratory and was artificially ventilated following tracheal intubation or tracheotomy if rat was not recovered following surgery. Following removal from the anaesthetic chamber, the dose of isoflurane was reduced to between 2% and 3% in the same gas mixture stated previously, to maintain surgical anaesthesia.

3.1.4 Surgical procedures

3.1.4.1 Induction of middle cerebral artery occlusion

Permanent occlusion of the left MCA was performed by intraluminal thread occlusion, as previously described (Enrique Zea Longa *et al.*, 1989b). All surgery was performed under a light operating microscope (Zeiss, Germany). A small ventral midline incision was made. Blunt dissection near the intersection of the sternomastoid and the sternohyoid muscles exposed the underlying carotid bifurcation. The common carotid artery (CCA) and internal carotid artery (ICA) were separated from the vagus nerve. A small cut on the ventral side of the CCA below the bifurcation was performed and a 4-0 nylon monofilament with silicone coated tip (403934PK10 or 404134PK10 Doccol Corporation, USA) from the bifurcation point of the right CCA and gently advanced into the circle of Willis until reaching a mild resistance, to occlude MCA. The filament was permanently left in position by a double knot around the CCA and ICA. The wound was closed using a 4-0 silk suture. In case of successful filament placement with complete occlusion of the MCA confirmed by MRI, the rat was placed in a preheated cage (with the heating pad under it) for recovery from anaesthesia.

Sham-operated animals were submitted to the above surgical procedure with the exception of the filament introduction. Briefly, animals were underwent skin incision, separation of the Vagus nerve from the CCA, and skin suturing, in the absence of CCA occlusion. Post-suturing, then returned to the heated cage to recover from anaesthesia.
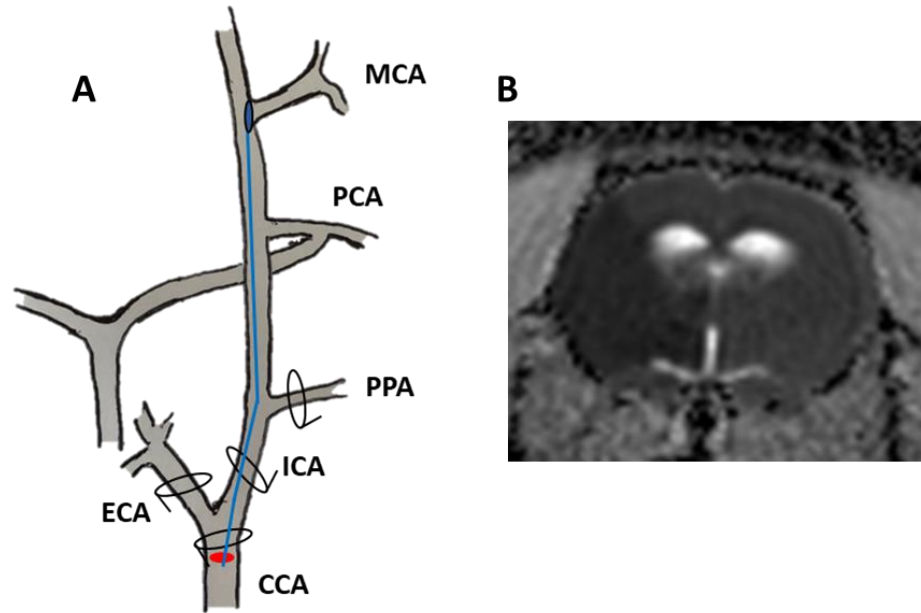
Figure 3-1. Diagram illustrating the intraluminal filament model of MCAO. (A) Common carotid artery (CCA), external carotid artery (ECA), and pterygopalatine artery (PPA) were tied off with a secure tie and a silicon-coated nylon filament was inserted to occlude the MCA. (B) The region of ischaemic damage appears dark on ADC maps image.

3.1.4.2 Intracranial pressure measurement

Intracranial pressure (ICP) measurements were obtained while under anaesthesia. Following MRI scanning at 24 hours post-MCAO or sham surgery, rats were re-anesthetised (5% isoflurane in 30:70 O_2/NO_2 mixture) and transferred to a stereotaxic frame where the head was secured in ear and tooth bars. The co-ordinates (Bregma 1.3 mm posterior, 2 mm lateral) for the lateral ventricles were identified from the rat brain stereotaxic atlas (Paxinos & Watson) and, where necessary, adjusted slightly to accommodate any brain swelling identified on the T_2 weighted MRI scans. Two burr holes were drilled over the ipsilateral and contralateral lateral ventricles and, for ICP monitoring, a 25-gauge needle connected by an air-free fluid system was placed in the ipsilateral ventricle and attached to a pressure transducer for continuous ICP recording. The probe was secured to the skull with cyanoacrylate glue to avoid leakage. The correct position of the ICP probe within the ventricle was confirmed by the presence of CSF pulsation within the catheter. Prior to ICP recording, pressure transducers were calibrated with a Sphygmomanometer and the ICP waveform signal was confirmed by response to abdominal compression, ensuring clear cardiac and respiratory waveforms were visible.
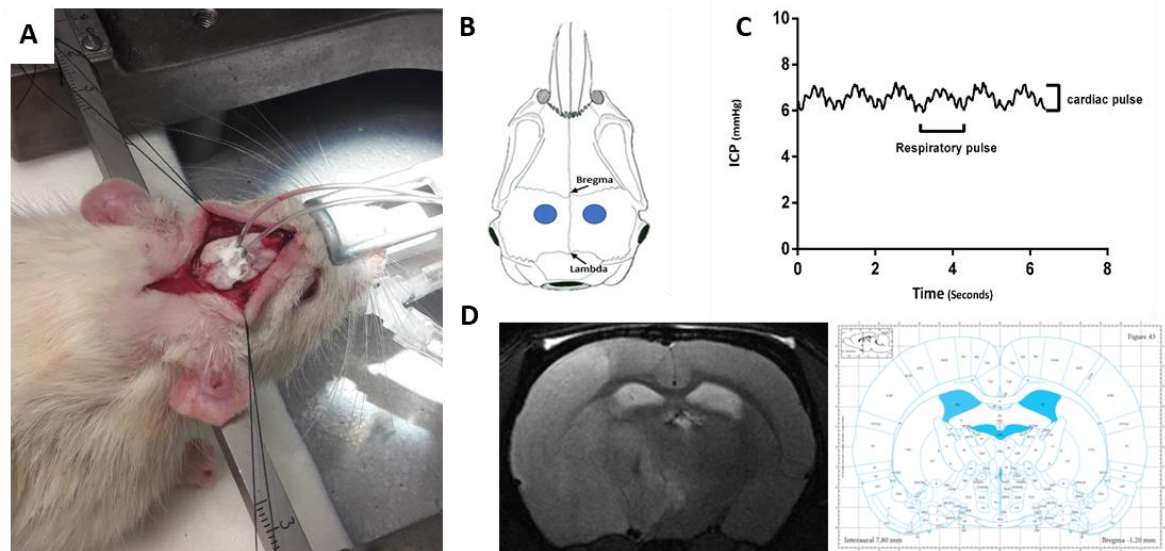
Figure 3-2. ICP recording from a rat. (A) Picture from the surgical procedure. The ventricular probe has already been placed and connected to the transducer to verify patency. (B) Illustration of location of the ICP and CSF probe on the rat skull. (C) ICP waveform signal was confirmed by clear cardiac and respiratory waveforms were visible. (D) In the case of post stroke rats, the coordinate needs to be adjusted slightly to accommodate any brain swelling. This can be achieved by acquiring T_2 weighted MRI scans and then matching the T_2 weighted slice with corresponding atlas slide. The coordinates will be adjusted to accommodate any brain swelling.

3.1.4.3 Cisterna magna cannulisation for MRI study

For MRI tracer infusion studies, all anaesthetised animals were transferred to a stereotaxic frame where the head was secured with ear and tooth bars. The head was tilted (45 degrees, snout down), and a midline skin incision was made to expose the dura mater overlying the cisterna magna space. A cisterna magna (CM) cannula (22-gauge PEEK, SAI, RCMC-01) connected to a closed-end PE10 tube (2.5 cm long, 0.28 mm ID × 0.61 mm OD, Braintree Scientific) loaded with artificial CSF (aCSF: NaCl 140 mmol/L, KCl 3 mmol/L, NaH2PO$_4$ 12 mmol/L, NaHCO$_3$ 18 mmol/L, CaCl$_2$ 2.5 mmol/L, pH 7.4) was advanced 2 mm into the intrathecal space and secured with cyanoacrylate glue to avoid leakage (see Figure 3-3). Finally, the skin and muscle incisions were sutured closed.
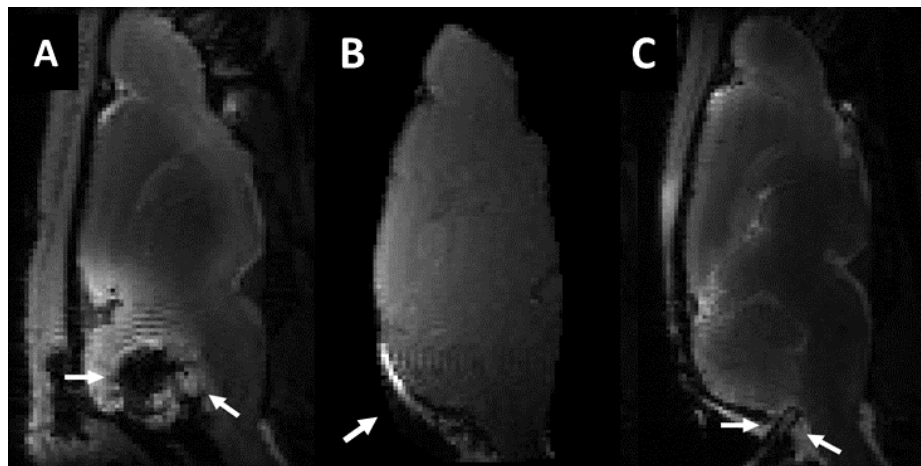
Figure 3-3. CM cannula position.(A) and (B) An example of incorrect CM cannula position. (C) cannula was correctly advanced into the cisterna magna.

In the early development experiments, a dye (0.5% in desired solutes) was added to the aCSF, to help in confirming the correct position of CM catheter. At the end of each experiment the brain was carefully dissected out of the skull and the flow of solutes was confirmed by visualising the movement of the dye along penetrating vessels on the surface of the rat brain. However, it was noticed that because of the iron content of the dye, it also acted as a weak paramagnetic contrast agent, causing an increase in T$_1$ weighted signal. In addition, the dye decreased transverse relaxation times, resulting in signal loss in T$_2$ weighted image (see Figure 3-4). In later experiments, the dye was not employed and the

correct position of the CM catheter within the cisterna magna space was confirmed by the presence of CSF pulsation within the catheter.
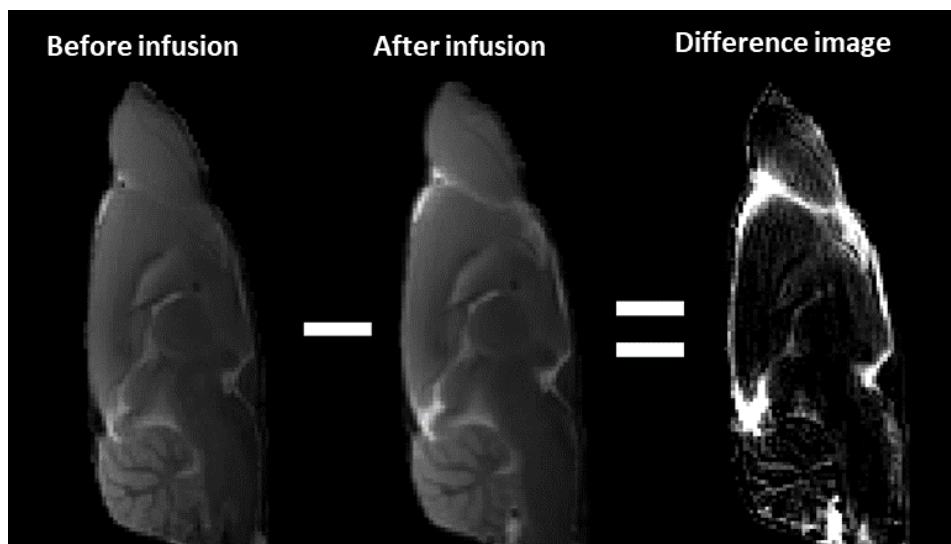
Figure 3-4. Blue dye effect on T$_2$ weighted images.

3.1.5 Physiological monitoring

Throughout the period of anaesthesia, a number of physiological parameters were monitored regularly, controlled and recorded at regular intervals. Body temperature was continuously monitored throughout surgery and MRI procedures with a rectal thermocouple (Thermalert TH-5, Physitemp) and maintained at 37 ± 0.5°C using homeothermic blanket (Harvard) and external heat lamp. The femoral artery was cannulated with PE-50 tubing for continuous monitoring of arterial blood pressure and heart rate (Biopac Systems, MP100). Arterial blood pressure values were acquired and monitored by connecting the femoral artery catheter to a blood pressure transducer which was linked to an MP150 Biopac system (Biopac systems Inc, USA).The "Acknowledge" software (Biopac systems Inc, USA) was used to acquire and present the mean arterial blood pressure (MAP) along with ICP and cerebral prefusion pressure (CPP) on a computer monitor. For the measurement of arterial blood gases and pH, a blood sample (~100μl) was withdrawn from the femoral artery cannula into a glass capillary tube and the tube was immediately taken to the blood gas analyser (Rapidlab 248/348, Siemens). The blood gas analyser adjusted the blood gas and pH values according to the animal's temperature when the sample was obtained.
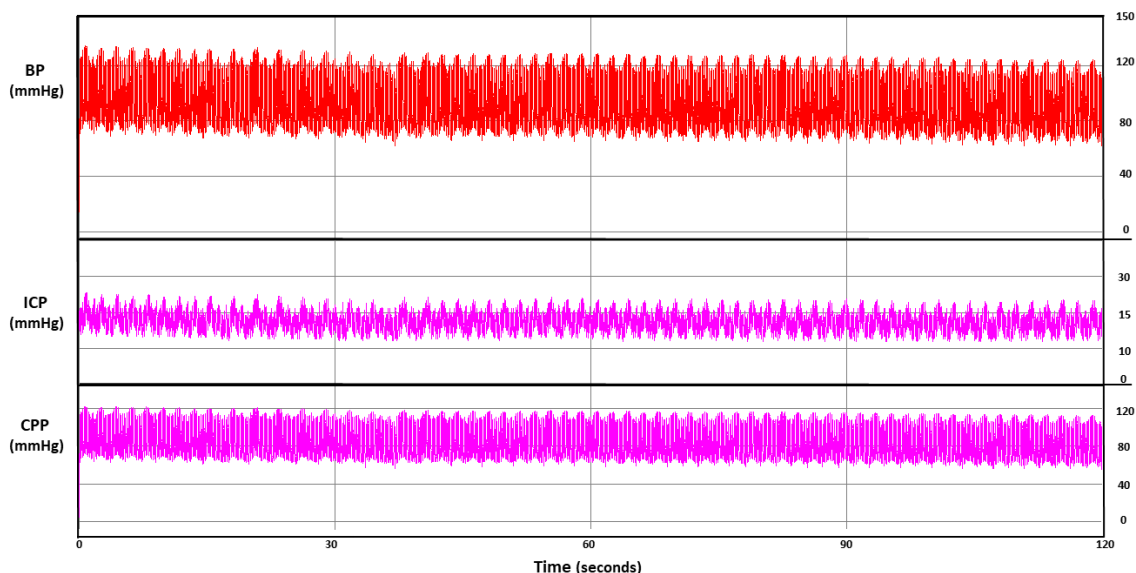
Figure 3-5. Example of continuous ICP, BP, and CPP measurements from an individual rat.

3.1.6 Animal recovery from surgery

At the end of pMCAO procedures in Chapter 4, where rats were recovered from surgery for 24 hours, the arterial cannula was removed and the small incision in the artery was closed overusing diathermy forceps. The wound was closed using 4-0 suture. The isoflurane concentration was decreased to 0% and the rats were ventilated with 100% oxygen until they became responsive to foot pinching and started to breathe without the ventilator. At this point the rat was disconnected from the ventilator and the intubation tube was removed. The rat was supplemented with 50% oxygen via a facemask until breathing became steady and the animal started to regain consciousness. Then, the rat was transferred to a clean cage lined with soft absorbent pads, containing softened food and water. The cage was transferred to a recovery room maintained at ~25°C during the recovery period, the rat was closely monitored for at least 2 hours post-surgery and details of the rat's condition were recorded on animal recovery sheet.

3.2 MRI image pre-processing steps

All MRI data in this thesis were acquired using a Bruker Pharmascan 7T/16 cm system controlled by Paravision 5.1 software (Bruker BioSpin, Ettlingen, Germany). The system had a gradient coil insert (internal diameter = 90 mm, 300 mT/m) and a four-channel phased-array surface receive coil used for rat brain imaging.

MRI data were processed using Matlab code developed in-house (Matlab R2018a, MathWorks Ltd., U.K.). All acquired MRI data in Chapters 6, 7 and 8 underwent several correction and pre-processing steps, which are summarized in Figure 3-6.
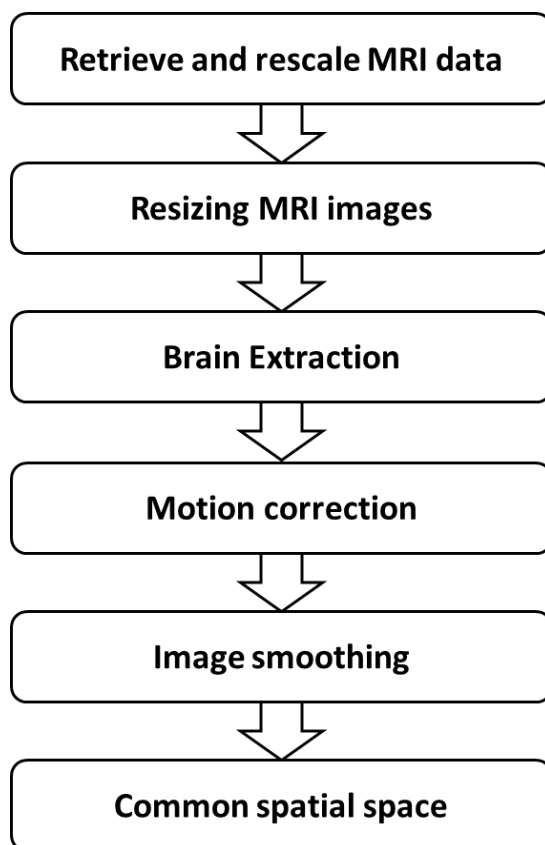
Figure 3-6. Simplified diagram of MRI image pre-processing steps.

3.2.1 Retrieve and rescale MRI Data

All acquired MR images were exported as DICOM files. Before starting any post-processing steps, image data were rescaled, as necessary, to the original intensity measurements using the Bruker format files. To do this, the image data were multiplied by the scaling factor, called Reco_Map_Slope, for each time point for each subject.

3.2.2 Resizing MRI images

In the current work, different MRI weighted images were acquired with different slice thickness. For example, the slice thickness of the T_2 weighted images was 1.5 mm, while the 3D T_1 weighted images was about 0.23 mm (Figure 3-7). In order to accommodate these variabilities in slice thickness, a protocol was developed to register and stack multiple T_1 weighted image slices to reflect the imaging slice thickness of the T_2 weighted images. A similar approach was used when 3D T_1 weighted images were compared with T_1 mapping images, which had a 2mm slice thickness.
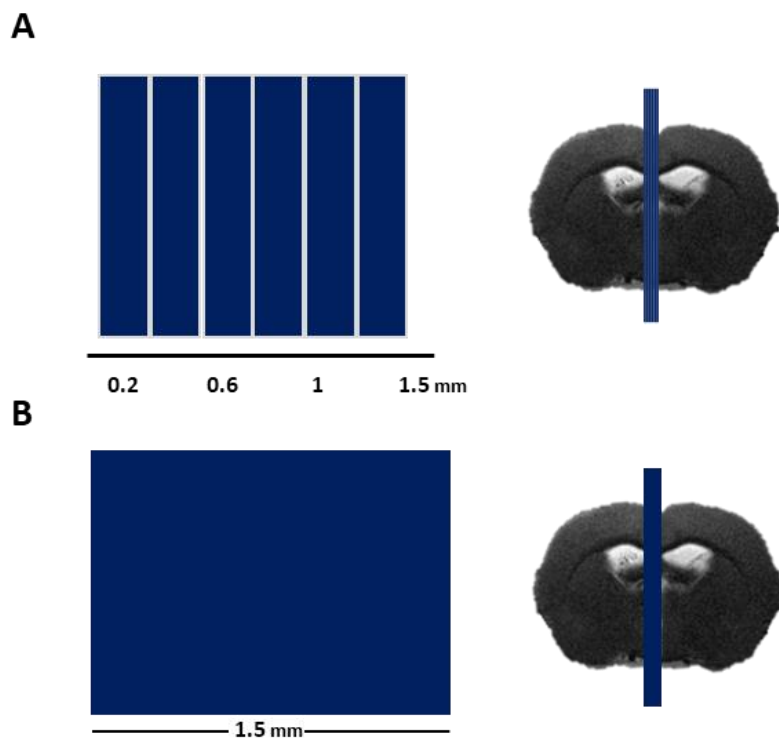
Figure 3-7. MRI image slice thickness adjustment. (A) Four evenly distributed T_1 weighted sagittal slices (0.23 mm) were selected from near midline at the level of the aqueduct to cover the 1.5 mm thickness of theT$_2$ weighted scans (B).

3.2.3 Brain extraction

Skull-stripping (or brain extraction) usually results in a binary brain mask of an MR image after removal of non-brain structures. In this work, all MR images were manually masked to separate the brain from non-brain tissues and, therefore, to reduce the computational complexity of the subsequent processing. In addition, the deformation of the non-brain tissues during the experiment affects proper co-registration of the volumes (see Figure 3-8).
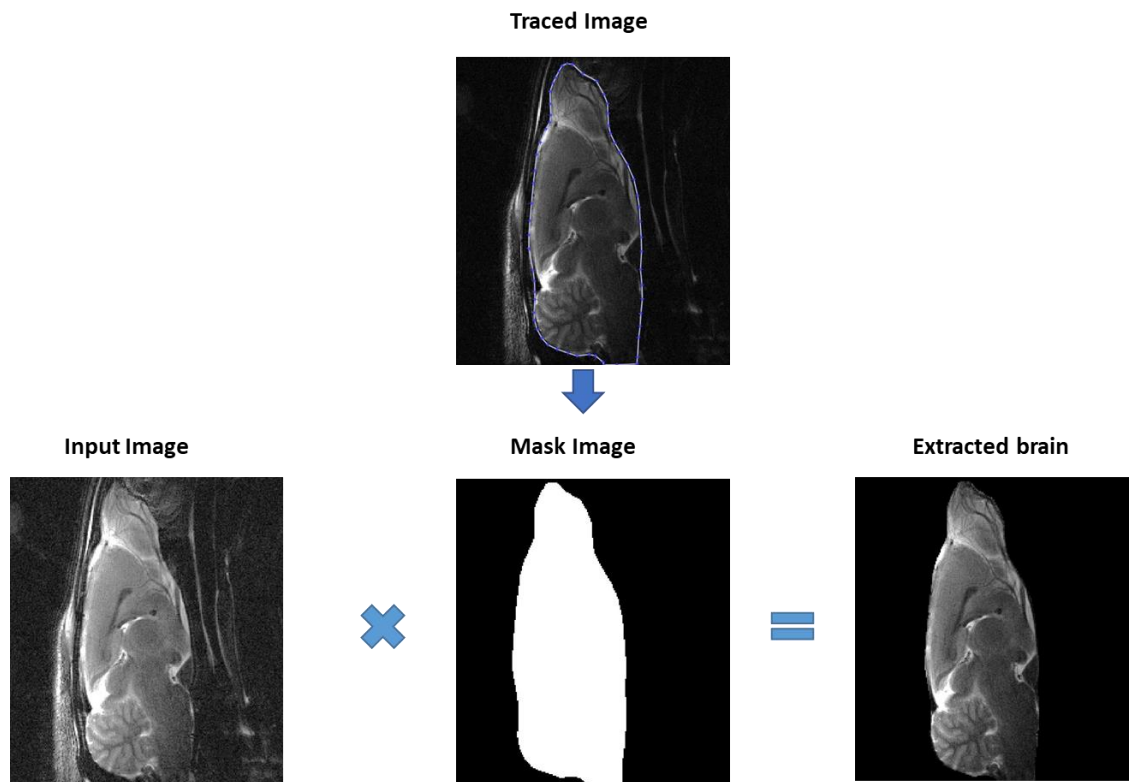
Figure 3-8. Schematic representation of brain extraction steps. The left image shows the original MRI image. This is multiplied by a manually drawn binary mask encompassing the entire brain volume and the resulting image includes only the brain without the background signal.

3.2.4 Motion correction

The small signal changes due the presence of the $H_2^{17}O$ tracer ($\sim$ 2-10 %), can be obscured by the apparent signal differences that can result from subject movement. To minimise subject motion, the rat was fixed in the cradle with both a tooth bar and ear bars. Because head movement in the scanner cannot be completely eliminated, retrospective motion correction was performed as a pre-processing step. This is especially important for long experiments, as is the case in the current thesis (> 80 minutes), where the animal's brain can sometimes move during the experiment. For each animal, head motion was compensated by rigid-body alignment of each post-contrast image to the first time point of the pre-contrast image (Figure 3-9).
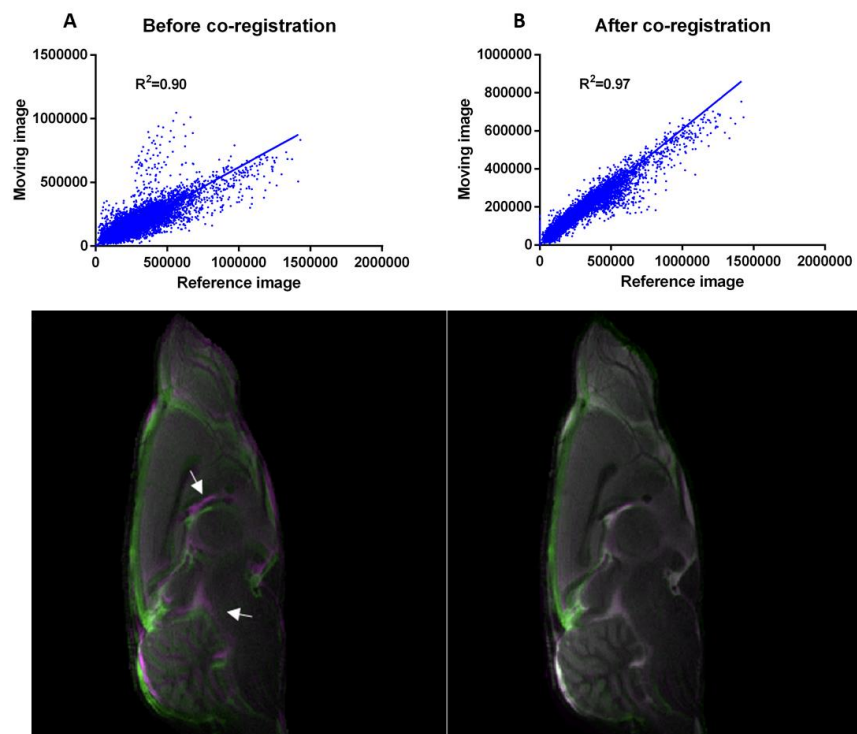
Figure 3-9. Visual assessment before and after T$_2$ weighted MR image co-registration. (A) 2D histogram of two overlapping images before co-registration. (B) 2D histogram of two overlapping images after co-registration using rigid transformation. In the overlapping images, grey areas correspond to areas that have similar intensities, while magenta and green areas show places where one image is brighter than the other. There is a noticeable improvement in the alignment of the images (before co-registration, R^2=0.90; after co-registration, R^2=0.97).

3.2.5 Image smoothing

Filtering techniques have the advantage of reducing the noise without affecting the acquisition process. There are number of common approaches that reduce the amplitude of noise fluctuations, but most of these methods also degrade sharp details such as lines or edges (Ming Zhang and Gunturk, 2008). In the current work, filtering methods were used, such as median filter and anisotropic diffusion filter techniques to remove noise and retain the edges in the image (Figure 3-10).
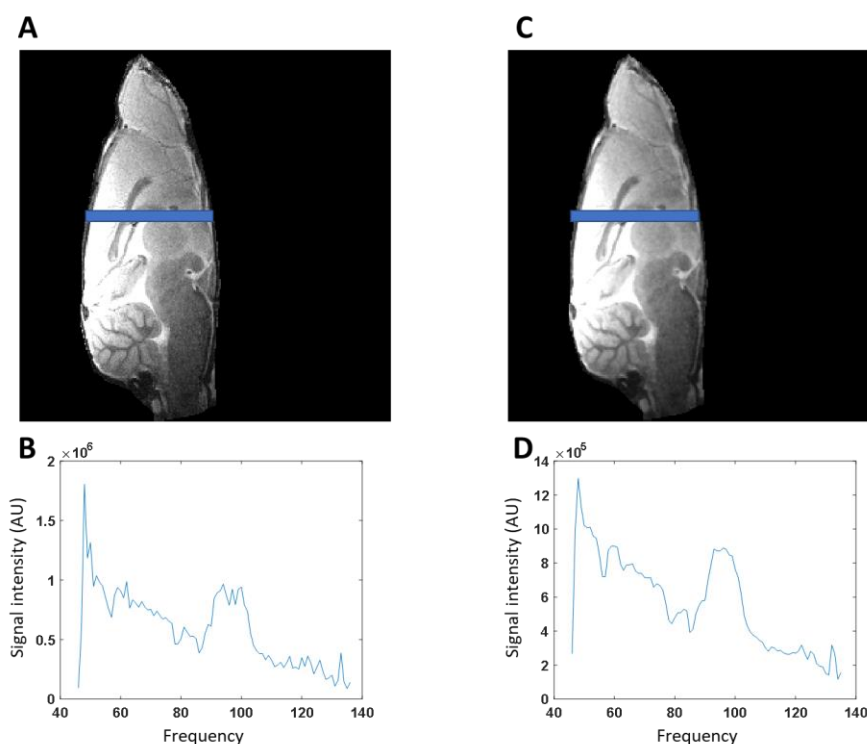
Figure 3-10. Filtering results for one slice of MRI dataset. (A) T$_2$ weighted image before applying filter along with (B) a line profile plot of the signal intensity (line shown in blue). (C) T$_2$ weighted image after applying anisotropic diffusion filter along with (D) a line profile plot of the signal intensity (line shown in blue).

3.2.6 Common spatial space

To maintain the same spatial position/orientation and reduce variability between animals, one animal was selected from each group as the reference against which all the other animals' images within the same group were aligned. To that end, each rat brain was aligned to the reference animal using an affine registration algorithm. All transformed MR images, including the baseline and contrast-enhanced scans, were averaged to create a template image with high-contrast. This image was manually segmented into multiple regions of interests (ROIs) for further analysis (see Figure 3-11).
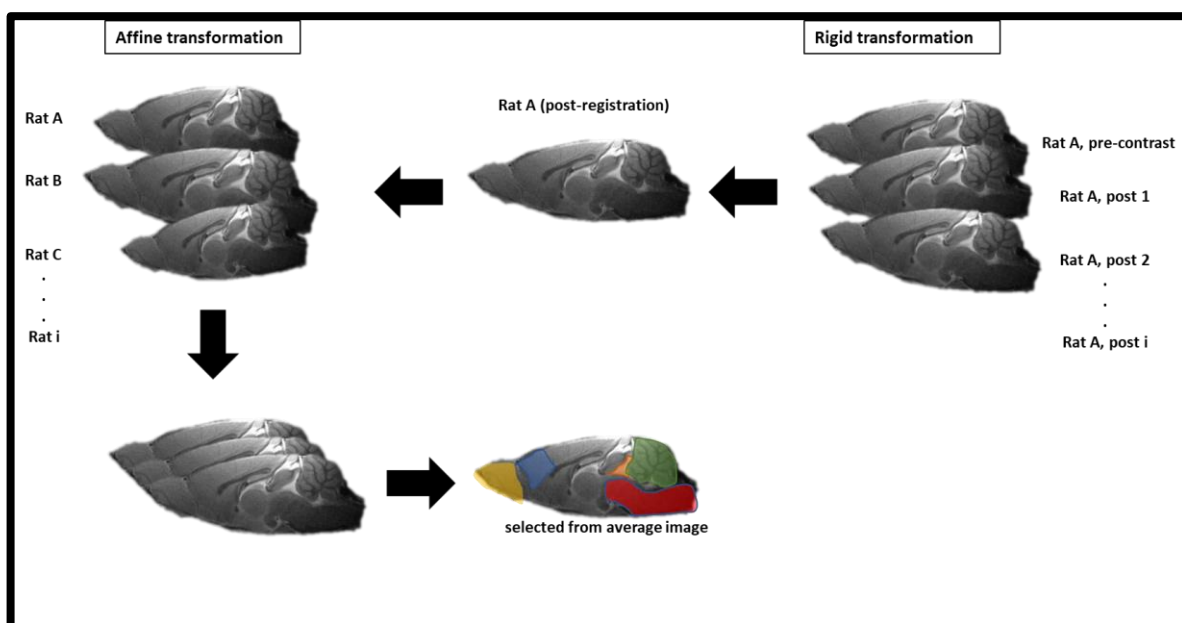
Figure 3-11. Schematic diagram illustrating the processing steps to acquire common spatial registration of all images and subsequent segmentation. First, for each rat all post-contrast images were registered to a baseline image using a rigid transformation process. Then, images were co-registered for each individual rat using an affine transformation process. Finally, an average image was created and segmented into multiple regions of interest for further analysis.

4 Chapter 4: CSF outflow resistance, the possible mechanism responsible for ICP elevation following ischaemic stroke

4.1 Introduction

Early neurological deterioration (END) can occur within the first 24-48 hours following acute ischaemic stroke, with prevalence being relatively common (>14%), and is strongly associated with poor outcome (Seners and Baron, 2018). END was defined as an increase in the National Institutes of Health Stroke Scale (NIHSS) score of > 4 points within the first 24 hours after admission (Seners *et al.*, 2015). Although some cases of END have a straightforward cause, such as symptomatic intracranial haemorrhage and malignant oedema, approximately ~2/3 of cases remain unexplained (Seners *et al.*, 2015). These unexplained END cases are associated with persistent proximal occlusion, large diffusion-perfusion mismatch, and diffusion weighted imaging lesion growth beyond the initial ischaemic penumbra (Hsu *et al.*, 2015).

Several mechanisms have been proposed, involving either compromised hemodynamic or other tissue-based mechanisms. Suggested mechanisms based on compromised hemodynamic include thrombus extension (Tisserand *et al.*, 2014), collateral failure (Beard *et al.*, 2015), and reduced mean arterial pressure (Kjeldsen and Berge, 2015). Other tissue-based mechanisms have included excitotoxicity (Castillo, Dávalos and Noya, 1997), inflammation (Vila *et al.*, 2003), hyperthermia (Audebert *et al.*, 2004), oedema (Frank and Frank, 2011), hyperglycaemia (Seners *et al.*, 2015), and hypoxia (Read *et al.*, 2000). Although these mechanisms may make some contribution, there is a lack of strong evidence associating them with END.

An intriguing alternative mechanism has recently been proposed suggesting that elevated ICP, resulting in reduced collateral flow and cerebral perfusion, may be responsible for unexplained END (Gaberel *et al.*, 2012). However, the mechanism for this rise in ICP is currently unknown. Conventionally, only patients with large malignant strokes are considered to be at risk of elevated ICP, due to space occupying vasogenic oedema within the closed cranial compartment (Schwab *et al.*, 1996). This logic has been extended to infer that

1   ICP does not become elevated in cases of smaller, non-malignant strokes, since

2   there is little or no vasogenic oedema. However, we can find no evidence in the

3   clinical literature to support this broad assumption, presumably because the

4   risks associated with invasive ICP measurement prevent its use. This assumption

5   is also contradicted by recent animal experiments, which show dramatic

6   increases in ICP occurring around 24 hours after stroke onset, even following

7   small strokes where there is little or no vasogenic oedema (Murtha *et al.*, 2015).

8   This evidence leads us to hypothesize that a mechanism, other than oedema, is

9   responsible for ICP elevation in these cases. Inspection of a mathematical model

10   of ICP indicates that changes in the CSF dynamics may be responsible for the

11   observed increases in ICP post-ischaemic stroke (Mann *et al.*, 1978; Marmarou,

12   Shulman and Rosende, 1978). Therefore, in the present study, we have

13   investigated the relationship between CSF dynamics, vasogenic oedema, and ICP

14   following experimental stroke.

15

16

17

18

19

20

21

22

23

24

25

4.2 Methods

4.2.1 Surgical procedure

Male Wistar Kyoto (WKY) rats (350 to 400 g, 22 to 26 weeks old) were initially anesthetised (5% isoflurane in 30:70 O_2/NO_2 mixture) in an induction chamber, then intubated, and artificially ventilated (with 2-3% isoflurane in 30:70 O_2/NO_2 mixture at flow rate 1-2 L/min). Animals were randomly allocated to either a permanent middle cerebral occlusion group (pMCAO, n=8) or a sham surgery group (sham, n=6). Permanent occlusion of the left MCA was performed as stated in Chapter 3, section 3.1.4.1. For sham group rats, surgery to reveal the MCA was carried out but the artery was not occluded. Immediately following surgery, rats were transferred to the MRI scanner and diffusion weighted imaging (DWI) was conducted to assess baseline lesion volume. Rats were then recovered from the anaesthesia and, 24 hours after surgery, re-anaesthetised for assessment of final infarct volume using T_2 weighted MRI. The animal was then transferred into the surgery room for ICP measurements. The experimental protocol is shown schematically in Figure 4-1.

4.2.2 Magnetic Resonance Imaging and Analysis

A pilot MRI T_2 weighted sequence was first acquired to determine the correct geometry. A DWI scan (4-shot, spin-echo, EPI) was performed 30 minutes after MCAO allowing quantitative apparent diffusion coefficient (ADC) maps to be produced (TE = 22 ms, TR = 4,000 ms, matrix = 96 x 96, field of view = 25mm x 25 mm, three directions (x, y, and z), b values = 0 and 1,000 s/mm^2, eight coronal slices, and 1.5 mm thickness). A T_2 weighted (RARE) scan was performed to assess infarct volume at 24 hours (TE = 46.6 ms, TR = 5,000 ms, RARE factor 8, averages 2, matrix 256 × 256, FOV 3.0 cm × 3.0 cm, 8 slices, and 0.75 mm thickness).

4.2.3 ICP measurement and CSF infusion

Following MRI scanning at 24 hours post-MCAO or sham surgery, rats were re-anesthetised (5% isoflurane in 30:70 O_2/NO_2 mixture) and transferred to a stereotaxic frame where the head was secured in ear and tooth bars. ICP probe was placed in the ipsilateral ventricle and attached to a pressure transducer for

1 continuous ICP recording as described in Chapter 2, section 3.1.4.2. CSF catheter

2 was inserted into the contralateral lateral ventricle and secured to the skull with

3 cyanoacrylate glue, then connected to an infusion pump (Graseby /3150 Syringe

4 Pump). CSF dynamics were probed via a steady-state infusion method, involving

5 stepwise increases in the intracerebroventricular infusion of artificial

6 cerebrospinal fluid (aCSF) (Hussey, Schanzer and Katzman, 1970). The baseline

7 ICP pressure was monitored for 30 minutes before starting infusion of aCSF. The

8 infusion rate was adjusted incrementally (1.67, 3.33, 5.00, 8.30, 11.67, 16.67,

9 25.00 and 33.3 µL/min), with 4-6 minutes allowed for a steady-state ICP to be

10 established after each increase (see Figure 4-2). During the infusion experiment,

11 mean arterial pressure (MAP), CPP and ICP were continuously monitored in all

12 rats. Blood gases (pH, partial pressure of oxygen (PaO_2), carbon dioxide ($PaCO_2$))

13 was measured before and after the infusion as described in chapter 3.

4.2.4 Mathematical modelling

15 Marmarou and colleagues developed a mathematical model of the CSF/ICP

16 system (Marmarou, Shulman and Rosende, 1978). Here we have extended their

17 steady-state case to include growth in brain oedema. In the closed cranial

18 cavity, steady-state ICP exists when rates balance.

$$\mathbf{Q}_{prod} + \mathbf{Q}_{oedema} = \mathbf{Q}_{abs} \qquad (4\text{-}1)$$

19 Where, Q_{prod} is the rate of CSF production and Q_{oedema} is the rate of oedema

20 growth. Assuming the rate of CSF absorption across the arachnoid villi, Q_{abs}, is

21 proportional to the corresponding pressure drop ΔP= P_{ICP} – P_{ss}. the venous sagittal

22 sinus pressure P_{ss} is small (ΔP $\cong$ P_{ICP}), with aCSF outflow resistance, R, gives:

$$\mathbf{P}_{ICP} = \mathbf{R}\mathbf{Q}_{abc} = \mathbf{R}(\mathbf{Q}_{prod} + \mathbf{Q}_{oedema}) \qquad (4\text{-}2)$$

23 In the case of the steady state infusion experiments, as the rate of infusion of

24 aCSF is greater than ($Q_{prod} + Q_{oedema}$), this becomes:

$$\Delta\mathrm{P}_{ICP} = \mathrm{R}\mathrm{Q}_{abc} \cong \mathrm{R}\mathrm{Q}_{inf} + \mathrm{c} \qquad (4\text{-}3)$$

where Q_{inf} is the rate of infusion of aCSF. It can be seen from equation (4-3) that the CSF outflow resistance is then obtained from the slope of the plot of ΔP_{ICP} vs Q_{inf}.

4.2.5 Data Analysis

Quantitative ADC maps, in units of square millimetres per second, were calculated from the Stejskal-Tanner equation using Image J software (http://rsb.info. nih.gov/ij/). A 23% reduction in mean contralateral ADC was used to determine ischemia lesion volume from the multi-slice ADC maps (Figure 4-3) (Gerriets *et al.*, 2004). Infarct volume was determined at 24 hours from T_2 weighted images by manual tracing of the hyperintense lesion area on each slice (Figure 4-4). This was then summed and multiplied by the slice thickness. The oedema-corrected lesion volume (LVe) and the space occupying effect in percent of oedema uncorrected lesion volume (SE) were calculated from equations derived by Gerriets (2004):

$$LVe = HVc + HVi - (HVc + HVi - LVu) \times \frac{(H + HVi)}{2HVc} \qquad (4\text{-}4)$$

$$SE = LVu - LVe \qquad (4\text{-}5)$$

HVi and HVc refer to the volumes of the ipsilateral and contralateral hemispheres, respectively. LVu represents the uncorrected lesion volume as delineated on the T_2 weighted images. All volumetric measurements were performed independently by two independent investigators. To examine interobserver reproducibility, investigator 2 determined infarct and oedema volumes on the same images and the calculated values were compared with the results obtained by investigator 1. Any cases with >10% discrepancy was flagged for review.

4.2.6 Impact of aCSF infusion on oedema size

To ensure that infusion of aCSF does not contribute to the development of brain oedema, a pilot experiment was conducted with the same infusion rates and durations used in the original experiments. An MRI compatible catheter was

inserted into the cisterna magna via Dural puncture and placement was confirmed by the presence of CSF pulsation within the catheter. The catheter was secured in place with cyanoacrylate glue and connected with peristaltic infusion pump. Following surgery, the rat was transferred to the MRI scanner, where it stayed for the whole duration of the experiment. The rat was fixed into position with ear bars and a tooth bar, preventing any motion of the head. An initial T_2 image was then acquired. Next, aCSF was infused, with the rate of infusion increased in steps manner similar to infusion rates and durations as used in the original experiments (Figure 4-10). T_2 images were acquired at each infusion rate. At the end of the experiment, Gadolinium based tracer (Gd-DTPA) was infused, and a T_1 weighted MRI scan was obtained to confirm that the catheter was held in place during the entire infusion study.

4.2.7 Impact of increased ICP on collateral flow

Following the induction of pMCAO, the rat (n=2) was returned to the stereotaxic frame with its head was secured by a tooth and ear bars. A cisterna magna (CM) catheter was inserted for aCSF infusion and ICP monitoring as described in Chapter 2, section 3.1.4.3. The catheter was connected with peristaltic infusion pump. A femoral arterial line was placed by surgical cutdown for continuous arterial blood pressure. For Laser speckle contrast imager (LSCI) imaging, the surface of the skull was exposed and thinned to ensure adequate transparency, hence signal during imaging. Real time changes in cortical blood flow were recorded by the LSCI (PeriCam PSI HD system, Perimed, Stockholm, Sweden), which is sensitive to the motion of intravascular red blood cells. The experimental protocol consisted of a baseline recording started at 30 minutes from the onset of stroke and continued until 2 hours post-MCAO. Then, ICP was increased by infusion of aCSF into cisterna magna of a rat. The infusion rate was increased in a stepwise manner, until the change of ICP reached 30 mmHg, with no significant change in arterial blood pressure (see Figure 4-11).

4.2.8 Statistical analysis

A sample size calculation was performed using pilot data (G*Power v.3.1.3 software) (see Figure 4-5), which estimated that six animals per group were required to detect a 60% difference in CSF outflow resistance and 6 mmHg

1   difference in ΔICP between the sham and pMCAO groups with standard settings

2   of alpha 0.05, power 0.8 (Erdfelder, 2007). Students t-tests were performed on

3   physiological parameters for illustrative purposes to highlight changes between

4   pMCAO and sham rats. Mann–Whitney U-tests were performed to compare mean

5   ICP and CSF resistance values between sham and post-stroke groups. Spearman's

6   correlation analysis was used to determine the correlation between ICP and

7   oedema volume, infarct volume and CSF resistance. For the CSF infusion test,

8   statistical analysis was performed with the Wilcoxon signed-rank test on ICP,

9   MAP, and CPP to detect differences between each infusion step point and

10   baseline values. Data are presented as mean ± standard deviation unless

11   otherwise stated. All tests were considered statistically significant for p values

12   <0.05.

13

14

15

16

17

18

19

20
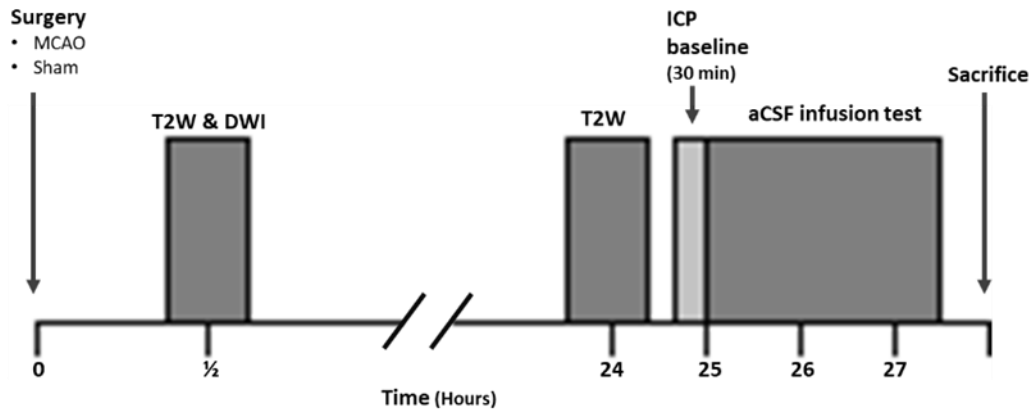
Figure 4-1. Experimental protocol. Immediately following pMCAO, rats underwent baseline MRI scanning for assessment of lesion volume and brain volume measurements. Rats were then recovered from anaesthesia and at 24 hours after MCAO, T_2 weighted MRI was carried out for infarct volume and oedema measurements. Following MRI scanning, rats then underwent ICP measurements.
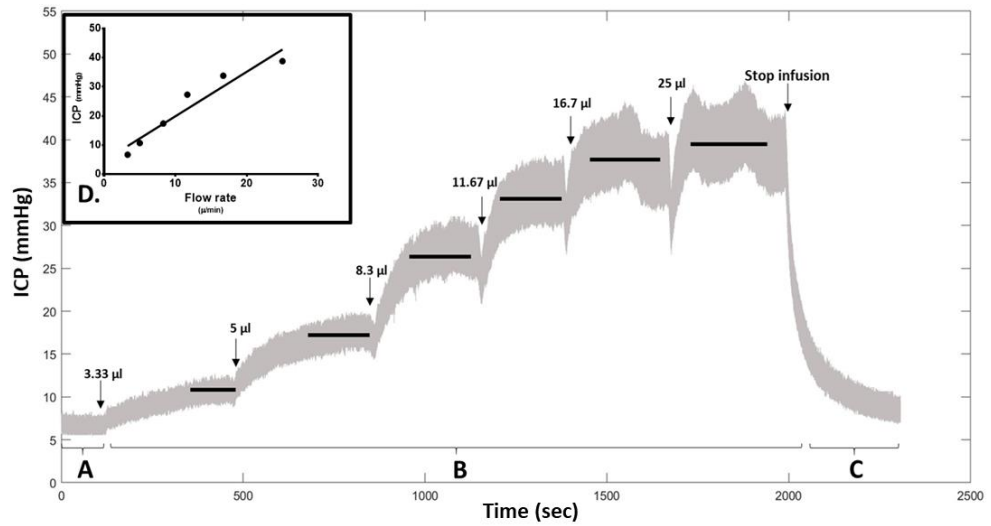
Figure 4-2. An example ICP recording as a function of time during a continuous infusion of aCSF. (A) Baseline ICP recording before starting infusion of aCSF. (B) Infusion rates were increased incrementally, and steady-state pressures were established (black line) at each infusion rate before increasing the infusion rate to the next level. (C) Relaxation phase; After infusion is stopped, ICP relaxes back to the initial baseline. (D) Mean pressure is plotted as a function of flow rate for infusion level. The initial slope of this curve constitutes the CSF outflow resistance.
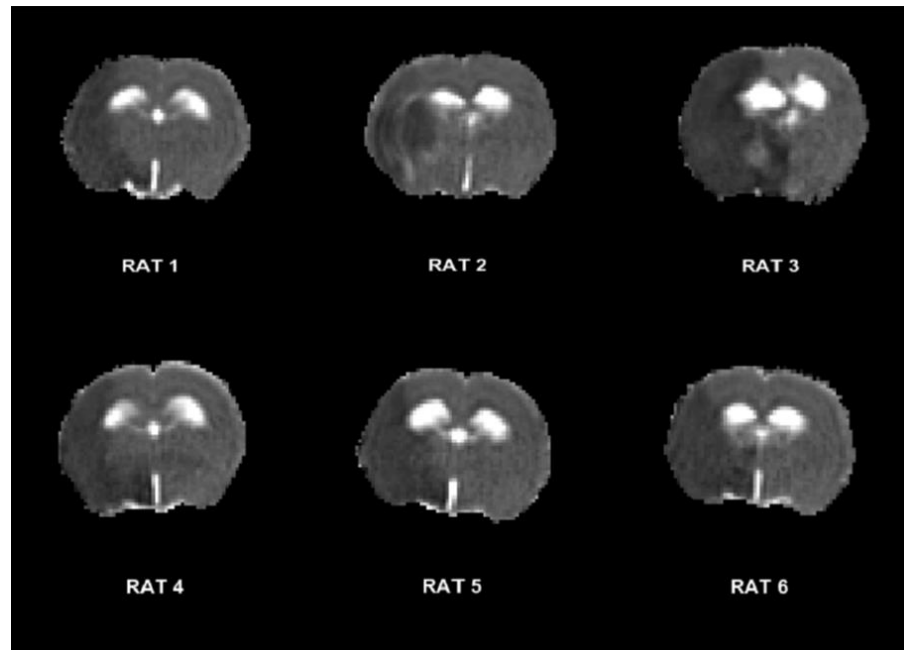
Figure 4-3. Representative ADC map at 30 minutes after MCAO (n=6). The area of hypointensity of the ADC map is representative of ischaemic lesion.
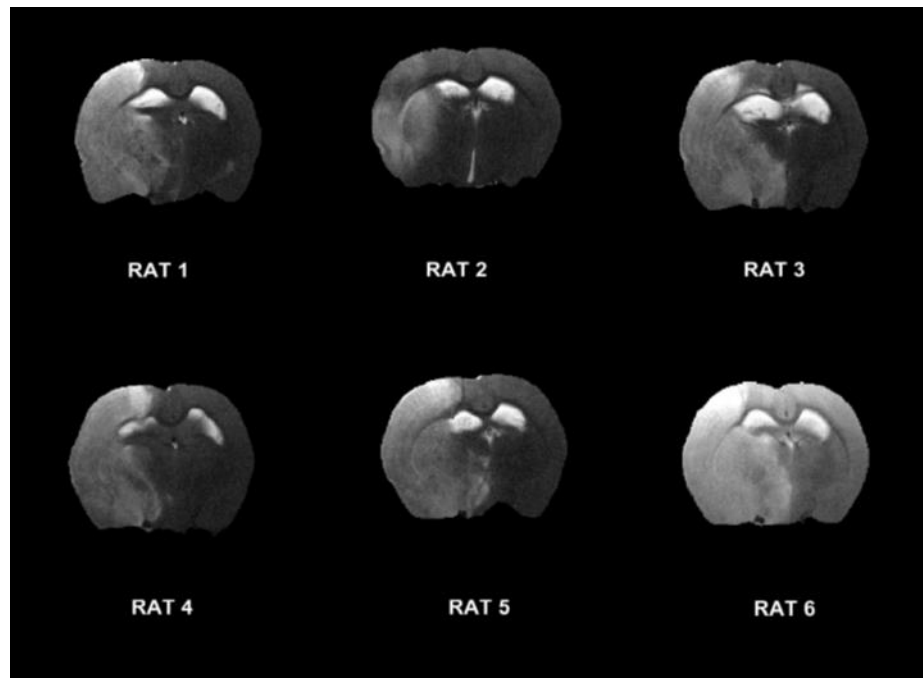
Figure 4-4. Representative T_2 weighted images 24 hours after MCAO (n=6). The area of infarct is depicted by the area of hyperintensity.
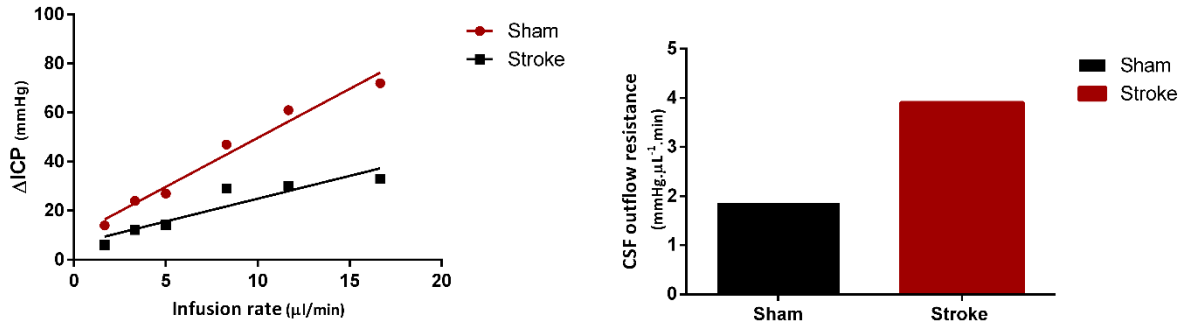
Figure 4-5. Pilot experiments were conducted on two rats, one after sham (N=1) and another after pMCAO (N=1) surgery, to estimate the proper sample size per group.

1

2

3

4

5

6

7

8

9

10

11

12

13

4.3 Results

4.3.1 Exclusion criteria

A total of 17 Wistar Kyoto (WKY) rats were used in this series of experiments. Two animals in the MCAO group were excluded due to technical problems (CSF leaks, unstable BP and death). Hence, 15 animals were available for data analysis: Sham (n=6), MCAO (n=6), LSCI (n=2), and aCSF + MRI (n=1).

4.3.2 ICP and Physiological variables

ICP oscillation with pulse pressure and respiration was detected in all experiments (Figure 4-6A). Median ICP at baseline in the pMCAO group at 24 hours (18.6 ± 5.84 mmHg) was demonstrated to be significantly greater than the sham group (6.01 ± 0.56 mmHg) (p=0.002) (Figure 4-6B). Physiological variables before and after infusion of aCSF are shown in Table 4-1. MAP was slightly lower at baseline in the pMCAO rats compared with the sham operated rats, however, this difference was not statistically significant. CPP (MAP – ICP) was significantly lower at baseline in pMCAO rats compared with the sham operated rats (65 ± 10 mmHg vs. 89 ± 8 mmHg, p = 0.049). There were no statistically significant differences between groups for intra-operative physiological indices with the exception of $PaCO_2$ (Table 4-1).

4.3.3 Oedema and Infarct volume vs. ICP

Mean oedema volume was 128.4 ± 19.3 mm^3 (range 100-146 mm^3) at 24 hours post-MCAO. The growth rate of oedema formation (0.09 ± 0.01 mm^3/min) was estimated by dividing the oedema volume by 1,440 minutes (i.e. 24 hrs). Mean oedema-corrected infarct volume was 342.5 ± 65 mm^3 (range 225–397 mm^3). There was no significant correlation between mean ICP at 24 hours and infarct volume ($R^2 = 0.09$, p = 0.5) or oedema volume ($R^2 = - 0.03$, p = 0.5) (Figure 4-7A and B).

4.3.4 ICP response to aCSF infusion

The time course for MAP, CPP and ICP changes after aCSF infusion in both pMCAO and sham groups is shown in Figure 4-8. After the start of aCSF infusion, ICP increased significantly (p < 0.001 for all time points) in both the pMCAO and sham group. Figure 4-9A shows how the steady state ICP changed from baseline (ΔICP) increases with increasing infusion rate. For both groups, plotting ΔICP versus infusion rate resulted in a linear relationship, in confirmation of equation (4-3). At the end of infusion, ICP dropped to the initial baseline value.

4.3.5 CSF outflow resistance

CSF outflow resistance was calculated for each animal, as in equation (4-3), from the initial slope of the ΔICP vs infusion rate plots, for infusion rates between 0 and 11.67 µL min^{-1} (Figure 4-9B). The mean CSF outflow resistance measured for the pMCAO group (2.27 ± 0.15 mmHg.µL^{-1}.min) was significantly greater than in the sham operated rats (0.93 ± 0.06 mmHg.µL^{-1}.min) (p = 0.002) (Figure 4-9C). A significant relationship was found between CSF outflow resistance and baseline ICP measured at 24 hours, using both pMCAO and sham rats (R^2 = 0. 85, p < 0.0001) (Figure 4-9D).

4.3.6 CSF production rate

Linear regression of the initial ICP versus infusion rate data to zero ICP (Figure 4-9A) allowed an indirect estimation of CSF production rate, indicating no significant change in CSF production rate following stroke (1.4 ± 1.54 µL/min) compared to sham controls (1.9 ± 1.49 µL/min) (p = 0.6).

4.3.7 Impact of aCSF infusion on oedema size in a single rat experiment

Figure 4-10 shows the T_2 images acquired before and during aCSF infusion. There was no change in the T_2 image with infusion. To show this more clearly, Figure 4-10 shows enlarged T_2 weighted images, from before the start of infusion (Figure 4-10A) and the final T_2 image measured at an infusion rate of 33.3 µL/min (Figure 4-10B). Between the initial and final T_2 images, ~441 µL of aCSF was infused over 40 minutes. With a simple visual inspection, there is no change

1   between any of the T_2 images. This fact is strongly highlighted in Figure 4-10C,

2   which shows the subtraction of the two images ($T_{2/initial}$ - $T_{2/final}$). This clearly

3   shows there was no change in the region of hyperintense T_2 signal (infarct)

4   between the initial and final images or, indeed, any changes in the brain. To

5   highlight this further, Figure 4-10D shows the same subtraction image, but with

6   the contrast greatly increased to show the actual image noise. Figure 4-10D very

7   strongly highlights that there was no change whatsoever in T_2 hyperintense

8   regions (i.e. oedema volumes), caused by infusion of aCSF. If there was any

9   change between the initial and final T_2 images due to infused aCSF increasing

10 oedema volume, the subtraction map would show this. Thus, we conclude that

11 ICP is not being affected by increased oedema volume.

12 **4.3.8 Impact of increased ICP on collateral flow**

13 Following pMCAO, LSCI showed that cortical perfusion was significantly

14 decreased in the ipsilateral hemisphere compared to the contralateral

15 hemisphere and perfusion recovery occurred at 2 hours from ischaemia onset.

16 Progressive elevation of ICP above baseline resulted in progressive reduction of

17 cortical perfusion in the ipsilateral hemisphere (see Figure 4-11). The current

18 observation suggested that artificially increase of ICP result in a reduction in

19 collateral blood flow.

20

21

22

23

24

25

26

27

1

2
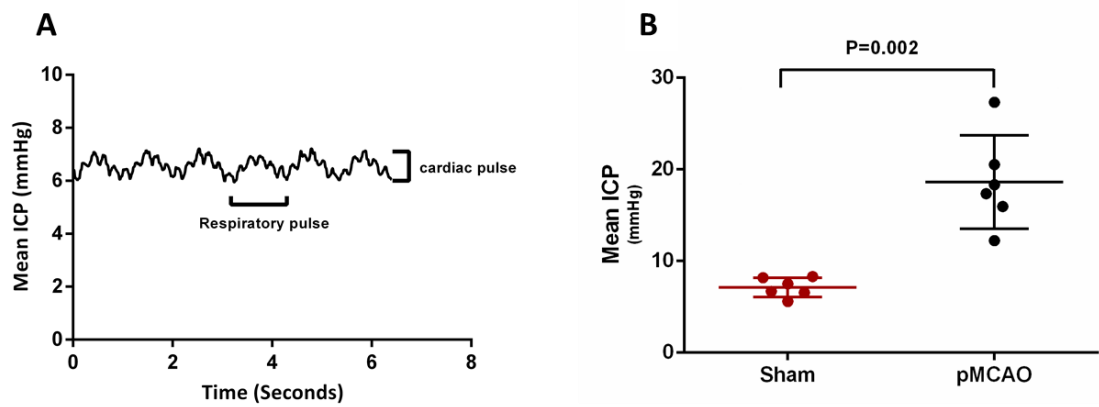
Figure 4-6. Example ICP recording from a rat at baseline following sham surgery. (A)The respiratory and cardiac pulses can be clearly visualised in the oscillations of the ICP waveform. (B) Median Intracranial pressure (ICP) measured at baseline, prior to infusion, in WKY rats at 24 hours following sham surgery or pMCAO. Baseline ICP was significantly elevated in the pMCAO treated rats compared to sham group (values are median ± SD).

8

9

10

11

12

13

14

15

16

17

18

19

1

Physiological parameters		Pre- infusion	Post- infusion
MAP (mmHg)	Sham	95 ± 8.8	94 ± 10
	Stroke	84.4 ± 11	82± 17
CPP (mmHg)	Sham	89±8	88±7
	Stroke	65±8*	67±7
PaO_2 (mmHg)	Sham	182 ± 25	174 ± 22
	Stroke	160 ± 35	145 ± 32†
$PaCO_2$ (mmHg)	Sham	32 ± 4	36.7 ± 8
	Stroke	36.3 ± 6*	52.1 ± 10
Temp (°C)	Sham	36·8 ± 0·3	36·9 ± 0·5
	Stroke	37·2 ± 0·7	37·1 ± 0·6
pH	Sham	7.64 ± 0.3	7.7 ± 0.4
	Stroke	7.43± 0.6	7.5± 0.3

2   **Table 4-1. Values for median MAP, $PaCO_2$, PaO_2, pH and temperature following stroke or**
3   **sham surgery. *p< 0·05 vs. control; †p < 0·05 vs. pre-infusion.**
4

5

6

7

1
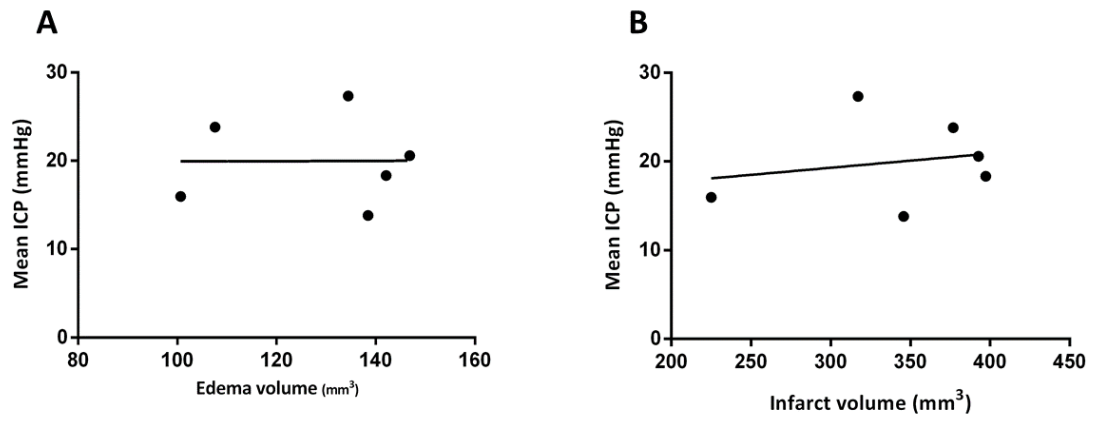
Figure 4-7. Intracranial pressure (ICP) versus infarct volume and cerebral oedema volume all measured 24 hours after pMCAO. No significant correlation of ICP baseline prior to infusion in MCAO treated rats, with infarct volume or oedema volume was seen in this study. (A, B) infarct volume: R^2 = 0.09, p = 0.5; oedema volume: R^2 = - 0.03, p = 0.5.
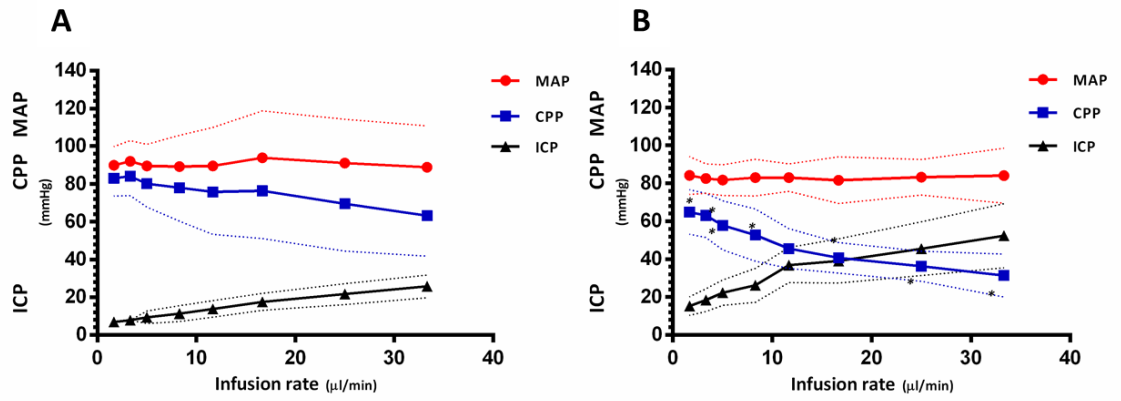
Figure 4-8. Change in ICP, CPP, and MAP following stepwise infusion of aCSF into the contralateral ventricle. (A) In sham operated rats, infusion of CSF resulted in an increase in ICP, little change in MAP and an associated decrease in CPP at higher infusion rates. (B) In rats at 24 hours following pMCAO, ICP increased significantly with a marked drop in CPP (*) and no change in MAP. All data are presented as mean ± SD.

Figure 4-9. CSF outflow resistance. (A) Scatter plot graph of the correlation between ΔICP and aCSF infusion rate in both pMCAO and sham animals. (B) Linear relation between ΔICP and low infusion rates in and sham group. (C) Individual CSF outflow resistance in pMCAO or sham animals. CSF outflow resistance in the pMCAO group was significantly greater than that of the sham group (p = 0.002). (D) Illustrates a significant positive correlation between CSF outflow resistances and baseline ICP (R^2 = 0. 85, p < 0.0001).
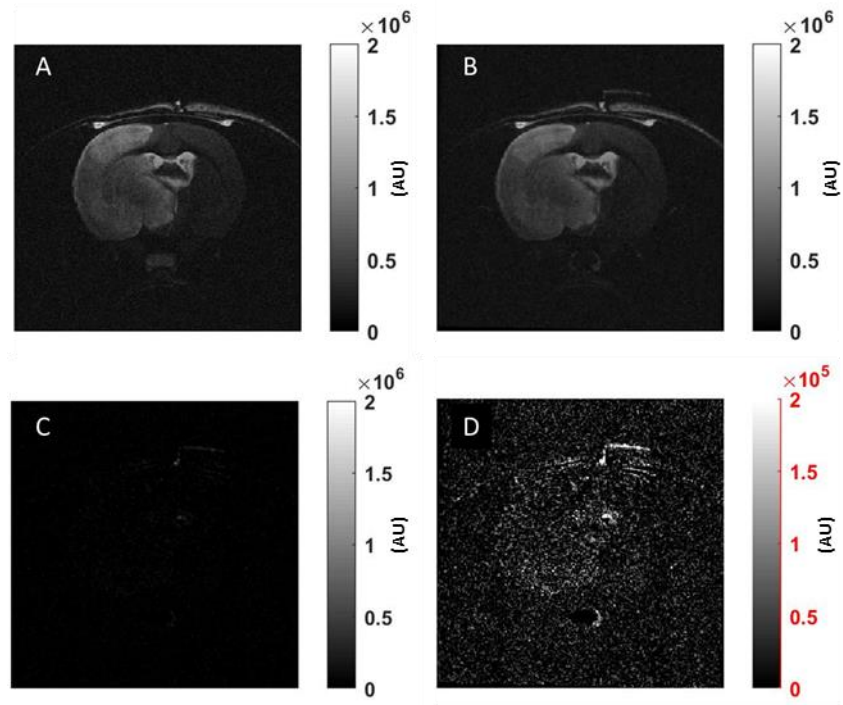
1

2 **Figure 4-10. MRI investigation of the effect of aCSF infusion over oedema size. (A) T_2**
3 **weighted image acquired before aCSF infusion ($T_{2/initial}$). (B) T_2 weighted image acquired**
4 **after aCSF infusion ($T_{2/final}$). (C) Subtracted image derived from subtraction of the two**
5 **images ($T_{2/initial}$ - $T_{2/final}$). (D) Subtracted image with higher contrast level (noise level). This**
6 **shows there was no change in T_2 weighted images, hence oedema, due to the infusion of**
7 **aCSF.**
8

9

10

11
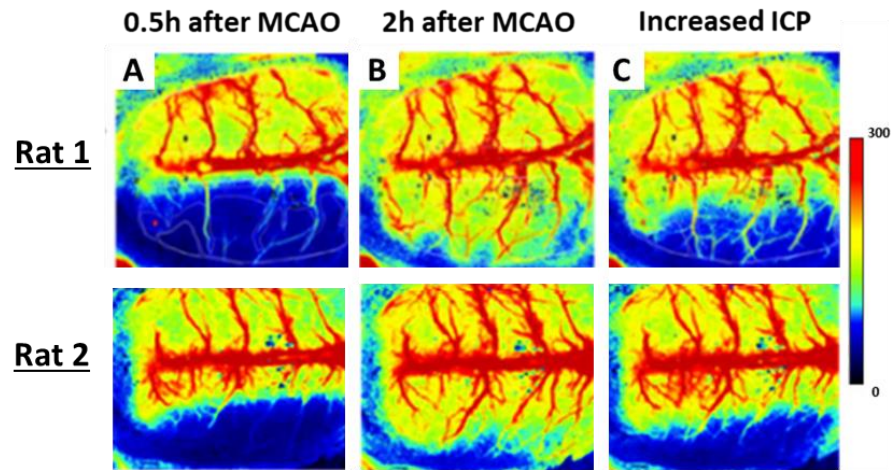
12

Figure 4-11. Collateral blood flow map from cortical surface of two rats. (A) Following pMCAO, cortical perfusion was significantly decreased in the ipsilateral hemisphere compared to the contralateral hemisphere. (B) 2 hours post pMCAO, cortical perfusion recovered in the ipsilateral hemisphere of rat. (C) Artificial elevation of ICP (Pressure change ≈ 30 mmHg) reduces the recovered cortical perfusion in the ipsilateral hemisphere of rat.

4.4 Discussion

It is conventionally assumed that ICP elevation post-stroke is the result of cerebral vasogenic oedema within the closed cranial compartment. Consequently, only patients with large malignant strokes and significant levels of brain oedema are assumed to be affected by intracranial hypertension. Though this view has persisted over several decades, no evidence can be found in the clinical literature to support this broad assumption, presumably because the risks associated with invasive ICP measurements have precluded their use in the vast majority of stroke patients. Recently this assumption has been challenged by animal experiments, which show ICP can become substantially elevated at 24 hours post stroke, even following small ischaemic strokes (sub-cortical lesions) where there is little or no 'space occupying' oedema. Further, these previous studies found no correlation between oedema volume and baseline ICP at 24 hours post-stroke (Kotwica and Persson, 1991; Murtha *et al.*, 2015). Data from the present study support these findings and also show an absence of correlation between oedema volume and baseline ICP in the pMCAO group (Figure 4-7) (Spearman correlation R^2 = - 0.03, p = 0.5). However, since the study's power calculations were based on CSF outflow resistance pilot data, the sample size used in our experiment (n=6) is likely underpowered with regard to definitively determining a lack of correlation.

It has previously been proposed that increases in ICP in the first 24 hours post-ischaemic stroke may provide an explanation for patients suffering a progressive stroke or unexplained END (Beard *et al.*, 2015). The effect of increasing ICP on collateral flow has been recently demonstrated in rats, using fluorescent microspheres to quantify flow through individual pial collateral vessels (Gaberel *et al.*, 2012). This showed progressive reductions in collateral flow with stepwise increases in ICP (up to 50% reduction in flow at 30mmHg). Consistent with these earlier studies, the current findings suggested even minor increases in ICP resulted in a decrease in the critical cerebral perfusion pressure (CPP) which is the driving pressure of the cerebral blood flow in the absence of autoregulation (Georgiadis *et al.*, 2015). Although CPP is regulated by both MAP and ICP, it is

1   remarkable how little attention the ICP component has received (Lewis *et al.*,

2   2014; Georgiadis *et al.*, 2015).

3   In the current study, laser speckle experiments (n=2) were conducted to test the

4   hypothesis that ICP elevation reduces collateral flow post stroke. Visual

5   inspection of collateral flow in rat with experimental MCAO have shown a global

6   reduction in collateral vessel flow within the penumbra territory, during an

7   artificial ICP elevation (Figure 4-11). However, the use of LSCI comes with some

8   limitations. One significant limitation to LSCI is the shallow penetration depth of

9   the images. Because of the illumination and detection geometry, the detected

10   photons sample only the superficial surface of the tissue, i.e. a few hundred

11   microns of tissue (Davis, Kazmi and Dunn, 2014). As a result, most brain

12   applications require removal of overlying tissues such as the skull. Moreover,

13   LSCI does not provide quantitative perfusion values owing to the undefined

14   mathematical relationship between speckle contrast and blood flow velocity

15   (Kazmi *et al.*, 2015). Further, physiologic motion artifacts are a concern. In

16   anesthetized animals, cardiac and respiratory motion can affect image quality

17   adversely, exhibited by greater image noise and reduced spatial resolution

18   (Kazmi *et al.*, 2015).

19   It has been suggested that any reductions in the already tenuous penumbral

20   perfusion would be expected to impact penumbral survival, leading to late

21   infarct expansion and END. Indeed, collateral failure has been associated with

22   infarct growth and has been proposed as a potential mechanism of unexplained

23   END (Thanvi, Treadwell and Robinson, 2008). In support of this, recent clinical

24   imaging studies have shown infarct growth beyond the initial penumbra and the

25   occurrence of "new DWI lesions" at day 7 post-stroke, outside the initial area of

26   hypo-perfusion (Alawneh *et al.*, 2011). In addition, there have been numerous

27   rodent studies of both permanent and transient MCAO which have shown infarct

28   volume expanding beyond 24 hours (Roehn *et al.*, 1995; McGarry *et al.*, 2017).

29   This raises the important question: if not oedema, what mechanism is

30   responsible for the substantial ICP elevations seen at 24 hours post-ischaemic

31   stroke? Inspection of the steady-state model of ICP (equation (4-2)) shows ICP is

32   dependent upon CSF outflow resistance, the rate of CSF production and the rate

33   of oedema growth. In confirmation of the mathematical model (equation (4-3)),

1   a linear relationship was found between the increase in ICP above baseline

2   (ΔICP) and the infusion rate of aCSF (Figure 4-9A) for both pMCAO and sham

3   groups. Measured values of CSF outflow resistance for the sham group (0.93 ±

4   0.06 mmHg.µL^{-1}.min) were consistent with previous measurements for rats,

5   which ranged from 0.5 to 1.8 mmHg.µL^{-1}.min (Kida, Pantazis and Weller, 1993;

6   Nagra *et al.*, 2010).

7   For the first time, the current findings have shown that CSF outflow resistance

8   increases significantly at 24 hours post-pMCAO compared with a sham operated

9   group (Figure 4-9C). This more than a two-fold increase in CSF outflow

10   resistance following ischaemic stroke and is of a similar magnitude to increases

11   previously encountered in studies on hydrocephalic rats (Jones and Bucknall,

12   1987). Further, for the first time, a significant correlation was found between

13   the baseline ICP at 24 hours post-pMCAO and the value of CSF outflow resistance

14   (Figure 4-9D).

15   The slow rate of CSF production is difficult to measure, with an estimate of the

16   rate being made by extrapolating the initial ICP versus infusion data back to zero

17   ICP. For the sham operated group this gave the rate of CSF production as 1.9 ±

18   1.49 µL/min, slightly lower than comparable data found in the literature (3.7 ±

19   0.1 µL/min) measured using a ventriculo-cisternal perfusion technique

20   (Orešković and Klarica, 2014). The rate of CSF production did not significantly

21   change in the pMCAO group (1.4 ± 1.54 µL/min) compared to the sham group

22   (1.9 ± 1.49 µL/min) (p=0.6). Moreover, in the pMCAO group, the rate of oedema

23   growth (0.09±0.01 µL/min) was found to be small compared with rate of CSF

24   production. Taken together, these results indicate the ICP elevation seen at 24

25   hours post-pMCAO was primarily driven by increased CSF outflow resistance

26   rather than an increased rate of CSF production or oedema growth.

27   A progressive increase in ICP can potentially lead to increased high-velocity

28   microvascular shunt (MVS) flow which, in turn, promotes the development of

29   brain oedema (Bragin, Bush and Nemoto, 2013). In Figure 4-9A, there is evidence

30   that the slope of the ICP versus infusion rate data changes above 11.7 µL min^{-1}.

31   To avoid this complication, CSF resistance (i.e. the slope) was measured using

32   only the lower infusion rate (low ICP) data, where the brain system has been

33   least perturbed (Figure 4-9D).

1   In the current study, blood gases measured after infusion showed a noticeable

2   (but not significant) increase in $PaCO_2$ values in the stroke group compared with

3   the sham group. Acute hypercapnia may lead to increased ICP, primarily through

4   cerebral vasodilatation and increases in cerebral blood volume (Pollock *et al.*,

5   2009). To test whether the elevated $PaCO_2$ encountered during the infusion

6   experiment might affect the baseline ICP, we continued to measure ICP after

7   infusion was stopped. Figure 4-2 shows, once the aCSF infusion is stopped, the

8   ICP rapidly reduces, returning to its pre-infusion baseline level. This clearly

9   indicates that the change in $PaCO_2$ levels during infusion did not translate into

10 an increase in baseline ICP in the current study.

11 In the current study, the relationship between CSF resistance and ICP was

12 investigated at 24 hours post permanent middle cerebral artery occlusion. These

13 types of stroke models represent with a large infarct and oedema volume.

14 Therefore, someone could argue that the presence of large infarct/oedema have

15 influenced the current findings of Figure 4-9 (different slopes of ICP curves).

16 However, we should emphasize that CSF resistance values were estimated based

17 on the linear relationship between steady state ICP levels and infusion rate (see

18 Figure 4-2). Based on the Davison model, steady state ICP will exist only when

19 the rate of aCSF infusion equals the rate of absorption of CSF, and independent

20 of compliance (oedema effect), where the rate of CSF outflow is proportional to

21 the intracranial pressure (Davson, Domer and Holungsworth, 1973). Importantly,

22 this is seen both in the MCAO group and in the sham group. Hence, oedema size

23 could not be said to directly affect CSF dynamics and therefore steady state ICP.

24 Yet, it may be wise to investigate the relation between CSF and ICP on variety of

25 different occlusion periods and recovery times, which can influence the resulting

26 lesions volumes. This would help to obtain a range in the size of infarct and

27 oedema, which help to obtain a clearer picture of whether the relation between

28 CSF resistance and ICP is exist following the reperfusion or not.

29 In summary, these are important results as they demonstrate CSF outflow

30 resistance, not oedema, is the mechanism responsible for ICP elevation

31 approximately 24 hours post-ischaemic stroke. This suggests the possibility that

32 intracranial hypertension may be occurring undetected in a much wider range of

33 stroke patients than is currently considered, not just in patients with large

1 malignant strokes and significant levels of brain oedema. The results presented

2 here, in conjunction with the work of Professor Sprat and colleagues (Murtha *et*

3 *al.*, 2014; Beard *et al.*, 2015; Wells *et al.*, 2015) and Professor Baron (Seners and

4 Baron, 2018), are consistent with the following mechanism behind unexplained

5 END; First, following ischaemic stroke, changes in CSF dynamics, namely

6 increased CSF outflow resistance, can result in a transient elevation of ICP at

7 approximately 24 hours from stroke onset. Second, these increases in ICP then

8 lead to a progressive reduction in collateral flow and cerebral perfusion in the

9 occluded arterial territory. Third, the tissue that was initially asymptomatic

10 (outside initial ischaemic core/penumbra) then becomes at risk and ultimately

11 evolves into infarct, leading to delayed infarct expansion and END.

12 Future work is needed to fully investigate the temporal changes in CSF dynamics

13 following ischaemic stroke. Ischaemic stroke can be a major stressor in the

14 physiology of brain cells, tissue, and fluid transport. This could lead to altered

15 CSF secretion or drainage as an outcome of ischaemic stroke and, consequently,

16 increased ICP since it plays a fundamental role in ICP regulation under normal

17 circumstances. It appears likely that the increase in CSF outflow resistance in

18 the pMCAO group found in this study, was the result of altering of one or more of

19 these CSF absorption pathways. Recent work suggests that part of the CSF is

20 recirculated into the brain via low resistance glymphatic systems on the surface

21 of the brain that facilitate CSF circulation (Iliff *et al.*, 2012). In the context of

22 neurological injury, glymphatic function appears to disturbed following

23 ischaemic stroke (Gaberel *et al.*, 2014). Dysfunction of the glymphatic

24 circulation has not yet been recognised as a source of increased ICP, but the

25 notion that perivascular space (PVS) provides a conduit for CSF influx prompted

26 us to reassess this idea. To date, many aspects of CSF dynamics are still poorly

27 understood, partly due to the difficulties involved in monitoring CSF flow.

28 Hence, in the next Chapters, we aimed to develop a new approach which would

29 be capable of directly imaging CSF water dynamics.

5 Chapter 5: In vivo T$_1$ mapping and T$_1$ weighted for quantifying Gd-DTPA uptake from CSF into brain

5.1 Introduction

The traditional concept of CSF hydrodynamics is being challenged by recent works (Iliff *et al.*, 2012). The traditional model believes that CSF is produced mainly by the choroid plexus located in the ventricular system. After circulating throughout the natural fluid passages of the ventricular system and subarachnoid space, CSF is returned to the vascular system. Recently, the glymphatic system was proposed as periarterial influx route of CSF from subarachnoid space (SAS) into the brain interstitial fluid (ISF), providing a pathway of organised convective fluid flow to drive clearance of interstitial wastes solutes from the brain (Iliff *et al.*, 2012). DCE-MRI studies provide a wider, more detailed picture of CSF circulation, above and beyond the single snapshot view enabled by florescent and radioactive tracers. Iliff et al. (2013) first employed MRI using an intracisternal tracer infusion approach to monitor CSF dynamic and glymphatic function. In their original MRI study, DCE-MRI was applied, and transport of the gadolinium-based tracers was tracked in the CSF and brain parenchyma over time. They also compared the influx of small molecular weight Gd-Diethylene Triamine Penta acetic Acid (Gd-DTPA, MW 938 Da) with a larger molecular weight polymeric Gd-chelate (GadoSpin, MW 200 kDa) over the early infusion period. This demonstrated clear differences in whole-brain distributions between the small and large Gadolinium based tracers. The distribution of the Gadolinium was monitored by a time series of a 3D T$_1$ weighted spoiled gradient echo (SPGR) scans, acquired during and after tracer delivered into the CSF space. The change in signal from the baseline gave an indication of the tracer concentration. This approach provides only values of signal enhancement, and not tracer concentrations (Weiskopf *et al.*, 2013). Instead, the use of the T$_1$ mapping method enables quantitative and longitudinal assessments of Gd concentration in tissues (Lee *et al.*, 2018). In the current work, the 3D-T$_1$ weighted method employed in the original MRI study by Iliff et al (2013) is replicated. Moreover, we employed a T$_1$ mapping method (IR-RARE) to quantitatively image Gd-DTPA (938 Da) concentration.

5.2 Methods

5.2.1 Animal preparation

A total of five male Wistar rats (body weight, 285 ± 50 g, 20 to 24 weeks old) were anesthetised (5% isoflurane in 30:70 O_2/NO_2 mixture at flow rate 1-2 L/min) in an induction chamber, then intubated, and artificially ventilated (with 2-3% isoflurane in 30:70 O_2/NO_2 mixture). A cisterna magna (CM) cannula was inserted as described in Chapter 3 (section 3.1.4.3) and connected to a closed-end PE10 tube loaded with Gd-DTPA (Magnevist, 13.5 mM) and attached to an infusion pump (Graseby 3150 Syringe Pump) for tracer delivery. Throughout the MRI acquisition, body temperature, respiration, BP, and blood gases (pH, partial pressure of oxygen (PaO_2), carbon dioxide ($PaCO_2$)) were continuously monitored as described in chapter 3.

5.2.2 Intracranial pressure measurement

To investigate the effects of tracer infusion rate on cranial compartments, ICP was measured during different rates of infusion in a single rat. ICP probe was inserted into lateral ventricle as described in Chapter 2, section 3.1.4.2. Data were recorded with MP150 Biopac system (Biopac systems Inc, USA) and analysed with the "Acknowledge" software (Biopac systems Inc, USA).

5.2.3 Magnetic Resonance Imaging Acquisitions

The scanning protocol consisted of baseline scans followed by the intrathecal infusion of Gd-DTPA (21 mM; 80 μL at 1.8 μL/min; total time ~45 min). Both T_1 weighted and T_1 map MRI images were continuously acquired in consecutive order over a period of approximately 120 minutes (Figure 5-1).

To measure the concentration of Gd-DTPA, a T_1 map was acquired using a 2D single slice inversion recovery sequence (IR-RARE). Inversion was performed using a hyperbolic secant pulse. The following imaging parameters were used: NA = 2; Inversion time = 30, 130, 230, 330, 430, 530, 630, 730, 830 and 930ms ; TR = 10000 ms; FOV = 2.0 x 2.0 cm; Matrix size = 150 x 256 , yielding an original image resolution of 0.2× 0.12× 1.5 mm. The total acquisition time for the experiment was 8 minutes 12 seconds.

To generate images with a T_1 weighted shortening effect, 3D T_1 weighted FLASH images were acquired in the sagittal plane. The following imaging parameters were used: TR/TE = 15 ms/3 ms, flip angle = 15°, NA = 1, FOV = 3.0×3.0×3.0 cm, acquisition matrix size = 128×128, yielding an original image resolution of 0.234× 0.234× 0.234 mm. The total scan time = 3 minutes 5 seconds.

5.2.4 MRI data analysis

The general post-processing procedure consisted of image resizing, brain extraction, image smoothing, and head motion correction, as previously described in Chapter 3, section 3.2. To generate T_1 maps, a voxel-wise T_1 calculation was performed using the IR-RARE sequence data, with image intensities fitted as a function of the inversion times, TI . The general equation used for the fitting procedure is:

$$M_z = M_0(1 - 2e^{\frac{-TI_n}{T_1}})$$
(5-1)

The unknown variables (M_0 and T_1) were calculated using the Nelder-Mead simplex nonlinear least squares fit algorithm (Swift and Connick, 1962).

GD-DTPA concentration maps (C) were then calculated from the T_1 map using the following equation:

$$C = \frac{1}{r_1}\left(\frac{1}{T_{1\,post}} - \frac{1}{T_{1\,pre}}\right)$$
(5-2)

Taking the longitudinal relaxivity of GD-DTPA at 7T as r_1= 3.18 ± 0.09 mM^{-1}sec^{-1} (Kalavagunta, Michaeli and Metzger, 2014).

In the T_1 weighted data, Gd-DTPA yields a shortening of T_1 and, thus, an increase in T_1 weighted intensity. The percentage change in signal intensity ($\Delta S_{\%}$) is given by:

$$\Delta S_\% = \frac{S_{1post} - S_{1pre}}{S_{1pre}} \times 100 \qquad (5\text{-}3)$$

The percentage change in T_1 values and T_1 weighted signal were plotted and the mean area under the curve (mAUC), which represented the area under the enhancement curve for 120 minutes, was calculated.

5.2.5 Coefficient of variation

To assess the relative variability of gadolinium distribution across individual rats, the Coefficient of variation (CoV) was calculated by dividing the standard deviation (SD) by the mean (CoV = SD/Mean) for each rat independently. Mean and CoV maps were generated for visual assessment.

5.2.6 Sample size estimation for future hypothetical study using either T_1 weighted or T_1 map dataset

Each dataset was treated as a preliminary study from which to estimate the number of rats per group, N, required in a hypothetical *in vivo* study to show meaningful differences between control and experimental group, with specified statistical power. We chose a conventional significance level of α = 0.05, and a study with 80% power. To detect 30 % difference between the two groups at each voxel the required number of animals in each arm of the study is given by (Florey, 1993):

$$N = \frac{2(Z_a - Z_{1-\beta})^2 T_{1,std}^2}{\Delta^2} \qquad (5\text{-}4)$$

Where Z_a = 1.96. $Z_{1-\beta}$ = 0.8416. $T_{1,std}$ is the standard deviation of the T_1 map or T_1 weighted datasets, from group-wise average images, at particular voxel. Sample size (N) was rounded up to the nearest integer.

5.2.7 Statistics

Physiological parameters were analysed using two-way ANOVA followed by Sidak's test to correct for multiple comparisons. Comparison of MRI data was statistically analysed using the Mann–Whitney U test, with $P < 0.05$ as being significantly different (Graphpad Prism Software, California, USA). Spearman's correlation analysis was used to determine the correlation between T_1 map and T_1 weighted dataset. Data are presented as mean ± SEM or mean ± SD.
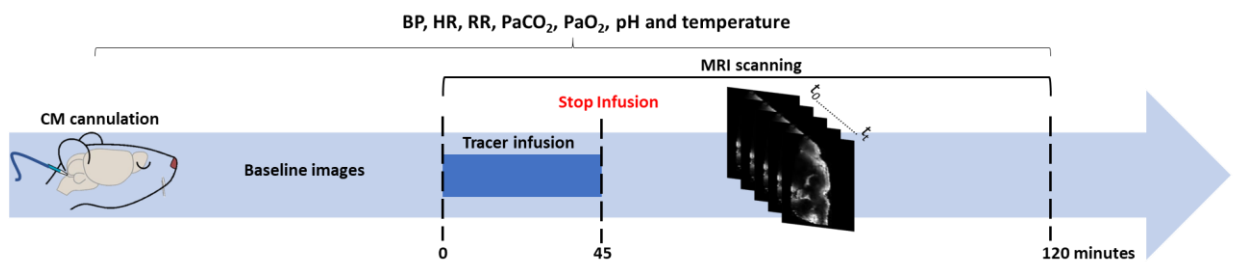
Figure 5-1. Experimental protocol.Following surgical implantation of an intracisternal cannula, the rat was placed in the supine position inside the MRI scanner and kept under anaesthesia. Pre-contrast baseline images were acquired. Next, during sequential acquisition of T_1 weighted / T_1 map images, 80 μL at 1.8 μL/min of Gd-DTPA was infused through the cannula for ~45 minutes, with MRI imaging continuing for a total of 120 minutes.

5.3 Results

5.3.1 Physiological data

All rats in the present study had stable physiological variables throughout the experimental protocol (Table 5-1). Physiological variables showed no significant changes throughout the entire experimental duration (p = 0.65 for pH, p = 0.19 for PaO_2, p = 0.22 for $PaCO_2$, p = 0.12 for MAP, and p = 0.34 for body temperature).

5.3.2 Impact of infusion rate on ICP

To avoid any physiological complication due to increased ICP generated by the infusion pump, ICP was measured at different infusion rates. As shown in Figure 5-2, infusion rates of 3 5, 0.9, 1.8, and 2.7 µL/min did not appreciatively alter ICP, whereas increasing the infusion rate to 3.6 µL/min, significantly elevated ICP. The infusion rate used in the current thesis (1.8 µL/min) did not increase ICP.

5.3.3 Gd-DTPA distribution within glymphatic system

In the presence of the paramagnetic Gd-DTPA tracer, the T_1 relaxation time is reduced, in a concentration dependent manner, see equation (5-2). In Figure 5-3, representative IR-RARE scans at the level of the midline sagittal plane are shown, for T_1 maps and concentration maps. The pre-contrast T_1 map (t=0) displays CSF filled cerebral ventricles as areas with high T_1 values (T_1 ~ 2.5 s) whereas normal brain tissue is characterised by T_1 values in the ~ 1.5 s range (Figure 5-3A). White matter regions in the cerebellum and corpus callosum can be clearly distinguished from grey matter as they exhibit lower T_1 values. Both the T_1 map and corresponding Gd-DTPA concentration map show time-dependent anatomical routes of perivascular influx (Figure 5-3B) over the early infusion period. The gadolinium was detected first in the basal cisterna, then in the ventricles, within minutes of injection. The concentration gradient then gradually built up from subarachnoid space into the most superficial part of the brain as early as 20 minutes after injection. Over time, Gd-DTPA slowly diffused into deeper structures of the brain. Later timepoints showed advancement throughout the brain, in the pineal recess and cerebellum, and more anterior

regions, such as the anterior cortex and the olfactory bulbs. Within the cortex subregions, anterior cortex exhibit Gd-DTPA uptake, yet the middle cortex remained free of detectable Gd-DTPA. Further, no Gd-DTPA enhancement was observed in deep brain white matter (Figure 5-3A). Quantification of Gd-DTPA uptake in multiple regions revealed heterogeneity of glymphatic inflow (Figure 5-4A). Figure 5-4B shows the mean AUC values (mAUCs), reflecting transit and uptake rates of Gd-DTPA, demonstrating differences in rates of glymphatic inflow in anatomically discreet regions.

5.3.4 Comparison of T_1 weighted and T_1 map methods

The temporal evolution of the time curves derived from the T_1 weighted and T_1 maps showed similar enhancement patterns (Figure 5-5A). Moreover, mAUC, which is an approximate index of the tracer distribution volume in the tissue, from multiple ROIs showed a strong correlation ($R^2 = 0.79$; $p<0.01$).

Visual inspection of the CoV parameter maps indicates the high quality of T_1 map with no gross artifacts (Figure 5-5C). By contrast with the T_1 map, the T_1 weighted images showed an inhomogeneous and slight higher CoV among rats (Figure 5-5D). The CoV for T_1 maps ranged from 0 to 0.9, while the CoV of T_1 weighted ranged from 0.2 to 2.

In order to assess the reproducibility of both the T_1 weighted and T_1 map methods, CoV maps across all rats were generated. Visual inspection of the CoV parameter maps indicates the high quality of the T_1 maps with no gross artifacts, with values ranging from 0 to 35 % (Figure 5-5C). By contrast, the CoV maps from the T_1 weighted images showed an inhomogeneous and higher CoV among rats, ranging from 0 to 100 % (Figure 5-5D).

To inform future imaging studies using T_1 map or T_1 weighted methods, we calculated sample sizes (N) for a hypothetical study ($\alpha = 0.05$ and 80% power) to detect a 30 % difference (see Figure 5-6). Under these conditions, the T_1 weighted imaging method would require N=15 animals to detect a statistically significant difference between experimental and control groups (see Figure 5-6A). Whereas, using the T_1 mapping method would only require N=10 animals per group (see Figure 5-6B).

Physiological parameters	30 min	90 min	120 min
PaO_2 (mmHg)	136 ± 2	138 ± 3	142 ± 14
$PaCO_2$ (mmHg)	34.4 ± 4	31.3 ± 6	31.3 ± 6
Temperature (°C)	37 ± 0.5	36.8 ± 0.3	36.9 ± 0.4
pH	7.5 ± 0.04	7.5 ± 0.08	7.5 ± 0.03
Blood Pressure (mmHg)	93. ± 15	88. ± 12	85. ± 16

Table 5-1. Physiological variables in rats, following tracer infusion. BP, blood pressure; $PaCO_2$, partial pressure of carbon dioxide; PaO_2, partial pressure of oxygen; Temp, temperature values are within physiological ranges for $H_2^{17}O$ Gd-DTPA and aCSF. Significant differences denoted by $p < 0.05$. Data presented as mean ± SD.
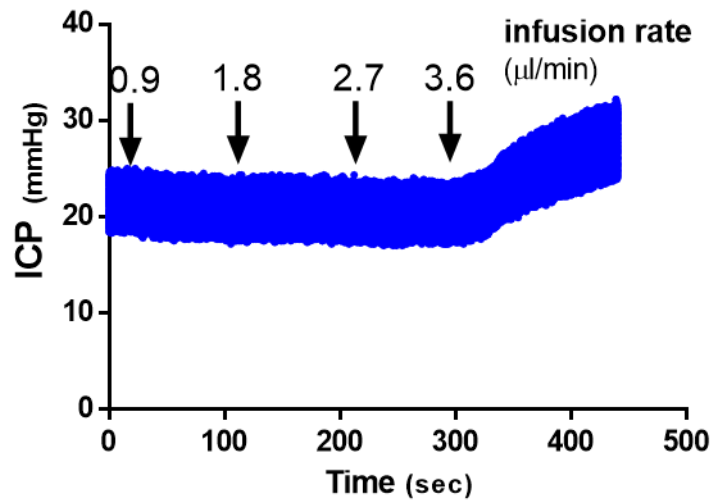
Figure 5-2. Defining the effect of CM infusion on ICP. Ventricular ICP (mmHg) was monitored and aCSF infused continuously at different infusion rates (0.9, 1.8, 2.7, and 3.6 μL/min) in a single rat. Infusion rates of 0.9, 1.8, and 2.7μl/min did not change the ICP, while a further stepwise increase in infusion rate to 3.6 μl/min clearly raised ICP.
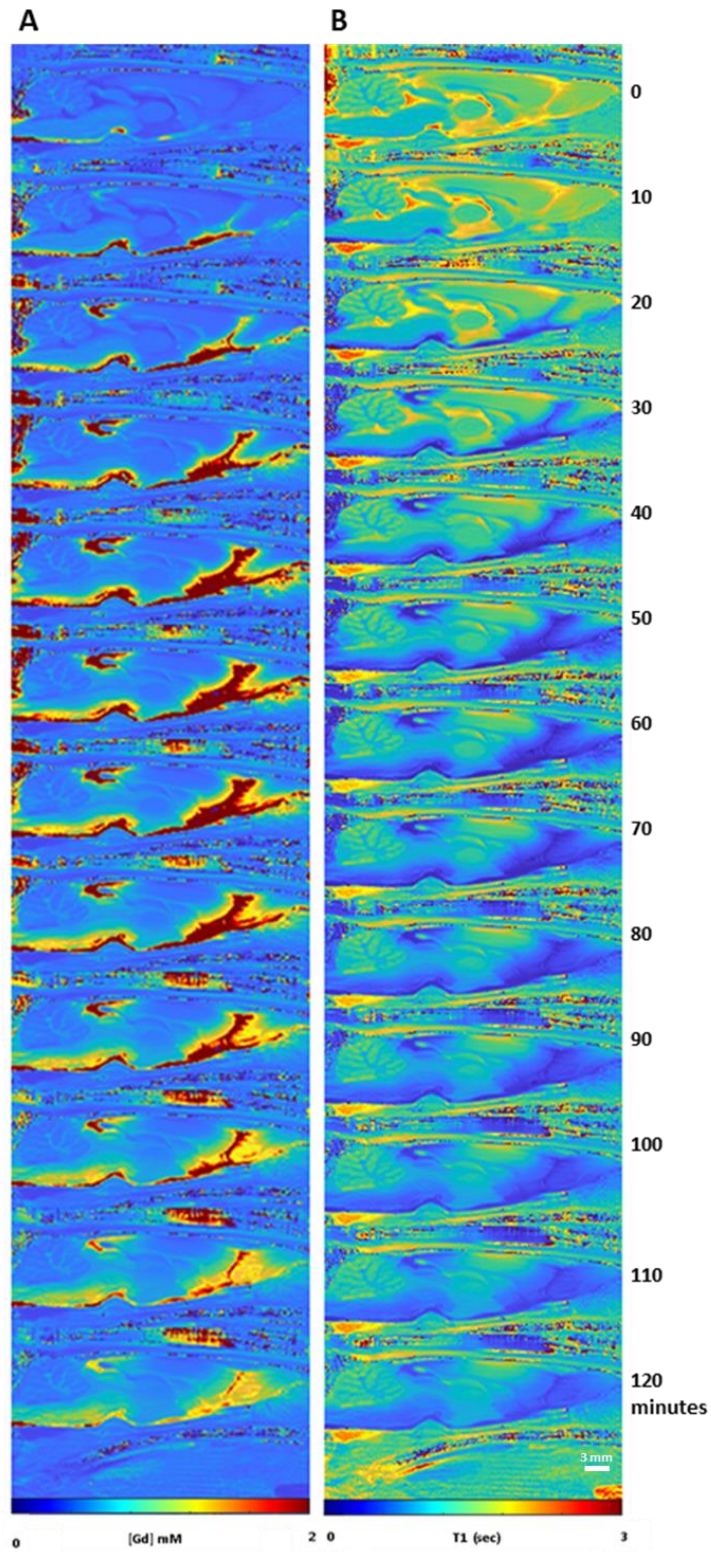
Figure 5-3. Gd-DTPA transport along glymphatic systems. (A) Population averaged Gd-DTPA concentration map (N = 5) over different times from the onset of the infusion. (B) Population averaged T₁ map (N = 5) over different times from the onset of the infusion.
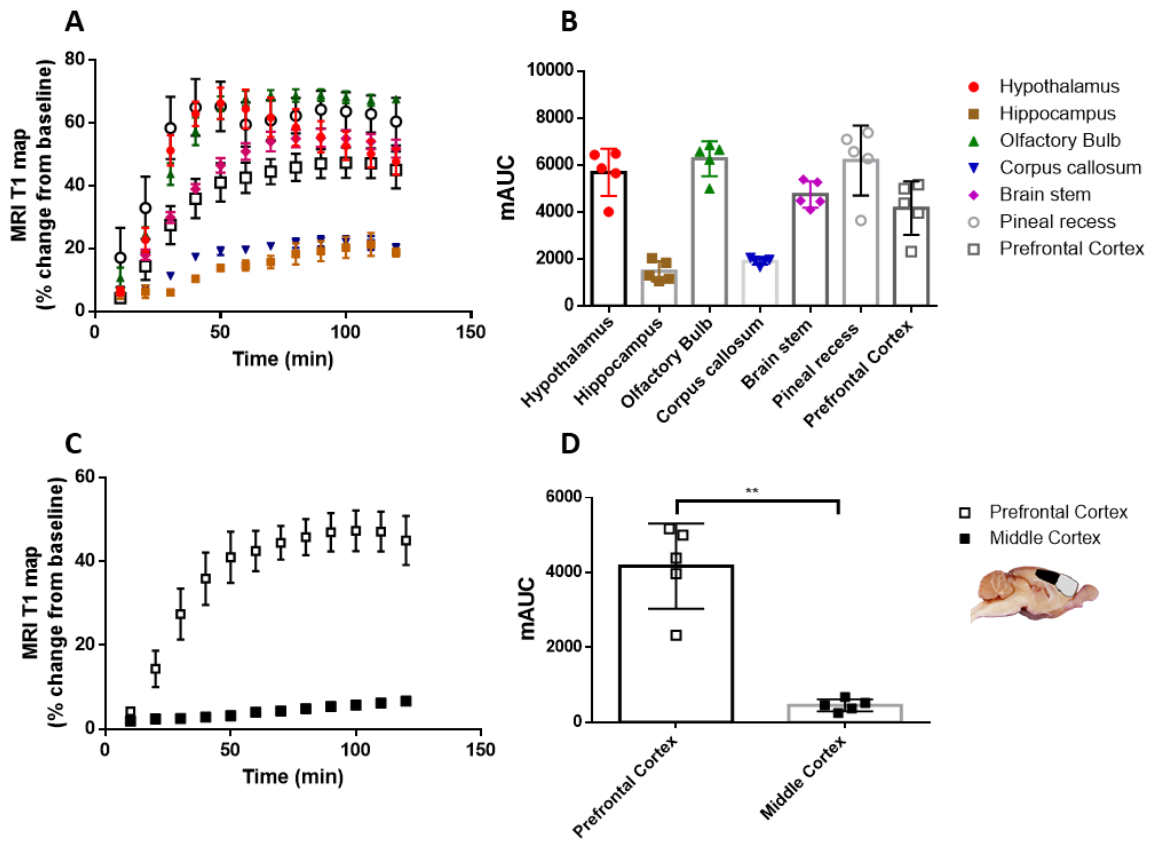
Figure 5-4. The temporal evolution of percentage change of T_1 values induced by Gd-DTPA at different brain regions. (A) Comparisons of percentage change of T_1 values in major brain regions (Hypothalamus, Hippocampus, Olfactory bulbs, Corpus callosum, Brainstem, Pineal recess, and anterior Cortex) over 2 hours period following start infusion of Gd-DTPA. (B) mAUC for each ROI's were calculated. (C) the anterior cortex was compared with deep middle cortex, demonstrating the difference of the extent of Gd-DTPA inflow into these two regions of the rat cortex. Data are represented as mean ± SEM.
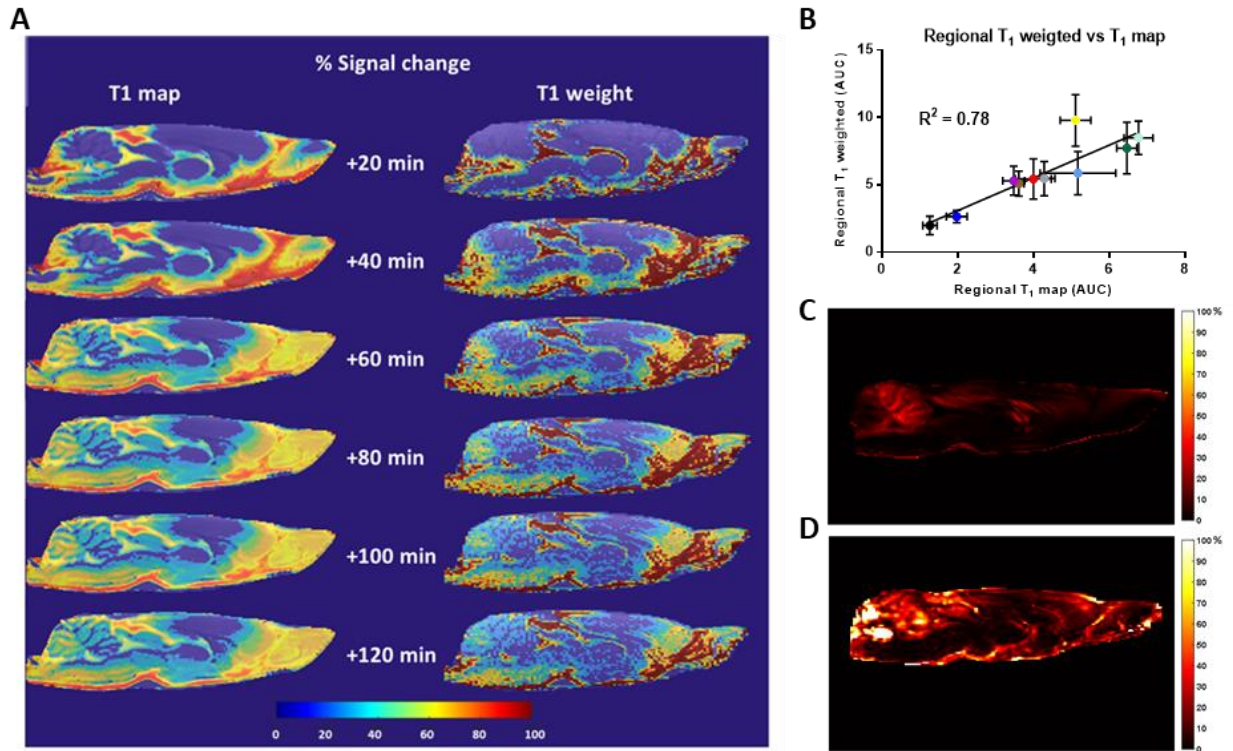
Figure 5-5. Glymphatic transport of Gd-DTPA captured by T_1 map and T_1 weighted. (A) Representative sagittal MRI demonstrating the temporal evolution of Gd-DTPA over 120 min of recording. (B) Comparisons of percentage change of T_1 values and T_1 weighted signal in major brain regions (hypothalamus, olfactory bulbs, cerebellum, cortex, 4th ventricle, hippocampus, corpus callosum, brain stem, 3rd ventricle, and pineal recess). The temporal evolution of percentage T_1 weighted signal from each region was extracted from nine different brain regions and plotted against T_1 values (mAUC). Each filled circle represents a brain region: red = Hypothalamus, green = Olfactory bulb, light blue = Cerebellum, magenta =anterior Cortex, yellow = 4th Ventricle, blue = Hippocampus, black = Corpus callosum, grey=Brainstem, brown = 3rd Ventricle, and light green=Pineal recess. Coefficient of variation (CoV) map across individual rats of (C) T_1 map and (D) T_1 weighted images.
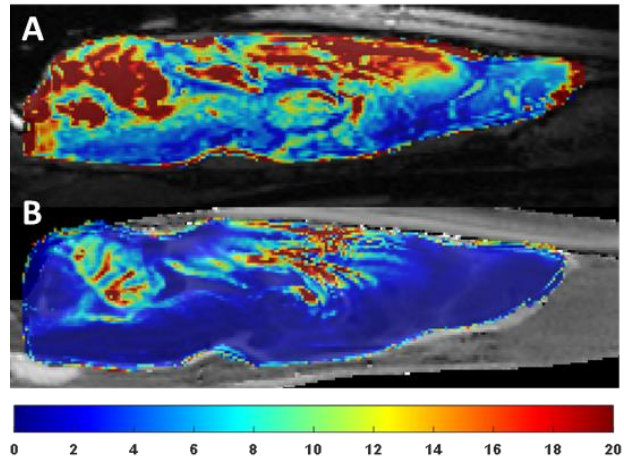
Figure 5-6. An estimated sample size map T_1 weighted data compared with T_1 map data. Sagittal equivalent slices (A) T_1 weighted and (B) T_1 map group wise average images, overlaid with sample size at each voxel.

5.4 Discussion

In this Chapter we were able to assess glymphatic function using the same T_1 weighted MRI protocol as previously published (Iliff *et al.*, 2013). In addition, we also employed T_1 mapping MRI, from which the tissue concentration of the Gd-DTPA tracer could be mapped. These concentration maps demonstrated glymphatic transport patterns consistent with previous studies (Iliff, *et al.*, 2013; Lee *et al.*, 2018).

A higher infusion rate of the Gd-DTPA tracer into the glymphatic systems, would provide a better visualization of glymphatic system. On the other hand, rapid infusion of fluid into the CSF system may interfere with CSF input/output rates, which in turn will alter ICP and the reliability of measurements (Marmarou, Shulman and Rosende, 1978). Here, the infusion rate did not appreciably alter pressure (see Figure 5-2). Therefore, the results obtained in this study should not be obscured by the infusion rate. The same infusion rate was also used in previous MRI and fluorescence experiments in mice alongside rats, where a comparable pattern of tracer distribution was observed in both species (Xie *et al.*, 2013).

The dynamic Gd-DTPA concentration maps showed that the time of tracer transport from the cisterna magna to the brain tissue adjacent to the perivascular space, occurred within approximately 10 minutes from the onset of Gd-DTPA infusion. In all the selected brain regions the concentration plateaued with time, giving no indication of early clearance. Notably, Gd-DTPA tracer did not arrive at the deeper brain interstitium (i.e. middle cortex and white matter regions) over the two hours scanned (Figure 5-4C). Indeed, Iliff et al.(2013) also failed to detect Gd-DTPA tracers in deep white matter brain regions despite acquisitions performed up to 4 hours after intracisternal injection, while observing enhancement in more superficial areas starting ~45 minutes after injection (Lee *et al.*, 2018).

The percentage signal change over time maps generated using the T_1 weighted and the T_1 mapping methods, paralleled each other (see Figure 5-5). However, the quantitative T_1 mapping method showed a higher reproducibility than the conventional T_1 weighted. The variation in T_1 weighted method was most

prominent in the superficial cortical areas and was reflected in a highly increased Coefficient of variation (CoV) ([Figure 5-5](#)C). A relatively small deviations in head positioning may lead to signal variation in T_1 weighted images among animals which may explain some of these variations (Thomas *et al.*, 2005). It is the stated policy of the United Kingdom government to replace, reduce or refine the use of animals in research. From these experiments we were able to conclude that the T_1 mapping was less variable than the T_1 weighted method. For a hypothetic study, using typical values of effect size and power, this would translate into a reduction in group size form N=14 to N=10.

While the T_1 mapping method provides a relatively stable measurement, conventional T_1 weighted MRI images have higher spatial and temporal resolution than the corresponding T_1-maps. In detail, the T_1 weighted 3D volume scans had 0.23 mm slice thickness, while the T_1-map slice thickness was 2 mm. Further, T_1 map method (IR-SE) requires an extremely long scan time (~8 min) in compare to T_1 weighted (~3 min).

Clearance of Gd-DTPA has previously been proposed to potentially resemble clearance of brain macromolecules with similar properties (Iliff *et al.*, 2013), including amyloid-β and tau (Yang *et al.*, 2013; Iliff *et al.*, 2014). A key question that remains to be answered in the body of neuroscience research, is whether the flow of Gd-DTPA tracer represents the true magnitude of CSF/water flow or it is only representing the flow of the Gd-DTPA within the CSF. In the current work, the spatial pattern and ingress of Gd-DTPA from the CSF space into the brain tissue were demonstrated using both conventional T_1 weighted and quantitative T_1 map. In the next Chapter, we aim to develop a novel MRI method that detects isotopically enriched water ($H_2^{17}O$, 90% ^{17}O, 19 Daltons) to directly image CSF water transport within the rat brain.

6 Chapter 6: Direct imaging of glymphatic flow using $H_2^{17}O$ MRI

6.1 introduction

The transport of solutes within the brain parenchyma is of fundamental importance to nutrient delivery and the clearance of metabolites, neurotransmitters, and toxic macromolecules (e.g. ß-amyloid). Conventionally, interstitial solutes were considered to be transported via diffusion, but several evidence suggested an additional bulk flow of the interstitial fluid (ISF) (Cserr and Ostrach, 1974; Rosenberg, Kyner and Estrada, 1980; Rennels *et al.*, 1985). Recently, the glymphatic system was proposed as a clearance mechanism that relies on aquaporin-4 (AQP4) water channels, expressed in the end feet of astrocytes, to drive the movement of CSF through brain interstitium, washing away toxic proteins and other waste as it proceeds (Iliff *et al.*, 2012).

The extent to which the glymphatic system accelerates solute transport in the brain interstitium is highly controversial, with both computational modelling and experimental studies being undertaken (Syková and Nicholson, 2008; Brinker *et al.*, 2014; Asgari, de Zélicourt and Kurtcuoglu, 2016; Jin, Smith and Verkman, 2016; Holter *et al.*, 2017). However, it should be emphasized that all the previous works and hypotheses of CSF dynamics and the glymphatic system were based on evaluating the transport of solutes with molecular sizes larger than that of water (e.g. Gd-DTPA, 938 Da). These results could be misinterpreted and lead to the wrong conclusions regarding CSF dynamics and the glymphatic flow. More importantly, AQP4 water channels were proposed by Dr. Nedergaard and her colleagues as a critical contributor to the bulk flow of ISF through extracellular spaces, yet as tracers will not pass through AQP4, most likely means that they did not clearly demonstrates the importance of AQP4 (Papadopoulos and Verkman, 2013).

The fact that these large tracers cannot be transported through AQP4 channels most likely means that previous tracer studies underestimated the true magnitude of ISF flow, which will depend on the rate at which CSF water molecules enter the interstitium. Therefore, we reasoned that using water molecules as a tracer would yield novel insights into glymphatic flow and the

role of AQP4 channels. Hence, we implemented a novel MRI method that detects isotopically enriched water (^{17}O water, 90% ^{17}O, 19 Da) via the effect of the quadrupolar ^{17}O nucleus on the ^{1}H MRI signal (Meiboom, 1961). The stable ^{17}O isotope possesses a quadrupolar nucleus which reduces the T_2 relaxation time of bonded hydrogen nuclei (see Chapter 2, section 2.2.3). This effect is further magnified by the exchange of hydrogen atoms with other surrounding water molecules. Thus, the presence of ^{17}O water can be detected by a reduction in the ^{1}H signal of T_2 weighted MRI scans.

In this work, first, we provide a compelling method capable of detecting water flow using an ^{17}O enriched water ($H_2^{17}O$) tracer, several image optimization measures were considered. Second, we used $H_2^{17}O$ to visualize brain-wide subarachnoid CSF-ISF exchange in live rat brains. Further, we directly compared our new method with the current standard for imaging glymphatic flow *in-vivo*, namely DCE-MRI using Gd-DTPA as previously described in Chapter 5. We found that glymphatic flow imaged using our $H_2^{17}O$ tracer was much more rapid and extensive than when imaged using a Gd-DTPA tracer. We propose that this $H_2^{17}O$ MRI approach may provide a new strategy for evaluating glymphatic system and associated neurological disorders.

6.2 Methods

6.2.1 Study 1: Optimising ^{17}O enriched water MRI for imaging CSF parenchymal flow

6.2.1.1 Influence of ^{17}O-^{1}H scalar coupling on ^{1}H relaxation of water / Phantom experiment

The efficacy of MRI contrast agents is determined mainly by their relaxivities (r_1 or r_2). The relaxivity of an MR contrast agent affects MRI detection sensitivity and, ultimately, reflects how the relaxation rate of a solution ($1/T_1$ or $1/T_2$) is altered as a function of the tracer concentration [C]. For transverse relaxation it is expressed as:

$$\frac{1}{T_2} = \frac{1}{T_2^0} + r_2[C]; \qquad\qquad (6\text{-}1)$$

The relaxivity (r_2) is a measure of the strength of the contrast agent, which determines the concentration [C] required to generate readily observable contrast. For all contrast agents, relaxivity depends on extrinsic factors such as the applied field, temperature and other physiological parameters (Koenig and Brown, 1984). To experimentally measure the relaxivity of $H_2^{17}O$, phantom solutions were placed in sealed falcon tubes. Those solutions contained different concentrations of $H_2^{17}O$ (NUKEM Isotopes Imaging GmbH) varying from natural abundance (0.037%) to 10% dissolved in distilled water (pH=7.5).

6.2.1.2 Sensitivity of $H_2^{17}O$ T_2 weighted signal to pH ranges

Tissue pH values have been found to be altered following neurological conditions (Siesjö, 1992; Mehrabian *et al.*, 2018). Cerebral ischaemia promptly induces a marked reductions of tissue pH to around 6.0 in the territory of the occluded vessel and can be easily explained by increased lactate formation, and hydrolysis of ATP (Rehncrona, 1985).

Meiboom (1961) studied the proton chemical exchange in ^{17}O-enriched water solution at different pH values. It was found that the change in enhanced T_2 relaxation, due to both ^{17}O-^{1}H scalar coupling and the chemical exchange between $H_2^{17}O$ and $H_2^{16}O$, can completely disappear when pH is shifted away

from neutral. To investigate whether the proton exchange rate between $H_2^{17}O$ and $H_2^{16}O$ is sensitive to pH, a second set of phantoms was prepared with a fixed $H_2^{17}O$ concentration (2.5%) and different pH levels varying between 2 and 12. The pH was adjusted by the addition of small amounts of HCL or NaOH solution and measured with pH Indicator Strips. The pH was measured both before and after the relaxation measurements.

6.2.1.3 MRI acquisition

T_2 values were measured with an MSME sequence that is based on the CPMG sequence, where the transverse magnetization from a 90^0 pulse is refocused by a train of 180^0 pulses, generating a series of echoes (see Chapter 2). As the data from each echo is acquired with a different TE, this enables the T_2 relaxation times to be calculated. The following imaging parameters were used: number of averages = 2; slice thickness of 2.0 mm; number of echoes = 64, with echo spacing = 7.3ms; repetition time TR = 6000 ms; FOV = 2.0 x 2.0 cm; matrix size= 256 x 256. The total acquisition time for the experiment was 19 minutes 12 seconds.

6.2.1.4 Measurement of T_2 map

To calculate T_2, circular ROIs were drawn on the images using the Image Sequence Analysis (ISA) tool package (Paravision 5.1, Bruker).This uses a fitting function [$y= A+S_0*exp(-t/T_2)$], where A is a constant baseline, S_0 is the initial signal intensity and T_2 represents the transverse relaxation time. The transverse relaxation rate (R_2) was calculated using the equation $R_2 = 1/T_2$ (s^{-1}). The transverse relaxivity was calculated as the slope of the linear regression line of a plot of relaxation rate against concentration of ^{17}O enriched water.

6.2.1.5 $H_2^{17}O$ tracer imaged with high-Signal to Noise Ratio (SNR) T_2 weighted imaging in rat brain

The challenge related to the use of $H_2^{17}O$ as a potential MRI tracer from ^1H MRI imaging, is that $H_2^{17}O$ has a low ^1H transverse relaxivity in biological samples (Alder and Yu, 1951). Therefore, the ^1H signal intensity induced by variations in $H_2^{17}O$ concentration is relatively small in tissue, due to the dominance of competing relaxation mechanisms. Furthermore, this small change must be

differentiated from basal fluctuations in the ^1H signal that occurs due to instrumental instabilities or physiological processes such as periodic motion and vasomotion (Van Dijk, Sabuncu and Buckner, 2012). To overcome this issue, $H_2^{17}O$ must be used at relatively high concentrations level. In the current project, animals were administered with 90% ^{17}O-enriched water. Additionally, it is necessary to optimize data collection sequences in order to further improve the signal to noise ratio (SNR) and detection limits.

6.2.1.6 Optimisation of T_2 RARE pulse sequence: SNR and optimal parameters

The SNR in an MR image is defined as the ratio between the amplitude of the signal and the standard deviation of the noise (McRobbie *et al.*, 2006). to improve SNR, a number of imaging parameters were optimized:

I.   **Reduce receiver bandwidth (RBW=±32.7 kHz):** RBW determines the range of frequencies that will be sampled by the frequency encoding gradient. As RBW decreases, less inherent noise is sampled along with the signal, thus, the signal to noise ratio increases.

$$SNR \propto \frac{1}{\sqrt{RBW}} \qquad\qquad (6\text{-}2)$$

Where:

$$RBW \propto \frac{1}{\Delta T_s} \qquad\qquad (6\text{-}3)$$

Where ΔT_s is the sample time between two successive frequency encoding points. Hence by increasing the sample time, more MRI signal to be captured.

II. **Increasing Field of view (FOV=60 × 60 mm^2):** For conventional sequences, increasing the voxel size results in a gain in SNR, with SNR proportional to the voxel volume. Voxel size can be increased by decreasing the imaging matrix for a fixed FOV, however, though this makes the scans faster it also results in more ghosting artefacts. Hence in the current work, it was found that increasing the FOV, keeping same matrix size, gave less ghosting artefact.

Less artefact was crucial in the current work, as the change in signal that need to be detected is very small (~2%).

III. **Signal averaging (NA=4), TR (~3000 ms) and RARE factor (12):** The SNR, which is proportional to the square root of the NA, improves as the NA increases, but acquisition time also increases linearly with the NA. For fixed scan time NA can be expressed as:

$$NA = \frac{TA}{TR} \cdot \frac{RARE\ factor}{N_{phase}} \cdot \qquad\qquad (6\text{-}4)$$

In order to increase NA without lengthening the acquisition time, other parameters such as TR and RARE factor were compromised. The MRI acquisition parameters before and after optimisation were summarised in Table 6-1.

6.2.2 Study 2: Comparison between $H_2^{17}O$ and Gd-DTPA in evaluating glymphatic flow

6.2.2.1 Study Design

Male Wistar rats (280 to 350 g, 20 to 24 weeks old) were randomly assigned to three experimental groups: 1) $H_2^{17}O$ (n=8), 2) Gd-DTPA (n=8), and 3) aCSF (n=4).

6.2.2.2 Surgery and physiological monitoring

All rats were initially anesthetised (5% isoflurane in 30:70 O_2/NO_2 ratio) in an induction chamber, intubated, and artificially ventilated (with 2-3% isoflurane in 30:70 O_2/NO_2 ratio). The animal was then transferred to a stereotaxic frame where the head was secured with ear and tooth bars. A CM cannula was inserted as described in Chapter 3 (section 3.1.4.3) and connected to a closed-end PE10 tube (2.5 cm long, 0.28 mm ID × 0.61 mm OD, Braintree Scientific) loaded with the desired tracer (13.5 mM Gd-DOTA, 90% ^{17}O water or aCSF) and attached to an infusion pump for tracer delivery. Using methods described in Chapter 3, body temperature, BP, HR and blood gases were continuously monitored for the duration of each experiment. At the end of each experiment, the animal was euthanised.

6.2.2.3 Magnetic Resonance Imaging

Two different tracers were used for this experiment: Gd-DTPA (Magnevist, 21 mM; MW, 938 Da; Bayer HealthCare Pharmaceuticals, Inc.) and $H_2^{17}O$ (90% ^{17}O-enriched water, NUKEM Isotopes, Germany). Furthermore, aCSF was used as a control condition for $H_2^{17}O$ (n=4). The scanning protocol for all studies consisted of 3 baseline scans followed by the intrathecal infusion of tracer via the CM catheter (50 µl at 1.8 µl/min; total time, 28 min). MRI images were continually acquired over a period of 85 minutes. To visualize the glymphatic systems using gadolinium (T_1 weighted shortening effects), 3D T_1 weighted FLASH images were acquired in the sagittal plane (TR/TE = 15 ms/3 ms, flip angle = 15˚, NA=1, field of view (FOV)=3.0×3.0×3.0 cm, total scan time = 3 min 5 s, acquisition matrix size = 128×128×128, yielding an original image resolution of 0.234× 0.234× 0.234 mm). To visualize the glymphatic systems using $H_2^{17}O$ (T_2 weighted shortening effects), T2 weighted images were acquired with a high signal-to-noise fast spin-

echo sequence (T$_2$ RARE). The experimental protocol is shown schematically in Figure 6-1.

6.2.2.4 MRI data analysis

MATLAB R2018b (MathWorks, UK) code was developed in-house for postprocessing MRI images. The general postprocessing procedure consisted of image resizing, brain extraction, head motion correction, image smoothing and voxel-by-voxel conversion to a percent signal change map (see Chapter 3, section 3.2). Briefly, protocol was developed to register and stack multiple T$_1$ weighted slices in order to reflect the T$_2$ weighted imaging slice thickness. Further, a brain mask was created for the removal of non-brain tissue, improving the performance of the following coregistration steps: using rigid body alignment of each scan to the mean pre-contrast image, scan-to-scan misregistration caused by head movement was corrected. The resulting registrations were visually inspected to ensure adequate alignment. To ensure that voxel intensity represented a percent change relative to the average baseline image, all time-series images were subtracted and divided by the baseline average image using the following expression For the Gd-DTPA T$_1$ weighted study:

$$\Delta S_{\%} = \frac{S_{1post} - S_{1pre}}{S_{1pre}} \times 100 \tag{6-5}$$

For the H$_2{}^{17}$O/aCSF T$_2$ weighted study:

$$\Delta S_{\%} = \frac{S_{1pre} - S_{1post}}{S_{1pre}} \times 100 \tag{6-6}$$

where $\Delta S_{\%}$ is the percent signal change from the baseline (S_{1pre}). The T$_1$ weighted and T$_2$ weighted averaged baseline images were used to anatomically guide the placement of regions of interest (ROIs). MATLAB code was developed to create maps of the tracer arrival time, were created on a voxel-by-voxel basis.

The averaged baseline images as well as the contrast-enhanced MRI images were used to anatomically guide placement of each region-of-interest (ROI). The mean values of image intensities in preselected anatomical areas were measured

on the registered images over time, which produced temporal evolution curve of percentage signal change in every specific ROI, due to the uptake tracer by regional brain tissue.

The 1-dimensional Einstein diffusion equation can be solved to give the

probability density function, *P(x,t)*, for particles undergoing Brownian motion:

$$P(x,t) = \frac{1}{\sqrt{4\pi Dt}} \; exp\left(-\frac{(x-x_0)^2}{4Dt}\right) \qquad \text{(6-7)}$$

Where D is the diffusion coefficient and *x* is the particle displacement from its

initial position x_0, during an observation time, t. For this Gaussian function the

root mean square displacement, x_{rms}, of an ensemble of particles is given by:

$$x_{rms} = \sqrt{2Dt} \qquad \text{(6-8)}$$

6.2.2.5 Statistics

No statistical methods were used to predetermine sample size, the sample sizes used were similar to those reported in a previous study (Iliff *et al.*, 2013). Statistical tests were performed using GraphPad Prism (GraphPad Prism Software, California, USA). Statistical comparisons between groups were performed by repeated measures two-way ANOVA followed by Sidak's test to correct for multiple comparisons. All tests were considered statistically significant for p values <0.05, with data presented as mean ± SD unless otherwise stated.
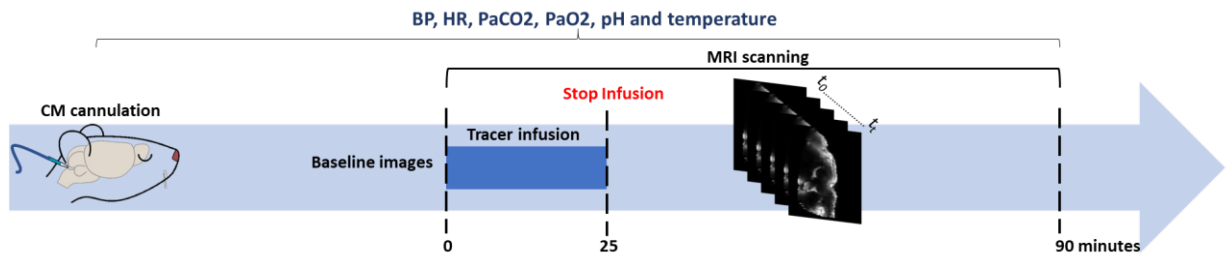
Figure 6-1 Experimental protocol. Following surgical implantation of an intracisternal cannula, the rat was placed in the supine position inside the MRI scanner and kept under anaesthesia. First, 3 precontrast baseline images were acquired. Then, during sequential acquisition of T_1/T_2 images, 50 µl at 1.8 µl/min of either Gd-DTPA (Magnevist, 21 mM) or 90% ^{17}O-enriched water was infused through the cannula over 28 minutes, and T_1/T_2 imaging continued for a total of 85 minutes.

6.3 Result

6.3.1 Study 1: Optimising ^{17}O enriched water MRI for imaging CSF parenchymal flow

6.3.1.1 H$_2$^{17}O relaxivity

Transverse relaxation rates (R$_2$) were measured in H$_2$^{17}O enriched water solutions ranging from 0 to 10 % H$_2$^{17}O, with pH 7.4 at 37 ˚C. Images of the phantoms are shown in **Error! Reference source not found.**B, where the darker circles belong to the samples with higher concentrations of H$_2$^{17}O. In a comparison with the phantom arrangement in **Error! Reference source not found.**A, it is evident that the signal intensity is directly correlated to the H$_2$^{17}O concentration in each tube. The transverse relaxivity (r$_2$) of H$_2$^{17}O was calculated as 2.32 s^{-1}mol^{-1} from the slope of the R$_2$ dependence on concentration (**Error! Reference source not found.**C). By following the pH dependence of the relaxation times, it is clear that equal concentrations of H$_2$^{17}O tracer do not produce the same magnitude of T$_2$ change when pH is shifted away from neutral (**Error! Reference source not found.**) (Meiboom, 1961b).

6.3.1.2 H$_2$^{17}O tracer imaged with high-Signal to Noise Ratio (SNR) T$_2$ weighted imaging in rat brain

The SNR was evaluated as mean signal/noise standard deviation. Figure 6-2 shows the plot of SNR at different slice position before and after T$_2$ weighted RARE parameters optimisation. Following the adjustment of MRI parameters, a ~800% increase in the SNR was achieved.

However, it is important to note that image quality depends not only on high SNR but also on the contrast to noise ratio (CNR) and visibility of the regions of interest and the absence of image artefacts. In the current sequence optimization approach, improving the SNR (by increasing voxel size) came at the cost of reducing CNR as shown in figure 6-5. This drop in CNR is potentially due to the increased partial volume effect due to the increasing of voxel size. Other possible reason for these differences in CNR is perhaps the result of different repetition times (TR) between Bruker and our optimised RARE. Or even due to use of different echo time (TE). However, it is noteworthy that our main aim in the current approach was to enhance the sensitivity of detecting H2^{17}O signal,

even if it came at the cost of CNR quality, which was basically not one of our interests in this study.

6.3.2 Study 2: Comparison between H₂¹⁷O and Gd-DTPA in evaluating glymphatic flow

6.3.2.1 Exclusion and protocol violations.

Animals were removed from the study if they died or were physiologically unstable during the experiment or if the study was not completed due to technical issues. A total of 20 animals were included in this study. Three rats (two in the $H_2^{17}O$ group and one in the Gd-DTPA group) showed no MRI signal change when the contrast agent was infused. Infusion failed either due to leakage or an incorrect CM cannula position. The animals were euthanized at that point and were excluded from the study. In addition, one rat from the control group (aCSF) had unstable blood pressure during the experiment and was excluded from the study. Hence, a total of seventeen rats were analysed for the 3 study groups: aCSF (n=3), $H_2^{17}O$ (n=7), and Gd-DTPA (n=7).

6.3.2.2 Physiological variables

Physiological variables before and after infusion of MRI tracer are shown in Table 6-2. Mean arterial pressure (MAP) was not statistically significant (p = 0.9424). Mean values for all groups remained within normal limits. Other physiological variables were stable throughout the experimental protocol with no significant differences between groups (p = 0.3506 for pH, p = 0.4852 for PaO^2, p = 0.5204 for $PaCO^2$ and p = 0.9521 for body temperature).

6.3.2.3 Perivascular influx of H₂¹⁷O into the brain parenchyma

Figure 6-6 shows the temporal evolution curve of percentage signal change observed in preselected anatomical regions. The curves plateaued once the infusion ceased with the exception of the parenchymal regions (olfactory bulb and cortex), where a gradual change in signal continued until the end of scanning. Compared with aCSF control conditions, the average change of signal from baseline over time was significantly larger in (A) prefrontal cortex (p< 0.0001), (B) pineal recess(p< 0.0001), (C) cerebellum (p< 0.0001), (D) pituitary

recess (p< 0.0001), (E) olfactory bulb (p< 0.0001), and (F) 4th ventricle (p< 0.0001) (see Figure 6-6).

6.3.2.4 Dynamic distribution of $H_2^{17}O$ and Gd-DTPA contrast

The distribution pattern of $H_2^{17}O$ tracer was directly compared against the Gd-DTPA tracer. Figure 6-7 shows a time series of colour-enhanced sagittal sections depicting the percentage signal change and distribution of the $H_2^{17}O$ tracer following injection into the cisterna magna. Figure 6-7 shows a time series of colour-enhanced sagittal sections depicting the percentage signal change and distribution of the Gd-DTPA tracer following injection into the cisterna magna. These are representative examples from one rat imaged with the $H_2^{17}O$ tracer and another rat imaged with the Gd-DTPA.

The dynamic time series of T_1 weighted MR images clearly revealed the time-dependent anatomical routes of perivascular influx when using tracers such as Gd-DTPA with a molecular size larger than water (Magnevist, MW, 938 Da). The Gd-DTPA agent first appeared in the cisterna magna and was then transported along vessels of the circle of Willis. Gd-DTPA continued to be transported along the olfactory arterial complex and into the olfactory bulb at~10 minutes after injection (Figure 6-7.). Finally, there was slow parenchymal enhancement of Gadolinium, continuing in some regions up to 85 minutes after injection (Figure 6-7. , 85 min). However, Gadolinium under the current experimental protocol was not detected in the deep cortical regions.

Following the infusion of the $H_2^{17}O$ tracer, the dynamic time series of T_2 weighted MR images clearly revealed a CSF parenchymal flow that was strikingly more rapid and extensive than that observed using conventional Gd-DTPA tracers. The $H_2^{17}O$ tracer rapidly appeared as early as 3.5 minutes following injection within the perivascular spaces of surface arteries and within regions close to the cisterna magna such as the cerebellum. $H_2^{17}O$ then began to move progressively deeper into the brain parenchyma and subsequently dispersed broadly within the whole brain parenchyma within ~10 minutes after injection (Figure 6-8). By comparing the $H_2^{17}O$ tracer distribution with that of the Gd-DTPA, it is evident that, within the first few time points after injection, the

$H_2{}^{17}O$ tracer distribution differed radically from the pattern observed with the Gd-DTPA tracers.

6.3.2.5 The influx of the $H_2{}^{17}O$ tracer was faster and was much more extensive across the whole brain

To provide a quantitative assessment of the temporal behaviour of both Gd-DTPA and $H_2{}^{17}O$ uptake within the whole brain, the times that the tracer arrived at each voxel after injection were estimated. This was achieved by identifying the time points at which the signals rose and kept rising for at least three successive time points. By comparing the arrival time maps shown in Figure 6-9, it can be seen that Gd-DTPA tracer took longer to reach certain brain regions, suggesting the lower bulk speed of the Gd-DTPA-tracer or more resistance. The signal changes induced within the parenchyma by Gd-DTPA peaked between 70 and 80 minutes after injection. By contrast, the $H_2{}^{17}O$ penetrated into the brain very rapidly and was distributed quickly, peaking throughout the whole brain between 10 and 30 minutes after injection.

From previous diffusion MRI experiments using a long observation time (600ms) (Qaisi et al., 2020), we measured the plateau diffusion coefficient of water within the rodent cortex as 0.00062 mm^2/s. From equation 6-8, the root mean square displacement, x_{rms}, of water for experiment times of 3.85min (231s), 7.65min (459s), 11.08min (665sec) and 14.83min (893sec) was calculated to be 0.53mm, 0.75mm ,0.91mm and 1.05mm, respectively. Gd-DTPA diffusivity in a tissue mimic material (polyvinyl alcohol-cryogel) have been performed in our lab using MRI, giving a diffusion coefficient of 0.00026 mm^2/s. From equation 6-8, the root mean square displacement, x_{rms}, of Gd-DTPA for experiment times of 7.65 min (459s), 11.08 min (665sec) and 14.83 min (893sec) were calculated to be 0.49 mm ,0.59 mm and 0.68 mm, respectively.

6.3.2.6 Comparison of regional tracer uptake

To assess the relative kinetics within the subregions of the brain, the temporal evolution curve was calculated after injection of the MRI tracer ($H_2{}^{17}O$ or Gd-DTPA) in the prefrontal cortex, pineal recess, cerebellum, pituitary recess, olfactory bulb and 4th ventricle (Figure 6-12). Since the change in MRI signal induced by $H_2{}^{17}O$ is a T_2 shortening effect and Gd DTPA is a T_1 shortening effect,

we were not able to perform direct comparisons of the percentage signal change over time induced by both tracers. To overcome this limitation, the mean percentage signal changes over time were normalised by dividing each time point by the maximum percentage signal change over the entire time period within the selected ROIs. The percentage signal change for $H_2^{17}O$ demonstrates an early and robust change in signal over the early infusion period in all brain parenchymal regions when compared with Gd-DTPA.

In the $H_2^{17}O$ dataset, larger signal changes were observed in the 4th ventricle and pineal recess compared with the brain parenchymal regions, with exception of cerebellum (Figure 6-11). These observations were consistent with those of the Gd-DTPA tracer (Figure 6-12). This could suggest that large portion of $H_2^{17}O$ molecules, even though they are freely diffusible molecules, preferentially travel along the perivascular channels in similar distribution patterns to other larger molecules like Gd-DTPA (see Figure 6-13).
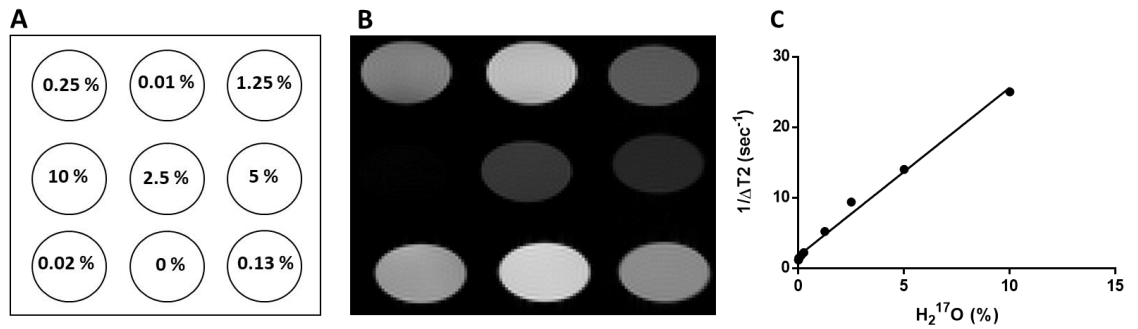
Figure 6-2. Measuring the relaxivity of $H_2^{17}O$ solutions. (A) Schematic drawing shows the layout of the phantoms. Numbers denote the percentage of $H_2^{17}O$ is solution. (B) Images of the phantoms acquired with MSME. (C) Relative increase of the proton relaxation rate as a function of $H_2^{17}O$ concentration. Relaxivity was measured from the slope of the linear regression.
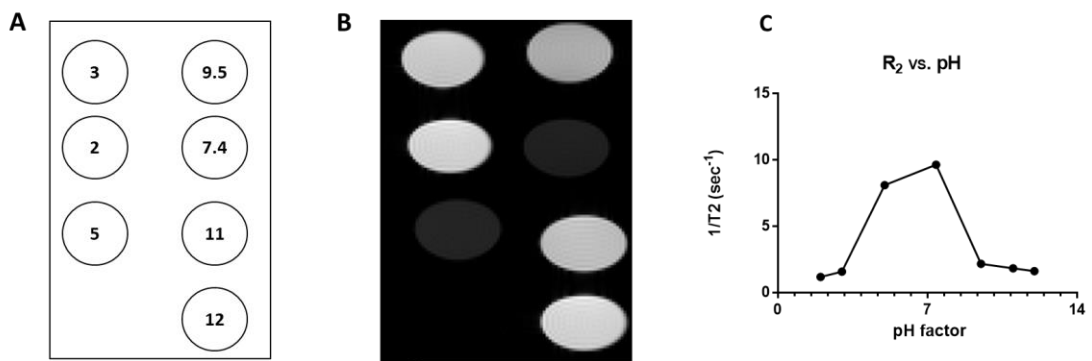
Figure 6-3. Influence of pH on T_2 relaxation rates. (A) Schematic drawing showing the layout of the phantoms. Numbers denote pH values. (B) Image of the phantom acquired with MSME. (C) The proton relaxation rate plotted as a function of pH values.

MRI parameters	Bruker default T_2 RARE sequence	Optimised T_2 RARE sequence
TR (ms)	6000	3000
TE (ms)	100	61.32
FOV (mm^2)	30 × 30	60 × 60
Data matrix	256	200
RARE factor	8	12
Number of averages	2	4
Bandwidth (kHz)	±50.0	±32.7
Voxel size (mm^3)	0.097 × 0.097 × 1.5	0.3 × 0.3 × 1.5
Scan duration (min)	3.21	3:12
Slice thickness (mm)	0.75	1.5

Table 6-1. MRI sequences parameters before and after T_2 weighted RARE optimisation.
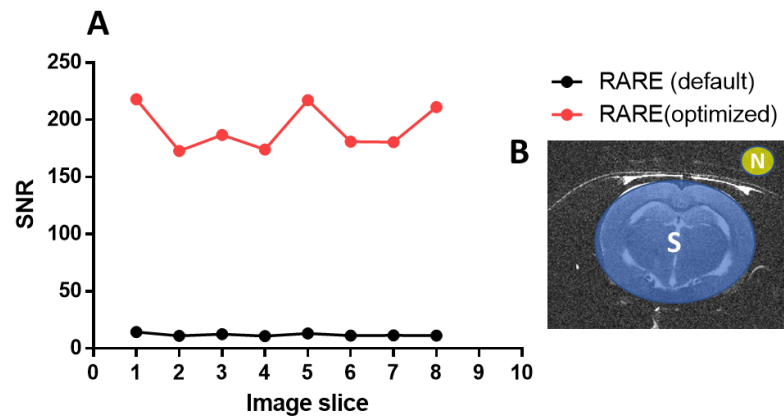
Figure 6-4. SNR computed for T$_2$ weighted images obtained with conventional RARE and optimised RARE sequence parameters. (A) The optimization of T$_2$ weighted RARE sequence parameters enabled an increase in SNR (~1200%) compared with the default T$_2$ weighted RARE sequence. (B)The mean image intensity ratio of the signal to standard deviation (SD) of noise. ROI is used for SNR estimation.
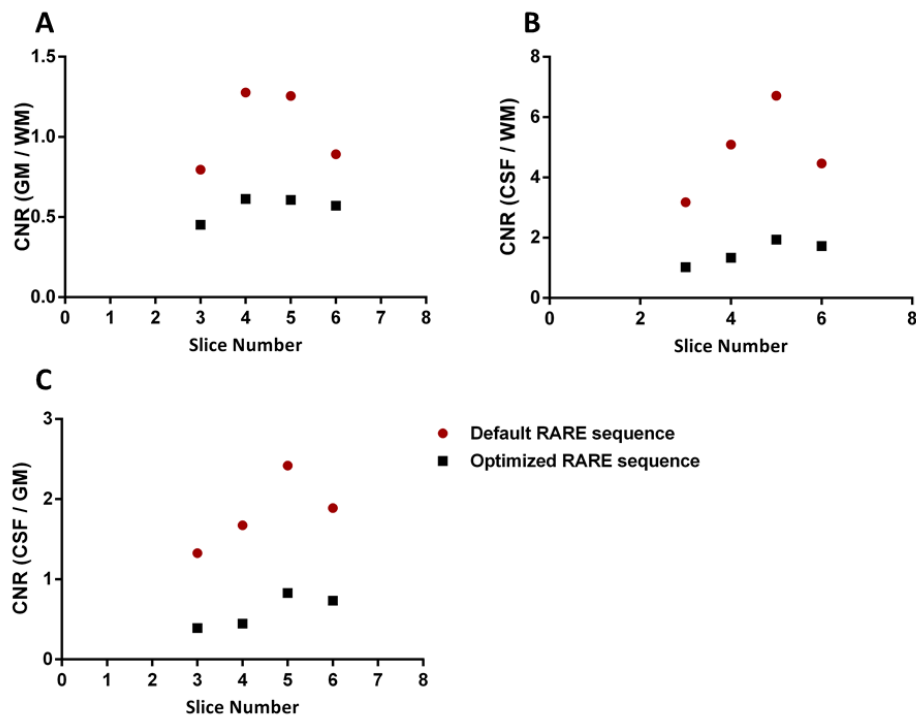
Figure 6-5. CNR computed for T2 weighted images obtained with conventional RARE and optimised RARE sequence parameters. (A) Grey and white matter CNR of RARE and optimised RARE images. (B) CSF and white matter CNR of RARE and optimised RARE images (C) CSF and Grey matter CNR of RARE and optimised RARE images.

Physiological parameters		Before infusion	Time from infusion 30 min	80 min
MAP (mmHg)	H$_2$^{17}O	88.1 ± 6.7	90.6 ± 8.2	85.9 ± 9.3
	Gd-DTPA	93 3± 5.1	94.7 ± 7.2	92.9 ± 6.6
	aCSF	90.5 ± 6.4	88.9 ± 8.7	87.5 ± 9.4
PaO$_2$ (mmHg)	H$_2$^{17}O	146.1 ± 5.7	144.6 ± 7.4	140.6 ±10.6
	Gd-DTPA	138.3 ± 10.1	143.7 ± 12	141.5 ± 7
	aCSF	142.5 ± 7.4	145.9 ± 8.2	148.5 ±10.4
PaCO$_2$ (mmHg)	H$_2$^{17}O	40± 6.6	37.2 ± 8	36 ± 9.7
	Gd-DTPA	36.9 ± 7	36.7 ± 8.5	42.3 ± 6.9
	aCSF	40·2 ± 6·6	41·1 ± 5·5	45.3 ± 10.5
Temp (°C)	H$_2$^{17}O	37 ± 0.6	37.2 ± 0.5	37.3 ± 0.3
	Gd-DTPA	36.9 ± 0.7	36.7 ± 0.8	36.8 ± 0.6
	aCSF	37·2 ± 0·6	37·1 ± 0·5	37·1 ± 0·4
pH	H$_2$^{17}O	7.5 ± 0.06	7.5 ± 0.08	7.4 ± 0.1
	Gd-DTPA	7.5 ± 0.02	7.4 ± 0.05	7.5 ± 0.2
	aCSF	7.5 ± 0.03	7.5 ± 0.05	7.5 ± 0.3

Table 6-2: Physiological variables in rats, following tracer infusion. MAP, mean arterial pressure; PaCO$_2$, partial pressure of carbon dioxide; PaO$_2$, partial pressure of oxygen; Temp, temperature values are within physiological ranges for H$_2$^{17}O Gd-DTPA and aCSF. Significant differences denoted by $p < 0.05$. Data presented as mean ± SD.
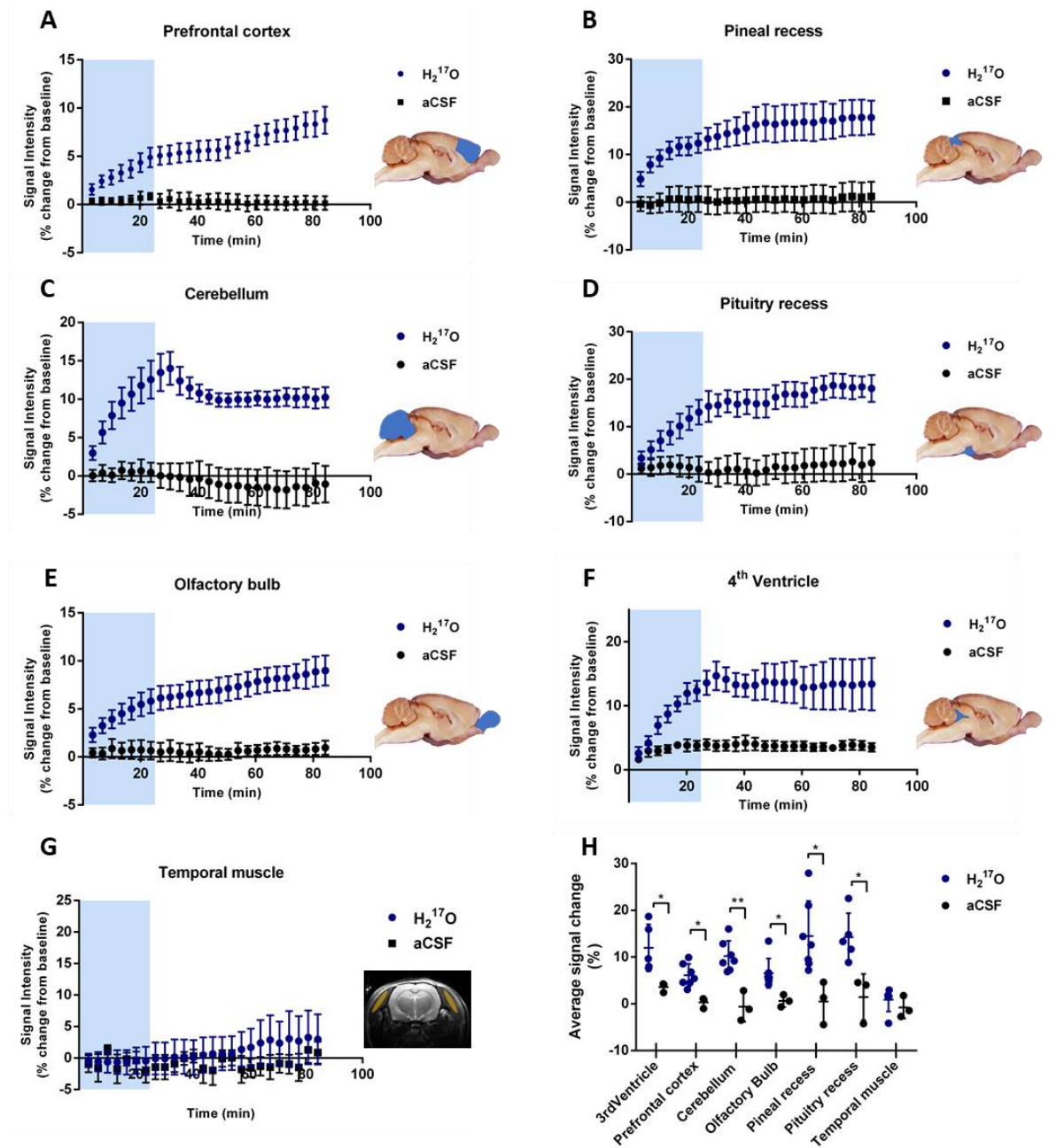
Figure 6-6. Comparisons of time-to-signal curves for $H_2^{17}O$ and aCSF in specific brain regions. Signal-to-time curves for $H_2^{17}O$ (blue circles) and aCSF (black box) are shown for the (A) Prefrontal cortex, (B) pineal recess, (C) cerebellum, (D) pituitary recess, (E) olfactory bulb, (F) 4th ventricle, and (G) Temporal muscle. (H) The average signal change was calculated within the period from the injection start of $H_2^{17}O$ and aCSF to the end of the scan. Significant differences denoted by asterisks: *$p < 0.05$, **$p < 0.01$, ***$p < 0.001$. Data presented as mean ± SEM.
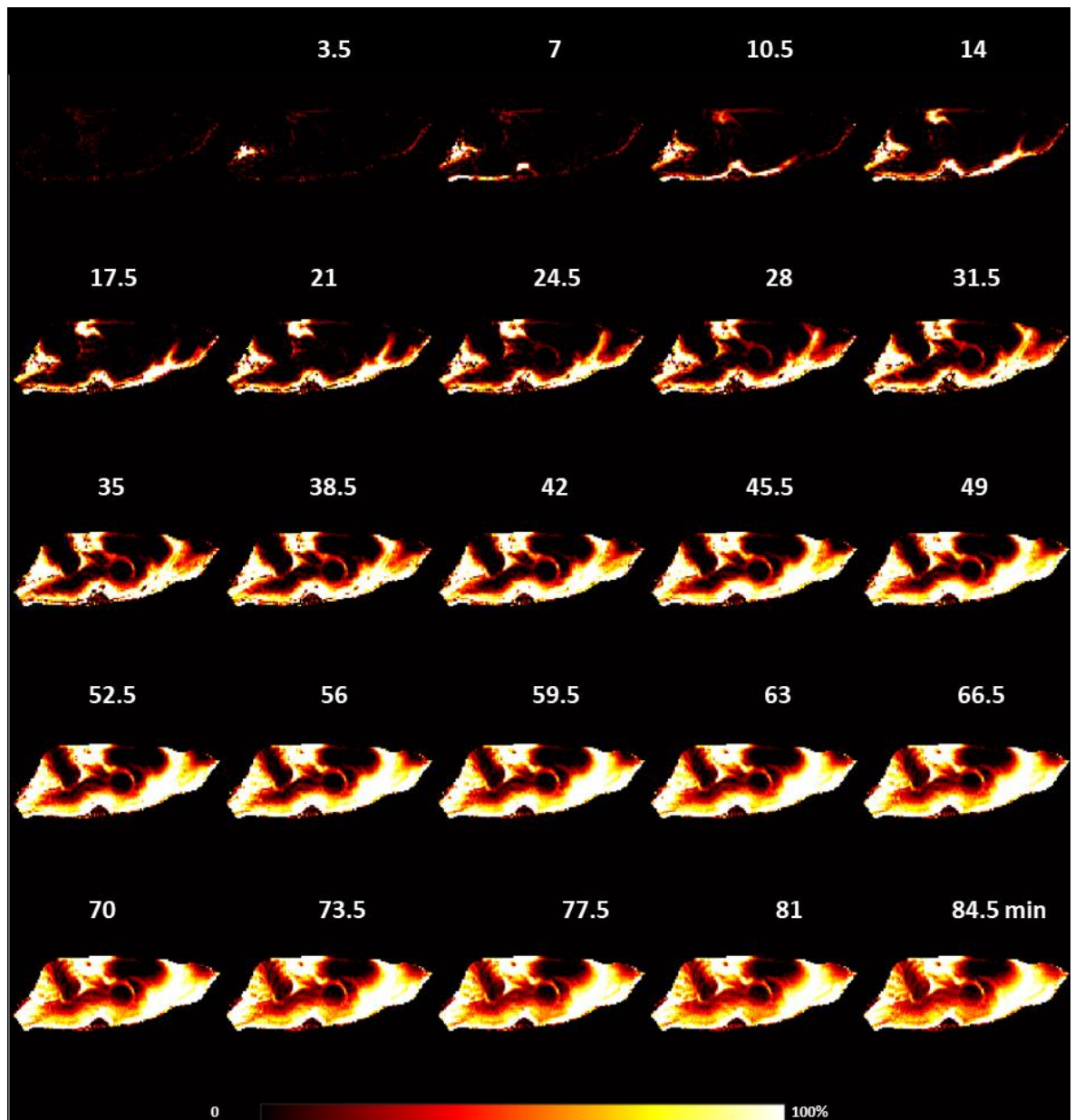
Figure 6-7. Representative sagittal temporal evolution maps of Gd-DTPA from the onset of infusion. Pseudo colour scaling illustrates tracer distribution of the Gd-DTPA (n=1).
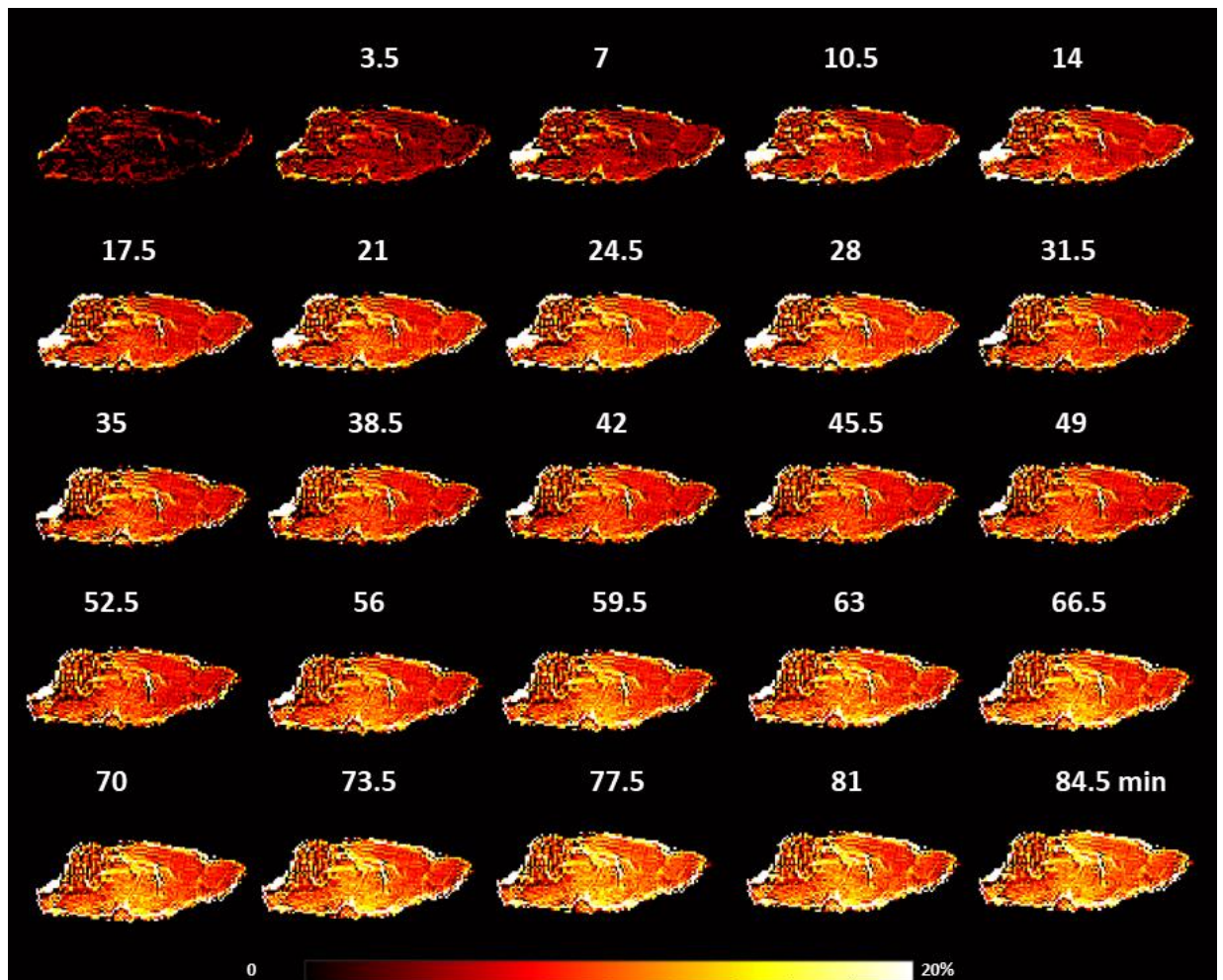
Figure 6-8. Representative sagittal temporal evolution maps of $H_2^{17}O$ water from the onset of infusion. Pseudo colour scaling illustrates tracer distribution of the $H_2^{17}O$ (n=1).
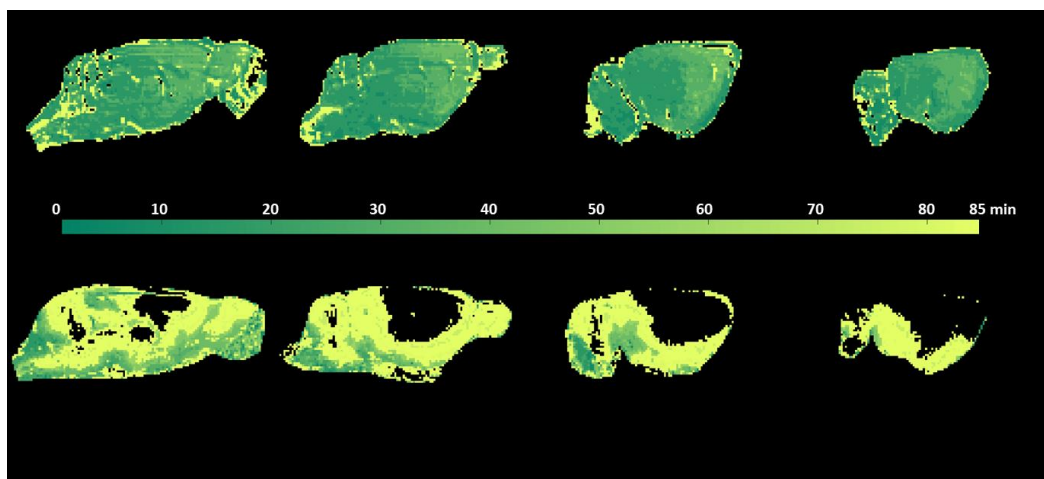
Figure 6-9. Representative arrival time maps. The upper panel images show a rat infused with $H_2^{17}O$ (MW, 19 Da) and the bottom panel images show one rat infused with Gd-DTPA (Magnevist; MW, 938 Da). Corresponding tracer arrival time maps for four sagittal slices, with shorter arrival times indicated by brighter colours. Black colour indicates that the tracer did not arrive within the 85 minutes recording.
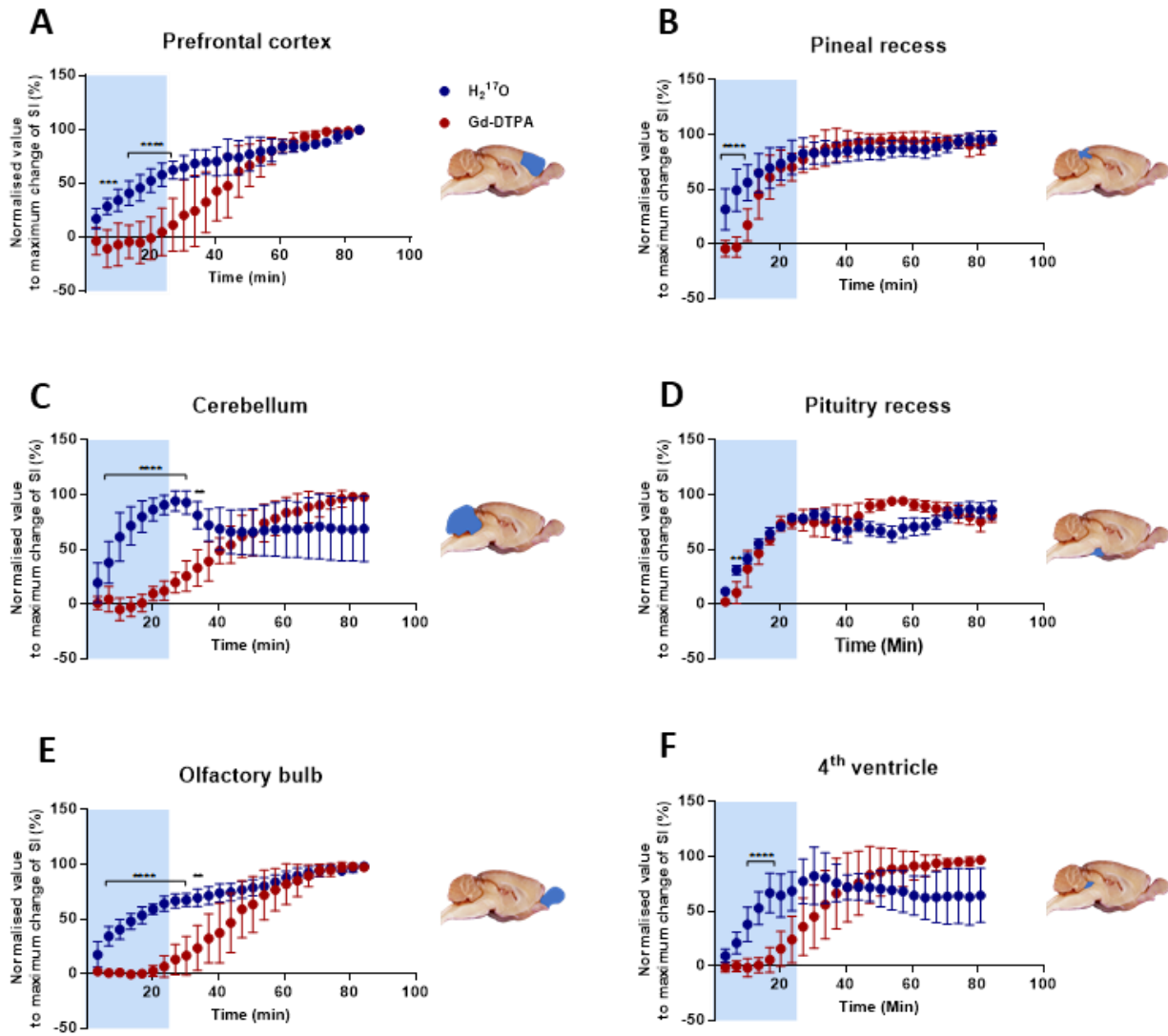
Figure 6-10. Comparisons of time-to-signal curves for H₂¹⁷O and Gd-DTPA in specific brain regions. Analyses were displayed to demonstrate the change of signal curves , which is normalised by its maximum value, for $H_2^{17}O$ (blue circles) and Gd-DTPA (red box) for the (A) Prefrontal cortex, (B) pineal recess, (C) cerebellum, (D) pituitary recess, (E) olfactory bulb, and (F) 4th ventricle. Significant differences denoted by asterisks: *$p < 0.05$, **$p < 0.01$, ***$p < 0.001$, ****$p < 0.0001$. Data presented as mean ± SD.
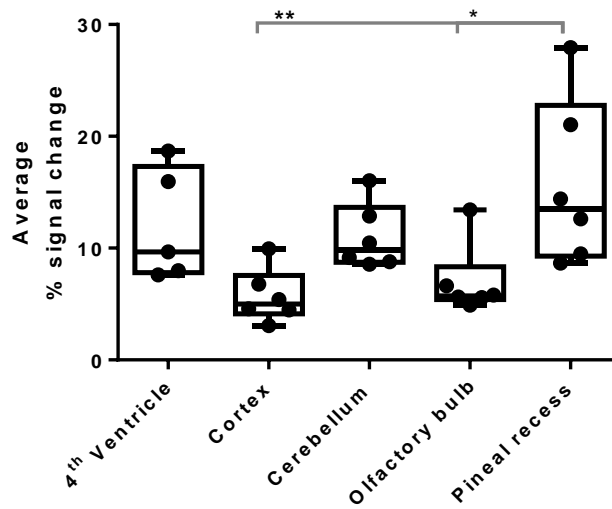
Figure 6-11. Comparisons of kinetic parameters of H$_2$^{17}O among different brain regions. Average percentage signal change were calculated for 4th ventricle, cortex, cerebellum, olfactory bulb, and pineal recess. Significant differences denoted by asterisks: *p < 0.05, **p < 0.01, ***p < 0.001. Data presented as mean ± SD.
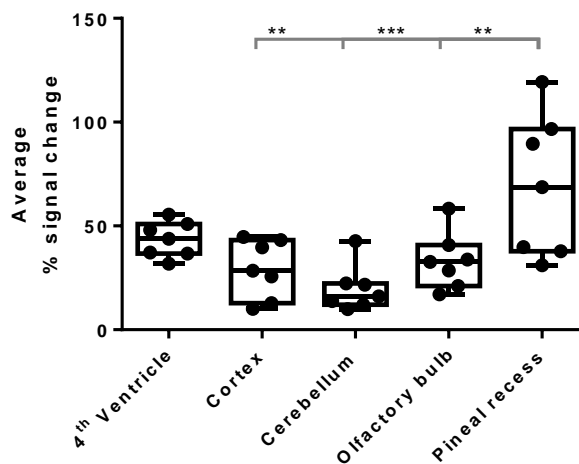
Figure 6-12. Comparisons of kinetic parameters of Gd-DTPA among different brain regions. Average percentage signal change were calculated for 4th ventricle, cortex, cerebellum, olfactory bulb, and pineal recess. Significant differences denoted by asterisks: *p < 0.05, **p < 0.01, ***p < 0.001. Data presented as mean ± SD.
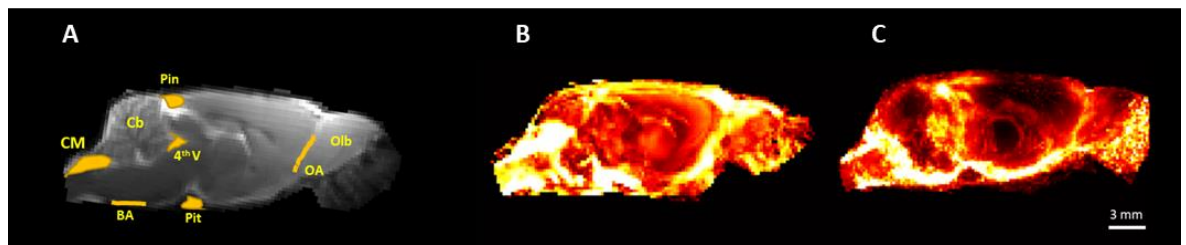
Figure 6-13. 3D visualization constructed images representing perivascular influx of H$_2$^{17}O and Gd-DTPA.(A) 2D T$_2$ weighted MRI with the anatomical structures displayed. (B) 3D visualization constructed from T$_2$ weighted images demonstrates H$_2$^{17}O distribution along perivascular spaces and in all brain regions. (C) 3D visualization constructed from T$_1$ weighted images demonstrates Gd-DTPA distribution along perivascular spaces with limited penetration into the brain.

6.4 Discussion

In this study, we employed the MRI $H_2^{17}O$ method, which enabled the direct imaging of glymphatic water transport in the *in-vivo* rat brain for the first time. The magnitude of the T_2 effect in various water solutions enriched with different $H_2^{17}O$ concentrations and pH values were determined. The changes in T_2 relaxation rate were linearly correlated with the percentage of $H_2^{17}O$ enrichment. The $H_2^{17}O$ MR sensitivity was also optimised in rat brain, leading to a high SNR T_2 weighted method. Further, this new method was directly compared with the current in-vivo gold standard of DCE-MRI with gadolinium-based contrast agents (Gd-DTPA).

Water molecules have previously been used as tracers by exploiting various isotopes. For example; tritiated water (^3H_2O) has been used to investigate CSF transport by measuring the radiation levels of blood samples using a liquid scintillation counter(Bulat, Klarica, *et al.*, 2008); $H_2^{15}O$ has been imaged with Positron Emission Topography (Schneider *et al.*, 1995), though its short half-life (122.2s) makes it impractical to study glymphatic function; the stable ^{17}O isotope is not radioactive but possesses a quadrupolar nucleus (I=5/2) that can be imaged using MRI, although direct imaging of ^{17}O signal is difficult due to its low gyromagnetic ratio and low natural abundance (0.037%) (Richardson, 1989). However, the presence of $H_2^{17}O$ can be detected indirectly via the effect of the quadrupolar ^{17}O nucleus on the ^1H MRI signal (Ronen and Navon, 1994), where the quadrupolar ^{17}O nucleus reduces the T_2 relaxation times of bonded hydrogen nuclei. This effect is further magnified by the exchange of hydrogen atoms with other surrounding water molecules (see Chapter 2, section 2.2.3). $H_2^{17}O$ produced from $^{17}O_2$ gas has been used to image metabolism (Tailor *et al.*, 2004) and $H_2^{17}O$ has also been administered as a tracer to image cerebral blood flow (Arai *et al.*, 1998). In a series of studies Nakada et al. also employed indirect ^1H detection of $H_2^{17}O$ to investigate the interstitial circulation. However, they used an intravenous bolus injection of $H_2^{17}O$ (20% ^{17}O) and showed that the exchange of blood water with the interstitial fluid and CSF, was dependent on AQP4 and not AQP1 (Igarashi *et al.*, 2013; Huber *et al.*, 2018; Kudo *et al.*, 2018). They also used the same intravenous bolus method to demonstrate that water influx into CSF was significantly impaired in SP-bearing transgenic mice (Igarashi, Suzuki, *et al.*, 2014). However, these previous studies did not directly investigate the

glymphatic system. In this work, to directly image glymphatic water transport within the rat brain, the $H_2^{17}O$ tracer was infused directly into the CSF at the cisterna magna, replicating the delivery approach used by Nedergaard et al in their seminal Gd-DTPA experiments. In order to detect the small signal changes generated from infusing tiny amounts of $H_2^{17}O$, it was necessary to employ a much greater concentration of $H_2^{17}O$ (90% ^{17}O-enriched water) and use a high SNR T_2 weighted imaging sequence (SNR 200:1).

Serial MRI revealed a glymphatic flow that was strikingly more rapid and extensive than previously observed using conventional Gd-DTPA tracers (Iliff *et al.*, 2013). To better understand the speed of the $H_2^{17}O$ into the neuropil interstitium, we generated maps of tracer arrival time (see Figure 6-9). The speed of the $H_2^{17}O$ influx reflects the rates of CSF-ISF exchange throughout the brain. Whereas $H_2^{17}O$ permeated virtually the entire brain volume within 10 minutes of injection, penetration of the higher–Gd-DTPA tracer was far slower and also more restricted. Interestingly, such rapid and extensive water movements were observed previously in small molecular tracer experiments. A much earlier study using deuterium oxide (D_2O) found high rates of water flux from vascular compartments and rapid distribution throughout brain and CSF compartments (Bering, 1952). These data suggested high rates of water flux which were more rapid and incompatible with previously estimated rates of CSF and ISF flow using larger tracers.

Reason for the discrepancy between the transport of $H_2^{17}O$ and Gd-DTPA tracers was the difference in the molecular weight of the tracers employed. As observed in previous data, molecular tracers that lack a specific molecular transport pathway (such as ion transporters or channels) are only able to reach the parenchyma through a 20-nm clefts between overlapping astrocyte end feet (Iliff *et al.*, 2013). Water, however, is able to travel freely from perivascular space into intersitial space through end feet gaps and the process can be speed up through intracellular space mediated by highly selective AQP4 water channels (Verkman *et al.*, 2013). These channels are expressed in astrocytic end feet that surround the entire vasculature in the CNS. Hence, previous experimental studies may have systematically underestimated subarachnoid CSF flow into the brain by basing their analyses on tracers larger than water. Asgari et al. (2015)

modelled the astrocytic syncytium between CSF and the compartment of the brain interstitium by including in their model AQP4 on the plasma membranes, an abundance of AQP4 on the perivascular surfaces, and 20nm inter-end feet gaps. They demonstrated that the resistance to water flow through ECS is two orders of magnitude larger than through the intracellular space (ICS) of astrocytes (Asgari, de Zélicourt and Kurtcuoglu, 2015).

While the current MRI imaging have shown a rapid and extensive distribution of $H_2^{17}O$ within the brain tissues, curiously the tracer does not penetrate deep into white matter regions within cerebellum (Figure 6-8). This absent of enhancement can be explained either because the penetration into white matter, which is away from the perivascular spaces, is too slow, or the lack of enhancement was attributed to concentrations of $H_2^{17}O$ probably being too small to be detected. Furthermore, following the rapid wash in of $H_2^{17}O$ withing brain parenchyma, we did not observe an indication of any early wash out of $H_2^{17}O$ over the entire study period (Figure 6-11).

There is much debate in the literature regarding the existence (Iliff *et al.*, 2013), or lack thereof (Verkman *et al.*, 2013), of a bulk convective flow of ISF. Arterial perivascular solute transport by dispersion can account for this behaviour. Dispersion refers to transport of solutes by the combined effect of diffusion and a macroscopic fluid motion with zero mean, i.e., oscillatory flow. However, previous computational modelling studies have suggested that arterial pulsation cannot be the sole driving force of net bulk flow as this would require additional driving forces. Furthermore, they concluded that rapid dispersion of solutes as a consequence of arterial pulsation does facilitate faster transport along perivascular routes inflow.

In the current study, we estimated the root mean squared (rms) displacement of water molecules in the brain to be 1.05 mm in 15 minutes, whereas, for Gd-DTPA molecules, it is 0.68 mm. This reflects the larger molecular weight of Gd-DTPA (938 Da) compared with $H_2^{17}O$ (19 Da). In addition, Gd-DTPA molecules are restricted to the extracellular compartment, whereas $H_2^{17}O$ is able to more freely diffuse into cells. However, comparing the estimated water displacements due to only diffusion, with the actual $H_2^{17}O$ images (Figure 6-4), it appears

unlikely that diffusion alone explains the rapid brain wide distribution of $H_2^{17}O$ after 15 minutes, supporting the argument for a bulk convective flow of the ISF.

6.4.1 Discussion of Alternative interpretations

An alternative hypothesis of CSF physiology has been proposed by Klarica et al (2019).They showed when tritiated water (^3H_2O) was injected into the CSF space of cats, water was absorbed locally into cerebral capillaries and finally drained into the sinuses. However, when macromolecular ^3H-inulin was infused into the CSF, large amount of tracer remained within the CSF compartments (Bulat *et al.*, 2008). Based on these and other observations, they proposed that CSF production and absorption occurs at the level of the capillaries and depends on hydrostatic and osmotic forces. Klarica et al. (2019) also suggested a continuous bidirectional mixing of water between the blood, ISF and the CSF compartments, with no unidirectional net flow of CSF along the CSF spaces.

The suggestion by Klarica et al. of an absence of unidirectional flow within CSF spaces, is not supported by our $H_2^{17}O$ experiments ([Figure 6-8]). Infusing $H_2^{17}O$ into the cisterna magna leads to a high uptake in the 4th ventricle (representing CSF space) and pineal recess (representing subarachnoid spaces and proximal perivascular channels), which implies that $H_2^{17}O$ largely flows through the CSF compartment and subarachnoid space. Also, AQP4 channels are absent from the endothelium of the capillaries within the brain, hence we proposed that the endothelial wall can be viewed as a high resistance pathway for the water. Further, the $H_2^{17}O$ signal change was greatest along the ventral brain surface and along the margins of the pineal recess and the olfactory bulb. These anatomical structures were previously identified by Illif et al. (2012) as the proximal glymphatic transport pathway for CSF within the wider subarachnoid space.

6.4.2 Summary

In summary, a serious limitation of previous *in-vivo* glymphatic experiments has been their use of large tracer molecules (e.g., MRI tracer Gd-DTPA, MW 938 Da) that cannot be transported by AQP4 water channels in the brain. We hypothesised that the use of these large tracer molecules would result in the underestimation of the rate that CSF water molecules enter the brain

parenchyma, thereby underestimating the true flow of interstitial water. By labelling actual water molecules, via $H_2^{17}O$ water, we were able to detect glymphatic water transport *in-vivo* using T_2 weighted MRI. The ability of our $H_2^{17}O$ MRI method to directly image water transport *in vivo* provides an accurate means of studying glymphatic flow. We have conclusively demonstrated that glymphatic flow imaged using our $H_2^{17}O$ tracer is much more rapid and extensive than when imaged using a Gd-DTPA tracer. Thus, there is strong evidence that the interstitial fluid experiences a substantial bulk flow, which can more rapidly clear waste molecules from the parenchyma than diffusion alone. In the next Chapter, the role of astrocytic AQP4 in the glymphatic flow was investigated.

7 Chapter 7: Exploring the role of AQP4 in Glymphatic system using H$_2$^{17}O MRI

7.1 Introduction

In the previous Chapter, we have directly imaged CSF water transport in the rat brain *in vivo* for the first time. Our results revealed glymphatic flow that was dramatically faster and more extensive than previously thought. It was, therefore, a logical next step to determine the role of astrocytic aquaporin-4 (AQP4) in the circulation of CSF water in perivascular compartments.

Water exchanges constantly between the different compartments of the brain (Bering, 1952). This process can be accelerated when water molecules travel through highly selective aquaporin water channels (AQPs) (Preston *et al.*, 1992). AQPs, driven by both passive osmotic and hydraulic pressure gradients, have the ability to transport water bidirectionally across cell membranes (Tait *et al.*, 2008; Papadopoulos and Verkman, 2013). Among the 14 different aquaporins that have been identified, AQP1, 4 and 9 have been reported in the brain (Papadopoulos and Verkman, 2013). Both AQP1 and 4 play an important role in maintaining volume homeostasis in the brain. AQP1 is found in the apical membrane of the choroid plexus epithelial cells and is involved in secretion of the CSF (Praetorius and Nielsen, 2006). AQP4 is the predominant water channel in the brain and is heavily enriched in a highly polarised manner at the astrocytic endfeet facing the BBB, the glia limitans of the brain surface and the perivascular spaces (PVS), as well as the ventricular ependymal cells and subependymal astrocytes (Suzuki *et al.*, 2013).

The permeability of AQP4 channels can be regulated as a potential therapeutic target (Igarashi *et al.*, 2011; Tang and Yang, 2016) and this has been implicated in the pathophysiology of a range of CNS disorders. For example in Alzheimer's disease (Xu *et al.*, 2015), vascular dementia (Venkat *et al.*, 2018), traumatic brain injury (Ren *et al.*, 2013), subarachnoid haemorrhage and acute ischaemia (Gaberel *et al.*, 2014).

It has been demonstrated that convective ISF flow, via the glymphatic system is dependent upon the perivascular expression of AQP4 water channels (Iliff *et al.*,

2012). Where AQP4 channels operate as a highway for CSF influx into the brain parenchyma. In a series of experiments, Nedergaard and her colleagues have demonstrated the important of AQP4 to the glymphatic system. In their original work, they injected a fluorescent ovalbumin to the cisterna magna of global AQP4 knockout mice and found significantly reduced CSF influx relative to wildtype animals (Iliff et al., 2012). This was interpreted as evidence for AQP4-dependent convection through astrocyte endfeet. However, as ovalbumin tracers will not pass through AQP4 channels, they did not directly demonstrate the importance of AQP4.

A major critique of the 'glymphatic' hypothesis involves the proposed contribution of AQP4 to this system. This has been questioned by Verkman and Smith (2018) who failed to replicate the original work by Iliff et al. in AQP4-null animals. They argued that AQP4 was not needed for solute removal from the brain (Smith and Verkman, 2018). Subsequently, study represented the work of five research groups using four different AQP4 knockout lines confirmed AQP4 gene deletion impairs glymphatic CSF tracer influx (Mestre *et al.*, 2018). Yet, all of the aforementioned *in vivo* studies have used non water tracers to track the movement of CSF fluid within the glymphatic compartments. Since tracer movement does not necessarily directly reflect underlying fluid flow as we have shown in previous chapter, the relative contribution of AQP4 in glymphatic flow remains unknown.

AQP4 levels and function have been modulated in wild type mice by siRNA or pharmacological functional inhibitors such as TGN-020. Treatment with siRNA has been shown to reduce expression to about 76% after 3 days *in vitro* (Nicchia *et al.*, 2003; Badaut *et al.*, 2011). Two intra-cortical injections of siRNA were required to decrease AQP4 expression by 27% *in vivo* (Nicchia *et al.*, 2003). A single dose of TGN-020 inhibits AQP4 function by 67% as soon as 2h post application in vitro (Mathiisen *et al.*, 2010) and shows an effect within 20-30 minutes in vivo (Igarashi *et al.*, 2011; Igarashi, Tsujita, Suzuki, *et al.*, 2013; Wei *et al.*, 2017; Pirici *et al.*, 2018). Additionally, TGN-020 can be administered intraperitoneally avoiding any potential effect on glymphatic function by opening the skull to deliver compounds into the brain.

7.1.1 Hypothesis

We hypothesised that by using $H_2^{17}O$ as a water labelled tracer, it would be possible to conclusively demonstrate the key role of astrocytic AQP4 in glymphatic system. We hypothesised that a pharmacological inhibitor of AQP4 (TGN-020) would block the water channels, reducing transport of $H_2^{17}O$ into the parenchyma.

7.2 Methods

7.2.1 Surgery and physiological monitoring

The experiment was designed to compare differences in CSF parenchymal flow between normal and AQP4 inhibited rats ([Figure 7-1](#)). Male Wistar rats (n=12, 300 to 350 g, aged 20 to 24 weeks) were randomly assigned to two experimental groups, namely, vehicle-treated rats (n=7) and rats treated with AQP4 inhibitor (TGN-020, n=8). All animals were initially anesthetised (5% isoflurane in 20:80 O^2/air mixture) in an induction chamber, intubated, and artificially ventilated (with 2-3% isoflurane in 30:70 O_2/NO_2 mixture). Anesthetised rats were then placed in a stereotaxic frame. The cisterna magna (CM) cannula was inserted into the subarachnoid cisterna magna space, as described in Chapter 3, section 3.1.4.3. Then, the CM cannula was connected to a closed-end PE10 tube loaded with 90% $H_2^{17}O$ tracer and attached to an infusion pump for tracer delivery. The animal was then transferred to MRI scanner, where the head was secured with ear pins and tooth bars. Using methods described in chapter 3, body temperature, respiration, blood pressure (BP) and blood gasses were continuously monitored throughout the MRI acquisition. At the end of each experiment, the animal was euthanized.

7.2.2 Preparation and administration of TGN-020

To assess the role of AQP4 in the function of the glymphatic system, selective AQP4 Inhibitor, 2-nicotinamido-1,3,4-thiadiazole (TGN-020) was used to block AQP4 mediated water transport. The in vitro inhibitory effects and in silico docking energies of TGN-020 with respect to AQP4 has been previously investigated by Huber et al. (2009). TGN-020 showed inhibitory activity in the in vitro with an IC50 = 3.1 Mm, furthermore, been confirmed in live animals. In silico studies using an rAQP4 M23 model identified the likely binding sites of TGN-020 as D69, M70, I73, F77, V145, I205, and R216 (Figure 7-1, purple residues), one of which is not conserved in hAQP4 (V145 is L145 in hAQP4 (Figure 7-2, white residues).

In the current study, TGN-020 (Sigma-Aldrich, St. Louis, MO) was dissolved in a solution of dimethyl sulfoxide (DMSO, Sigma-Aldrich, 10 mM) to increase its

solubility and then rapidly vortexed and maintained at 37°C until injection. The concentration of DMSO used for injection was adjusted at 0.2% in 0.9% sterile saline. TGN-020 was administered by intraperitoneal injection (200 mg/kg in 20ml/kg body weight) 15 minutes before starting the MRI study. The vehicle group also received equal volumes of vehicle solution (0.2% DMSO) intraperitoneally 15 minutes before starting the MRI. This concentration was deemed to be above the physiologically effective values, as reported by other studies (Igarashi *et al.*, 2011; Pirici *et al.*, 2017; Wei *et al.*, 2017).

7.2.3 Magnetic Resonance Imaging

The scanning protocol were carried out as stated in Chapter 6 of this thesis.

7.2.4 MRI data analysis

MATLAB R2018b (MathWorks, UK) code was developed in-house for postprocessing MRI images. The general postprocessing procedure consisted of brain extraction, head motion correction, and voxel-by voxel conversion to a percentage signal change map, as described in Chapter 3, section 3.2.

A baseline T_2 weighted image was acquired before infusion. This was subtracted from corresponding images after the infusion of $H_2^{17}O$ and the resulting difference image reflected the distribution of $H_2^{17}O$ in the observed brain. All subtracted images were divided by the baseline average image using the following expression:

$$\Delta S_\% = \frac{S_{1pre} - S_{1post}}{S_{1pre}} \times 100 \qquad (7\text{-}1)$$

where $\Delta S_\%$ is the percent signal change from the baseline (S_{1pre}).

The placement of regions of interest (ROIs) was guided anatomically by the use of T_2 weighted averaged baseline images and the Paxinos and Watson 2007 (Paxinos and Watson, 2007) histological atlas for reference. The mean values of percentage signal change in preselected anatomical areas were measured on the registered images over time. This produced temporal evolution curve of percentage signal change in every specific ROI, due to the uptake of $H_2^{17}O$ by

regional brain tissue. From each curve, the area-under-curve (AUC) during the first 85 min was calculated.

7.2.5 Evaluate the effect of pharmacological inhibition of AQP4 following a single MRI DWI experiment

To determine whether TGN-020 had a direct impact on astrocyte microstructure, Diffusion-weighted magnetic resonance imaging (DW MRI) experiment was set up before and after TGN-020 injection in a single 330 g Wistar rat. The anaesthetic protocol used was similar to that used for the main experiment. Diffusion weighted images (DWI) with long observation times (Δ=400 & 600 ms) of the whole brain were acquired, using the Stimulated echo-DWI method, before TGN-020 injection and then at 20, 40, and 60 minutes post-injection.

7.2.6 Ventricular volumes calculation

T_2 weighted MRI images were also assessed to estimate the size of the ventricular system. Ventricular volumes were estimated from T_2 weighted images. Ventricles were manually delineated for each slice. Total ventricular volumes were determined by adding the areas of all the ventricular structures on the monitored slices, multiplied by the slice thickness. To avoid differences related with the brain size, the total ventricular volume was normalized with the total brain volume of each rat analysed.

7.2.7 Statistics

Body temperature, pH, PaO_2, $PaCO_2$ and MABP were analysed using a two-way ANOVA followed by Sidak's test to correct for multiple comparisons. Mean area under the curve (mAUC) for ROIs and relative percentage signal change were analysed using unpaired, two tailed Student's t-test (GraphPad Prism Software, California, USA). Statistical significance was set at $p \leq 0.05$. All data are presented as mean $\pm$ SEM unless otherwise stated.
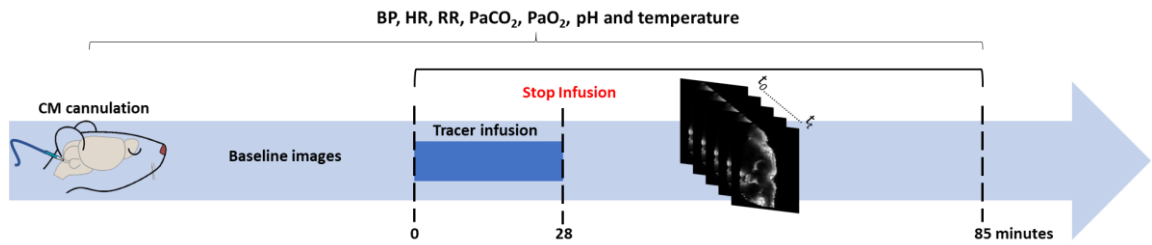
Figure 7-1. Experimental protocol. Following surgical implantation of an intracisternal cannula, the rat was placed in the supine position inside the MRI scanner and kept under anaesthesia. TGN-020 or vehicle was administered 15 minutes prior to MRI experiment. Pre-contrast baseline images were acquired. Then, during sequential acquisition of T_2 images, ~50 µL at 1.8 µL/min of 90% $H_2^{17}O$ was infused through the cannula for 28 min, and T_2 imaging continued for a total of 85 min.
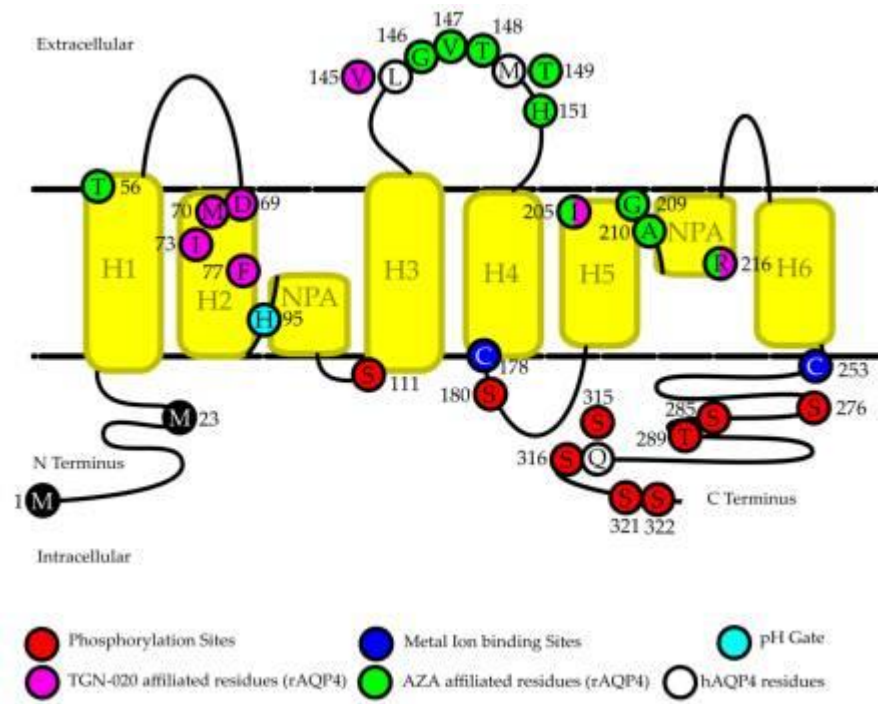
Figure 7-2. AQP4 structure and main residues in AQP4 regulation. White residues indicate the human equivalent to sites which were identified in rat AQP4 (rAQP4) as having important regulatory functions but are not conserved in human AQP4 (hAQP4). Numbering is based off of human AQP4 (Figure adapted from (Abir-Awan *et al.*, 2019)).

7.3 Result

7.3.1 Exclusion and protocol violations

Image series from 3 rats were excluded from the analysis either because of failed infusion of $H_2^{17}O$ (2 rats) or premature termination of the experiment for physiological reasons (unstable BP, one rat). Hence, a total of 13 rats were analysed for the study groups: TGN-020 treated group (n=7), and Vehicle group (n=6).

7.3.2 Effect of pharmacological inhibition of aquaporin-4 on glymphatic transport

All rats included in the analyses were physiologically stable for the duration of the scan. Body weights, physiological parameters, and statistical comparisons are summarised in Table 7-1.

To test the role of AQP4 in glymphatic inflow, TGN-020 or vehicle was administered 15 minutes prior to cisternal infusion of $H_2^{17}O$, followed by serial acquisition of high SNR T_2 weighted MR images. We first confirmed that the amount of $H_2^{17}O$ delivered into the CM was the same for both groups. Figure 7-3 show that the delivered $H_2^{17}O$ (~50 μL at 1.8 μL/min; total time, 28 min) into CSF space, via the CM, produced consistent signal changes in all rats.

Following the intracisternal infusion of $H_2^{17}O$ tracer, there was a significant overall decrease in tracer entry in rats treated with TGN-020 compared to controls. Figure 7-4 shows a time series of colour-enhanced multiple sagittal sections depicting the percentage signal change and distribution of $H_2^{17}O$ tracer in a vehicle treated rat. $H_2^{17}O$ signal was initially observed in CM followed by very rapid advancement of the signal to all brain regions (Figure 7-4). However, rats treated with TGN-020 exhibited significant reductions in gross $H_2^{17}O$ tracer distributions (Figure 7-5). In TGN-020 treated rats, $H_2^{17}O$ appeared in the ventral brain surface within 7 minutes of the start of the infusion. However, the inflow of $H_2^{17}O$ into brain parenchyma was substantially retarded. This was evident in the cortex (p=< 0.0001) and cerebellum (p=< 0.0001), with significantly reduced percentage change signal being observed in TGN-020 treated rats compared with vehicle treated rats (Figure 7-6). Exacerbated suppression of CSF tracer influx

was still observed in TGN-020 treated rats at 85 minutes after the start of the injection. However, penetration of parenchyma by $H_2^{17}O$ was not totally diminished in TGN-020 treated animals, as we think that $H_2^{17}O$ tracer could still reach the brain by passive diffusion process across astrocytes or through gap junctions, rather than through AQP4.

7.3.3 Comparison of regional $H_2^{17}O$ uptake

To calculate kinetic glymphatic parameters, the temporal evolution curve of percentage signal change was calculated from CSF and brain subregions, shown in Figure 7-6A. The analysis showed differences in regional brain uptake of $H_2^{17}O$ between the TGN-020 and the vehicle treated groups. Statistical analysis showed that regional uptake of $H_2^{17}O$ in the olfactory bulb ((p=< 0.0001), cerebellum (p=< 0.0001) and prefrontal cortex (p=< 0.0001) was statistically lower in the TGN-020 treated group than in the vehicle group. No significant difference was observed in the ventricles and pineal recess (representing subarachnoid spaces and proximal perivascular channels) of TGN-020 treated rats and vehicle rats. In parenchymal regions the maximum percentage change achieved in the TGN-020 treated group was significantly reduced compared with vehicle treated group, suggesting that a large fraction of infused $H_2^{17}O$ was prevented from penetrating the parenchyma (Figure 7-6C).

7.3.4 The effect of AQP4 inhibition observed by MRI DWI

To investigate whether the AQP4 inhibitor might affect astrocyte microstructure, long observation time diffusion MRI experiments were performed. These showed differences in the apparent diffusion coefficient before and after TGN-020 injection in the cortical region. When we measured the diffusion coefficient using longer observation time (600 ms), these changes became more apparent (Figure 7-7), suggesting microstructural changes.

7.3.5 Ventricular volumes measurements

To study the specific contribution of AQP4 to ventricular volume, the volume occupied by the CSF ventricular system was assessed in vehicle and TGN-020 rats. Ventricle size was measured from sagittal T_2 weighted images and was represented as the ratio of total ventricular volume/brain volume for all

experimental groups (Figure 7-8). As indicated in Figure 7-8, there was slight increase in the ventricle size of the TGN-020 group (not significant, p=0.6) compared with the vehicle group.

Physiological parameters		Pre-injection	Post injection
MAP (mmHg)	TGN 020	98 ± 13	95 ± 10
	Vehicle	94± 14	91 ± 11
PaO$_2$ (mmHg)	TGN 020	136.3 ± 16	149.9 ± 19
	Vehicle	157.8 ± 32	170.3 ± 40
PaCO$_2$ (mmHg)	TGN 020	35.4 ± 5.2	37.2 ± 9.2
	Vehicle	33.4 ± 9.7	24.7 ± 8.1
Temp ($C°$)	TGN 020	36.7 ± 0.5	36.9 ± 0.4
	Vehicle	36.8 ± 0.3	37.1 ± 0.2
pH	TGN 020	7.5 ± 0.04	7.5 ± 0.08
	Vehicle	7.5 ± 0.03	7.5 ± 0.3

Table 7-1. Physiological variables in rats, following tracer infusion. MAP, mean arterial pressure; PaCO$_2$, partial pressure of carbon dioxide; PaO$_2$, partial pressure of oxygen; Temp, temperature values are within physiological ranges for TGN-020 and vehicle treated groups. Significant differences denoted by P < 0.05. Data presented as mean ± SD.
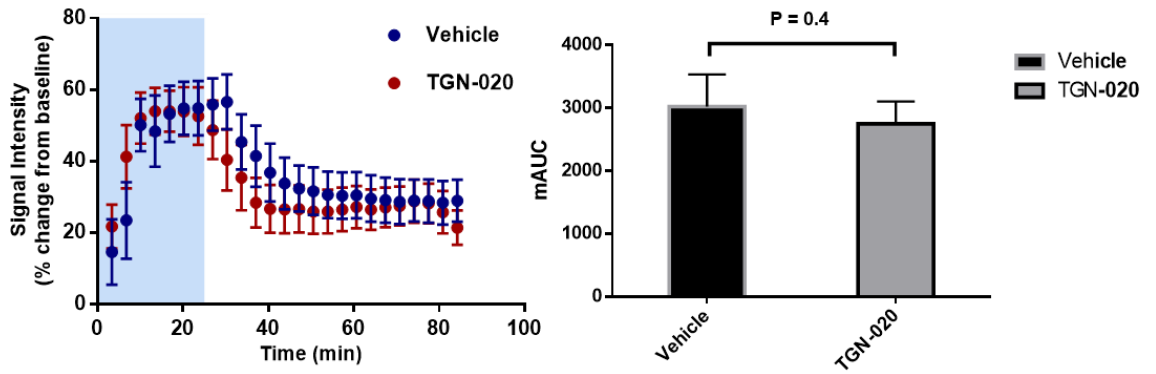
Figure 7-3. H$_2$^{17}O uptake from the cisterna magna of TGN-020 and vehicle rats.As can be observed, the temporal evolution curve of percentage signal change associated with infusion of H$_2$^{17}O into the CM of both groups are identical. By calculating the mean AUC of both curves, there was no statistical difference between the two groups (p=0.4). Data are presented as mean ± SD.
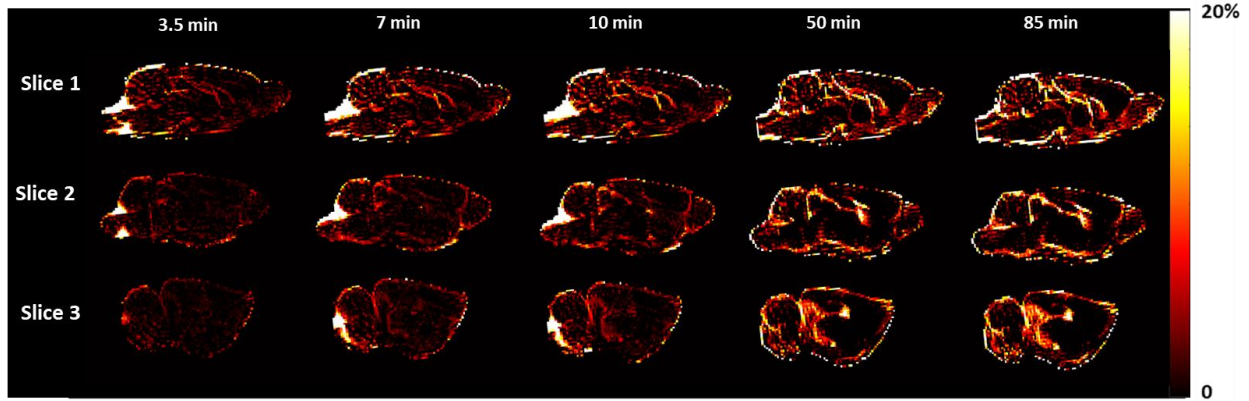
Figure 7-4. Glymphatic transport of $H_2^{17}O$ in TGN-020 rat brain by T_2 weighted.
Representative sagittal MRI (three slices) demonstrating the temporal evolution of $H_2^{17}O$ for
85 min of recording of one rat from the TGN-020 group. Pseudo colour scaling illustrates
tracer distribution of 90% $H_2^{17}O$ at different times from the onset of infusion (i.e., 3.5, 7, 10,
50 and 85 min).
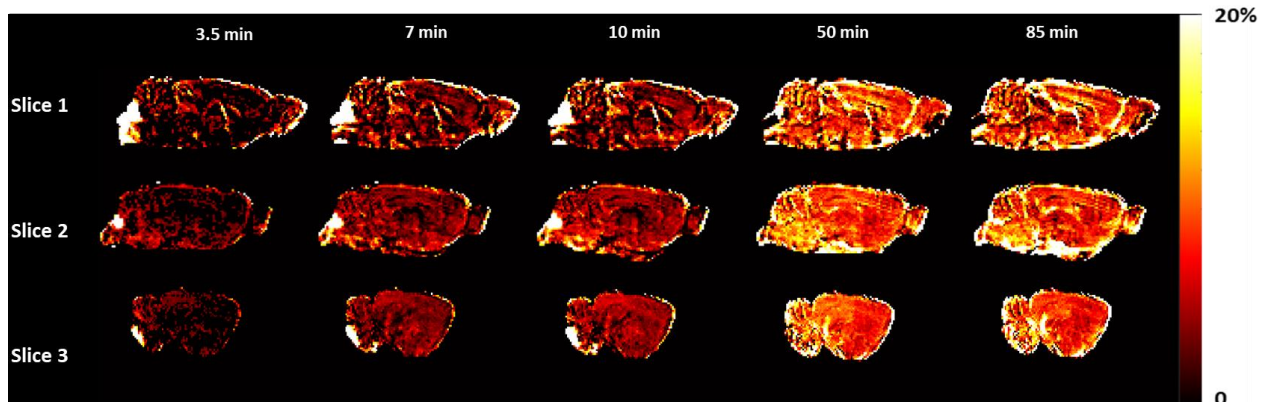
Figure 7-5. Glymphatic transport of $H_2^{17}O$ in vehicle rat brain by T_2 weighted.Representative
sagittal MRI (three slices) demonstrating the temporal evolution of $H_2^{17}O$ for 85 min of
recording obtained of one rat from the vehicle group. Pseudo colour scaling illustrates
tracer distribution of 90% $H_2^{17}O$ at different times from the onset of infusion (i.e., 3.5, 7, 10,
50 and 85 min).
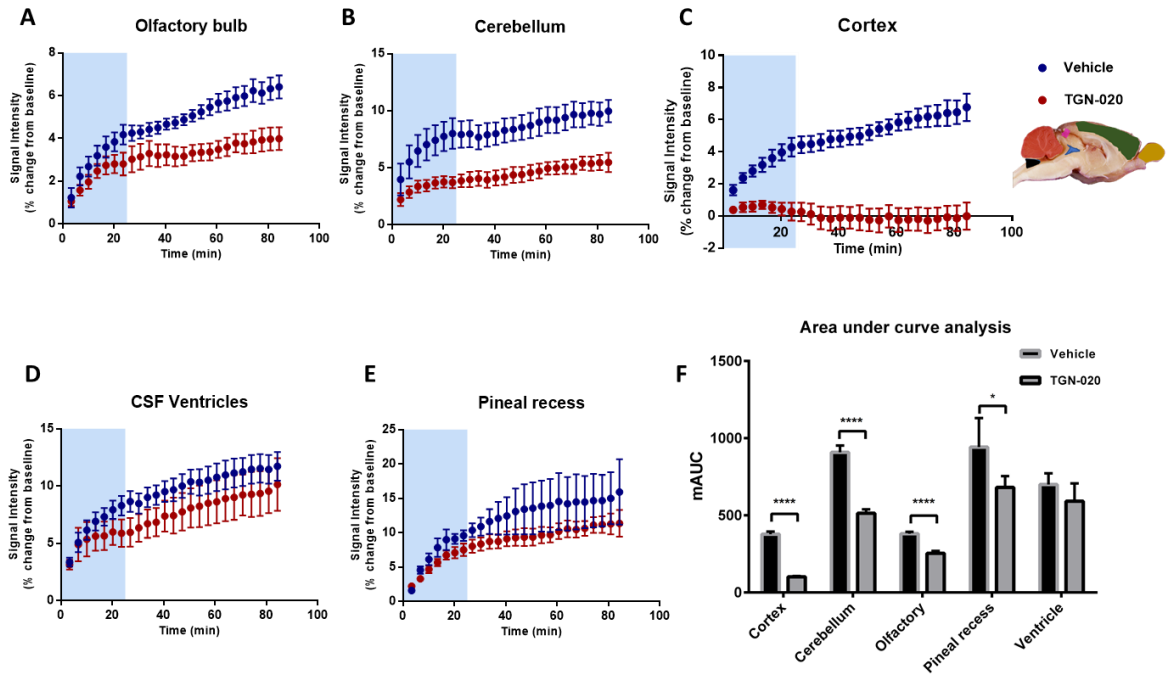
Figure 7-6. Comparisons of dynamic curves for $H_2^{17}O$ in TGN-020 and vehicle rats. the temporal evolution curve of percentage signal change for TGN-020 (red circles) and vehicle (blue circle) are shown for the (A) olfactory bulb, (B) cerebellum, (C) anterior cortex, (D) 4th ventricle, and (E) pineal recess, demonstrating significant inhibition of glymphatic inflow in three aspects of the TGN-020 treated animal brain. Blue shading denotes the infusion period. (F) shows mean AUC values (mAUC) reflecting tissue uptake, quantified from the curves in A – E. (G). Significant differences denoted by asterisks: *P < 0.05, **P < 0.01, ***P < 0.001. Data presented as mean ± SEM.
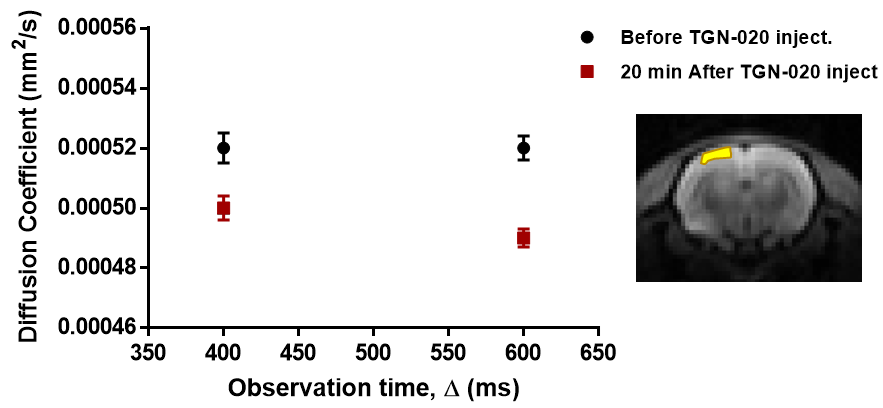
Figure 7-7. Diffusion-weighted magnetic resonance imaging in a single rat.Diffusion coefficient values are shown for two different observation times (400 & 600 ms) in the cortex region, before and after TGN-020 injection. Data presented as Diffusion coefficient values and SD of the fit.
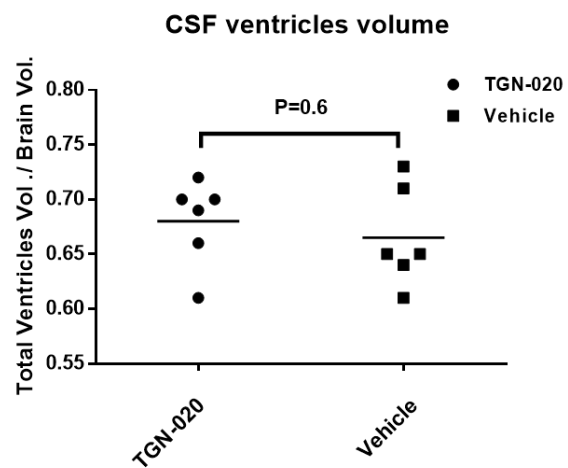
Figure 7-8. Total CSF volume.CSF in the ventricles was calculated and normalized with the total brain volume of each rat analysed (n = 6 for each group).

7.4 Discussion

We investigated the importance of the astrocytic water channel AQP4 to brain wide glymphatic transport using MRI and $H_2^{17}O$ administered into the CM of anesthetized rats. The major finding of our study is that, following AQP4 channel inhibition with a TGN-020 solution, the distribution of intracisternal $H_2^{17}O$ was significantly impaired compared to vehicle treated rats. Thus, our observations provide a strong and concordant support for the glymphatic hypothesis demonstrating that AQP4 is the dominant mechanism for perivascular influx of CSF into the parenchyma.

It has been previously demonstrated that convective flow through the glymphatic system is dependent upon the perivascular expression of AQP4 water channels (Mestre *et al.*, 2018). Original data supporting this hypothesis came from the use of AQP4 null mice, in which glymphatic function was impaired by ~70% compared to wildtype animals, resulting in a ~55% reduction in Aβ clearance from the brain (Iliff *et al.*, 2014). In the present study, we provide the first direct comparison of *in vivo* glymphatic CSF influx in AQP4 inhibitor rat. The current data demonstrated that, after the start of the injection, elevated levels of $H_2^{17}O$ were immediately detected in both vehicle and TGN-020 treated rats, particularly along the ventral surface of the brain (Figure 7-4). However, following the arrival of $H_2^{17}O$ into brain interstitium, the $H_2^{17}O$ signal change within the parenchyma of TGN-020 treated rats was significantly reduced compared with vehicle treated rats (Figure 7-6). These observations illustrate that the perivascular localization of AQP4 contributes to the kinetics of CSF water influx into the brain parenchyma. Hence, the necessity of AQP4 channels for normal glymphatic function is believed to lie in their capacity to reduce the resistance of water molecules moving from the perivascular space into the brain parenchyma (Solenov *et al.*, 2004)

Regional assessment revealed decreased $H_2^{17}O$ distribution in TGN-020 rats, which was most pronounced in brain parenchymal regions, whereas a comparable pattern of tracer distribution was observed within the subarachnoid space (SAS) in both species (Figure 7-6). By inspecting the time enhancement curve of the cortical region for both groups. $H_2^{17}O$ uptake in the TGN-020 treated cortex was significantly reduced compared to vehicle treated animals (Figure

7-6). The temporal evolution curve of the $H_2^{17}O$ uptake generated for ventricles compartments showed similar influx pattern. The $H_2^{17}O$ uptake was also observed around the region close to the middle cerebral artery. One possible explanation is that the hindrance to AQP4 function caused the infused $H_2^{17}O$ tracer to take the paths of least resistance, the large interconnecting fluid filled spaces and major periarterial spaces, as glymphatic inflow became more restricted.

Previous glymphatic data demonstrated the role of AQP4 using various approaches to AQP4 gene deletion (Iliff *et al.*, 2012; Mestre *et al.*, 2018). Here, the blocking of AQP4 was achieved by using a pharmacological inhibitor. TGN-020 has small heteroaromatic group which enables deeper penetration into the hydrophobic region of the water channel. Previous studies showed that *in vitro* treatment with TGN-020 inhibits AQP4, with a half maximal inhibitory concentration (IC50) of 3 μM, is not known to have significant biological activity (Huber, Tsujita and Nakada, 2009). There have been several reports which identified TGN-020 as a potent AQP4 inhibitor (Igarashi *et al.*, 2011; Pirici *et al.*, 2017; Debacker *et al.*, 2020; Harrison *et al.*, 2020; Oosuka *et al.*, 2020). However, It is also unclear if there are any off target effects of TGN-020 on AQP1, given 60% homology between the two (Yool *et al.*, 2013) and whether this effects CSF production and therefore potentially glymphatic function by reducing the amount of CSF in the system. However, evidence suggests that AQP1 may have a limited role in CSF production (Oshio *et al.*, 2005), and therefore any off target effects that might occur likely have a limited impact.

To understand the implications of using TGN-020 on the permeability of AQP4 and astrocyte microstructure, we conducted DW-MRI experiment in single rat. Following AQP4 channel inhibition with a TGN-020 solution, a decrease in diffusion coefficient was readily observed in the cortex, which could give an indication of more restricted water diffusion, as a result of blocking AQP4 channels (Debaker *et al.*, 2020). However, this assumption needs further confirmation by conducting DW-MRI in cohorts of animals.

It should also be noted that AQP4 is not only located within end-feet of astrocytes at the blood–brain barrier (BBB), but it is also highly expressed within ventricular ependymal cells (brain-CSF barrier) (Brinker *et al.*, 2014). It has been

reported that AQP4 deficient mice exhibit a sporadic rate of spontaneous hydrocephalus and that kaolin-induced hydrocephalus in AQP4 deficient mice results in an accelerated progression of hydrocephalus (Verkman *et al.*, 2017). To study the specific contribution of AQP4 to the ventricular volume, the volume occupied by the cerebral ventricular system was measured in both TGN-020 rats and vehicle rats. However, in the current study, while the ventricular volume in the TGN-020 group slightly increased, this increase was not significant (Figure 7-8, p=0.6).

Alterations in AQP4 expression or loss of polarization, or both, is now reported in variety of neurological disease and therefore pharmacologically manipulation of AQP4 may emerge as a viable therapeutic strategy of these conditions. In aging mice, there was a reduced parenchymal influx of CSF which found to be likely caused by reduced vascular compliance, increased AQP4 expression and AQP4 mislocalization away from the astrocytic end-feet (Pizzo *et al.*, 2018). In murine models of Alzheimer's disease, changes in AQP4 expression in astrocyte end feet could affect the clearance of beta amyloid (Aß) from the perivascular space.(Xu *et al.*, 2015). In rodent models of ischemic stroke, mice lacking AQP4 develop less pronounced cerebral oedema after stroke in a mouse model of severe permanent cerebral ischemia (Pirici *et al.*, 2017). In rodent models of traumatic brain injury (TBI), AQP4 plays a role in astrogliosis after the injury (Plog *et al.*, 2015). In models that use kaolin to induce acute hydrocephalus, AQP4 deficient mice had an accelerated progression of hydrocephalus compare with wildtype mice (Mao, Enno and Del Bigio, 2006).

7.4.1 Summary

Although previous experimental studies confirm the role of AQP4 in supporting glymphatic flow, the precise mechanisms of this role remain unresolved (Simon and Iliff, 2019; Smith and Verkman, 2019). In the current work, by tracking of labelled water, we were able to conclusively demonstrate that these glymphatic flows are strongly mediated by AQP4 as previously stated. These experiments clearly demonstrate that the rapid penetration of $H_2^{17}O$ into the parenchyma, Figure 7-5, is strongly dependent on the astrocytic water channel AQP4. We also believe that our current method represents a promising tool for not only answer much of the controversy surrounding the glymphatic hypothesis, but also provide

a valuable new tool for future investigations into associated neurological disorders.

8 Chapter 8: Conclusion

This chapter contains a summary of the studies conducted throughout the thesis. It also discusses some of the successes and limitations of each study and outlines potential avenues for future development.

8.1 Summary of the thesis

The results that I have demonstrated in this thesis are both novel and, potentially, very important for understanding the role of CSF dynamics in elevated ICP during ischaemic stroke as well as the nature of CSF-ISF dynamics. Firstly, I have demonstrated in **Chapter 4** that increased CSF outflow resistance, rather than oedema, is the primary mechanism involved in post-stroke ICP elevation. This was supported by a series of *in vivo* studies showing that ICP can become substantially elevated at 24 hours, even following small ischaemic strokes (sub-cortical lesions) where there is little or no space-occupying oedema (Tariq and Khatri, 2008; Murtha *et al.*, 2014; Murtha *et al.*, 2015; Beard *et al.*, 2015; Wells *et al.*, 2015). The current results challenge nearly a century of accepted wisdom that oedema is the sole mechanism of increased ICP after ischaemic stroke.

In the following chapters, MRI tracer methods were established to provide real-time observation of CSF flow and the glymphatic system. **In Chapter 5**, by first reproducing the experimental work in the seminal publication of Iliff et al. (2013), the spatial pattern and entry of Gd-DTPA from the CSF space into the brain tissue were demonstrated using both conventional T_1 weighted and quantitative T_1 mapping. These gadolinium-based tracers experiments represent the gold standard, which has previously been used to define CSF exchange with the brain interstitium in rodents, non-human primates, and in humans (Iliff *et al.*, 2013; Absinta *et al.*, 2017; Eide *et al.*, 2018).

In **Chapter 7**, an $H_2^{17}O$ MRI method was established to image brain-wide CSF water circulation in live rat brains. This method was also directly compared with a Gd-DTPA. The results demonstrated that CSF flow through the glymphatic system using an $H_2^{17}O$ tracer was much more rapid and extensive than when imaged using a Gd-DTPA tracer. Finally, in **Chapter 8**, the role of astrocytic

AQP4 in the CSF parenchymal flow was directly investigated for the first time. By using a selective pharmacological AQP4 inhibitor (TGN-020), the distribution of intracisternal $H_2^{17}O$ was found to be strongly dependent on the permeability of AQP4 channels. These results conclusively demonstrated the crucial role of AQP4 in the glymphatic system, as hypothesised, and will end the long running controversy surrounding this topic (Verkman *et al.*, 2013; Mestre *et al.*, 2018; Smith and Verkman, 2019).

8.2 Thesis limitation

The administration site of MRI tracers into CSF is important to consider. Large pools of CSF are found in the lateral ventricles and subarachnoid space of the brain. Access to the subarachnoid space in rodents is easiest via the cisterna magna (Iliff et al., 2012). Because of its easy access, in the current work, MRI tracers were injected via the cisterna magna. However, injection into the cisterna magna, especially when large volumes are to be administered might affect brainstem respiratory or cardiac centre function, both of which are critical to the generation of CSF pulsation (Kazmi *et al.*, 2015). Therefore, cisterna magna injections themselves may alter flow dynamics. Tracer administration into the lateral ventricle, on the other hand, requires CSF to pass through the third and fourth ventricles before reaching the subarachnoid space, so tracers injected here may take longer to reach glymphatic pathways. Iliff et al. (2012) showed that much less dye in the parenchyma at 30 minutes after injection into the lateral ventricle compared to the cisterna magna. Additionally, ventricular cannulation requires penetration of brain tissue. Even passing small cannulas through the parenchyma can cause slower glymphatic flow (Mestre, Mori and Nedergaard, 2020). This is also a concern for intraparenchymal tracer injections, which are useful for determining dye movement from a specific brain region but not for studying overall CSF circulation. Future studies could consider investigating the effect of tracer administration site on glymphatic flow.

Additional considerations for studying the glymphatic system include the sleep/wake state and anaesthetic regimen. In the current thesis, all experiments were conducted in rats anesthetized with isoflurane alone. General anaesthesia has been shown to enhance the transport of CSF tracers (e.g., Gd-DTPA). Studies

by the Nedergaard group reported CSF tracer transport was highest under ketamine/xylazine (K/X) anaesthesia and lower with α-chloralose, Avertin, or isoflurane, because of their varying effects on central adrenergic tone (Hablitz *et al.*, 2019). At least one of the effects of anaesthesia appears to be closely linked to expansion of the interstitial fluid space (Xie *et al.*, 2013), which may explain the enhanced transport of extracellular tracers. However, as the $H_2^{17}O$ tracer can more freely travel through intracellular and extracellular space, we would hypothesize that sleep or general anaesthesia may have less influence on its rate of transport. In order to address this hypothesis, future experiments are warranted to measure glymphatic system function in rodent brain using different anaesthetic regimes. It may be that water transport might be insensitive to differences in anaesthetic regimes, whereas those of a non-transported solute may be very sensitive indeed to these changes.

Studies in this thesis were subject to some limitations. Firstly, in **Chapter 4,** The model used in this study, pMCAO, result in large strokes (infarct 228 ± 36 mm^3; approximately 45% of contralateral hemisphere) and large volumes of oedema. For this reason, MCAO is described as a 'malignant' model of stroke. Oedema and infarct volumes were assessed at 24 hours post-MCAO. However, at this time point in MCAO models, the infarct and oedema are still evolving (Kazmi *et al.*, 2015). Therefore, a limitation of the current studies is that the effect on final infarct volume may have not been assessed accurately due to the use of the 24-hour time point. Future work is needed to fully examine the temporal changes in infarct and oedema evolution post ischemic stroke and investigating if the causative relationship between CSF resistance and ICP elevation still exist when oedema is fully evolved. Hence, this give further and potentially more translatable insight into the effects of CSF resistance on ICP after stroke. I was not blind to the induction of stroke and sham surgery. This means it was obvious which group was being used during CSF infusion. Further, due to the nature of the CSF-ICP experiment, using the 'gold-standard' oedema calculation, wet–dry weight method was unfeasible. So, the oedema measurements were calculated from RARE T_2-weighted images. Hence it is thought to include some error due to the manual delineation of the infarct, based on increased signal intensity. The development of a threshold for oedema volume calculations from T_2 maps would

reduce inherent inter- and intra-investigator error when using this MRI technique.

As noted in **Chapter 5**, the relatively small sample sizes may have limited the statistical power of this study. In **Chapter 6**, due to the nature of the investigation ($H_2^{17}O$ T_2 weighted vs Gd-DTPA T_1 weighted), it was impossible to be blinded to study subjects. The studies in **Chapters 7** and **8,** did not include a wash-out phase as the scan duration was only one and half hours from the commencement of infusion. The $H_2^{17}O$ method applied in this thesis used a "baseline" pre-injection scan, followed by post-injections scans, thus allowing the change in signal to be determined. However, this could be improved by using ^{17}O decoupling. The interaction between the ^{17}O quadrupolar nucleus and the bonded ^1H in water molecules, can be eliminated by irradiating at the ^{17}O resonance frequency during ^1H MR imaging. MRI data in chapter 7 and 8 did not present the dynamic images averaged across the animal group. This is because that $H_2^{17}O$ images were acquired with large voxel sizes (0.3 mm), which limits the ability to register all $H_2^{17}O$ images to the same space. Instead, we showed the MRI data for individual rats.

8.3 Future direction

How might CSF dynamics be altered following ischaemic stroke? The findings of this thesis demonstrate that increased CSF outflow resistance is responsible for ICP elevation 24 hours after ischaemic stroke. Yet, the mechanisms behind the increased CSF resistance are not understood. The main outflow route is assumed to be the arachnoid granulations as described by Dandy (1914). However, there is also compelling evidence of flow directly from the subarachnoid space to the lymphatic system (see chapter 1). Experiments carried out by Johnston's lab explored the influence of inhibiting the transport of CSF through the nasal pathway by sealing the extracranial surface of the cribriform plate of sheep (Silver *et al.*, 2002). This procedure led to significantly increased in ICP and increased CSF outflow resistance in response to fluid infusions into the ventricles. This indicates that changes in just this one pathway for CSF to leave the brain can compromise overall CSF clearance. If coupled with a stroke, could this lead to a further increase in ICP at 24 hours as CSF resistance is further increased?

Glymphatic circulation as shown in the current thesis plays a major role in enhancing CSF parenchyma flow. CSF outflow through the glymphatic pathway has been found to decline during the acute stage of ischaemic stroke. Further Gaberel et al. (2014) reported glymphatic impairment when vessel occlusion was present at 3 hours post-stroke but no impairment when vessels were spontaneously recanalized at 24 hours. Cortical spreading depressions, which can occur following excitotoxicity in stroke, may also play a role in reduced glymphatic function in tissue adjacent to the stroke by closing the perivascular spaces (Mestre *et al.*, 2020). If the glymphatic circulation is a significant outflow route for CSF, the increased CSF resistance found in our study, maybe a direct result of glymphatic dysfunction. Future work is needed to assess different CSF outflow routes and their importance in increasing ICP after ischaemic stroke. In addition, the use of $H_2^{17}O$ as a novel CSF water tracer can provide a quantitative assessment of all these different CSF outflow routes.

Many controversies and open issues exist concerning the glymphatic model. This includes the opposite directions of fluid flow, anatomical and functional differences, potential driving forces, and their role in health and disease (Carare *et al.*, 2008; Bakker *et al.*, 2016). Also, there have been several discussions on the possible mechanisms and forces by which the glymphatic system works. Three possible mechanisms have been suggested: 1) diffusion, a size-dependent random molecular walk, 2) advection or bulk flow, a molecular size-independent force produced by chemical or hydrostatic or electrical gradient, or dispersion (Diffusion + oscillating flow). Also, Smith and Verkman (2019) showed that the glymphatic system is unlikely driven by bulk flow. Their results suggest that water movement in the cranial subarachnoid space is driven by bulk flow, while that within the parenchyma is driven by diffusion (Smith and Verkman, 2019). In the current thesis, the ability of our $H_2^{17}O$ MRI method to directly image water transport *in vivo* provides an accurate means of studying glymphatic transport. Also, $H_2^{17}O$ has the advantage of considering most of the glymphatic fluid phenomena, as it can travel through the intracellular space mediated by highly selected AQP4 water channels. For this reason, it is likely that previous experimental studies and computational models based on large tracer molecules have misinterpret the glymphatic system. Hence, we do believe that our $H_2^{17}O$ data will provide a valuable tool for future computational models to accurately

predict the movement of glymphatic flow and provide some answers to several controversies and unresolved questions regarding glymphatic system.

ICP is the possible explanation for 'collateral failure' in stroke-in-progression. ICP elevation following ischaemic stroke can have severe consequences such as reduced CBF, BBB disruption and altered brain fluid movement. Further, increased ICP in the first 24 hours post-ischaemic stroke has been linked with collateral failure in a subset of ischaemic stroke patients presenting with progressive stroke. This allows the possibility that ICP elevation may be occurring undetected in a much wider range of stroke patients than is currently considered, not just in patients with large malignant strokes and significant levels of brain oedema. Future work is needed to fully investigate the temporal changes in CSF dynamics and ICP post-ischemic stroke and how they impact on temporal changes in cerebral blood flow, tissue at risk, and infarct evolution (Figure 8-1).
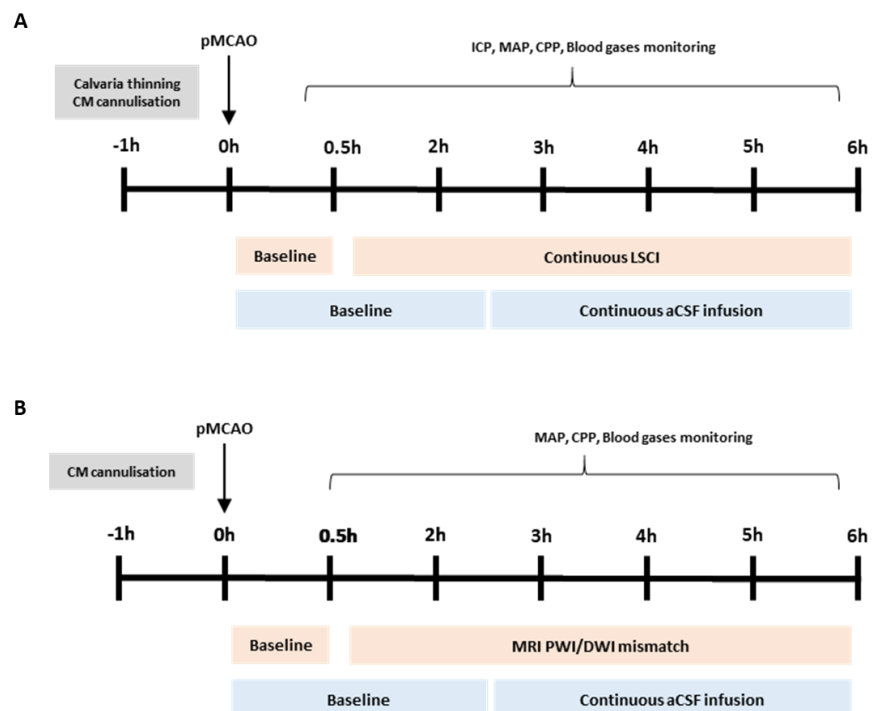
Figure 8-1. Future experimental protocols. (A) Study I aimed to determine the effect of ICP elevation on collateral flow following ischaemic stroke, using laser speckle contrast imaging (LSCI) to measure the measure perfusion changes. Baseline recordings commenced 30 minutes from the onset of stroke and continued until 6 hours post-MCAO. Once perfusion recovered, CSF was infused into the cisterna magna to artificially increase ICP. (B) Study 2 aimed to measure the effect of increased ICP on the whole brain perfusion

changes following pMCAO. After baseline MRI PWI/DWI scans, PWI/DWI was cautiously captured following pMCAO. Infusion of CSF into the cisterna magna was initiated to artificially increase ICP.

Potential H217O approaches for other neurological diseases. A) Investigation of glucose metabolism using enriched [17]O-glucose. Glucose homeostasis plays a key role in numerous fundamental aspects of life, and its dysregulation is associated with many important human diseases such as cancer. During cancer progression, tumour cells gain energy by anaerobic glycolysis (Warburg effect) and therefore have an elevated glucose turnover compared with normal tissue. At present, 2-deoxy-2-[^{18}F] fluoro-glucose (^{18}F-FDG) is the gold standard to monitor the metabolic rates of glucose. As an alternative to PET, our laboratory has developed a novel method which involves administrating highly labelled [17]O-glucose, together with dynamic[1]H-MRI which might provide a non-radioactive alternative to FDG-PET to monitor up glucose consumption during glycolysis (Figure 8-2).
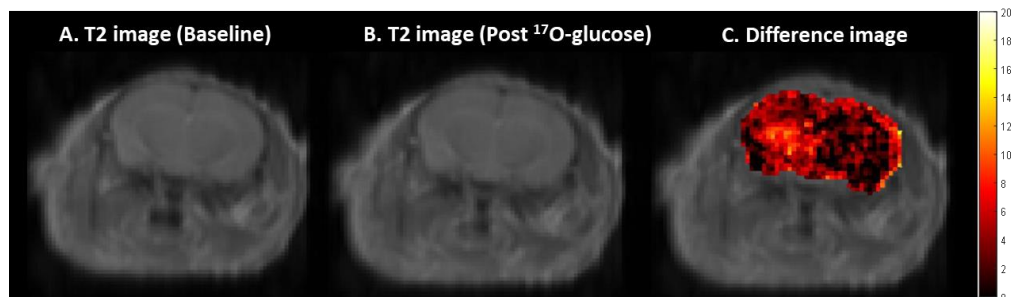
Figure 8-2. A pilot study of MRI of a GBM mouse following intravenous injection of [17]O-Glucose. A) Baseline T_2 image. B) T_2 after [17]O-Glucose infusion (5 minutes). C) Difference image (red overlay), where the signal intensity is proportional to the metabolism of [17]O-Glucose into $H_2{}^{17}O$. The tumour (Rt hemisphere) is quite visible and distinct from other surrounding tissue.

B) Metabolic assessment of cerebral ischaemia. The ability to image aerobic metabolism, which is directly related to cellular energy metabolism, is a better predictor of tissue survival following ischaemic stroke. The current gold standard for imaging aerobic metabolism is [15]O PET. This method has practical and fundamental limitations for use in the clinical stroke setting (Kameyama, Murakami and Jinzaki, 2016). Preliminary *in vivo* studies from our laboratory have suggested that tissue metabolism can be directly imaged by using the MRI

properties of the ^{17}O isotope, namely its effect on the ^{1}H signal when $^{17}O_2$ is metabolically converted to $H_2{}^{17}O$.

C) Metabolic assessment of myocardial viability. Measurements of myocardial oxygen consumption (MVO$_2$), which reflect the total oxygen demand of the myocardium, may provide an important assessment of the viability of the ischemic myocardium. ^{15}O PET has been the primary non-invasive modality for measuring MVO2 (Wong *et al.*, 2013), but its use is limited. An alternative approach based on ^{17}O, using intravenous delivery of oxygen carriers pre-saturated with $^{17}O_2$ gas and ^{17}O decoupled ^{1}H MRI, is currently being undertaken in our laboratory.

Appendices

ORIGINAL ARTICLE

Change in CSF Dynamics Responsible for ICP Elevation After Ischemic Stroke in Rats: a New Mechanism for Unexplained END?

Mohammed S. Alshuhri [1,2] · Lindsay Gallagher [1] · Christopher McCabe [1] · William M. Holmes [1]

Abstract

It has been proposed that intracranial pressure (ICP) elevation and collateral failure are responsible for unexplained early neurological deterioration (END) in stroke. The study's aims were to investigate whether cerebral spinal fluid (CSF) dynamics, rather than edema, are responsible for elevation of ICP after ischemic stroke. Permanent middle cerebral artery occlusion (pMCAO) was induced with an intraluminal filament. At 24 h after stroke, baseline ICP was measured and CSF dynamics were probed via a steady-state infusion method. Diffusion-weighted imaging (DWI) and T2-weighted magnetic resonance imaging were performed to define cerebral ischemic damage and the volume of brain swelling. We found that the pMCAO group exhibited a significant increase in CSF outflow resistance (2.27 ± 0.15 mmHg μL^{-1} min) compared with the sham group (0.93 ± 0.06 mmHg μL^{-1} min, $p = 0.002$). There was no correlation between mean ICP at 24 h post-pMCAO and edema ($r^2 = -0.03$, $p = 0.5$) or infarct volumes ($r^2 = 0.09$, $p = 0.5$). However, for the first time, we found a significant correlation between the baseline ICP at 24 h post-stroke and the value of CSF outflow resistance. Results show that CSF outflow resistance, rather than edema, was the mechanism responsible for ICP elevation following ischemic stroke. This challenges current concepts and suggests the possibility that intracranial hypertension may be occurring undetected in a much wider range of stroke patients than is currently considered to be the case. In addition, this further supports the hypothesis that unexplained early neurological deterioration is the result of elevated ICP, leading to reduced collateral flow and cerebral perfusion.

Keywords Intracranial pressure · Early neurological deterioration · Ischemic stroke · Cerebrospinal fluid · MRI

Introduction

Early neurological deterioration (END) can occur within the first 24–48 h following acute ischemic stroke, with prevalence being relatively common (> 14%), and is strongly associated with poor outcome [1]. END was defined as an increase in the National Institutes of Health Stroke Scale (NIHSS) score of >

✉ William M. Holmes
William.Holmes@glasgow.ac.uk

[1] Glasgow Experimental MRI Centre (GEMRIC), Wellcome Surgical Institute, Institute of Neuroscience and Psychology, Garscube Estate, University of Glasgow, Glasgow, Scotland G61 1QH, UK

[2] Radiology and Medical Imaging Department, College of Applied Medical Sciences, Prince Sattam bin Abdulaziz University, Kharj, Saudi Arabia

Springer

4 points within the first 24 h after admission [2]. Although some cases of END have a straightforward cause, such as symptomatic intracranial hemorrhage and malignant edema, approximately 2/3 of cases remain unexplained [3]. These unexplained END cases are associated with persistent proximal occlusion, large diffusion-perfusion mismatch, and diffusion-weighted imaging lesion growth beyond the initial ischemic penumbra [3]. Several mechanisms have been proposed, involving either compromised hemodynamics (thrombus extension [1], collateral failure [4], reduced mean arterial pressure [5]), or other tissue-based mechanisms (excitotoxicity [6], inflammation [7], hyperthermia [8], edema [9], hyperglycemia [3], and hypoxia [10]). Although these mechanisms may make some contribution, there is a lack of strong evidence associating them with END. An intriguing alternative mechanism has recently been proposed suggesting that elevated intracranial pressure (ICP), resulting in reduced collateral flow and cerebral perfusion, may be responsible for unexplained END [11]. However, the mechanism for this rise in ICP is currently unknown.

Conventionally, only patients with large malignant strokes are considered to be at risk of elevated ICP, due to space occupying vasogenic edema within the closed cranial compartment. This logic has been extended to infer that ICP does not become elevated in cases of smaller, non-malignant strokes, since there is little or no vasogenic edema. However, we can find no evidence in the clinical literature to support this broad assumption, presumably because the risks associated with invasive ICP measurement prevent its use.

This assumption is also contradicted by recent animal experiments, which show dramatic increases in ICP occurring around 24 h after stroke onset, even following small strokes where there is little or no vasogenic edema [12]. This evidence leads us to hypothesize that a mechanism, other than edema, is responsible for ICP elevation in these cases. Inspection of a mathematical model of ICP indicates that changes in the cerebral spinal fluid (CSF) dynamics may be responsible for the observed increases in ICP post-ischemic stroke [13, 14]. Therefore, in the present study, we have investigated the relationship between CSF dynamics, vasogenic edema, and ICP following experimental stroke.

Materials and Methods

Animals and Experimental Protocol

Experiments were carried out under license from the UK Home Office in accordance with the Animals (Scientific Procedures) Act, 1986, incorporating European Directive 2010/63/EU and approved by the University of Glasgow Ethical Review Panel. Male Wistar Kyoto (WKY) rats (350 to 400 g, 24 to 32 weeks old) were initially anesthetized (5% isoflurane in 20:80 O_2/air mixture) in an induction chamber, then intubated, and artificially ventilated (with 2–3% isoflurane in 20:80 O_2/air mixture at flow rate 1–2 L/min). Body temperature was monitored throughout surgery with a rectal thermocouple and maintained at 37 ± 0.5 °C. The femoral artery was cannulated with PE-50 tubing for continuous monitoring of arterial blood pressure and heart rate (Biopac Systems, MP100) and for the measurement of arterial blood gases (Bayer, Rapidlab 248). Animals were randomly allocated to either a permanent middle cerebral occlusion group (pMCAO, $n = 8$) or a sham surgery group (sham, $n = 6$).

Middle Cerebral Artery Occlusion

Permanent occlusion of the left MCA was performed by intraluminal thread occlusion, as previously described [15]. The left common carotid artery was isolated and an arteriotomy was performed to allow for the insertion of a 4-0 nylon silicone-coated tip monofilament (403934PK10 or

404134PK10 Doccol Corporation, USA) through the internal carotid artery until it blocked the origin of the MCA. The filament was left in place to induce a pMCAO. For sham group rats, surgery to reveal the MCA was carried out but the artery was not occluded. Immediately following pMCAO, rats were transferred to the MRI scanner and diffusion-weighted imaging (DWI) was conducted to assess baseline lesion volume. Rats were then recovered from the anesthesia and, 24 h after pMCAO, re-anesthetized for assessment of final infarct volume using T2-weighted MRI. The animal was then transferred into the surgery room for ICP measurements. The experimental protocol is shown schematically in Fig. 1.

Intracranial Pressure Measurement

Following MRI scanning at 24 h post-MCAO or sham surgery, rats were re-anesthetized (5% isoflurane in 20:80 O_2/air mixture) and transferred to a stereotaxic frame where the head was secured in ear and tooth bars. The coordinates (Bregma 1.3 mm posterior, 2 mm lateral) for the lateral ventricles were identified from the rat brain stereotaxic atlas (Paxinos and Watson) and, where necessary, adjusted slightly to accommodate any brain swelling identified on the T_2-weighted MRI scans. Two burr holes were drilled over the ipsilateral and contralateral lateral ventricles and, for ICP monitoring, a 25-gauge needle connected by an air-free fluid system was placed in the ipsilateral ventricle and attached to a pressure transducer for continuous ICP recording. The probe was secured to the skull with cyanoacrylate glue to avoid leakage. The correct position of the ICP probe within the ventricle was confirmed by the presence of CSF pulsation within the catheter. Prior to ICP recording, pressure transducers were calibrated with a sphygmomanometer and the ICP waveform signal was confirmed by a response to abdominal compression, ensuring clear cardiac, and respiratory waveforms were visible.

CSF Infusion

CSF dynamics were probed via a steady-state infusion method [16], involving stepwise increases in the intracerebroventricular infusion of artificial cerebrospinal fluid (aCSF) (Supplemental Fig. 1). A catheter was inserted into the contralateral lateral ventricle and secured to the skull with cyanoacrylate glue, then connected to an infusion pump (Graseby/3150 Syringe Pump). The baseline ICP pressure was monitored for 30 min before starting infusion of aCSF (aCSF: NaCl 140 mmol/L, KCl 3 mmol/L, NaH2PO4 12 mmol/L, NaHCO3 18 mmol/L, CaCl2 2.5 mmol/L, pH 7.4). The infusion rate was adjusted incrementally 1.67, 3.33, 5.00, 8.30, 11.67, 16.67, 25.00, and 33.3 μL/min, with 3–6 min allowed for a steady-state ICP to be established after each increase. During the infusion experiment, mean arterial pressure
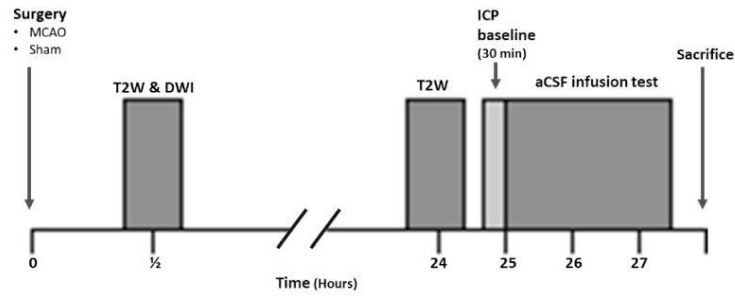
Fig. 1 Experimental protocol; immediately following pMCAO, rats underwent baseline MRI scanning for assessment of lesion volume and brain volume measurements. Rats were then recovered from anesthesia and at 24 h after MCAO, T2-weighted MRI was carried out for infarct volume and edema measurements. Following MRI scanning, rats then underwent ICP measurements

(MAP) and ICP were continuously monitored in all rats. Blood gases (pH, partial pressure of oxygen [P_aO_2], carbon dioxide [P_aCO_2]) were measured before and after the infusion.

Mathematical Modeling

Marmarou and colleagues [14] developed a mathematical model of the CSF/ICP system. Here we have extended their steady-state case to include growth in brain edema. In the closed cranial cavity, steady-state ICP exists when rates balance.

$$Q_{prod} + Q_{edema} = Q_{abs} \qquad (1)$$

where Q_{prod} is the rate of CSF production and Q_{edema} is the rate of edema growth. Assuming the rate of CSF absorption across the arachnoid villi Q_{abs} is proportional to the corresponding pressure drop $\Delta P = P_{ICP} - P_{ss}$, where the venous sagittal sinus pressure P_{ss} is small, with a CSF outflow resistance R, gives

$$P_{ICP} = R\, Q_{abs} = R\left(Q_{prod} + Q_{edema}\right) \qquad (2)$$

In the case of the steady-state infusion experiments, as the rate of infusion of aCSF is greater than ($Q_{prod} + Q_{edema}$), this becomes

$$P_{ICP} = R\, Q_{abs} \simeq R\, Q_{inf} + c \qquad (3)$$

where Q_{inf} is the rate of infusion of aCSF. It can be seen from Eq. 3 that the CSF outflow resistance is then obtained from the slope of the plot ΔP vs Q_{inf}.

Magnetic Resonance Imaging and Analysis

MRI data were acquired using a Bruker Pharmascan 7T/16 cm system (Ettlingen, Germany) with a gradient coil insert (internal diameter = 90 mm, 300 mT/m) and a four-channel phased-array surface receive coil used for brain imaging. During MRI scanning, a pilot sequence was first acquired to determine the correct geometry. A diffusion-weighted imaging (DWI) scan (4-shot, spin-echo, EPI) was performed 30 min after MCAO allowing quantitative apparent diffusion coefficient (ADC) maps to be produced (echo time [TE] = 22 ms; repetition time [TR] = 4000 ms; matrix = 96 × 96; field of view = 25 mm × 25 mm; three directions = x, y, z; B values = 0; and 1000 s/mm^2; eight coronal slices; 1.5 mm thickness). A T2-weighted (RARE) scan was performed to assess the infarct volume at 24 h (effective TE = 46.6 ms, TR = 5000 ms, RARE factor 8, averages 2, matrix 256 × 256, FOV 3.0 cm × 3.0 cm, 8 slices, 0.75 mm thickness).

Data Analysis

Quantitative ADC maps, in units of square millimeters per second, were calculated from the Stejskal-Tanner equation using Image J software (http://rsb.info. nih.gov/ij/). A 23% reduction in mean contralateral ADC was used to determine ischemia lesion volume from the multi-slice ADC maps [17] (Supplemental Fig. 2). Infarct volume was determined at 24 h from T2-weighted images by manual tracing of the hyperintense lesion area on each slice. This was then summed and multiplied by the slice thickness (Supplemental Fig. 3). The edema-corrected lesion volume (LVe) and the space-occupying effect in percent of edema uncorrected lesion volume (SE) were calculated from equations derived by Gerriets [17]:

$$LVe = HVc + HVi - (HVc + HVi - LVu) \times \frac{HVc + HVi}{2HVc} \qquad (4)$$

$$SE = LVu - LVe \qquad (5)$$

HVi and HVc refer to the volumes of the ipsilateral and contralateral hemispheres, respectively. LVu represents the

uncorrected lesion volume as delineated on the T2W images. All volumetric measurements were performed independently by two independent investigators. To examine interobserver reproducibility, investigator 2 determined infarct and edema volumes on the same images and the calculated values were compared with the results performed by investigator 1. Any cases with > 10% discrepancy was flagged for review.

Exclusion Criteria

A total of 14 Wistar Kyoto (WKY) rats were used in this series of experiments. Two animals in the MCAO group were excluded due to technical problems (CSF leaks, unstable BP, and death). Hence, 12 animals were available for data analysis (6 in each group).

Impact of aCSF Infusion on Edema Size

To ensure that infusion of aCSF does not contribute to the development of brain edema, a pilot experiment was conducted with the same infusion rates and durations used in the original experiments (experimental details are described in Supplemental Figs. 4 and 5). Serial T2 MRI revealed that there is no change in edema with aCSF infusion.

Statistical Analysis

A sample size calculation was performed using pilot data (G*Power v.3.1.3 software) [18], which estimated that six animals per group were required to detect a 60% difference in CSF outflow resistance and 12 mmHg difference in ΔICP between the sham and pMCAO groups with standard settings of alpha 0.05, power 0.8. Student t tests were performed on physiological parameters for illustrative purposes to highlight changes between pMCAO and sham rats. Mann–Whitney U tests were performed to compare mean ICP and CSF resistance values between sham and post-stroke groups. Spearman's correlation analysis was used to determine the correlation between ICP and edema volume, infarct volume and CSF resistance. For the CSF infusion test, statistical analysis was performed with the Wilcoxon signed-rank test on ICP, MAP, and cerebral perfusion pressure (CPP) to detect differences between each infusion step point and baseline values. Data are presented as mean ± standard deviation unless otherwise stated. All tests were considered statistically significant for p-values < 0.05.

Results

ICP and Physiological Variables

ICP oscillation with pulse pressure and respiration was detected in all experiments (Fig. 2a). Median ICP at baseline in the pMCAO group at 24 h (18.6 ± 5.84 mmHg) was demonstrated to be significantly greater than the sham group (6.01 ± 0.56 mmHg) ($p = 0.002$) (Fig. 2b). Physiological variables before and after infusion of aCSF are shown in Table 1. MAP was slightly lower at baseline in the pMCAO rats compared with the sham operated rats; however, this difference was not statistically significant. CPP (MAP–ICP) was significantly lower at baseline in pMCAO rats compared with the sham operated rats (65 ± 10 mmHg vs 89 ± 8 mmHg, $p = 0.049$). There were no statistically significant differences between groups for intra-operative physiological indices with the exception of P_aCO_2 (Table 1).

Edema and Infarct Volume vs ICP

Mean edema volume was 128.4 ± 19.3 mm^3 (range 100–146 mm^3) at 24 h post-MCAO (online-only Data Supplemental Fig. 2). The growth rate of edema formation (0.09 ± 0.01 μL/min) was estimated by dividing the edema volume by 1440 min (i.e., 24 h). Mean edema-corrected infarct volume was 342.5 ± 65 mm^3 (range 225–397 mm^3). There was no significant correlation between mean ICP at 24 h and infarct volume ($r^2 = 0.09$, $p = 0.5$) or edema volume ($r^2 = -0.03$, $p = 0.5$) (Fig. 3a and b).

ICP Response to aCSF Infusion

The time course for MAP, CPP, and ICP changes after aCSF infusion in both pMCAO and sham groups is shown in Fig. 4. After the start of aCSF infusion, ICP increased significantly ($p < 0.001$ for all time points) in both the pMCAO and sham groups. Figure 5a shows how the steady-state ICP changed from baseline (ΔICP) increases with increasing infusion rate. For both groups, plotting ΔICP vs infusion rate resulted in a linear relationship, in confirmation of Eq. 3. At the end of infusion, ICP dropped to the initial baseline value.

CSF Outflow Resistance

CSF outflow resistance was calculated for each animal, as in Eq. 3, from the initial slope of the ΔICP vs infusion rate plots, for infusion rates between 0 and 11.67 μL min^{-1} (Fig. 5b). The mean CSF outflow resistance measured for the pMCAO group (2.27 ± 0.15 mmHg μL^{-1} min) was significantly greater than that in the sham-operated rats (0.93 ± 0.06 mmHg μL^{-1} min) ($p = 0.002$) (Fig. 5c). A significant relationship was found between CSF outflow resistance and baseline ICP measured at 24 h, using both pMCAO and sham rats ($r^2 = 0.85$, $p < 0.0001$) (Fig. 5d).
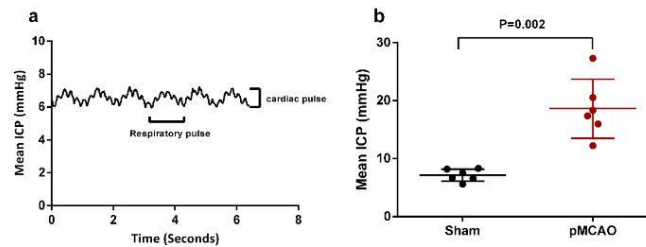
Fig. 2 (a) Example ICP recording from a rat at baseline following sham surgery. The respiratory and cardiac pulses can be clearly visualized in the oscillations of the ICP waveform. (b) Median intracranial pressure (ICP) measured at baseline, prior to infusion, in WKY rats at 24 h following sham surgery or pMCAO. Baseline ICP was significantly elevated in the pMCAO-treated rats compared with the sham group (values are median ± SD)

CSF Production Rate

Linear regression of the initial ICP vs infusion rate data to zero ICP (Fig. 5a) allowed an indirect estimation of CSF production rate, indicating no significant change in CSF production rate following stroke (1.4 ± 1.54 μL/min) compared with sham controls (1.9 ± 1.49 μL/min) ($p = 0.6$).

Discussion

It is conventionally assumed that ICP elevation post-stroke is the result of cerebral vasogenic edema within the closed cranial compartment. Consequently, only patients with large

Table 1 Physiological parameters

Physiological parameters		Pre-infusion	Post-infusion
MAP (mmHg)	Sham	95 ± 8.8	94 ± 10
	Stroke	84.4 ± 11	82 ± 17
CPP (mmHg)	Sham	89 ± 8	88 ± 7
	Stroke	$65 \pm 8*$	67 ± 7
PaO2 (mmHg)	Sham	182 ± 25	174 ± 22
	Stroke	160 ± 35	$145 \pm 32†$
PaCO2 (mmHg)	Sham	32 ± 4	36.7 ± 8
	Stroke	$36.3 \pm 6*$	52.1 ± 10
Temp (°C)	Sham	36.8 ± 0.3	36.9 ± 0.5
	Stroke	37.2 ± 0.7	37.1 ± 0.6
pH	Sham	7.64 ± 0.3	7.7 ± 0.4
	Stroke	7.43 ± 0.6	7.5 ± 0.3

Values for median MAP, PaCO2, PaO2, pH, and temperature: *MAP*, mean arterial pressure; *PaCO2*, partial pressure of carbon dioxide; *PaO2*, partial pressure of oxygen; *Temp*, temperature at 24 h following stroke or sham surgery

$*p < 0.05$ vs control; $†p < 0.05$ vs pre-infusion

malignant strokes and significant levels of brain edema are assumed to be affected by intracranial hypertension. Though this view has persisted over several decades, we can find no evidence in the clinical literature to support this broad assumption, presumably because the risks associated with invasive ICP measurements have precluded their use in the vast majority of stroke patients. Recently, this assumption has been challenged by animal experiments, which shows ICP can become substantially elevated at 24 h, even following small ischemic strokes (sub-cortical lesions) where there is little or no "space occupying" edema. Further, these previous studies found no correlation between edema volume and baseline ICP at 24 h post-stroke [12, 19]. Data from the present study support these findings and also show an absence of correlation between edema volume and baseline ICP in the pMCAO group (Fig. 3) (Spearman correlation $r = -0.03$, $p = 0.5$). However, since our power calculations were based on CSF outflow resistance pilot data, the sample size used ($n = 6$) is likely underpowered with regard to definitively determining a lack of correlation.

It has previously been proposed that increases in ICP in the first 24 h post-ischemic stroke may provide an explanation for patients suffering a progressive stroke or unexplained END [20]. The effect of increasing ICP on collateral flow has been recently demonstrated in rats, using fluorescent microspheres to quantify flow through individual pial collateral vessels [21]. This showed progressive reductions in collateral flow with stepwise increases in ICP (up to 50% reduction in flow at 30 mmHg). Consistent with these earlier studies, we found even minor increases in ICP resulted in a decrease in the critical cerebral perfusion pressure (CPP) which is the driving pressure of the cerebral blood flow in the absence of autoregulation [22]. Although CPP is regulated by both MAP and ICP, it is remarkable how little attention the ICP component has received [22, 23].

It has been suggested that any reductions in the already tenuous penumbral perfusion would be expected to impact penumbral survival, leading to late infarct expansion and
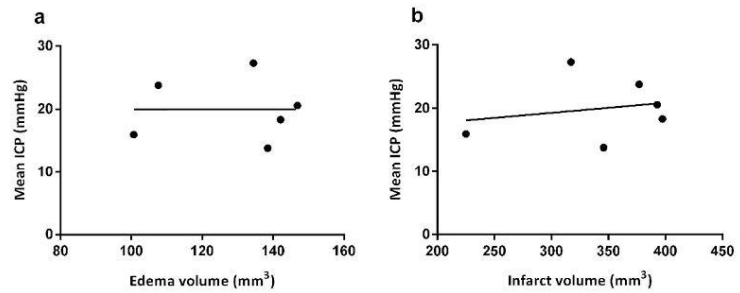
Fig. 3 Intracranial pressure (ICP) vs infarct volume and cerebral edema volume all measured 24 h after pMCAO. No significant correlation of ICP baseline prior to infusion in MCAO-treated rats, with infarct volume or edema volume was seen in this study. (a, b) Infarct volume $r^2 = 0.09$, $p = 0.5$; edema volume $r^2 = -0.03$, $p = 0.5$

END. Indeed, collateral failure has been associated with infarct growth and has been proposed as a potential mechanism of unexplained END [24]. In support of this, recent clinical imaging studies have shown infarct growth beyond the initial penumbra and the occurrence of "new DWI lesions" at day seven post-stroke, outside the initial area of hypo-perfusion [25]. In addition, there have been numerous rodent studies of both permanent and transient MCAO which have shown infarct volume expanding beyond 24 h [26, 27].

This raises the important question: if not edema, what mechanism is responsible for the substantial ICP elevations seen at 24 h post-ischemic stroke? Inspection of the steady-state model of ICP (Eq. 2) shows ICP is dependent upon CSF outflow resistance, the rate of CSF production, and the rate of edema growth. In confirmation of the mathematical model (Eq. 3), we found a linear relationship between the increase in ICP above baseline (ΔICP) and the infusion rate of aCSF (Fig. 5a) for both pMCAO and sham groups. Measured values of CSF outflow resistance for the sham group (0.93 ± 0.06 mmHg μL^{-1} min) were consistent with previous measurements for rats, which ranged from 0.5 to 1.8 mmHg μL^{-1} min [28, 29].

For the first time, we have shown that CSF outflow resistance increases significantly at 24 h post-pMCAO compared with a sham-operated group (Fig. 5c). This is more than a two-fold increase in CSF outflow resistance following ischemic

stroke and is of a similar magnitude to increases previously encountered in studies on hydrocephalic rats [30]. Further, for the first time, we found a significant correlation between the baseline ICP at 24 h post-pMCAO and the value of CSF outflow resistance (Fig. 5d).

The slow rate of CSF production is difficult to measure, with an estimate of the rate being made by extrapolating the initial ICP vs infusion data back to zero ICP. For the sham-operated group, this gave the rate of CSF production as 1.9 ± 1.49 μL/min, slightly lower than comparable data found in the literature (3.7 ± 0.1 μL/min) measured using a ventriculo-cisternal perfusion technique [31]. We found the rate of CSF production did not significantly change in the pMCAO group (1.4 ± 1.54 μL/min) compared with the sham group (1.9 ± 1.49 μL/min) ($p = 0.6$). Moreover, in the pMCAO group, the rate of edema growth (0.09 ± 0.01 μL/min) was found to be small compared with the rate of CSF production. Taken together, these results indicate the ICP elevation seen at 24 h post-pMCAO was primarily driven by increased CSF outflow resistance rather than an increased rate of CSF production or edema growth.

In all mammalian species, CSF is produced mainly by the choroid plexus located in the ventricular system. After circulating throughout the natural fluid passages of the ventricular system and subarachnoid space, CSF is returned to the vascular system via diverse outflow pathways, including arachnoid
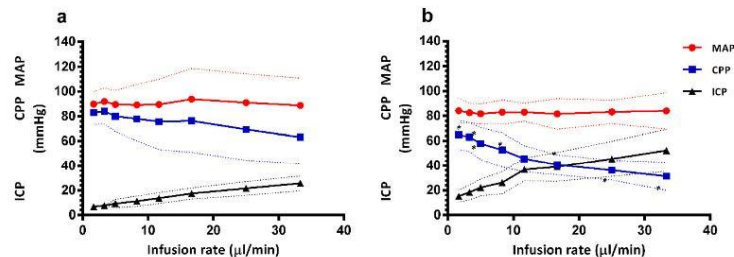
Fig. 4 Change in ICP, CPP, and MAP following stepwise infusion of aCSF into the contralateral ventricle. (a) In sham-operated rats, infusion of CSF resulted in an increase in ICP, little change in MAP and an associated decrease in CPP at higher infusion rates. (b) In rats at 24 h following pMCAO, ICP increased significantly with a marked drop in CPP (*) and no change in MAP. All data are presented as mean ± SD
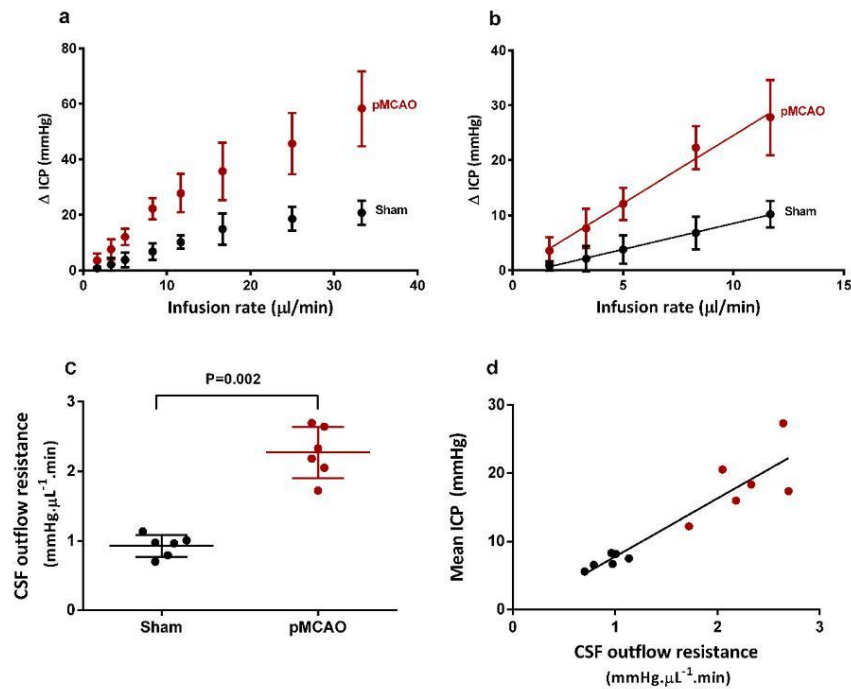
Fig. 5 (a) Scatter plot graph of the correlation between ΔICP and aCSF infusion rate in both pMCAO and sham animals. (b) Linear relation between ΔICP and low infusion rates in and sham group. (c) Individual CSF outflow resistance in pMCAO or sham animals. CSF outflow resistance in the pMCAO group was significantly greater than that of the sham group ($p = 0.002$). (d) Illustrates a significant positive correlation between CSF outflow resistances and baseline ICP ($r^2 = 0.85$, $p < 0.0001$)

granulations (villi) and along the cervical lymphatic system via the olfactory perineural space (see Supplemental Fig. 6) [32]. In addition, recent work suggests that part of the CSF is recirculated into the brain via low-resistance glymphatic pathways on the surface of the brain that facilitates CSF circulation [33]. It appears likely that the increase in CSF outflow resistance in the pMCAO group, found in this study, was the result of impairment of one or more of these CSF absorption pathways.

A progressive increase in ICP can potentially lead to increased high-velocity microvascular shunt (MVS) flow which, in turn, promotes the development of brain edema [34]. In Fig. 5a, there is evidence that the slope of the ICP vs infusion rate data changes above 11.7 μL min^{-1}. To avoid this complication, CSF resistance (i.e., the slope) was measured using only the lower infusion rate (low ICP) data, where the brain system has been least perturbed (Fig. 5b).

In summary, these are important results as they demonstrate that CSF outflow resistance, not edema, is the mechanism responsible for ICP elevation approximately 24 h

post-ischemic stroke. This suggests the possibility that intracranial hypertension may be occurring undetected in a much wider range of stroke patients than is currently considered, not just in patients with large malignant strokes and significant levels of brain edema. The results presented here, in conjunction with the work of Professor Sprat and colleagues [4, 12, 20, 21, 35] and Professor Baron [1], are consistent with the following mechanism behind unexplained END (see Supplemental Fig. 7); First, following ischemic stroke, changes in CSF dynamics, namely increased CSF outflow resistance, can result in a transient elevation of ICP at approximately 24 h from stroke onset. Second, these increases in ICP then lead to a progressive reduction in collateral flow and cerebral perfusion in the occluded arterial territory. Third, the tissue that was initially asymptomatic (outside initial ischemic core/penumbra) then becomes at risk and ultimately evolves into infarct, leading to delayed infarct expansion and END. Future work is needed to fully investigate the temporal changes in CSF dynamics and ICP post-ischemic stroke and how

they impact on temporal changes in cerebral blood flow, tissue at risk, and infarct evolution.

Compliance with Ethical Standards

Conflict of Interest The authors declare that they have no conflict of interest.

Ethical Approval All applicable international and national guidelines for the care and use of animals were followed.

References

1. Seners P, Baron JC. Revisiting 'progressive stroke': incidence, predictors, pathophysiology, and management of unexplained early neurological deterioration following acute ischemic stroke. J Neurol. 2018;265(1):216–25.
2. Seners P, Turc G, Oppenheim C, Baron J-C. Incidence, causes and predictors of neurological deterioration occurring within 24 h following acute ischaemic stroke: a systematic review with pathophysiological implications. J Neurol Neurosurg Psychiatr. 2015;86(1): 87–94 Available from: http://jnnp.bmj.com/lookup/doi/10.1136/jnnp-2014-308327.
3. Seners P, Turc G, Oppenheim C, Baron J-C. Incidence, causes and predictors of neurological deterioration occurring within 24 h following acute ischaemic stroke: a systematic review with pathophysiological implications. J Neurol Neurosurg Psychiatry. 2015;86:87–94. https://doi.org/10.1136/jnnp-2014-308327.
4. Beard DJ, Logan CL, McLeod DD, Hood RJ, Pepperall D, Murtha LA, et al. Ischemic penumbra as a trigger for intracranial pressure rise-a potential cause for collateral failure and infarct progression? J Cereb Blood Flow Metab. 2015;36(5):917–27.
5. Kjeldsen SE, Berge E. Blood pressure and early neurological deterioration in acute ischemic stroke. J Hypertens. 2015;33(10):2020–1.
6. Castillo J, Dávalos A, Noya M. Progression of ischaemic stroke and excitotoxic aminoacids. Lancet. 1997;349(9045):79–83.
7. Vila N, Castillo J, Dávalos A, Esteve A, Planas AM, Chamorro Á. Levels of anti-inflammatory cytokines and neurological worsening in acute ischemic stroke. Stroke. 2003;34(3):671–5.
8. Audebert HJ, Pellkofer TS, Wimmer ML, Haberl RL. Progression in lacunar stroke is related to elevated acute phase parameters. Eur Neurol. 2004;51(3):125–31.
9. Frank JI. Large hemispheric infarction, deterioration, and intracranial pressure. Neurology. 1995;45:1286–1290.
10. Read SJ, Hirano T, Abbott DF, Markus R, Sachinidis JI, Tochon-Danguy HJ, et al. The fate of hypoxic tissue on 18F-fluoromisonidazole positron emission tomography after ischemic stroke. Ann Neurol. 2000;48:228–35.
11. Gaberel T, Gakuba C, Goulay R, De Lizarrondo SM, Hanouz JL, Emery E, et al. Intracranial pressure and collateral blood flow. Stroke. 2012;9(1):1695–700 Available from: http://www.fluidsbarrierscns.com/content/9/1/3.
12. Murtha LA, McLeod DD, Pepperall D, McCann SK, Beard DJ, Tomkins AJ, et al. Intracranial pressure elevation after ischemic stroke in rats: cerebral edema is not the only cause, and short-duration mild hypothermia is a highly effective preventive therapy. J Cereb Blood Flow Metab. 2015;35(4):592–600. https://doi.org/10.1038/jcbfm.2014.230.
13. Mann JD, Butler AB, Rosenthal JE, Maffeo CJ, Johnson RN, Bass NH. Regulation of intracranial pressure in rat, dog, and man. Ann Neurol. 1978;3(2):156–65.
14. Marmarou A, Shulman K, Rosende RM. A nonlinear analysis of the cerebrospinal fluid system and intracranial pressure dynamics. J Neurosurg. 1978;48(3):332–44 Available from: http://www.ncbi.nlm.nih.gov/pubmed/632857.
15. Longa EZ, Weinstein PR, Carlson S, Cummins R. Reversible middle cerebral artery occlusion without craniectomy in rats. Stroke. 1989;20(1):84–91.
16. Hussey F, Schanzer B, Katzman R. A simple constant infusion manometric test for measurement of CSF absorption: II. Clinical studies. Neurology. 1970;20(June):665.
17. Gerriets T, Stolz E, Walberer M, Müller C, Kluge A, Bachmann A, et al. Noninvasive quantification of brain edema and the space-occupying effect in rat stroke models using magnetic resonance imaging. Stroke. 2004;35(2):566–71.
18. Faul F, Erdfelder E, Lang A-G, Buchner A. G*Power 3: A flexible statistical power analysis program for the social, behavioral, and biomedical sciences. Behav Res Methods. 2007;39:175–191. https://doi.org/10.3758/BF03193146.
19. Kotwica Z, Hardemark HG, Persson L. Intracranial pressure changes following middle cerebral artery occlusion in rats. Res Exp Med (Berl). 1991;191:99–104.
20. Beard DJ, Mcleod DD, Logan CL, Murtha LA, Imtiaz MS, Van Helden DF, et al. Intracranial pressure elevation reduces flow through collateral vessels and the penetrating arterioles they supply. A possible explanation for "collateral failure" and infarct expansion after ischemic stroke. J Cereb Blood Flow Metab. 2015;35(5):861–72. https://doi.org/10.1038/jcbfm.2015.2.
21. Beard DJ, Murtha LA, McLeod DD, Spratt NJ. Intracranial pressure and collateral blood flow. Stroke. 2016;47(6):1695–700.
22. Georgiadis D, Schwarz S, Baumgartner RW, et al. Influence of positive end expiratory pressure on intracranial pressure and cerebral perfusion pressure in patients with acute stroke. Stroke. 2001;32:2088-92. https://doi.org/10.1161/hs0901.095406.
23. Lewis PM, Smielewski P, Rosenfeld JV, Pickard JD, Czosnyka M. A continuous correlation between intracranial pressure and cerebral blood flow velocity reflects cerebral autoregulation impairment during intracranial pressure plateau waves. Neurocrit Care. 2014;21(3): 514–25.
24. Thanvi B, Treadwell S, Robinson T. Early neurological deterioration in acute ischaemic stroke: predictors, mechanisms and management. Postgrad Med J. 2008;84(994):412–7.
25. Alawneh JA, Jones PS, Mikkelsen IK, et al. Infarction of 'non-core-non-penumbral' tissue after stroke: multivariate modelling of clinical impact. Brain. 2011;134:1765–1776.
26. Hoehn-Berlage M, Norris DG, Kohno K, Mies G, Leibfritz D, Hossmann KA. Evolution of regional changes in apparent diffusion coefficient during focal ischemia of rat brain: the relationship of quantitative diffusion NMR imaging to reduction in cerebral blood flow and metabolic disturbances. J Cerebr Blood F Met. 1995;15: 1002–1011.
27. McGarry BL, Jokivarsi KT, Knight MJ, Grohn OHJ, Kauppinen RA. A magnetic resonance imaging protocol for stroke onset time estimation in permanent cerebral ischemia. J Vis Exp [Internet]. 2017;(127):1–6. Available from: https://www.jove.com/video/55277/a-magnetic-resonance-imaging-protocolfor-stroke-onset-time. Accessed 7 May 2018.
28. Kida S, Pantazis A, Weller RO. CSF drains directly from the sub-arachnoid space into nasal lymphatics in the rat. Anatomy,

histology and immunological significance. Neuropathol Appl Neurobiol. 1993;19(6):480–488.

29. Nagra G, Wagshul ME, Rashid S, Li J, McAllister JP, Johnston M. Elevated CSF outflow resistance associated with impaired lymphatic CSF absorption in a rat model of kaolin-induced communicating hydrocephalus. Cerebrospinal Fluid Res. 2010;7:1–8.

30. Johanson CE, Jones HC, Stopa EG, Ayala C, Duncan JA, McMillan PN. Enhanced expression of the Na-K-2 Cl cotransporter at different regions of the blood-CSF barrier in the perinatal H-Tx rat. Eur J Pediatr Surg. 2002;12:S47–49.

31. Orešković D, Klarica M. Measurement of cerebrospinal fluid formation and absorption by ventriculo-cisternal perfusion: what is really measured? Croat Med J. 2014;55(4):317–27 Available from: http://www.ncbi.nlm.nih.gov/pmc/articles/PMC4157383/.

32. Sweetman B, Linninger AA. Cerebrospinal fluid flow dynamics in the central nervous system. Ann Biomed Eng. 2011;39(1):484–96.

33. Jessen NA, Finmann Munk AS, Lundgaard I, Nedergaard M. The glymphatic system – a beginner's guide nadia. Neurochem Res. 2015;40(12):2583–99.

34. Bragin DE, Bush RC, Nemoto EM. Effect of cerebral perfusion pressure on cerebral cortical microvascular shunting at high intracranial pressure in rats. Stroke. 2013;44(1):177–81.

35. Murtha LA, Mcleod DD, Mccann SK, Pepperall D, Chung S, Levi CR, et al. Short-duration hypothermia after ischemic stroke prevents delayed intracranial pressure rise. Int J Stroke. 2014;9(5): 553–9.

List of References

Abbott, N. J. (2004) 'Evidence for bulk flow of brain interstitial fluid: Significance for physiology and pathology', *Neurochemistry International*, 45(4), pp. 545–552. doi: 10.1016/j.neuint.2003.11.006.

Abbott, N. J. *et al.* (2018) 'The role of brain barriers in fluid movement in the CNS: is there a "glymphatic" system?', *Acta Neuropathologica*. Springer Berlin Heidelberg, 135(3), pp. 387–407. doi: 10.1007/s00401-018-1812-4.

Abir-Awan, M. *et al.* (2019) 'Inhibitors of mammalian aquaporin water channels', *International Journal of Molecular Sciences*, 20(7). doi: 10.3390/ijms20071589.

Absinta, M. *et al.* (2017) 'Human and nonhuman primate meninges harbor lymphatic vessels that can be visualized noninvasively by MRI', *eLife*, 6. doi: 10.7554/eLife.29738.

Aho, K. *et al.* (1980) 'Cerebrovascular disease in the community: results of a WHO collaborative study.', *Bulletin of the World Health Organization*, 58(1), pp. 113–30. Available at: http://www.ncbi.nlm.nih.gov/pubmed/6966542.

Alawneh, J. A. *et al.* (2011) 'tissue after stroke : multivariate modelling of clinical impact'. doi: 10.1093/brain/awr100.

Alder, F. and Yu, F. C. (1951) 'On the Spin and Magnetic Moment of O17', *Physical Review*, 81(6), pp. 1067–1068. doi: 10.1103/PhysRev.81.1067.

Arai, T. *et al.* (1998) 'Measurement of Local Cerebral Blood Flow By Magnetic Resonance Imaging: In Vivo Autoradiographic Strategy Using 17O-Labeled Water', *Brain Research Bulletin*, 45(5), pp. 451–456. doi: 10.1016/S0361-9230(97)00369-9.

Arboix, A. (2014) 'Stroke of Cardioembolic Origin: What We Have Learnt in the Past 10 Years?', *Journal of Cardiology and Therapy*, 1(5), pp. 98–101. doi: 10.6051/j.issn.2309-6861.2014.01.34.

Arnold, W., Ritter, R. and Wagner, W. H. (1973) 'Quantitative Studies On The Drainage Of The Cerebrospinal Fluid Into The Lymphatic System', *Acta Oto-Laryngologica*, 76(1–6), pp. 156–161. doi: 10.3109/00016487309121494.

Asgari, M., de Zélicourt, D. and Kurtcuoglu, V. (2015) 'How astrocyte networks may contribute to cerebral metabolite clearance', *Scientific Reports*, 5(1), p. 15024. doi: 10.1038/srep15024.

Asgari, M., de Zélicourt, D. and Kurtcuoglu, V. (2016) 'Glymphatic solute transport does not require bulk flow', *Scientific Reports*, 6(1), p. 38635. doi: 10.1038/srep38635.

Audebert, H. J. *et al.* (2004) 'Progression in lacunar stroke is related to elevated acute phase parameters', *European Neurology*, 51(3), pp. 125–131. doi: 10.1159/000077012.

Badaut, J. *et al.* (2011) 'Brain water mobility decreases after astrocytic aquaporin-4 inhibition using RNA interference', *Journal of Cerebral Blood Flow and Metabolism*, 31(3), pp. 819–831. doi: 10.1038/jcbfm.2010.163.

Bakker, E. N. T. P. *et al.* (2016) 'Lymphatic Clearance of the Brain: Perivascular, Paravascular and Significance for Neurodegenerative Diseases', *Cellular and Molecular Neurobiology*. Springer US, 36(2), pp. 181–194. doi: 10.1007/s10571-015-0273-8.

Basser, P. J., Mattiello, J. and LeBihan, D. (1994) 'MR diffusion tensor spectroscopy and imaging', *Biophysical Journal*, 66(1), pp. 259–267. doi: 10.1016/S0006-3495(94)80775-1.

Battal, B. *et al.* (2011) 'Cerebrospinal fluid flow imaging by using phase-contrast MR technique', *British Journal of Radiology*, 84(1004), pp. 758–765. doi: 10.1259/bjr/66206791.

Beard, D. J., Mcleod, D. D., *et al.* (2015) 'Intracranial pressure elevation reduces flow through collateral vessels and the penetrating arterioles they supply. A possible explanation for "collateral failure" and infarct expansion after ischemic stroke', *Journal of Cerebral Blood Flow and Metabolism*. Nature Publishing Group, 35(5), pp. 861–872. doi: 10.1038/jcbfm.2015.2.

Beard, D. J., Logan, C. L., *et al.* (2015) 'Ischemic penumbra as a trigger for intracranial pressure rise-A potential cause for collateral failure and infarct progression?', *Journal of Cerebral Blood Flow and Metabolism*, 36(5), pp. 917–927. doi: 10.1177/0271678X15625578.

Beard, D. J. *et al.* (2016) 'Intracranial Pressure and Collateral Blood Flow', *Stroke*, 47(6), pp. 1695–1700. doi: 10.1161/STROKEAHA.115.011147.

Bering, E. A. (1952) 'Water Exchange of Central Nervous System and Cerebrospinal Fluid', *Journal of Neurosurgery*, 9(3), pp. 275–287. doi: 10.3171/jns.1952.9.3.0275.

BERING, E. A. (1959) 'Cerebrospinal fluid production and its relationship to cerebral metabolism and cerebral blood flow.', *The American journal of physiology*, 197(6), pp. 825–828. doi: 10.1152/ajplegacy.1959.197.4.825.

Bering, E. A. and Sato, O. (2009) 'Hydrocephalus: Changes in Formation and Absorption of Cerebrospinal Fluid Within the Cerebral Ventricles', *Journal of Neurosurgery*, 20(12), pp. 1050–1063. doi: 10.3171/jns.1963.20.12.1050.

Borowiak, R. *et al.* (2017) 'Initial investigation of glucose metabolism in mouse brain using enriched 17 O-glucose and dynamic 17 O-MRS', *NMR in Biomedicine*,

30(8), p. e3724. doi: 10.1002/nbm.3724.

Bothwell, S. W., Janigro, D. and Patabendige, A. (2019) 'Cerebrospinal fluid dynamics and intracranial pressure elevation in neurological diseases', *Fluids and Barriers of the CNS*. BioMed Central, 16(1), pp. 1–18. doi: 10.1186/s12987-019-0129-6.

Bradbury, M. W. and Kleeman, C. R. (1967) 'Stability of the potassium content of cerebrospinal fluid and brain.', *The American journal of physiology*, 213(2), pp. 519–528. doi: 10.1152/ajplegacy.1967.213.2.519.

Bradley, W. G. (2015) 'CSF Flow in the Brain in the Context of Normal Pressure Hydrocephalus', *AJNR. American journal of neuroradiology*, 36(5), pp. 831–838. doi: 10.3174/ajnr.A4124.

Bragin, D. E., Bush, R. C. and Nemoto, E. M. (2013) 'Effect of cerebral perfusion pressure on cerebral cortical microvascular shunting at high intracranial pressure in rats', *Stroke*, 44(1), pp. 177–181. doi: 10.1161/STROKEAHA.112.668293.

Brinker, T. *et al.* (2014) 'A new look at cerebrospinal fluid circulation', *Fluids and Barriers of the CNS*, 11(1), p. 10. doi: 10.1186/2045-8118-11-10.

Brugieres, P. *et al.* (2000) 'CSF flow measurement in syringomyelia', *American Journal of Neuroradiology*, 21(10), pp. 1785–1792.

Bryant, D. J. *et al.* (1984) 'Measurement of Flow with NMR Imaging Using a Gradient Pulse and Phase Difference Technique', *Journal of Computer Assisted Tomography*, 8(4). Available at: https://journals.lww.com/jcat/Fulltext/1984/08000/Measurement_of_Flow_with_NMR_Imaging_Using_a.2.aspx.

Bueno, D. and Garcia-Fernàndez, J. (2016) 'Evolutionary development of embryonic cerebrospinal fluid composition and regulation: An open research field with implications for brain development and function', *Fluids and Barriers of the CNS*. BioMed Central, 13(1), pp. 1–12. doi: 10.1186/s12987-016-0029-y.

Bulat, M., Lupret, V., *et al.* (2008) 'Transventricular and transpial absorption of cerebrospinal fluid into cerebral microvessels.', *Collegium antropologicum*, 32 Suppl 1, pp. 43–50. Available at: http://www.ncbi.nlm.nih.gov/pubmed/18405057.

Bulat, M., Klarica, M., *et al.* (2008) 'Transventricular and transpial absorption of cerebrospinal fluid into cerebral microvessels', *Collegium Antropologicum*, 32(SUPPL. 1), pp. 43–50.

Callaghan, P. T. (1993) *Principles of Nuclear Magnetic Resonance Microscopy*. Clarendon Press (Oxford science publications). Available at: https://books.google.co.uk/books?id=yjrjT_W5hygC.

Campbell, B. C. V. *et al.* (2013) 'Failure of collateral blood flow is associated with infarct growth in ischemic stroke', *Journal of Cerebral Blood Flow and Metabolism*, 33(8), pp. 1168–1172. doi: 10.1038/jcbfm.2013.77.

Caplan, L. R. (1991) 'Treatment of "progressive" stroke.', *Stroke*, 22(5), pp. 694–695. doi: 10.1161/01.STR.22.5.694.

Carare, R. O. *et al.* (2008) 'Solutes, but not cells, drain from the brain parenchyma along basement membranes of capillaries and arteries: Significance for cerebral amyloid angiopathy and neuroimmunology', *Neuropathology and Applied Neurobiology*, 34(2), pp. 131–144. doi: 10.1111/j.1365-2990.2007.00926.x.

Casellas, J. (2011) 'Inbred mouse strains and genetic stability: a review', *animal*, 5(1), pp. 1–7. doi: 10.1017/S1751731110001667.

Castillo, J., Dávalos, A. and Noya, M. (1997) 'Progression of ischaemic stroke and excitotoxic aminoacids', *Lancet*, 349(9045), pp. 79–83. doi: 10.1016/S0140-6736(96)04453-4.

Cenci, M. A., Whishaw, I. Q. and Schallert, T. (2002) 'Animal models of neurological deficits: How relevant is the rat?', *Nature Reviews Neuroscience*, 3(7), pp. 574–579. doi: 10.1038/nrn877.

Cercignani, M., Dowell, N. G. and Tofts, P. S. (2018) *Quantitative MRI of the Brain: Principles of Physical Measurement, Second edition*. CRC Press (Series in Medical Physics and Biomedical Engineering). Available at: https://books.google.co.uk/books?id=1dArDwAAQBAJ.

Cohen, H. and Davies, S. (1937) 'The Development of the Cerebrospinal Fluid Spaces and Choroid Plexuses in the Chick.', *Journal of anatomy*, 72(Pt 1), pp. 23–53.

Cserr, H. F., Cooper, D. N. and Milhorat, T. H. (1977) 'Flow of cerebral interstitial fluid as indicated by the removal of extracellular markers from rat caudate nucleus', *Experimental Eye Research*, 25, pp. 461–473. doi: 10.1016/S0014-4835(77)80041-9.

Cserr, H. F. and Ostrach, L. H. (1974) 'Bulk flow of interstitial fluid after intracranial injection of Blue Dextran 2000', *Experimental Neurology*, 45(1), pp. 50–60. doi: 10.1016/0014-4886(74)90099-5.

Dandy, W. and Blackfan, K. (1914) 'AN EXPERIMENTAL, CLINICAL AND PATHOLOGICAL STUDY: Part 1.—Experimental Studies', *American Journal of Diseases of Children*, VIII(6), pp. 406–482. doi: 10.1001/archpedi.1914.02180010416002.

Davis, M. A., Kazmi, S. M. S. and Dunn, A. K. (2014) 'Imaging depth and multiple scattering in laser speckle contrast imaging', *Journal of Biomedical Optics*,

19(8), p. 086001. doi: 10.1117/1.jbo.19.8.086001.

Davson, H. (1969) 'The Cerebrospinal Fluid', in Lajtha, A. (ed.) *Handbook of Neurochemistry: Volume II: Structural Neurochemistry*. Boston, MA: Springer US, pp. 23–48. doi: 10.1007/978-1-4899-7321-4_3.

Davson, H., Domer, F. R. and Hollingsworth, J. R. (1973) 'The mechanism of drainage of the cerebrospinal fluid', *Brain*, 96(2), pp. 329–336. doi: 10.1093/brain/96.2.329.

Davson, H., Domer, F. R. and Holungsworth, J. R. (1973) 'THE MECHANISM OF DRAINAGE OF THE CEREBROSPINAL FLUID As there is a continuous production of cerebrospinal fluid (CSF) primarily by the choroid plexuses of the cerebral ventricles , there must be a drainage mechanism by which this fluid is returned to th', pp. 329–336.

Debacker, C. *et al.* (2020) 'Diffusion MRI reveals in vivo and non-invasively changes in astrocyte function induced by an aquaporin-4 inhibitor.', *PloS one*, 15(5), p. e0229702. doi: 10.1371/journal.pone.0229702.

Debaker, C. S. *et al.* (2020) 'Diffusion MRI reveals in vivo and non-invasively changes in astrocyte function induced by an aquaporin-4 inhibitor', *bioRxiv*, p. 2020.02.13.947291. doi: 10.1101/2020.02.13.947291.

Demiral, Ş. B. *et al.* (2019) 'Apparent diffusion coefficient changes in human brain during sleep – Does it inform on the existence of a glymphatic system?', *NeuroImage*, 185, pp. 263–273. doi: 10.1016/j.neuroimage.2018.10.043.

Derugin, N. *et al.* (2000) 'Evolution of brain injury after transient middle cerebral artery occlusion in neonatal rats', *Stroke*, 31(7), pp. 1752–1761. doi: 10.1161/01.STR.31.7.1752.

Van Dijk, K. R. A., Sabuncu, M. R. and Buckner, R. L. (2012) 'The influence of head motion on intrinsic functional connectivity MRI', *NeuroImage*, 59(1), pp. 431–438. doi: 10.1016/j.neuroimage.2011.07.044.

Eide, P. K. *et al.* (2018a) 'Magnetic resonance imaging provides evidence of glymphatic drainage from human brain to cervical lymph nodes', *Scientific Reports*. Springer US, 8(1), pp. 1–10. doi: 10.1038/s41598-018-25666-4.

Eide, P. K. *et al.* (2018b) 'Magnetic resonance imaging provides evidence of glymphatic drainage from human brain to cervical lymph nodes', *Scientific Reports*, 8(1), p. 7194. doi: 10.1038/s41598-018-25666-4.

Ekstedt, J. (1977) 'CSF hydrodynamic studies in man. 1. Method of constant pressure CSF infusion.', *Journal of neurology, neurosurgery, and psychiatry*, 40(2), pp. 105–119. doi: 10.1136/jnnp.40.2.105.

Ekstedt, J. a N. (1978) 'CSF hydrodynamic studies in man', *Journal of Neurology,*

and Psychiatry, 41, pp. 345–353.

Elster, A. D. (1994) *Questions and Answers in Magnetic Resonance Imaging*. Mosby. Available at: https://books.google.co.uk/books?id=4nlxQgAACAAJ.

Ennis, S. R. and Keep, R. F. (2006) 'The effects of cerebral ischemia on the rat choroid plexus', *Journal of Cerebral Blood Flow and Metabolism*, 26(5), pp. 675–683. doi: 10.1038/sj.jcbfm.9600224.

Erdfelder, E. (2007) 'G * Power 3 : A flexible statistical power analysis program for the social , behavioral , and biomedical sciences', 39(2), pp. 175–191.

Florey, C. D. (1993) 'Sample size for beginners.', *BMJ*, 306(6886), pp. 1181–1184. doi: 10.1136/bmj.306.6886.1181.

Frank, J. I. and Frank, J. I. (2011) 'pressure Large hemispheric infarction , deterioration , and intracranial pressure', (July).

Fraser, C. and Plant, G. T. (2011) 'The syndrome of pseudotumour cerebri and idiopathic intracranial hypertension', *Current Opinion in Neurology*, 24(1), pp. 12–17. doi: 10.1097/WCO.0b013e328341f94a.

Fujii, M. *et al.* (2013) 'Early Brain Injury, an Evolving Frontier in Subarachnoid Hemorrhage Research', *Translational Stroke Research*, 4(4), pp. 432–446. doi: 10.1007/s12975-013-0257-2.

Gaberel, T. *et al.* (2012) 'Intracranial Pressure and Collateral Blood Flow', *Stroke*. BioMed Central Ltd, 9(1), pp. 1695–1700. doi: 10.1161/STROKEAHA.115.011147.

Gaberel, T. *et al.* (2014) 'Impaired glymphatic perfusion after strokes revealed by contrast-enhanced MRI: A new target for fibrinolysis?', *Stroke*, 45(10), pp. 3092–3096. doi: 10.1161/STROKEAHA.114.006617.

Georgiadis, D. *et al.* (2015) 'Influence of Positive End-Expiratory Pressure on Intracranial Pressure and Cerebral Perfusion Pressure in Patients With Acute Stroke', pp. 2088–2093.

Gerriets, T. *et al.* (2004) 'Noninvasive Quantification of Brain Edema and the Space-Occupying Effect in Rat Stroke Models Using Magnetic Resonance Imaging', *Stroke*, 35(2), pp. 566–571. doi: 10.1161/01.STR.0000113692.38574.57.

GIAUQUE, W. F. and JOHNSTON, H. L. (1929) 'An Isotope of Oxygen of Mass 17 in the Earth's Atmosphere', *Nature*, 123(3109), p. 831. doi: 10.1038/123831a0.

Go, A. S. (2009) 'The ACTIVE Pursuit of Stroke Prevention in Patients with Atrial Fibrillation', *New England Journal of Medicine*, 360(20), pp. 2127–2129. doi: 10.1056/NEJMe0902676.

Gomez, D. G. *et al.* (1983) 'The arachnoid granulations of the newborn human: An ultrastructural study', *International Journal of Developmental Neuroscience*, 1(2), pp. 139–146. doi: 10.1016/0736-5748(83)90040-0.

Goudie, C., Burr, J. and Blaikie, A. (2018) 'Incidence of idiopathic intracranial hypertension in Fife', *Scottish Medical Journal*. doi: 10.1177/0036933018809727.

de Graaf, R. A. *et al.* (2008) 'Natural abundance 17O NMR spectroscopy of rat brain in vivo', *Journal of Magnetic Resonance*, 193(1), pp. 63–67. doi: 10.1016/j.jmr.2008.04.019.

Greitz, D., Franck, A. and Nordell, B. (1993) 'On the pulsatile nature of intracranial and spinal CSF-circulation demonstrated by MR imaging', *Acta Radiologica*, 34(4), pp. 321–328. doi: 10.1177/028418519303400403.

Haase, A. *et al.* (1986) 'FLASH imaging. Rapid NMR imaging using low flip-angle pulses', *Journal of Magnetic Resonance (1969)*, 67(2), pp. 258–266. doi: 10.1016/0022-2364(86)90433-6.

Hablitz, L. M. *et al.* (2019) 'Increased glymphatic influx is correlated with high EEG delta power and low heart rate in mice under anesthesia', *Science Advances*, 5(2). doi: 10.1126/sciadv.aav5447.

Hahn, E. L. (1950) 'Spin Echoes', *Physical Review*, 80(4), pp. 580–594. doi: 10.1103/PhysRev.80.580.

Hammock, M. K. and Milhorat, T. H. (1973) 'Recent studies on the formation of cerebrospinal fluid', *Dev Med Child Neurol Suppl*, (1914), pp. 27–34. Available at: http://www.ncbi.nlm.nih.gov/pubmed/4359384.

Harrison, I. F. *et al.* (2018) 'Non-1 invasive imaging of CSF-mediated brain clearance pathways via assessment of perivascular fluid movement with diffusion tensor MRI', *eLife*, 7, pp. 1–14. doi: 10.7554/eLife.34028.

Harrison, I. F. *et al.* (2020) 'Impaired glymphatic function and clearance of tau in an Alzheimer's disease model', *Brain*, 143(8), pp. 2576–2593. doi: 10.1093/brain/awaa179.

Hassin, G. B. (1924) 'Notes on the nature and origin of the cerebrospinal fluid', *Journal of Nervous and Mental Disease*, pp. 113–121. doi: 10.1097/00005053-192402000-00001.

Hassin, G. B. (1948) 'The Morphology of the Pial Blood Vessels and its Bearing on the Formation and Absorption of the Cerebrospinal Fluid*', *Journal of Neuropathology & Experimental Neurology*, 7(4), pp. 432–438. doi: 10.1097/00005072-194810000-00005.

Vander Heiden, M. G., Cantley, L. C. and Thompson, C. B. (2009) 'Understanding the Warburg Effect: The Metabolic Requirements of Cell Proliferation', *Science*,

324(5930), pp. 1029–1033. doi: 10.1126/science.1160809.

Herscovitch, P., Mintun, M. A. and Raichle, M. E. (1985) 'Brain oxygen utilization measured with oxygen-15 radiotracers and Positron emission tomography: Generation of metabolic images', *Journal of Nuclear Medicine*, 26(4), pp. 416–417.

Hladky, S. B. and Barrand, M. A. (2014) 'Mechanisms of fluid movement into, through and out of the brain: Evaluation of the evidence', *Fluids and Barriers of the CNS*, 11(1), pp. 1–32. doi: 10.1186/2045-8118-11-26.

Holter, K. E. *et al.* (2017) 'Interstitial solute transport in 3D reconstructed neuropil occurs by diffusion rather than bulk flow', *Proceedings of the National Academy of Sciences*, 114(37), pp. 9894–9899. doi: 10.1073/pnas.1706942114.

Hsu, C.-Y. *et al.* (2015) 'Perfusion-diffusion Mismatch Predicts Early Neurological Deterioration in Anterior Circulation Infarction without Thrombolysis', *Current Neurovascular Research*, 12(3), pp. 277–282. doi: 10.2174/1567202612666150605122536.

Huber, V. J. *et al.* (2018) 'Aquaporin-4 facilitator TGN-073 promotes interstitial fluid circulation within the blood–brain barrier', *NeuroReport*, 29(9), pp. 697–703. doi: 10.1097/WNR.0000000000000990.

Huber, V. J., Tsujita, M. and Nakada, T. (2009) 'Identification of Aquaporin 4 inhibitors using in vitro and in silico methods', *Bioorganic & Medicinal Chemistry*, 17(1), pp. 411–417. doi: 10.1016/j.bmc.2007.12.040.

Hunter, A. J., Green, A. R. and Cross, A. J. (1995) 'Animal models of acute ischaemic stroke: can they predict clinically successful neuroprotective drugs?', *Trends in Pharmacological Sciences*, 16(4), pp. 123–128. doi: 10.1016/S0165-6147(00)88999-3.

Hussey, F., Schanzer, B. and Katzman, R. (1970) 'A simple constant infusion manometric test for measurement of CSF absorption: II. Clinical studies', *Neurology*, 20(July), p. 665.

Igarashi, H. *et al.* (2011) 'Pretreatment with a novel aquaporin 4 inhibitor, TGN-020, significantly reduces ischemic cerebral edema', *Neurological Sciences*, 32(1), pp. 113–116. doi: 10.1007/s10072-010-0431-1.

Igarashi, H., Tsujita, M., Suzuki, Y., *et al.* (2013) 'Inhibition of aquaporin-4 significantly increases regional cerebral blood flow', *NeuroReport*, 24(6), pp. 324–328. doi: 10.1097/WNR.0b013e32835fc827.

Igarashi, H., Tsujita, M., Kwee, I. L., *et al.* (2013) 'Water influx into cerebrospinal fluid is primarily controlled by aquaporin-4, not by aquaporin-1', *NeuroReport*, p. 1. doi: 10.1097/WNR.0000000000000042.

Igarashi, H., Tsujita, M., *et al.* (2014) 'Water influx into cerebrospinal fluid is primarily controlled by aquaporin-4, not by aquaporin-1: 17O JJVCPE MRI study in knockout mice', *NeuroReport*, 25(1), pp. 39–43. doi: 10.1097/WNR.0000000000000042.

Igarashi, H., Suzuki, Y., *et al.* (2014) 'Water influx into cerebrospinal fluid is significantly reduced in senile plaque bearing transgenic mice, supporting beta-amyloid clearance hypothesis of Alzheimer's disease', *Neurological Research*, 36(12), pp. 1094–1098. doi: 10.1179/1743132814Y.0000000434.

Iliff *et al.* (2012) 'A Paravascular Pathway Facilitates CSF Flow Through the Brain Parenchyma and the Clearance of Interstitial Solutes, Including Amyloid', *Science Translational Medicine*, 4(147), pp. 147ra111-147ra111. doi: 10.1126/scitranslmed.3003748.

Iliff, J. J. *et al.* (2012) 'A Paravascular Pathway Facilitates CSF Flow Through the Brain Parenchyma and the Clearance of Interstitial Solutes, Including Amyloid', *Science Translational Medicine*, 4(147), pp. 147ra111-147ra111. doi: 10.1126/scitranslmed.3003748.

Iliff, Jeffrey J., Wang, M., *et al.* (2012) 'A paravascular pathway facilitates CSF flow through the brain parenchyma and the clearance of interstitial solutes, including amyloid ß', *Science Translational Medicine*, 4(147). doi: 10.1126/scitranslmed.3003748.

Iliff, Jeffrey J., Chen, M. J., *et al.* (2012) 'A Paravascular Pathway Facilitates CSF Flow Through the Brain Parenchyma and the Clearance of Interstitial Solutes, Including Amyloid ß', *Science Translational Medicine*, 4(147), pp. 147ra111 LP-147ra111. doi: 10.1126/scitranslmed.3003748.

Iliff, Jeffrey J., Lee, H., *et al.* (2013a) 'Brain-wide pathway for waste clearance captured by contrast-enhanced MRI', *Journal of Clinical Investigation*, 123(3), pp. 1299–1309. doi: 10.1172/JCI67677.

Iliff, Jeffrey J., Lee, H., *et al.* (2013b) 'Brain-wide pathway for waste clearance captured by contrast-enhanced MRI', *Journal of Clinical Investigation*, 123(3), pp. 1299–1309. doi: 10.1172/JCI67677.

Iliff, Jeffrey J, Nedergaard, M., *et al.* (2013) 'Brain-wide pathway for waste clearance captured by contrast-enhanced MRI Find the latest version : Technical advance Brain-wide pathway for waste clearance captured by contrast-enhanced MRI', 123(3), pp. 1299–1309. doi: 10.1172/JCI67677.2-photon.

Iliff, J. J., Wang, M., *et al.* (2013a) 'Cerebral Arterial Pulsation Drives Paravascular CSF-Interstitial Fluid Exchange in the Murine Brain', *Journal of Neuroscience*, 33(46), pp. 18190–18199. doi: 10.1523/JNEUROSCI.1592-13.2013.

Iliff, J. J., Wang, M., *et al.* (2013b) 'Cerebral Arterial Pulsation Drives Paravascular CSF-Interstitial Fluid Exchange in the Murine Brain', *Journal of Neuroscience*, 33(46), pp. 18190–18199. doi: 10.1523/JNEUROSCI.1592-13.2013.

Iliff, Jeffrey J, Wang, M., *et al.* (2013) 'NIH Public Access', 4(147). doi: 10.1126/scitranslmed.3003748.A.

Iliff, J. J. *et al.* (2014a) 'Impairment of Glymphatic Pathway Function Promotes Tau Pathology after Traumatic Brain Injury', *The Journal of Neuroscience*, 34(49), pp. 16180–16193. doi: 10.1523/JNEUROSCI.3020-14.2014.

Iliff, J. J. *et al.* (2014b) 'Impairment of Glymphatic Pathway Function Promotes Tau Pathology after Traumatic Brain Injury', *The Journal of Neuroscience*, 34(49), pp. 16180–16193. doi: 10.1523/JNEUROSCI.3020-14.2014.

Jackson, R. T., Tigges, J. and Arnold, W. (1979) 'Subarachnoid Space of the CNS, Nasal Mucosa, and Lymphatic System', *Archives of Otolaryngology - Head and Neck Surgery*, 105(4), pp. 180–184. doi: 10.1001/archotol.1979.00790160014003.

Jeong, H. L. *et al.* (2004) 'CSF flow quantification of the cerebral aqueduct in normal volunteers using phase contrast cine MR imaging', *Korean Journal of Radiology*, 5(2), pp. 81–86.

Jergović, I. *et al.* (2016) 'Transient obstructive hydrocephalus in patients with intracerebral hemorrhage: Report of two cases', *Acta Clinica Croatica*, 55(3), pp. 497–499. doi: 10.20471/acc.2016.55.03.21.

Jessen, N. A. *et al.* (2015) 'The Glymphatic System – A Beginner's Guide Nadia', *Neurochemical Research*, 40(12), pp. 2583–2599. doi: 10.1007/s11064-015-1581-6.The.

Jiang, Q. *et al.* (2017) 'Impairment of the glymphatic system after diabetes', *Journal of Cerebral Blood Flow and Metabolism*, 37(4), pp. 1326–1337. doi: 10.1177/0271678X16654702.

Jin, B.-J., Smith, A. J. and Verkman, A. S. (2016) 'Spatial model of convective solute transport in brain extracellular space does not support a "glymphatic" mechanism', *Journal of General Physiology*, 148(6), pp. 489–501. doi: 10.1085/jgp.201611684.

Jones, H. C. and Bucknall, R. M. (1987) 'Changes in cerebrospinal fluid pressure and outflow from the lateral ventricles during development of congenital hydrocephalus in the H-Tx rat', *Experimental Neurology*, 98(3), pp. 573–583. doi: 10.1016/0014-4886(87)90266-4.

Jordan, J. D. and Powers, W. J. (2012) 'Cerebral autoregulation and acute ischemic stroke', *American Journal of Hypertension*, 25(9), pp. 946–950. doi: 10.1038/ajh.2012.53.

Jorge, F. (2010) 'Fluid transport across leaky epithelia: Central role of the tight junction and supporting role of aquaporins', *Physiological Reviews*, 90(4), pp. 1271–1290. doi: 10.1152/physrev.00025.2009.

Kalavagunta, C., Michaeli, S. and Metzger, G. J. (2014) 'In vitro Gd-DTPA relaxometry studies in oxygenated venous human blood and aqueous solution at 3 and 7T', *Contrast Media and Molecular Imaging*, 9(2), pp. 169–176. doi: 10.1002/cmmi.1568.

Kameyama, M., Murakami, K. and Jinzaki, M. (2016) 'Comparison of [(15)O] H2O Positron Emission Tomography and Functional Magnetic Resonance Imaging in Activation Studies.', *World journal of nuclear medicine*, 15(1), pp. 3–6. doi: 10.4103/1450-1147.172139.

Kao, C. H. *et al.* (1998) 'Detection of recurrent or persistent nasopharyngeal carcinomas after radiotherapy with 18-fluoro-2-deoxyglucose positron emission tomography and comparison with computed tomography.', *Journal of Clinical Oncology*, 16(11), pp. 3550–3555. doi: 10.1200/JCO.1998.16.11.3550.

Katzman, R. *et al.* (1977) 'Report of Joint Committee for Stroke Resources. IV. Brain edema in stroke.', *Stroke*, 8(4), pp. 512–540. doi: 10.1161/01.STR.8.4.512.

Kazmi, S. M. S. *et al.* (2015) 'Expanding applications, accuracy, and interpretation of laser speckle contrast imaging of cerebral blood flow', *Journal of Cerebral Blood Flow and Metabolism*, 35(7), pp. 1076–1084. doi: 10.1038/jcbfm.2015.84.

Key and Peele (1875) 'Studien in der Anatomie des Nervensystems und des Bindegewebes'.

Kida, S., Pantazis, A. and Weller, R. O. (1993) 'CSF drains directly from the subarachnoid space into nasal lymphatics in the rat. Anatomy, histology and immunological significance', *Neuropathology and Applied Neurobiology*, 19(6), pp. 480–488. doi: 10.1111/j.1365-2990.1993.tb00476.x.

Kjeldsen, S. E. and Berge, E. (2015) 'Blood pressure and early neurological deterioration in acute ischemic stroke', *Journal of Hypertension*, 33(10), pp. 2020–2021. doi: 10.1097/HJH.0000000000000689.

Klarica, M., Radoš, M. and Orešković, D. (2019a) 'The Movement of Cerebrospinal Fluid and Its Relationship with Substances Behavior in Cerebrospinal and Interstitial Fluid', *Neuroscience*, 414, pp. 28–48. doi: 10.1016/j.neuroscience.2019.06.032.

Klarica, M., Radoš, M. and Orešković, D. (2019b) 'The Movement of Cerebrospinal Fluid and Its Relationship with Substances Behavior in Cerebrospinal and Interstitial Fluid', *Neuroscience*, 414, pp. 28–48. doi: 10.1016/j.neuroscience.2019.06.032.

Koenig, S. H. and Brown, R. D. (1984) 'Relaxation of solvent protons by paramagnetic ions and its dependence on magnetic field and chemical environment: implications for NMR imaging', *Magnetic Resonance in Medicine*, 1(4), pp. 478–495. doi: 10.1002/mrm.1910010407.

Kotwica, Z., H, H. G. and Persson, L. (1991) 'Intracranial pressure changes following middle cerebral artery occlusion in rats', pp. 99–104.

Kudo, K. *et al.* (2018a) 'Indirect proton MR imaging and kinetic analysis of 17O-labeled water tracer in the brain', *Magnetic Resonance in Medical Sciences*, 17(3), pp. 223–230. doi: 10.2463/mrms.mp.2017-0094.

Kudo, K. *et al.* (2018b) 'Indirect Proton MR Imaging and Kinetic Analysis of 17O-Labeled Water Tracer in the Brain', *Magnetic Resonance in Medical Sciences*, 17(3), pp. 223–230. doi: 10.2463/mrms.mp.2017-0094.

Lalou, A. D. *et al.* (2018) 'Cerebral autoregulation, cerebrospinal fluid outflow resistance, and outcome following cerebrospinal fluid diversion in normal pressure hydrocephalus', *Journal of Neurosurgery*, pp. 1–9. doi: 10.3171/2017.7.JNS17216.

Lee, H. *et al.* (2015) 'The Effect of Body Posture on Brain Glymphatic Transport', *Journal of Neuroscience*, 35(31), pp. 11034–11044. doi: 10.1523/JNEUROSCI.1625-15.2015.

Lee, H. *et al.* (2018a) 'Quantitative Gd-DOTA uptake from cerebrospinal fluid into rat brain using 3D VFA-SPGR at 9.4T', *Magnetic Resonance in Medicine*, 79(3), pp. 1568–1578. doi: 10.1002/mrm.26779.

Lee, H. *et al.* (2018b) 'Quantitative Gd-DOTA uptake from cerebrospinal fluid into rat brain using 3D VFA-SPGR at 9.4T', *Magnetic Resonance in Medicine*, 79(3), pp. 1568–1578. doi: 10.1002/mrm.26779.

Lee, H. *et al.* (2018c) 'Quantitative Gd-DOTA uptake from cerebrospinal fluid into rat brain using 3D VFA-SPGR at 9.4T', *Magnetic resonance in medicine*, 79(3), p. 1568—1578. doi: 10.1002/mrm.26779.

Levine, J. E., Povlishock, J. T. and Becker, D. P. (1982) 'The morphological correlates of primate cerebrospinal fluid absorption', *Brain Research*, 241(1), pp. 31–41. doi: 10.1016/0006-8993(82)91225-2.

Levitt, M. H. (2013) *Spin Dynamics: Basics of Nuclear Magnetic Resonance*. Wiley. Available at: https://books.google.co.uk/books?id=bysFAa4MPQcC.

Lewis, P. M. *et al.* (2014) 'A Continuous Correlation Between Intracranial Pressure and Cerebral Blood Flow Velocity Reflects Cerebral Autoregulation Impairment During Intracranial Pressure Plateau Waves', *Neurocritical Care*, 21(3), pp. 514–525. doi: 10.1007/s12028-014-9994-7.

Liao, S. and Padera, T. P. (2013) 'Lymphatic Function and Immune Regulation in Health and Disease', *Lymphatic Research and Biology*, 11(3), pp. 136–143. doi: 10.1089/lrb.2013.0012.

Longa, E Z *et al.* (1989) 'Reversible middle cerebral artery occlusion without

craniectomy in rats.', *Stroke*, 20(1), pp. 84–91. doi: 10.1161/01.STR.20.1.84.

Longa, Enrique Zea *et al.* (1989a) 'Reversible middle cerebral artery occlusion without craniectomy in rats', *Stroke*, 20(1), pp. 84–91. doi: 10.1161/01.STR.20.1.84.

Longa, Enrique Zea *et al.* (1989b) 'Reversible middle cerebral artery occlusion without craniectomy in rats', *Stroke*, 20(1), pp. 84–91. doi: 10.1161/01.STR.20.1.84.

Louveau, A. *et al.* (2015) 'Structural and functional features of central nervous system lymphatic vessels', *Nature*, 523(7560), pp. 337–341. doi: 10.1038/nature14432.

Mann, J. D. *et al.* (1978) 'Regulation of intracranial pressure in rat, dog, and man', *Annals of Neurology*, 3(2), pp. 156–165. doi: 10.1002/ana.410030212.

Mao, X., Enno, T. L. and Del Bigio, M. R. (2006) 'Aquaporin 4 changes in rat brain with severe hydrocephalus', *European Journal of Neuroscience*, 23(11), pp. 2929–2936. doi: 10.1111/j.1460-9568.2006.04829.x.

Marmarou, A., Shulman, K. and Rosende, R. M. (1978) 'A nonlinear analysis of the cerebrospinal fluid system and intracranial pressure dynamics.', *Journal of neurosurgery*, 48(3), pp. 332–44. doi: 10.3171/jns.1978.48.3.0332.

Mathiisen, T. M. *et al.* (2010) 'The perivascular astroglial sheath provides a complete covering of the brain microvessels: An electron microscopic 3D reconstruction', *Glia*, 58(9), pp. 1094–1103. doi: 10.1002/glia.20990.

May, C. *et al.* (1990) 'Cerebrospinal fluid production is reduced in healthy aging', *Neurology*, 40(3, Part 1), pp. 500–500. doi: 10.1212/WNL.40.3_Part_1.500.

McGarry, B. L. *et al.* (2017) 'A Magnetic Resonance Imaging Protocol for Stroke Onset Time Estimation in Permanent Cerebral Ischemia', *Journal of Visualized Experiments*, (127), pp. 1–6. doi: 10.3791/55277.

McRobbie, D. W. *et al.* (2006) *MRI From Picture to Proton*. Cambridge: Cambridge University Press. doi: 10.1017/CBO9780511545405.

Meadows, J. *et al.* (2000) 'Asymptomatic Chiari Type I malformations identified on magnetic resonance imaging', *Journal of Neurosurgery*, 92(6), pp. 920–926. doi: 10.3171/jns.2000.92.6.0920.

Mehrabian, H. *et al.* (2018) 'Evaluation of Glioblastoma Response to Therapy With Chemical Exchange Saturation Transfer', *International Journal of Radiation Oncology*Biology*Physics*, 101(3), pp. 713–723. doi: 10.1016/j.ijrobp.2018.03.057.

Meiboom, S. (1961a) 'Nuclear magnetic resonance study of the proton transfer in water', *The Journal of Chemical Physics*, 34(2), pp. 375–388. doi: 10.1063/1.1700960.

Meiboom, S. (1961b) 'Nuclear magnetic resonance study of the proton transfer in water', *The Journal of Chemical Physics*, 34(2), pp. 375–388. doi: 10.1063/1.1700960.

Meiboom, S. (1961c) 'Nuclear Magnetic Resonance Study of the Proton Transfer in Water', *The Journal of Chemical Physics*, 34(2), pp. 375–388. doi: 10.1063/1.1700960.

Meiboom, S. and Gill, D. (1958) 'Modified Spin-Echo Method for Measuring Nuclear Relaxation Times', *Review of Scientific Instruments*, 29(8), pp. 688–691. doi: 10.1063/1.1716296.

Mestre, H. *et al.* (2018) 'Aquaporin-4-dependent glymphatic solute transport in the rodent brain', *eLife*, 7. doi: 10.7554/eLife.40070.

Mestre, H., Hablitz, L. M., *et al.* (2020) 'Cerebrospinal fluid influx drives acute ischemic tissue swelling', *Science*, 13.

Mestre, H., Du, T., *et al.* (2020) 'Cerebrospinal fluid influx drives acute ischemic tissue swelling', *Science*, 367(6483), p. eaax7171. doi: 10.1126/science.aax7171.

Mestre, H., Mori, Y. and Nedergaard, M. (2020) 'The Brain's Glymphatic System: Current Controversies', *Trends in Neurosciences*. The Author(s), 43(7), pp. 458–466. doi: 10.1016/j.tins.2020.04.003.

Mhairi, M. I. (1992) 'New models of focal cerebral ischaemia.', *British Journal of Clinical Pharmacology*, 34(4), pp. 302–308. doi: 10.1111/j.1365-2125.1992.tb05634.x.

Ming Zhang and Gunturk, B. K. (2008) 'Multiresolution Bilateral Filtering for Image Denoising', *IEEE Transactions on Image Processing*, 17(12), pp. 2324–2333. doi: 10.1109/TIP.2008.2006658.

Mobasheri, A. and Marples, D. (2004) 'Expression of the AQP-1 water channel in normal human tissues: A semiquantitative study using tissue microarray technology', *American Journal of Physiology - Cell Physiology*, 286(3 55-3), pp. 529–537. doi: 10.1152/ajpcell.00408.2003.

Mokri, B. (2001) 'The Monro-Kellie hypothesis: Applications in CSF volume depletion', *Neurology*, 56(12), pp. 1746–1748. doi: 10.1212/WNL.56.12.1746.

Murtha, Lucy A. *et al.* (2014) 'Cerebrospinal fluid is drained primarily via the spinal canal and olfactory route in young and aged spontaneously hypertensive rats', *Fluids and Barriers of the CNS*, 11(1), pp. 1–9. doi: 10.1186/2045-8118-11-12.

Murtha, L. A. *et al.* (2014) 'Short-duration hypothermia after ischemic stroke prevents delayed intracranial pressure rise', *International Journal of Stroke*, 9(5), pp. 553–559. doi: 10.1111/ijs.12181.

Murtha, Lucy A. *et al.* (2015) 'Intracranial pressure elevation after ischemic stroke in rats: Cerebral edema is not the only cause, and short-duration mild hypothermia is a highly effective preventive therapy', *Journal of Cerebral Blood Flow and Metabolism*. Nature Publishing Group, 35(4), pp. 592–600. doi: 10.1038/jcbfm.2014.230.

Murtha, Lucy A *et al.* (2015) 'Intracranial Pressure Elevation after Ischemic Stroke in Rats: Cerebral Edema is not the only Cause, and Short-Duration Mild Hypothermia is a Highly Effective Preventive Therapy', *Journal of Cerebral Blood Flow & Metabolism*, 35(12), pp. 2109–2109. doi: 10.1038/jcbfm.2015.209.

Nagra, G. *et al.* (2010) 'Elevated CSF outflow resistance associated with impaired lymphatic CSF absorption in a rat model of kaolin-induced communicating hydrocephalus', *Cerebrospinal Fluid Research*, 7, pp. 1–8. doi: 10.1186/1743-8454-7-4.

Ng, Y. S. *et al.* (2007) 'Comparison of clinical characteristics and functional outcomes of ischemic stroke in different vascular territories', *Stroke*, 38(8), pp. 2309–2314. doi: 10.1161/STROKEAHA.106.475483.

Nicchia, G. P. *et al.* (2003) 'Inhibition of AQP4 expression in astrocytes by RNAi determines alterations in cell morphology, growth, and water transport and induces changes in ischemia related genes', *FASEB Journal*, 17(11). doi: 10.1096/fj.02-1183fje.

Ohara, S. *et al.* (1988) 'MR imaging of CSF pulsatory flow and its relation to intracranial pressure', *Journal of Neurosurgery*, 69(5), pp. 675–682. doi: 10.3171/jns.1988.69.5.0675.

Oliver, G. (2004) 'Lymphatic vasculature development', *Nature Reviews Immunology*, 4(1), pp. 35–45. doi: 10.1038/nri1258.

Oosuka, S. *et al.* (2020) 'Effects of an Aquaporin 4 Inhibitor, TGN-020, on Murine Diabetic Retina', *International Journal of Molecular Sciences*, 21(7), p. 2324. doi: 10.3390/ijms21072324.

Orešković, D. and Klarica, M. (2014) 'Measurement of cerebrospinal fluid formation and absorption by ventriculo-cisternal perfusion: what is really measured?', *Croatian Medical Journal*, 55(4), pp. 317–327. doi: 10.3325/cmj.2014.55.317.

Oshio, K. (2004) 'Reduced cerebrospinal fluid production and intracranial pressure in mice lacking choroid plexus water channel Aquaporin-1', *The FASEB Journal*, 17, pp. 1–17. doi: 10.1096/fj.04-1711fje.

Oshio, K. *et al.* (2005) 'Reduced cerebrospinal fluid production and intracranial pressure in mice lacking choroid plexus water channel Aquaporin-1', *The FASEB Journal*, 19(1), pp. 76–78. doi: 10.1096/fj.04-1711fje.

Papadopoulos, M. C. and Verkman, A. S. (2013) 'Aquaporin water channels in the nervous system', *Nature Reviews Neuroscience*, 14(4), pp. 265–277. doi: 10.1038/nrn3468.

Patlak, C. and Fenstermacher, J. (1975) 'Measurements of dog blood-brain transfer constants by ventriculocisternal perfusion', *American Journal of Physiology-Legacy Content*, 229(4), pp. 877–884. doi: 10.1152/ajplegacy.1975.229.4.877.

Paxinos, G. and Watson, C. (2007) 'The rat brain atlas in stereotaxic coordinates 6th edition', *Elsevier*.

Pirici, I. *et al.* (2017) 'Inhibition of Aquaporin-4 Improves the Outcome of Ischaemic Stroke and Modulates Brain Paravascular Drainage Pathways', *International Journal of Molecular Sciences*, 19(1), p. 46. doi: 10.3390/ijms19010046.

Pirici, I. *et al.* (2018) 'Inhibition of aquaporin-4 improves the outcome of ischaemic stroke and modulates brain paravascular drainage pathways', *International Journal of Molecular Sciences*, 19(1), pp. 1–18. doi: 10.3390/ijms19010046.

Pizzo, M. E. *et al.* (2018) 'Intrathecal antibody distribution in the rat brain: surface diffusion, perivascular transport and osmotic enhancement of delivery', *The Journal of Physiology*, 596(3), pp. 445–475. doi: 10.1113/JP275105.

Plog, B. A. *et al.* (2015) 'Biomarkers of Traumatic Injury Are Transported from Brain to Blood via the Glymphatic System', *The Journal of Neuroscience*, 35(2), pp. 518–526. doi: 10.1523/JNEUROSCI.3742-14.2015.

Pollay, M. and Curl, F. (1967) 'Secretion of cerebrospinal fluid by the ventricular ependyma of the rabbit.', *The American journal of physiology*, 213(4), pp. 1031–1038. doi: 10.1152/ajplegacy.1967.213.4.1031.

Pollay, M. and Welch, K. (1962) 'The function and structure of canine arachnoid villi', *Journal of Surgical Research*, 2(5), pp. 307–311. doi: 10.1016/S0022-4804(62)80039-0.

Pollock, J. M. *et al.* (2009) 'Hypercapnia-induced cerebral hyperperfusion: An underrecognized clinical entity', *American Journal of Neuroradiology*, 30(2), pp. 378–385. doi: 10.3174/ajnr.A1316.

Praetorius, J. and Nielsen, S. (2006) 'Distribution of sodium transporters and aquaporin-1 in the human choroid plexus', *American Journal of Physiology-Cell Physiology*, 291(1), pp. C59–C67. doi: 10.1152/ajpcell.00433.2005.

Preston, G. M. *et al.* (1992) 'Appearance of Water Channels in Xenopus Oocytes Expressing Red Cell CHIP28 Protein', *Science*, 256(5055), pp. 385–387. doi: 10.1126/science.256.5055.385.

Price, S. J. and T. (2008) '基因的改变NIH Public Access', *Bone*, 23(1), pp. 1–7. doi: 10.1038/jid.2014.371.

Ratner, V. *et al.* (2015) 'Optimal-mass-transfer-based estimation of glymphatic transport in living brain', *Proceedings of SPIE--the International Society for Optical Engineering*. 2015/03/20, 9413, p. 94131J. doi: 10.1117/12.2076289.

Ray, L., Iliff, J. J. and Heys, J. J. (2019) 'Analysis of convective and diffusive transport in the brain interstitium', *Fluids and Barriers of the CNS*. BioMed Central, 16(1), pp. 1–18. doi: 10.1186/s12987-019-0126-9.

Read, S. J. *et al.* (2000) 'The fate of hypoxic tissue on 18F-fluoromisonidazole positron emission tomography after ischemic stroke', *Annals of Neurology*, 48, pp. 228–235. doi: 10.1002/1531-8249(200008)48:2<228::AID-ANA13>3.0.CO;2-B.

Rehncrona, S. (1985) 'Brain acidosis', *Annals of Emergency Medicine*, 14(8), pp. 770–776. doi: 10.1016/S0196-0644(85)80055-X.

Ren, Z. *et al.* (2013) '"Hit & Run" model of closed-skull traumatic brain injury (TBI) reveals complex patterns of post-traumatic AQP4 dysregulation', *Journal of Cerebral Blood Flow and Metabolism*. Nature Publishing Group, 33(6), pp. 834–845. doi: 10.1038/jcbfm.2013.30.

Rennels, M. L. *et al.* (1985) 'Evidence for a "Paravascular" fluid circulation in the mammalian central nervous system, provided by the rapid distribution of tracer protein throughout the brain from the subarachnoid space', *Brain Research*, 326(1), pp. 47–63. doi: 10.1016/0006-8993(85)91383-6.

Richardson, S. J. (1989) 'Contribution of proton exchange to the oxygen-17 nuclear magnetic resonance transverse relaxation rate in water and starch-water systems', *Cereal Chemistry*, 66,(3), pp. 244–246.

Ringstad, G., Vatnehol, S. A. S. and Eide, P. K. (2017) 'Glymphatic MRI in idiopathic normal pressure hydrocephalus', *Brain*, 140(10), pp. 2691–2705. doi: 10.1093/brain/awx191.

Roehn-berlage, M. *et al.* (1995) 'Evolution of Regional Changes in Apparent Diffusion Coefficient During Focal Ischemia of Rat Brain : The Relationship of Quantitative Diffusion NMR Imaging to Reduction in Cerebral Blood Flow and Metabolic Disturbances', pp. 1002–1011.

Rolfe, D. F. and Brown, G. C. (1997) 'Cellular energy utilization and molecular origin of standard metabolic rate in mammals', *Physiological Reviews*, 77(3), pp. 731–758. doi: 10.1152/physrev.1997.77.3.731.

Ronen, I. and Navon, G. (1994) 'A new method for proton detection of H217O with potential applications for functional MRI', *Magnetic Resonance in Medicine*, 32(6), pp. 789–793. doi: 10.1002/mrm.1910320616.

Ropper, A. H. (1984) 'Brain Edema After Stroke', *Archives of Neurology*, 41(1), p. 26. doi: 10.1001/archneur.1984.04050130032017.

Rosenberg, G. A., Kyner, W. T. and Estrada, E. (1980) 'Bulk flow of brain interstitial fluid under normal and hyperosmolar conditions', *American Journal of Physiology-Renal Physiology*, 238(1), pp. F42–F49. doi: 10.1152/ajprenal.1980.238.1.F42.

Sakka, L., Coll, G. and Chazal, J. (2011) 'Anatomy and physiology of cerebrospinal fluid', *European Annals of Otorhinolaryngology, Head and Neck Diseases*, 128(6), pp. 309–316. doi: 10.1016/j.anorl.2011.03.002.

SATO, O. *et al.* (1971) 'Formation of Cerebrospinal Fluid in Spinal Subarachnoid Space', *Nature*, 233(5315), pp. 129–130. doi: 10.1038/233129a0.

Schneider, F. *et al.* (1995) 'Mood effects on limbic blood flow correlate with emotional self-rating: A PET study with oxygen-15 labeled water', *Psychiatry Research: Neuroimaging*, 61(4), pp. 265–283. doi: 10.1016/0925-4927(95)02678-Q.

Schwab, S. *et al.* (1996) 'The value of intracranial pressure monitoring in acute hemispheric stroke', *Neurology*, 47(2), pp. 393–398. doi: 10.1212/WNL.47.2.393.

Segal, M. B. and Pollay, M. (1977) 'The Secretion o f Cerebrospinal Fluid Sherrington School of Physiology , St Thomas ' s Hospital Medical School , London S . E . 1 , England Division of Neurosurgery , University of New Mexico School of Medicine , Albuquerque , New Mexico , U . S . A . (a', pp. 127–148.

Seners, P. *et al.* (2015) 'Incidence, causes and predictors of neurological deterioration occurring within 24 h following acute ischaemic stroke: a systematic review with pathophysiological implications', *Journal of Neurology, Neurosurgery & Psychiatry*, 86(1), pp. 87–94. doi: 10.1136/jnnp-2014-308327.

Seners, P. and Baron, J. C. (2018) 'Revisiting "progressive stroke": incidence, predictors, pathophysiology, and management of unexplained early neurological deterioration following acute ischemic stroke', *Journal of Neurology*. Springer Berlin Heidelberg, 265(1), pp. 216–225. doi: 10.1007/s00415-017-8490-3.

Siesjö, B. K. (1992) 'Pathophysiology and treatment of focal cerebral ischemia', *Journal of Neurosurgery*, 77(2), pp. 169–184. doi: 10.3171/jns.1992.77.2.0169.

Silasi, G., MacLellan, C. L. and Colbourne, F. (2009) 'Use of telemetry blood pressure transmitters to measure intracranial pressure (ICP) in freely moving rats.', *Current neurovascular research*, 6(1), pp. 62–69. doi: 10.2174/156720209787466046.

Silver, I. *et al.* (2002) 'Cerebrospinal fluid outflow resistance in sheep: Impact of blocking cerebrospinal fluid transport through the cribriform plate', *Neuropathology and Applied Neurobiology*, 28(1), pp. 67–74. doi: 10.1046/j.1365-2990.2002.00373.x.

Simon, M. and Iliff, J. (2019) 'Rebuttal from Matthew Simon and Jeffrey Iliff', *The Journal of Physiology*, 597(17), pp. 4425–4426. doi: 10.1113/JP278460.

Smith, A. J. and Verkman, A. S. (2018) 'The "glymphatic" mechanism for solute clearance in Alzheimer's disease: game changer or unproven speculation?', *FASEB journal : official publication of the Federation of American Societies for Experimental Biology*. 2018/01/03. Federation of American Societies for Experimental Biology, 32(2), pp. 543–551. doi: 10.1096/fj.201700999.

Smith, A. J. and Verkman, A. S. (2019) 'Rebuttal from Alex J. Smith and Alan S. Verkman', *The Journal of Physiology*, 597(17), pp. 4427–4428. doi: 10.1113/JP278461.

Solenov, E. *et al.* (2004) 'Sevenfold-reduced osmotic water permeability in primary astrocyte cultures from AQP-4-deficient mice, measured by a fluorescence quenching method', *American Journal of Physiology-Cell Physiology*, 286(2), pp. C426–C432. doi: 10.1152/ajpcell.00298.2003.

Stejskal, E. O. and Tanner, J. E. (1965) 'Spin Diffusion Measurements: Spin Echoes in the Presence of a Time-Dependent Field Gradient', *The Journal of Chemical Physics*, 42(1), pp. 288–292. doi: 10.1063/1.1695690.

Stevens E, Emmett E, W. (2017) 'The Burden of Stoke in Europe', *London: Stroke Alliance for Europe*.

Strandgaard, S. (2004) 'The management of elevated blood pressure in acute stroke: Preferential use of angiotensin II receptor antagonists?', *Journal of Hypertension*, 22(5), pp. 877–878. doi: 10.1097/00004872-200405000-00004.

Stroke.org.uk (2018) 'State of the Nation Stroke Statistics'.

Suzuki, Y. *et al.* (2013) 'Aquaporin-4 Positron Emission Tomography Imaging of the Human Brain: First Report', *Journal of Neuroimaging*, 23(2), pp. 219–223. doi: 10.1111/j.1552-6569.2012.00704.x.

Swift, T. J. and Connick, R. E. (1962) 'NMR-Relaxation Mechanisms of O 17 in Aqueous Solutions of Paramagnetic Cations and the Lifetime of Water Molecules in the First Coordination Sphere', *The Journal of Chemical Physics*, 37(2), pp. 307–320. doi: 10.1063/1.1701321.

Syková, E. and Nicholson, C. (2008) 'Diffusion in Brain Extracellular Space', *Physiological Reviews*, 88(4), pp. 1277–1340. doi: 10.1152/physrev.00027.2007.

Szentistvanyi, I. *et al.* (1984) 'Drainage of interstitial fluid from different regions

of rat brain', *American Journal of Physiology-Renal Physiology*, 246(6), pp. F835–F844. doi: 10.1152/ajprenal.1984.246.6.F835.

Tailor, D. R. *et al.* (2004) 'Proton MRI of metabolically produced H217O using an efficient 17O2 delivery system', *NeuroImage*, 22(2), pp. 611–618. doi: 10.1016/j.neuroimage.2004.02.024.

Tait, M. J. *et al.* (2008) 'Water movements in the brain: role of aquaporins', *Trends in Neurosciences*, 31(1), pp. 37–43. doi: 10.1016/j.tins.2007.11.003.

Tang, G. and Yang, G.-Y. (2016) 'Aquaporin-4: A Potential Therapeutic Target for Cerebral Edema', *International Journal of Molecular Sciences*, 17(10), p. 1413. doi: 10.3390/ijms17101413.

Taoka, T. *et al.* (2018) 'Impact of the Glymphatic System on the Kinetic and Distribution of Gadodiamide in the Rat Brain: Observations by Dynamic MRI and Effect of Circadian Rhythm on Tissue Gadolinium Concentrations', *Investigative Radiology*, 53(9). Available at: https://journals.lww.com/investigativeradiology/Fulltext/2018/09000/Impact_of_the_Glymphatic_System_on_the_Kinetic_and.3.aspx.

Tariq, N. and Khatri, R. (2008) 'Leptomeningeal collaterals in acute ischemic stroke.', *Journal of vascular and interventional neurology*, 1(4), pp. 91–5. Available at: http://www.ncbi.nlm.nih.gov/pubmed/24721756.

Thanvi, B., Treadwell, S. and Robinson, T. (2008) 'Early neurological deterioration in acute ischaemic stroke: Predictors, mechanisms and management', *Postgraduate Medical Journal*, 84(994), pp. 412–417. doi: 10.1136/pgmj.2007.066118.

Thomas, D. L. *et al.* (2005) '3D MDEFT imaging of the human brain at 4.7 T with reduced sensitivity to radiofrequency inhomogeneity', *Magnetic Resonance in Medicine*, 53(6), pp. 1452–1458. doi: 10.1002/mrm.20482.

Tisserand, M. *et al.* (2014) 'Mechanisms of unexplained neurological deterioration after intravenous thrombolysis', *Stroke*, 45(12), pp. 3527–3534. doi: 10.1161/STROKEAHA.114.006745.

Ueno, M. *et al.* (2014) 'Clearance of Beta-Amyloid in the Brain', *Current Medicinal Chemistry*, 21(35), pp. 4085–4090. doi: 10.2174/0929867321666141011194256.

Venkat, P. *et al.* (2018) 'White matter damage and glymphatic dysfunction in a model of vascular dementia in rats with no prior vascular pathologies', pp. 96–106. doi: 10.1016/j.neurobiolaging.2016.11.002.White.

Verkman, A. S. *et al.* (2013) 'Biology of AQP4 and Anti-AQP4 Antibody: Therapeutic Implications for NMO', *Brain Pathology*, 23(6), pp. 684-695. doi: 10.1111/bpa.12085.

Verkman, A. S. *et al.* (2017) 'Aquaporin Water Channels and Hydrocephalus', *Pediatric Neurosurgery*, 52(6), pp. 409–416. doi: 10.1159/000452168.

Vila, N. *et al.* (2003) 'Levels of anti-inflammatory cytokines and neurological worsening in acute ischemic stroke', *Stroke*, 34(3), pp. 671–675. doi: 10.1161/01.STR.0000057976.53301.69.

Walter, E. (2015) '(2) the Profound'.

Warlow, C. *et al.* (2003) 'Stroke', *The Lancet*, 362(9391), pp. 1211–1224. doi: 10.1016/S0140-6736(03)14544-8.

Weed, L. H. (1914) 'Studies on Cerebro-Spinal Fluid. No. IV : The dual Source of Cerebro-Spinal Fluid.', *The Journal of medical research*, 31(1), pp. 93-118.11. Available at:
http://www.ncbi.nlm.nih.gov/pubmed/19972195%0Ahttp://www.pubmedcentral.nih.gov/articlerender.fcgi?artid=PMC2094440.

Wei, F. *et al.* (2017) 'The pathway of subarachnoid CSF moving into the spinal parenchyma and the role of astrocytic aquaporin-4 in this process', *Life Sciences*. Elsevier Inc., 182, pp. 29–40. doi: 10.1016/j.lfs.2017.05.028.

Weiskopf, N. *et al.* (2013) 'Quantitative multi-parameter mapping of R1, PD*, MT, and R2* at 3T: A multi-center validation', *Frontiers in Neuroscience*, (7 JUN). doi: 10.3389/fnins.2013.00095.

WELCH, K., ARAKI, H. and ARKINS, T. (1972) 'Electrical Potentials of the Lamina Epithelialis Choroidea of the Fourth Ventricle of the Cat In Vitro: Relationship to the CSF Blood Potential', *Developmental Medicine & Child Neurology*, 14, pp. 146–151. doi: 10.1111/j.1469-8749.1972.tb09788.x.

Wells, A. J. *et al.* (2015) 'Elevated intracranial pressure and cerebral edema following permanent MCA occlusion in an ovine model', *PLoS ONE*, 10(6), pp. 1–20. doi: 10.1371/journal.pone.0130512.

Wiendl, H. *et al.* (2015) 'Gaps Between Aims and Achievements in Therapeutic Modification of Neuronal Damage ("Neuroprotection")', *Neurotherapeutics*, 12(2), pp. 449–454. doi: 10.1007/s13311-015-0348-8.

Williamson, M. R. *et al.* (2019) 'Acetazolamide Mitigates Intracranial Pressure Spikes Without Affecting Functional Outcome After Experimental Hemorrhagic Stroke', *Translational Stroke Research*. Translational Stroke Research, 10(4), pp. 428–439. doi: 10.1007/s12975-018-0663-6.

Wong, Y. Y. *et al.* (2013) '11C-Acetate Clearance as an Index of Oxygen Consumption of the Right Myocardium in Idiopathic Pulmonary Arterial Hypertension: A Validation Study Using 15O-Labeled Tracers and PET', *Journal of Nuclear Medicine*, 54(8), pp. 1258-1262. doi: 10.2967/jnumed.112.115915.

Xie, L. *et al.* (2013) 'Sleep drives metabolite clearance from the adult brain', *Science*, 342(6156), pp. 373–377. doi: 10.1126/science.1241224.

Xu, Z. *et al.* (2015a) 'Deletion of aquaporin-4 in APP/PS1 mice exacerbates brain Aß accumulation and memory deficits', *Molecular Neurodegeneration*. Molecular Neurodegeneration, 10(1), pp. 1–16. doi: 10.1186/s13024-015-0056-1.

Xu, Z. *et al.* (2015b) 'Deletion of aquaporin-4 in APP/PS1 mice exacerbates brain Aß accumulation and memory deficits', *Molecular Neurodegeneration*, 10(1), p. 58. doi: 10.1186/s13024-015-0056-1.

Yamada, S. *et al.* (2013) 'Influence of respiration on cerebrospinal fluid movement using magnetic resonance spin labeling', *Fluids and Barriers of the CNS*, 10(1), p. 36. doi: 10.1186/2045-8118-10-36.

Yang, L. *et al.* (2013) 'Evaluating glymphatic pathway function utilizing clinically relevant intrathecal infusion of CSF tracer', *Journal of Translational Medicine*, 11(1), p. 107. doi: 10.1186/1479-5876-11-107.

Yool, A. J. *et al.* (2013) 'AqF026 is a pharmacologic agonist of the water channel aquaporin-1', *Journal of the American Society of Nephrology*, 24(7), pp. 1045–1052. doi: 10.1681/ASN.2012080869.

Yoshimoto, S. *et al.* (1990) 'Cerebral microvessel endothelium is producing endothelin', *Brain Research*, 508(2), pp. 283–285. doi: 10.1016/0006-8993(90)90407-3.

Zhu, X.-H. *et al.* (2005) 'In vivo17O NMR approaches for brain study at high field', *NMR in Biomedicine*, 18(2), pp. 83–103. doi: 10.1002/nbm.930.

Zhu, X.-H. and Chen, W. (2011) 'In vivo oxygen-17 NMR for imaging brain oxygen metabolism at high field', *Progress in Nuclear Magnetic Resonance Spectroscopy*, 59(4), pp. 319–335. doi: 10.1016/j.pnmrs.2011.04.002.